THE RELICS OF STRUCTURE FORMATION

HIGH-VELOCITY CLOUDS AROUND THE ANDROMEDA GALAXY AND THE MILKY WAY

Dissertation

zur

Erlangung des Doktorgrades (Dr. rer. nat.)

der

Mathematisch-Naturwissenschaftlichen Fakultät

 der

Rheinischen Friedrich-Wilhelms-Universität Bonn

vorgelegt von

Tobias Westmeier

aus

Korbach

Bonn, Februar 2007

Angefertigt mit Genehmigung der Mathematisch-Naturwissenschaftlichen Fakultät der Rheinischen Friedrich-Wilhelms-Universität Bonn.

Erstgutachter und Betreuer: PD Dr. Jürgen Kerp

Zweitgutachter: Prof. Dr. Klaas S. de Boer

Fachnaher Gutachter: Prof. Dr. Klaus Desch
Fachangrenzender Gutachter: Prof. Dr. Andreas Bott
Externe Gutachterin: Dr. Mary E. Putman

Tag der Promotion: 6. Juni 2007

"Our belief in any particular natural law cannot have a safer basis than our unsuccessful critical attempts to refute it."

(Sir Karl R. Popper, "Conjectures and Refutations: The Growth of Scientific Knowledge", 1969)

Part of this work is based on observations with the 100-m radio telescope of the MPIfR (Max-Planck-Institut für Radioastronomie) at Effelsberg.

The Westerbork Synthesis Radio Telescope is operated by the ASTRON (Netherlands Foundation for Research in Astronomy) with support from the Netherlands Foundation for Scientific Research (NWO).

The National Radio Astronomy Observatory is a facility of the National Science Foundation operated under cooperative agreement by Associated Universities, Inc.

Contents

A	Abstract – Kurzfassung 11				
1	Intr	roduction	15		
	1.1	The discovery and definition of HVCs	15		
	1.2	The distribution of HVCs across the sky	16		
	1.3	The physical parameters of HVCs	20		
		1.3.1 Radial velocities	20		
		1.3.2 Distances	21		
		1.3.3 Metal abundances	23		
		1.3.4 Multi-phase structure	24		
		1.3.5 Interaction with the ambient medium	25		
	1.4	HVC detections at other wavelengths	26		
		1.4.1 Molecular gas in HVCs	26		
		1.4.2 Thermal dust emission from HVCs	27		
		1.4.3 $H\alpha$ emission from HVCs	27		
		1.4.4 X-ray emission from HVCs	28		
	1.5	The origin of HVCs	29		
		1.5.1 Hypotheses about the origin of HVCs	29		
		1.5.2 HVCs as primordial dark-matter halos?	31		
		1.5.3 Compact high-velocity clouds	32		
	1.6	Summary	35		
2	Effe	elsberg HI survey for HVCs around M31	37		
	2.1	The Andromeda Galaxy	37		
		2.1.1 Historic studies	37		
		2.1.2 Modern studies	39		
		2.1.3 The HVC population of M 31	41		
	2.2	Observations, data reduction, and analysis	42		
		2.2.1 Observations	42		
		2.2.2 Data reduction	45		
		2.2.3 Data analysis	47		
		2.2.4 Completeness of the data	47		
	2.3	Search for the CHVC population of M 31	51		

6 Contents

		2.3.1	Discovery of CHVC candidates	
		2.3.2	Consequences of our non-detection	
	2.4		* *	58
		2.4.1	1 1	58
		2.4.2	o a constant of the constant o	65
	2.5	-	<u>*</u>	67
		2.5.1		67
		2.5.2	•	75
		2.5.3	•	78
	2.6	Summa	ry and conclusions	80
3		_		83
	3.1			83
	3.2	Observ	ations and data reduction	
		3.2.1	Sample selection	
		3.2.2	Observations	85
		3.2.3	Data reduction	86
	3.3	Results		88
		3.3.1	General properties of the HVCs	88
		3.3.2	Description of individual HVCs	90
	3.4	The in	ernal structure of the HVCs	93
		3.4.1	Multi-phase structure	93
		3.4.2	Dynamical masses	94
		3.4.3	Virial masses	95
	3.5	The or	gin of the HVCs	96
		3.5.1	Evidence for tidal interaction	96
		3.5.2	Evidence for dark-matter-dominated clouds	98
		3.5.3	Comparison with the satellite galaxies of M 31	00
	3.6	Summa	ary and conclusions	02
4	Low	colum	n density gas in the Galactic halo	15
	4.1	Introdu	action	15
	4.2	Observ	ations	17
		4.2.1	Optical spectroscopy with UVES	17
		4.2.2	HI observations with Effelsberg	18
		4.2.3	HI observations with the VLA	18
	4.3	Results	and discussion	19
	4.4	Summa	ary and conclusions	22
5	Sun	nmary	and outlook 12	25
	5.1		arch for HVCs around M 31	25
	5.2	Optica	absorption line studies of HVCs around M 31	28
\mathbf{Li}	st of	commo	on abbreviations 13	31
Bi	bliog	raphy	1;	33

List of Figures

1.1	The 25-m radio telescope at Dwingeloo	16
1.2	HI Column density map and spectrum of HVC 357.8+12.4-159	17
1.3	All-sky H I column density map of high-velocity clouds	18
1.4	All-sky radial velocity map of high-velocity clouds	19
1.5	Position-velocity diagrams of a model HVC population	21
1.6	${ m H{\sc i}}$ spectrum of HVC 050-68-193 showing a two-component line profile	24
1.7	Examples for head-tail and horseshoe morphology	25
1.8	Sketch of possible formation scenarios for HVCs	29
1.9	Cumulative number of dark-matter halos as a function of circular velocity	31
1.10	HI column density map of HVC 289+33+251	33
1.11	All-sky map showing the distribution and velocities of CHVCs	34
2.1	The Andromeda Galaxy at different wavelengths	38
2.2	The 100-m radio telescope at Effelsberg	40
2.3	LDS map showing the outline of our Effelsberg survey of M 31	42
2.4	Two example spectra from the Effelsberg H I blind survey of M 31	44
2.5	Flow chart of the spectral baseline correction procedure	45
2.6	Antenna pattern of the Effelsberg telescope at $\lambda = 21$ cm	46
2.7	The geometry of the field mapped around M 31	49
2.8	Spatial completeness of the M 31 survey as a function of projected distance.	50
2.9	Fraction of detected spectral lines as a function of signal-to-noise ratio	51
	HI column density maps of our blind survey of M 31	52
	Map of the positions of HVC/CHVC candidates	54
	Example spectra of two CHVC candidates	55
	Locations of the 17 HVCs detected in the Effelsberg survey	58
	Two position-velocity diagrams across M 31 and its HVCs	59
	Histograms of the observational parameters of the 17 detected HVCs. $$	61
	HI spectra of HVCs number 1–9 around M 31	62
	H I spectra of HVCs number 10–17 around M 31	63
	Comparison of HI and virial masses of the HVCs	64
	HI column density map of Davies' Cloud	65
	The extra-planar gas near the eastern and south-eastern edge of M 31. $$	66
2.21	Radial distribution and mass spectrum of the HVCs around M 31	72

8 List of Figures

2.22	Distribution of HVCs as a function of projected distance and HI mass	73
2.23	KS probability for different radial scale lengths	74
2.24	KS probability for different radial scale lengths, combining the HVC complex.	75
2.25	Comparison of HVCs and satellite galaxies around M 31	77
2.26	HI mass vs. projected distance of HVCs and satellite galaxies around M 31.	78
2.27	Distribution of dark-matter satellites around their parent halo	79
3.1	The Westerbork Synthesis Radio Telescope	84
3.2	The uv coverage and continuum map of one of our observations	85
3.3	Overview of the 9 fields observed around M 31 with the WSRT	88
3.4	Densities, velocities, and velocity gradients of M 31 HVCs 1–12	90
3.5	HI column densities and radial velocities of M 31 HVCs 2–12	92
3.6	Two position-velocity diagrams across M 31 HVCs 1–12	93
3.7	High-resolution H I spectra of M 31 HVC 1 and M 31 HVC 7	94
3.8	Comparison of RGB stars and H I gas around M 31	97
3.9	Comparison of HVCs and satellite galaxies around M 31	100
3.10	${\rm HI}$ mass vs. projected distance of HVCs and satellite galaxies around M 31.	101
3.11	Maps and profiles of M 31 HVC 1	104
3.12	Maps and profiles of M 31 HVC 2	105
3.13	Maps and profiles of M 31 HVC 3	106
3.14	Maps and profiles of M 31 HVC 4	107
	Maps and profiles of M 31 HVC 6	
	Maps and profiles of M 31 HVC 13	
	Maps and profiles of M 31 HVC 14	
	Maps and profiles of M 31 HVC 15	
	Maps and profiles of M 31 HVC 16	
	High-resolution maps of M 31 HVCs 1 and 2	
3.21	High-resolution maps of M 31 HVCs 3 and 5	114
4.1	HI, CaII, and NaI spectra in the direction of PKS 1448-232	116
4.2	The uv coverage and continuum map of our VLA observations	119
4.3	HI map of the HVCs observed in the direction of PKS 1448–232	120
4.4	H I spectra of the HVCs observed in the direction of PKS 1448 -232	121
5.1	Comparison of M 31 in neutral hydrogen and RGB stars	
5.2	Ca II absorption in the direction of two quasars	129

List of Tables

2.2	Observational parameters of the Effelsberg H I blind survey of M 31 43 List of the 17 discrete HVCs around M 31 detected in our survey 60 List of M 31 satellite galaxies
	Physical parameters of the high-velocity clouds found near M 31 87 Determination of the dynamical masses of M 31 HVCs 1, 2, 6, 8, and 10 95
	Summary of the UVES Ca II and Na I observations of PKS 1448-232 122 Summary of the VLA H I observations in the direction of PKS 1448-232 122

10 List of Tables

Abstract - Kurzfassung

English

More than 40 years after their discovery by Muller et al. (1963) the origin of high-velocity clouds (HVCs) is still in dispute, the main reason being the lack of reliable distance measurements for most HVCs around the Milky Way. Consequently, a large number of different hypotheses about the origin of HVCs have been proposed over the past decades. A solution to this problem is the study of HVCs around external galaxies. In this case we would look at the corresponding HVC population from the outside, allowing us to directly determine the spatial distribution of the clouds. In addition, we would be able to determine several important physical parameters of HVCs, such as HI mass and density, which are still widely unknown.

Therefore, we used the 100-m radio telescope at Effelsberg to map a large area around the Andromeda Galaxy, M 31, in the 21-cm line of neutral atomic hydrogen with the aim of studying the expected HVC population around M 31 out to large projected distances in excess of 100 kpc. In addition to extended regions of diffuse, extra-planar gas we identified and confirmed the existence of 17 individual HVCs near M 31 with projected distances of less than 50 kpc. The H I masses of the detected HVCs are in the range of about $10^5 \dots 10^6 \ M_{\odot}$ with the exception of Davies' Cloud which has a significantly higher H I mass of $1.3 \times 10^7 \ M_{\odot}$. However, we could not confirm the existence of an extended population of compact high-velocity clouds (CHVCs) around M 31 as predicted by different observations and models (e.g., Braun & Burton 1999; de Heij et al. 2002a). Our results suggest that HVCs and CHVCs are forming circumgalactic populations around both the Milky Way and M 31 with typical distances of $\lesssim 50$ kpc from their corresponding host galaxy.

To study the HVCs around M 31 with higher resolution and sensitivity we observed nine fields of high-velocity gas in H I with the Westerbork Synthesis Radio Telescope (WSRT). At an angular resolution of 2' FWHM (corresponding to 450 pc at the distance of M 31) we are able to resolve the internal structure of most HVCs. The detected clouds have diameters of the order of 1 kpc (FWHM) and H I masses between a few times $10^4~M_{\odot}$ and $6\times10^5~M_{\odot}$. Several of the HVCs are arranged in a filamentary complex spatially and kinematically overlapping with the giant stellar stream of M 31 (Ibata et al. 2001a), suggesting a tidal origin. Other HVCs detected with the WSRT are isolated from M 31 and any of its known satellite galaxies. They are promising candidates for the primordial

dark-matter halos predicted by structure formation scenarios in the framework of CDM cosmology. Our results are in good agreement with the numerical simulations of Sternberg et al. (2002) and Kravtsov et al. (2004).

With our observations we could demonstrate that HVCs and CHVCs are most likely forming circumgalactic populations around the large spiral galaxies in the Local Group. Hypotheses placing the HVC population across the entire Local Group (e.g., Blitz et al. 1999) can be considered unlikely. Our results suggest that both tidal interactions and primordial dark-matter halos have contributed to the observed HVC populations. The next logical step in the study of HVCs will be the systematic determination of metal abundances with the help of absorption line spectroscopy of suitable background objects. We have started to study HVCs in the Galactic halo through the systematic analysis of quasar absorption lines in the optical. Extending these studies to the HVCs of M 31 in the future will allow us to verify the results obtained by our previous observations.

Deutsch

Mehr als 40 Jahre nach ihrer Entdeckung durch Muller et al. (1963) ist der Ursprung der Hochgeschwindigkeitswolken (HVCs) noch immer kontrovers. Der wesentliche Grund hierfür ist das Fehlen zuverlässiger Entfernungsbestimmungen für einen Großteil der HVCs. Infolge dessen wurden über die vergangenen Jahrzehnte hinweg zahllose verschiedene Hypothesen über den Ursprung der HVCs vorgeschlagen. Eine Lösung dieses Problems stellt die Untersuchung von HVCs in der Nähe anderer Galaxien dar. In diesem Fall nämlich würden wir die entsprechende HVC-Population von außen betrachten, so daß sich die räumliche Verteilung der Wolken unmittelbar ableiten ließe. Außerdem wären wir in der Lage, wichtige und weitgehend unbekannte physikalische Parameter der HVCs zu bestimmen, z.B. HI-Masse oder Dichte.

Aus diesem Grund haben wir mit Hilfe des 100-m-Radioteleskops in Effelsberg einen großen Bereich um die Andromeda-Galaxie (M 31) herum in der 21-cm-Linie des neutralen, atomaren Wasserstoffs kartiert. Ziel dieser Kartierung war die Untersuchung der erwarteten HVC-Population von M 31 bis hinaus zu projizierten Entfernungen von mehr als 100 kpc. Neben ausgedehnten Regionen diffusen Gases nahe der Scheibe von M 31 konnten wir 17 einzelne HVCs identifizieren und bestätigen, die projizierte Entfernungen von M 31 von weniger als 50 kpc aufweisen. Die H I-Massen der detektierten HVCs liegen im Bereich von etwa $10^5 \dots 10^6~M_{\odot}$ mit Ausnahme von Davies' Cloud, die eine deutlich höhere H I-Masse von $1.3 \times 10^7~M_{\odot}$ aufweist. Jedoch konnten wir keine Hinweise auf die Existenz einer ausgedehnten Population kompakter Hochgeschwindigkeitswolken (CHVCs) um M 31 herum finden, die von verschiedenen Beobachtungen und Modellen vorhergesagt wurde (z.B. Braun & Burton 1999; de Heij et al. 2002a). Unsere Ergebnisse zeigen, daß HVCs und CHVCs sehr wahrscheinlich zirkumgalaktische Populationen um die Milchstraße und M 31 herum bilden mit typischen Entfernungen von ihrer jeweiligen Zentralgalaxie von $\lesssim 50~\mathrm{kpc}$.

Um die HVCs rings um M 31 mit höherer Auflösung und Sensitivität zu untersuchen, haben wir neun Felder mit HVC-Emission in H I mit dem Westerbork Synthese-Radioteleskop (WSRT) beobachtet. Bei einer Winkelauflösung von 2' FWHM (entsprechend 450 pc in der Entfernung von M 31) sind wir in der Lage, die innere Struktur der meisten HVCs

aufzulösen. Die detektierten Wolken haben Durchmesser in der Größenordnung von 1 kpc und HI-Massen im Bereich von einigen $10^4~M_{\odot}$ bis hin zu $6\times10^5~M_{\odot}$. Viele der HVCs sind in einem filamentären Komplex angeordnet, der sich räumlich und kinematisch mit dem stellaren Strom von M 31 (Ibata et al. 2001a) überschneidet und möglicherweise durch Gezeitenwechselwirkung entstand. Andere mit dem WSRT detektierte HVCs erscheinen von M 31 und ihren bekannten Satellitengalaxien isoliert und sind aussichtsreiche Kandidaten für die primordialen Dunkle-Materie-Halos, die von Strukturentstehungs-Szenarien im Rahmen der CDM-Kosmologie vorhergesagt werden. Unsere Ergebnisse sind in guter Übereinstimmung mit den Ergebnissen der numerischen Simulationen von Sternberg et al. (2002) und Kravtsov et al. (2004).

Mit unseren Beobachtungen konnten wir zeigen, daß HVCs und CHVCs sehr wahrscheinlich zirkumgalaktische Populationen um die großen Spiralgalaxien der Lokalen Gruppe herum bilden. Hypothesen, die eine Verteilung der HVCs über die gesamte Lokale Gruppe hinweg annehmen (z.B. Blitz et al. 1999), können als unwahrscheinlich gelten. Unsere Ergebnisse legen zudem nahe, daß sowohl Gezeitenwechselwirkungen als auch primordiale Dunkle-Materie-Halos zu den beobachteten HVC-Populationen beigetragen haben. Der nächste logische Schritt in der Erforschung der HVCs wird die systematische Bestimmung der Metallizitäten mit Hilfe von Absorptionslinien-Spektroskopie geeigneter Hintergrundobjekte sein. Wir haben bereits begonnen, HVCs im Halo der Milchstraße durch die systematische Auswertung von Quasar-Absorptionslinien im Optischen zu untersuchen. Durch Erweiterung dieser Untersuchungen auf die HVCs von M 31 in der Zukunft werden wir in der Lage sein, die Ergebnisse unserer bisherigen Beobachtungen zu überprüfen.

CHAPTER 1

Introduction

1.1 The discovery and definition of HVCs

Several observations in the early 1950s indicated that the Galaxy was surrounded by an extended interstellar corona. Evidence for the presence of coronal gas came from the detection of interstellar Na I and Ca II absorption lines in the spectra of stars at high Galactic latitudes (e.g., Spitzer et al. 1950; Routly & Spitzer 1952), suggesting that the corresponding interstellar gas clouds were in pressure equilibrium with a surrounding hot ionised gas. Additional evidence came from the detection of "radio noise" around the Galaxy and M 31 at a wavelength of 3.7 m (Baldwin 1954, 1957) which was assumed to originate from an extended component of ionised gas. Based on these and other observations, Spitzer (1956) suggested that the Galaxy was filled with an interstellar coronal gas with a temperature of the order of 10^6 K, an electron density of 5×10^{-4} cm⁻³, and an extension of 8 kpc perpendicular to the Galactic plane. In the same year Jan Hendrik Oort suggested that clouds of neutral hydrogen gas might condense out of the Galactic corona and fall back towards the Galactic plane with high velocities (Wakker & van Woerden 1997). Two years later Ernst Raimond began to search for these high-velocity clouds (HVCs), using the new 25-m radio telescope in Dwingeloo in the Netherlands (Fig. 1.1). After the installation of new receivers Muller et al. (1963) finally announced the discovery of HVCs with LSR radial velocities in excess of 100 km s⁻¹ along four different lines of sight.

High-velocity clouds are gas clouds with radial velocities in excess of what can be explained by a simple model of Galactic rotation, although there is no exact definition of a velocity limit for HVCs. Earlier works followed the heuristic approach of a fixed velocity of 90 or 100 km s⁻¹ in the LSR frame to separate HVCs from low- and intermediate-velocity gas. A fixed velocity limit in the LSR frame, however, is unsatisfactory in consideration of the high rotation velocity of the Galactic disk of 220 km s⁻¹. In some regions of the sky radial velocities of $|v_{\rm LSR}| > 100$ km s⁻¹ are still compatible with regular gas in the Galactic disk. To overcome this problem, Wakker (1991) introduced the so-called deviation velocity, $v_{\rm dev}$, to characterise high-velocity gas. Based on a simple model of the Galaxy, the allowed velocity range of the Galactic disk gas can be determined. According to Wakker (1991),



Fig. 1.1: Using the 25-m radio telescope at Dwingeloo, Muller et al. (1963) detected the first high-velocity clouds. The telescope was also used to carry out the Leiden/Dwingeloo Survey (Hartmann & Burton 1997) which was later used by Braun & Burton (1999) to identify the population of compact high-velocity clouds.

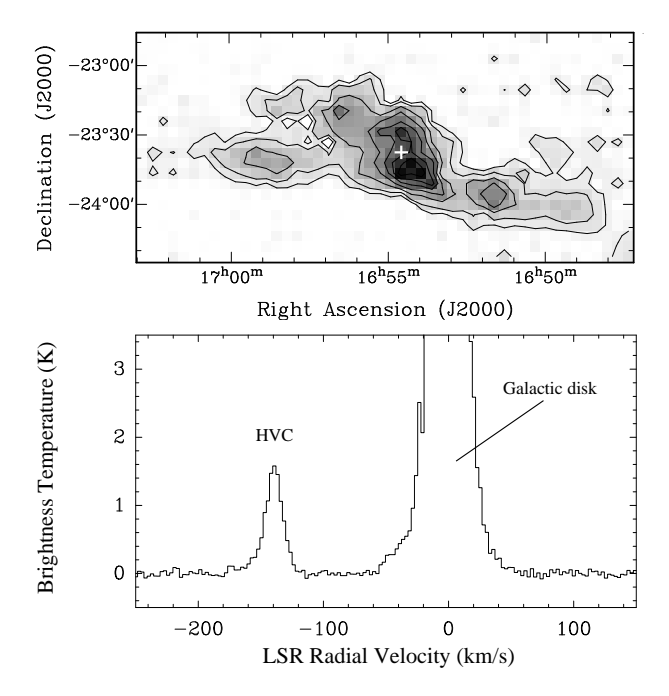
the deviation velocity of a gas cloud is the difference between its observed radial velocity and the extreme value of the velocity of the disk emission in this direction as determined from the model. A fixed value for the deviation velocity (e.g., $v_{\rm dev} = 50~{\rm km\,s^{-1}}$) can then be used to separate HVCs from low- and intermediate-velocity gas. A more detailed description of this concept can be found in Wakker (2004). A typical example for an HVC is shown in Fig. 1.2.

High-velocity clouds are observed at both positive and negative radial velocities in the range of $v_{\rm LSR} \simeq -400...+400~{\rm km\,s^{-1}}$ (see Wakker 2004). The HVC with the highest radial velocity known so far is HVC 111–07–466 with $v_{\rm LSR} = -466~{\rm km\,s^{-1}}$ (Braun & Burton 1999), of course excluding the equivalents of HVCs seen around external galaxies.

1.2 The distribution of HVCs across the sky

An all-sky map of HVCs, based on the Leiden/Argentine/Bonn (LAB) Galactic H I Survey (Kalberla et al. 2005; Hartmann & Burton 1997; Arnal et al. 2000; Bajaja et al. 2005), is shown in Fig. 1.3 and 1.4. To exclude the HI emission of the Galactic disk, a simple model of the Milky Way was constructed. In this model, the Galactic disk extends out to a radius of r=26 kpc with a height of z=2 kpc (i.e. a thickness of 4 kpc) in the inner part. Outside the Sun's orbital radius of 8 kpc (Reid 1993) the height of the disk increases linearly to z = 4 kpc at the outer edge. The rotation velocity was assumed to be constant at all radii with $v_{\rm rot} = 220 \; {\rm km \, s^{-1}}$. Based on this model, the maximum and minimum radial velocity of the Milky Way disk along each line of sight was determined. This range of allowed radial velocities of the Galactic disk was extended by a deviation velocity of $v_{\rm dev}=65~{\rm km\,s^{-1}}$ (see Wakker 1991, 2004), and all H I emission outside this extended radial velocity range was considered high-velocity gas. The HI column density (Fig. 1.3) and the radial velocity (Fig. 1.4) of the high-velocity gas were calculated from the zeroth and first moments of the data cube modified with respect to the model described above. The nomenclature of the HVCs follows Wakker & van Woerden (1991), Wakker (2001), Wakker (2004), and Brüns et al. (2005).

Fig. 1.2: Top: HI column density map of HVC 357.8+12.4-159, an example for a typical HVC. The contour lines are drawn at 5×10^{18} cm⁻² and from 1×10^{19} cm⁻² in steps of 1×10^{19} cm⁻². Bottom: HI spectrum at the position marked with the white cross in the upper map. Due to its different radial velocity the spectral line of the HVC clearly stands out against the emission of the Galactic disk.



From the column density map in Fig. 1.3 it is obvious that HVCs are not homogeneously distributed across the sky. Instead, they are forming numerous extended structures, the so-called HVC complexes. The most extended of these complexes is the Magellanic Stream which is likely to be of tidal origin in connection with the interaction of the Magellanic Clouds with each other and the Milky Way. Parts of the Magellanic Stream were already observed by Dieter (1965) and Wannier & Wrixon (1972). The first investigation of the stream over its entire extent was published by Mathewson et al. (1974) who also realised that the stream was associated with the Magellanic Clouds. Recently, detailed and sensitive studies were carried out by Putman et al. (2003b) and Brüns et al. (2005). The northern, leading part of the Magellanic Stream, the so-called Leading Arm, was already known in the early 1970s (Wannier et al. 1972; Mathewson et al. 1974), but its association with the Magellanic Clouds had been hypothetical over many years. Numerical simulations by Gardiner & Noguchi (1996) provided additional evidence for a tidal origin of the Leading Arm in connection with the Magellanic Clouds, recently supported by sensitive H I observations of Putman et al. (1998) and Brüns et al. (2005).

The northern Galactic hemisphere is dominated by the large HVC complexes A, C, and M, the first two of which were among the first HVCs ever detected by Muller et al. (1963) with the 25-m Dwingeloo telescope. Their origin is not yet known, although distance measurements towards parts of complex A (Wakker et al. 1996; van Woerden et al. 1999b) and complex M (Danly et al. 1993; Ryans et al. 1997) suggest that they are nearby objects with heights above the Galactic plane of only a few kpc. Other extended and coherent complexes include the Anti-Centre complex (AC), the Anti-Centre Shell, complex H, complex K, and the Wannier Clouds, WA–WE, first systematically studied by Wannier et al. (1972).

Apart from these large, coherent structures numerous smaller and more fragmented HVCs can be found all over the sky. A few of them have been grouped into HVC complexes on the basis of similar positions and radial velocities, namely complex L, complex G, and

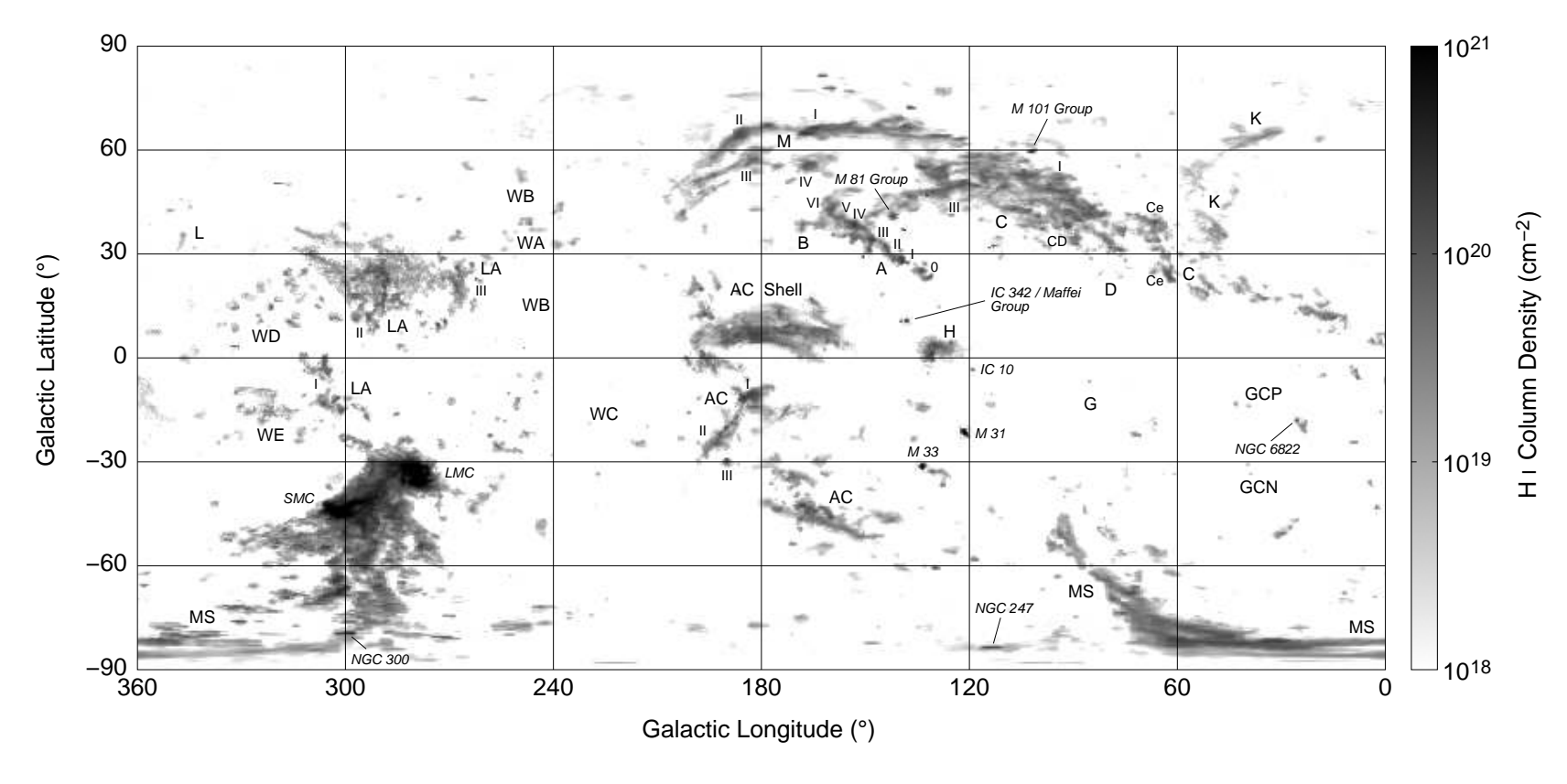


Fig. 1.3: All-sky HI column density map of high-velocity gas, based on the Leiden/Argentine/Bonn Galactic HI Survey (Kalberla et al. 2005; Hartmann & Burton 1997; Arnal et al. 2000; Bajaja et al. 2005). The HI emission of the Galactic disk was removed from the original data cube by constructing a simple model of Galactic rotation as explained in the text. The most prominent HVC complexes are labelled with Roman letters. The map also includes several nearby galaxies, some of which are labelled with slanted letters. The small Roman numerals and letters denote individual sub-structures in some of the HVC complexes.

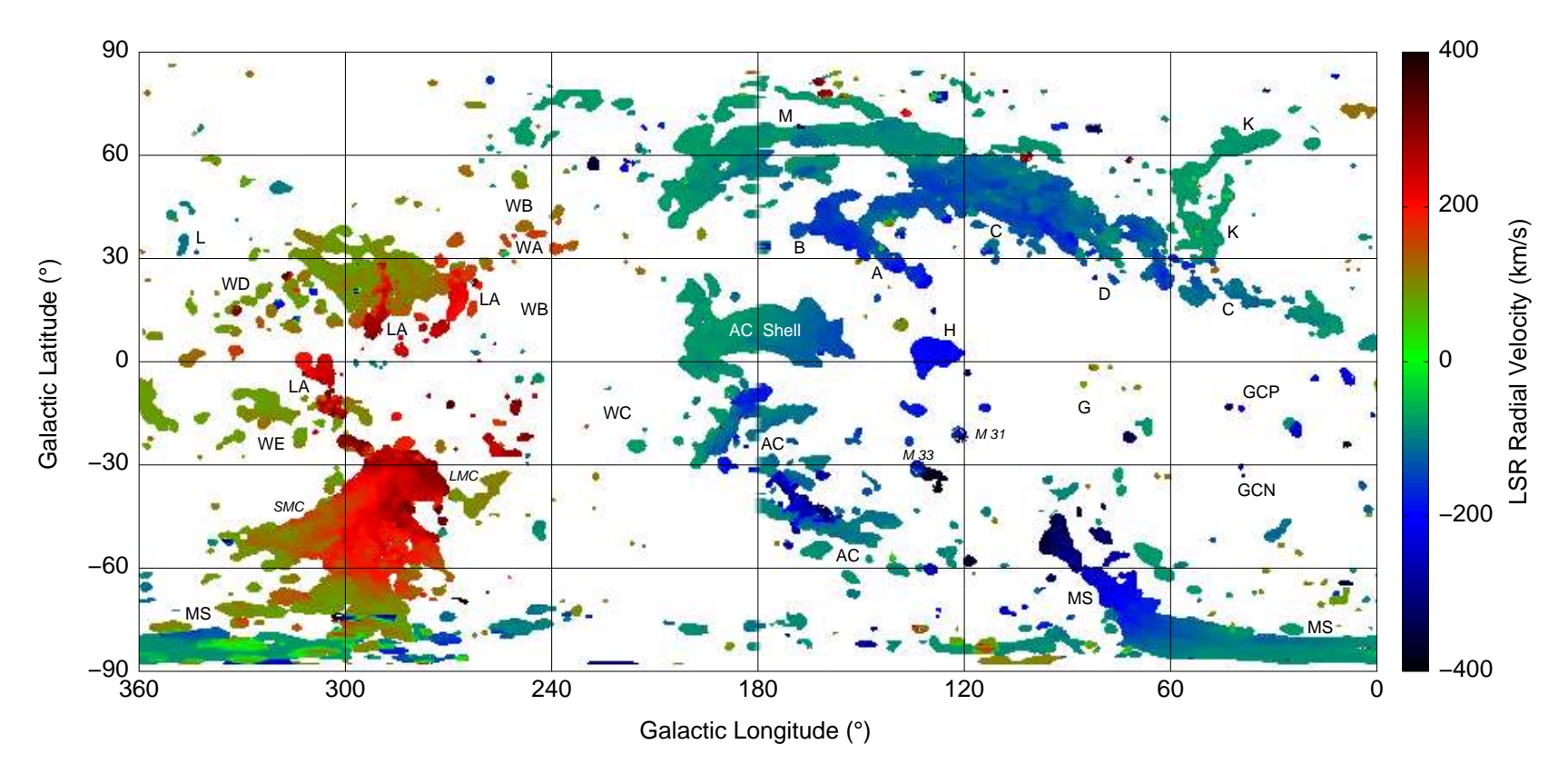


Fig. 1.4: All-sky radial velocity map of high-velocity gas in the LSR frame, based on the Leiden/Argentine/Bonn Galactic HI Survey (Kalberla et al. 2005; Hartmann & Burton 1997; Arnal et al. 2000; Bajaja et al. 2005). The HI emission of the Galactic disk was removed from the original data cube by constructing a simple model of Galactic rotation as explained in the text. The most prominent HVC complexes are labelled with Roman letters. The map also includes a number of nearby galaxies, the most famous of which are labelled with slanted letters.

the complexes towards the Galactic centre with positive and negative radial velocities (GCP and GCN, respectively). A detailed list of HVCs and an overview of all HVC complexes and their nomenclature can be found in Wakker & van Woerden (1991).

1.3 The physical parameters of HVCs

1.3.1 Radial velocities

A general misconception about HVCs is that they constitute a population of purely infalling clouds. This misconception also influenced the attempts to explain the origin of HVCs. The impression of a general infall of HVCs onto the Galaxy arose with the first HVC detections which were made with telescopes in the northern hemisphere near the direction in which the Galactic disk is rotating. As a result, the observed radial velocities of HVCs were predominantly negative. The effect is illustrated in Fig. 1.5. Let us assume a population of HVCs which are isotropically distributed all across the sky with GSR radial velocities equally distributed in the range of $|v_{\rm GSR}| \leq 150~{\rm km\,s^{-1}}$. The position-velocity diagram of such a population is plotted in Fig. 1.5 A based on a model with 10⁸ test particles. The linear greyscale represents the normalised number of HVCs per map element, $\Delta l \times \Delta v$, with the choice of $\Delta l = 10^{\circ}$ and $\Delta v = 25 \text{ km s}^{-1}$ in our case. If we convert all radial velocities into the LSR frame we get a sine-shaped distribution in the position-velocity diagram as shown in Fig. 1.5 B. Now the selection criteria begin to take effect. First of all, HVCs are defined by their high radial velocities of $|v_{\rm LSR}| \gtrsim 100~{\rm km\,s^{-1}}$, as clouds with lower velocities would not be recognised any more against the strong HI emission of the Galactic disk. Second, telescopes in the northern hemisphere cannot access the sky below a declination of $\delta \approx -30^{\circ}$. Removing all clouds from the model which do not fulfil these criteria leads to the situation plotted in Fig. 1.5 C. Obviously, the limitation in declination range resulted in the exclusion of mainly those clouds with positive LSR velocities which are expected to be concentrated in the southern sky. As a result, the mean radial velocity of the HVC population is negative, misleadingly suggesting a global infall. In our example we obtain $\langle v_{\rm LSR} \rangle = -70 \; \rm km \, s^{-1}$ although we chose completely random velocities in the original model. This situation does not change when converting the velocities back into the GSR frame as shown in Fig. 1.5 D. The mean GSR velocity remains negative with $\langle v_{\rm GSR} \rangle = -16 \; \rm km \, s^{-1}$ in our example.

But even with an all-sky survey it is not necessarily possible to draw conclusions about the overall kinematics of HVCs based on the mean velocity of the HVC population alone. First of all, there may be additional selection effects such as a combination of different formation scenarios for HVCs which would also influence the observed distribution of radial velocities. Furthermore, an infall of an HVC onto the Galaxy need not result in a negative radial velocity in the GSR frame. Consider, for example, a cloud falling in the direction of the Galactic centre. If the cloud is located in between us and the Galactic centre it will be moving away from us, and its velocity will be positive. If instead the cloud is located behind the Galactic centre it will move towards us, resulting in a negative radial velocity in both the LSR and GSR frames. Therefore, it is not advisable to draw conclusions about the overall kinematics of HVCs without knowing the three-dimensional position and velocity of each cloud.

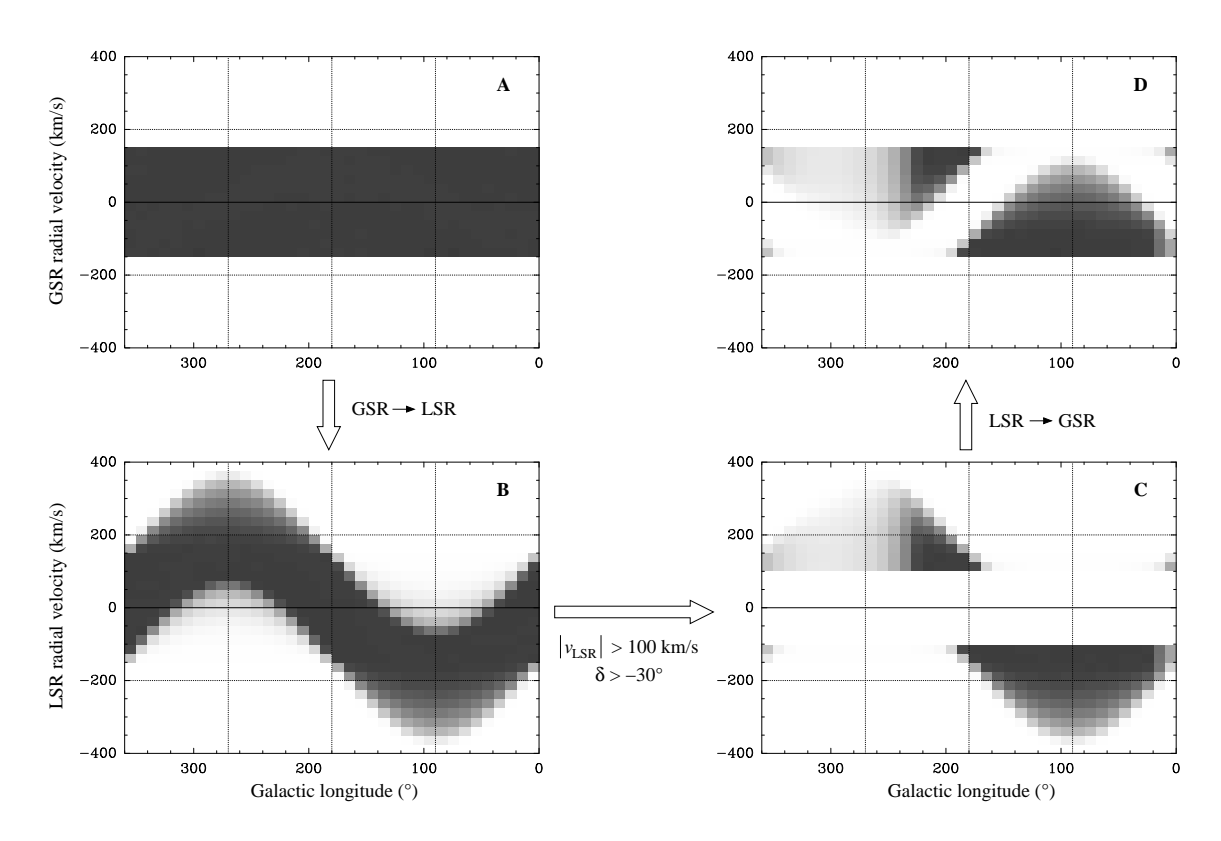


Fig. 1.5: Position-velocity diagrams of a model HVC population illustrating the selection effects which led to the misconception of a net infall of HVCs onto the Galaxy. The linear greyscale represents the normalised density of HVCs per map element of size $\Delta l = 10^{\circ}$ and $\Delta v = 25 \text{ km s}^{-1}$. In particular the restriction in the declination range accessible to northern hemisphere observatories, $\delta > -30^{\circ}$, led to the result of a net negative radial velocity of the observable HVC population. The individual charts are explained in detail in Section 1.3.1.

Today, HVCs all across the sky with positive and negative velocities are known (see Fig. 1.4 for an all-sky velocity map). The most extreme velocities in the LSR frame are observed towards the far end of the Magellanic Stream with $v_{\rm LSR} \simeq -400~{\rm km\,s^{-1}}$ and in the direction of the Leading Arm where velocities of $v_{\rm LSR} \gtrsim +300~{\rm km\,s^{-1}}$ are observed (Brüns et al. 2005). As discussed before, however, the LSR velocities are dominated by the projection of the rotation velocity of the Milky Way, resulting in negative radial velocities near $l=90^{\circ}$ and positive velocities near $l=270^{\circ}$.

1.3.2 Distances

Distance is probably the most controversially discussed parameter of HVCs. On the one hand, there are no direct methods to determine the distance of a diffuse gas cloud. On the other hand, knowledge of the distance, d, is crucial to determine other, distance-dependent parameters such as the mass, $M \sim d^2$, the radius, $R \sim d$, or the density, $n \sim d^{-1}$, of an HVC. In addition, distance determinations would allow us to distinguish between the different formation scenarios proposed for HVCs.

The lack of direct methods to determine their distances is connected with the absence of stars in HVCs. Ivezić & Christodoulou (1997) used IRAS¹ data to identify a handful of young stellar objects (YSOs) in the direction of complex M and complex H. Due to the lack of distance information, however, an association of the YSOs with the corresponding HVCs remains circumstantial. The question whether HVCs have a stellar component was also addressed by Simon & Blitz (2002), Davies et al. (2002), Hopp et al. (2003), and Siegel et al. (2005) with the help of deep optical and near-infrared observations. However, no extensive stellar population was found in any of the investigated HVCs, indicating that HVCs did not form stars on a grand scale. The results rule out the possibility that HVCs are faint dwarf galaxies, unless their V-band surface brightness is at least about 1 mag per square arc second lower than that of any previously known Local Group galaxy (Simon & Blitz 2002). Recently, several faint companions of our Milky Way and the Andromeda Galaxy have been discovered. Some of these dwarf galaxies, such as Andromeda IX and Andromeda X (Zucker et al. 2004, 2006b) or the recently identified Canes Venatici and Bootes dwarf galaxies (Zucker et al. 2006a; Belokurov et al. 2006b), have a central surface brightness of $\mu_{\rm V} \simeq 27 \dots 28$ mag per square arc second which is well below the detection limits of optical surveys in search of stars in HVCs. None of these faint dwarfs, however, is known to contain a significant amount of neutral gas which argues against a general connection between HVCs and dwarf galaxies. Very recently Irwin et al. (2007) announced the discovery of a new dwarf galaxy in the Local Group, Leo T, which appears to contain neutral gas with an HI mass of about $10^5 M_{\odot}$. The discovery of a young stellar population also suggests the presence of gas in Leo T.

The most accurate indirect method to determine the distances of HVCs uses stellar spectroscopy. Stars which are located behind an HVC should show absorption lines in their spectra as their light passes through the high-velocity gas, whereas stars in front of a cloud do not show any such absorption lines. Determining the distances of the stars then yields an upper and lower limit for the distance of the HVC. Of course this method can only be applied to nearby HVCs where adequate background stars in the Galactic halo are available. So far, the distances of only four HVC complexes have been successfully determined through the stellar absorption line method. Danly et al. (1993) found a height of a part of complex M (M III) above the Galactic plane of 1.5 < z < 4.4 kpc. A more sensitive reanalysis of the corresponding sight lines by Ryans et al. (1997) led to an improved upper limit of z < 3.5 kpc for complex M. They argue, however, that the lower limit determined by Danly et al. (1993) is not significant due to the absence of HI emission in the direction of the star HD93521. The distance of complex A was determined to be 4 < d < 10 kpc (corresponding to 2.5 < z < 7 kpc) by Wakker et al. (1996) and van Woerden et al. (1999b). Recently, Thom et al. (2006) could deduce a narrow distance range of 7.7 < d < 8.8 kpc for a part of complex WB. In addition, Wakker (2001) reported an upper distance limit of d < 12.8 kpc (corresponding to z < 3.2 kpc) for complex WE, but no lower limit (other than zero) is known. For several other HVC complexes, including the large complex C (de Boer et al. 1994), only lower distance limits exist which are typically of the order of a few kpc (see Wakker & van Woerden 1997 and Wakker 2001 for details). All these results suggest that the large HVC complexes observed in the northern Galactic hemisphere are most likely circumgalactic objects with heights

¹ Infrared Astronomical Satellite

above the Galactic plane of only a few kpc. Similar extra-planar gas structures were also found in a few external galaxies, e.g. NGC 253 (Boomsma et al. 2005), NGC 2403 (Fraternali et al. 2002), or NGC 4559 (Barbieri et al. 2005). They could be the equivalents of the large HVC complexes close to the disk plane of the Milky Way. In some of these cases, however, strong starburst activity could have triggered a distinctive galactic fountain process which, e.g., is likely to have produced the extra-planar gas in NGC 253.

In other cases, the distances are not well constrained. The Magellanic Stream and the Leading Arm are assumed to be connected with the Magellanic Clouds, implying distances of the order of 50 kpc. However, no stars have been found in the stream (e.g., Recillas-Cruz 1982; Brück & Hawkins 1983), eliminating the possibility of direct distance determinations. Because of the expected large distances of the Magellanic Stream and the Leading Arm, suitable foreground and background stars for indirect distance determinations are not available either. The distances of the numerous compact and isolated HVCs all over the sky are also unknown and can only be assessed by statistical methods based on their spatial and kinematic distribution and their physical parameters. Such a statistical approach has been used to support the idea of an intergalactic population of HVCs in the Local Group (e.g., Blitz et al. 1999; Braun & Burton 1999). The Local Group scenario, however, is not endorsed by recent results (including this work) and can be considered unlikely (for a detailed discussion see Section 1.5.3).

1.3.3 Metal abundances

Knowledge of the metal abundances of HVCs is crucial to discriminate between the different scenarios proposed to explain the origin of HVCs. Over the past years, numerous metallicity measurements have been obtained by studying absorption lines in the spectra of active galactic nuclei, quasars, and stars located behind HVCs. Among the most commonly detected ions are NI, OI, NaI, MgII, SII, and CaII for which abundance measurements are available for several high- and intermediate-velocity clouds. The general consensus of these measurements is that high-velocity gas is characterised by metal abundances of the order of 0.1 of the solar values with a slightly higher value of about 0.3 for the Magellanic Stream and the Leading Arm (see Wakker 2001 for a comprehensive summary of individual measurements). As a consequence, the gas in most of the studied HVCs cannot be primordial but must have been processed, either in the environment of the Galaxy or in present or former satellite galaxies of the Milky Way. The observed metal abundances are also in conflict with the hypothesis that HVCs were formed in the Galactic fountain process or by individual supernovae, as in this case solar or supersolar abundances would be expected.

With typical values in the range of about 0.5...2 solar (Richter et al. 2000; Wakker 2001) the measured abundances of IVCs tend to be significantly higher than those of HVCs. This result indicates that IVCs consist of processed gas and have their origin in the Galaxy. They could either be condensed, infalling halo gas or material originating from individual supernovae, Galactic winds, or the Galactic fountain process. This is also consistent with the typically smaller distances of IVCs of $z \simeq 1$ kpc. HVCs, on the other hand, appear to be located at somewhat larger distances from the Galactic plane with subsolar abundances indicating an origin outside the Milky Way. According to Wakker (2001), measurements towards HVC complex M yield an S⁺ abundance in the range of

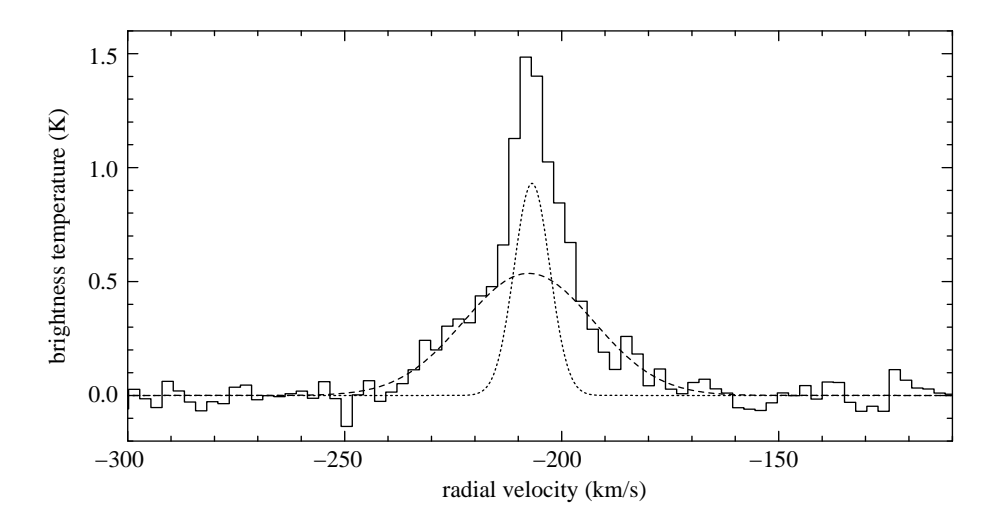


Fig. 1.6: HI spectrum of HVC 050-68-193, an example for an HVC with a two-component line profile (from Westmeier et al. 2005b). The dotted and dashed lines show the results of a two-component Gaussian fit to the data. A narrow line component of cold neutral gas (dotted line) is superposed on a broad component of warm neutral gas (dashed line), indicating the coexistence of two gas phases in HVC 050-68-193. These two-component profiles are widely observed in both compact HVCs as well as extended HVC complexes.

0.4...1.8 times the solar value, which is significantly higher than the abundances of other HVCs and consistent with the idea that complex M is connected with the Intermediate-Velocity Arch (IV Arch).

1.3.4 Multi-phase structure

A common phenomenon in HVCs is the coexistence of warm and cold neutral gas (e.g., Cram & Giovanelli 1976, Wolfire et al. 1995, Braun & Burton 2000, Westmeier et al. 2005b, Kalberla & Haud 2006). In these multi-phase HVCs, compact cores of cold gas are embedded in an extended, diffuse envelope of warm gas. The cold neutral medium is characterised by H I line widths in the range of about 5...10 km s⁻¹ FWHM, corresponding to upper limits of the kinetic temperature of the order of 1000 K. In extreme cases, line widths as low as 2 km s⁻¹ FWHM are observed with gas temperatures falling below 100 K. Line widths of the warm neutral medium are typically in the range of 20...30 km s⁻¹ FWHM with corresponding upper limits of the kinetic temperature of the order of 10⁴ K. The coexistence of cold and warm gas phases is usually indicated by two- or multi-component line profiles in the H I spectra in which a strong, narrow line component appears to be superposed on a weak, broad line component. An example H I spectrum of HVC 050-68-193 with a two-component line profile is shown in Fig. 1.6.

Kalberla & Haud (2006) accomplished a statistical analysis of multi-component line profiles in HVCs based on the all-sky LAB Survey. They found a multi-phase structure in 24% of all sight lines with high-velocity gas emission. The corresponding contribution of cold clumps to the total HI column density is 21%. Their results indicate that a multi-component structure is a common phenomenon among HVCs, although the situa-

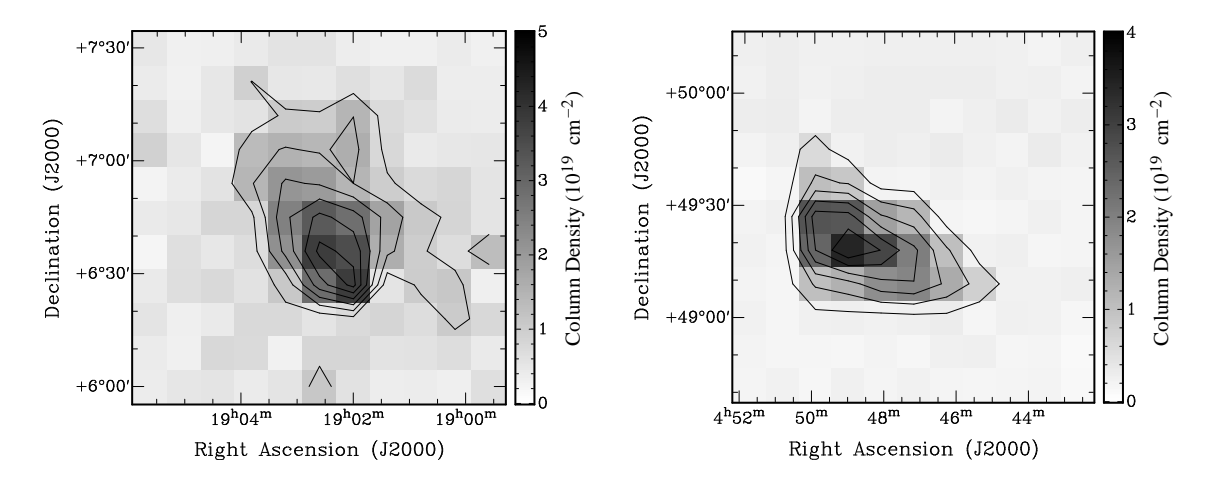


Fig. 1.7: HI column density maps of HVC 040+01-279 (left) and HVC 157+03-186 (right), two examples of CHVCs with a distinct head-tail structure and horseshoe shape, respectively (from Westmeier et al. 2005b). Such morphologies are widely observed among HVCs, indicating that gas has been stripped off the clouds by the ram pressure of an ambient medium. Both observations were made with the 100-m radio telescope at Effelsberg.

tion for individual HVC complexes may differ. According to Kalberla & Haud (2006), a large fraction of multi-phase structures is also observed in the Magellanic Stream and the Leading Arm with values ranging from 7.5% to more than 50% in different regions along the stream.

The coexistence of a cold and warm gas component in HVCs could be reproduced by Sternberg et al. (2002) with hydrostatic simulations. They considered their spherical HVCs to be gravitationally dominated by a dark-matter halo and additionally supported by the pressure of an external medium. Their simulations were focusing on an extragalactic origin of HVCs with typical distances of $d\approx 150$ kpc (circumgalactic model) and $d\gtrsim 750$ kpc (Local Group model). In both cases a multi-phase cold/warm neutral medium core was established, embedded in a warm envelope of neutral and ionised gas. The dominant cooling mechanism in the cold neutral medium—depending on the gas density—is the fine structure emission of C II and C I at 158 μ m and 609 μ m, respectively, whereas the warm neutral medium is mainly cooling through Ly α emission.

1.3.5 Interaction with the ambient medium

Deep HI observations have shown that many HVCs have a rather complex morphology instead of being spherically-symmetric (Brüns et al. 2000, 2001; Westmeier et al. 2005b; Ben Bekhti et al. 2006). As an example, HI maps of two compact high-velocity clouds with a so-called *head-tail structure* and a *horseshoe shape*, respectively, are shown in Fig. 1.7. Brüns et al. (2000) studied the morphology of 252 HVCs in the northern hemisphere on the basis of the Leiden/Dwingeloo Survey (Hartmann & Burton 1997). Nearly 20% of the clouds show a head-tail structure with a compact core being embedded in an asymmetric envelope with a cometary appearance. These head-tail structures are usually accompanied by a radial velocity gradient along the major axis of the cloud, indicating that the head is

moving with a different velocity than the diffuse tail. The most plausible explanation for head-tail structures is ram-pressure interaction with an ambient medium. When HVCs are moving through their environment, gas at the interface of the clouds may be stripped and form the diffuse tail. This would naturally explain the velocity gradient observed across the clouds. In this scenario, the tail need not be trailing. If the HVC is moving along an orbit in the gravitational field of the Milky Way, a deceleration of gas in its envelope may result in a lower orbit for the stripped gas which would subsequently overtake the primary cloud and appear as a leading tail.

Three-dimensional hydrodynamic simulations by Quilis & Moore (2001) support the concept of interacting HVCs. They simulated both dark-matter-dominated clouds as well as pure gas clouds moving through a diffuse coronal gas. In both cases, ram-pressure stripping can create faint gas tails with HI column densities of $N_{\rm H\,I} \simeq 10^{19}~{\rm cm}^{-1}$ if the density of the surrounding medium exceeds about $10^{-4}~{\rm cm}^{-3}$. The interaction between HVCs and a hot ambient medium was also studied by Konz et al. (2002) in two-dimensional magnetohydrodynamic simulations. Their simulations can also explain the observed head-tail structures. In addition, a magnetic barrier of increased field strength is built up around the cloud, stabilising it against thermal conduction and the diffusion of hot plasma into the neutral gas.

1.4 HVC detections at other wavelengths

1.4.1 Molecular gas in HVCs

Several attempts have been made to detect molecular gas towards high column density clumps in HVCs. After several unpublished observations (Wakker & van Woerden 1997) the first published non-detection of CO towards an HVC (complex A) was announced by Kim et al. (1989). They concluded that either the studied HVC is mainly composed of atomic gas with a normal CO abundance or the cloud is predominantly molecular with a CO deficiency of at least a factor 10. Wakker et al. (1997) carried out observations in the direction of complex A, complex M, complex H, and HVC 114–10–440 to detect the $J=1 \rightarrow 0$ transition of ¹²CO. They did not detect CO emission in any of the eight studied cores, resulting in upper limits for the H₂ column density in the range of $(9 \dots 25) \times 10^{18}$ cm⁻². In a more sophisticated approach, Akeson & Blitz (1999) searched for HI, CO, and HCO⁺ absorption against bright radio continuum sources in the direction of several HVCs. They did not detect any of the studied HVCs in absorption, implying upper limits for the H₂ column density in the range of $(5 \dots 17) \times 10^{18}$ cm⁻².

The first successful detection of molecular hydrogen in an HVC was announced by Richter et al. (1999). They detected HVC 279–33+120 in far-ultraviolet H_2 absorption towards a bright star in the Large Magellanic Cloud, using the échelle spectrograph of the *Orbiting and Retrievable Far and Extreme Ultraviolet Spectrometer* (ORFEUS). The total H_2 column density of the high-velocity gas in this direction is very low with only $(2.2...3.6) \times 10^{15}$ cm⁻². Absorption spectroscopy towards 27 quasars, although at millimetre wavelengths, was also used by Combes & Charmandaris (2000) to search for high-velocity HCO⁺ absorption lines. Except for one tentative detection they did not find any absorption lines associated with HVCs.

All these results indicate that absorption spectroscopy is the most promising method to detect molecular gas in HVCs. Nonetheless, the detection of molecular transitions in HVCs remains sophisticated. Apart from typically low densities of the gas in HVCs, the numerous non-detections could be due to low metal abundances or, in the case of emission line observations, insufficient excitation of the gas. The formation of molecular hydrogen in the clouds strongly depends on the interstellar radiation field near the Galaxy and therefore on the distance of the clouds. Wakker et al. (1997) concluded that—under the assumption of standard $\rm H_2$ formation mechanisms—they would have detected CO emission if the studied HVCs were closer to the Galaxy than about 2 kpc.

1.4.2 Thermal dust emission from HVCs

The first attempt to detect the thermal emission of dust in HVCs was made by Wakker & Boulanger (1986). They studied 100-µm data taken with the *Infrared Astronomical Satellite* (IRAS). However, they did not find any correlation between the IRAS 100-µm data and H I column density maps in two fields around complexes A III, A IV, and M I. They concluded that either the dust in HVCs is cooler than expected, resulting in lower 100-µm fluxes, or that the relative dust content of HVCs is by a factor of 3 or more lower than that of low-velocity gas. The first case would result in a lower distance limit for HVCs of 11.5 kpc.

Recently, Miville-Deschênes et al. (2005) claimed the first detection of thermal dust emission in an HVC (complex C). They compared 24- μ m and 160- μ m data observed with the Spitzer Space Telescope and 60- μ m and 100- μ m IRAS data with 21-cm H I observations obtained with the 100-m Green Bank Telescope (GBT). Using a χ^2 minimisation method, they decomposed the infrared emission into local, intermediate-velocity, and high-velocity components, assuming a correlation between the H I column density and the corresponding infrared emission for each of these components. The residual term in their fit, however, is not a constant, but a function of position. Their main statistical argument for the detection of complex C in the infrared is that the standard deviation of the residual term is in good agreement with the expected cosmic infrared background fluctuations. However, maps of the residual term and the high-velocity component of the infrared emission are not presented, making an interpretation of their results difficult.

1.4.3 $H\alpha$ emission from HVCs

If HVCs were located close to the Galaxy they should also show $H\alpha$ emission due to collisional ionisation, photoionisation by the Galactic radiation field, or recombination of highly ionised gas. The first successful detection of $H\alpha$ emission was announced by Kutyrev (1986) and Kutyrev & Reynolds (1989) who found a signal of 80 mR in the direction of the Anti-Centre complex, using the Wisconsin 15-cm Fabry-Pérot spectrometer.

Another attempt to detect $H\alpha$ emission of HVCs was made by Reynolds (1987), who also used the Wisconsin 15-cm Fabry-Pérot spectrometer to map 6 HVCs, including parts of complexes C and M. However, he did not detect any emission connected with the HVCs, yielding upper limits for the $H\alpha$ intensity in the range of 200...600 mR. Reynolds (1987) concluded that the studied HVCs were primarily neutral and located in an environment of low gas density and low ionising radiation.

A successful detection of H α emission was announced by Songaila et al. (1989). They detected a very low intensity of about 30 mR at two different positions in complex C, which is an order of magnitude lower than the upper limits published by Reynolds (1987). Later, Tufte et al. (1998) detected H α emission in complexes A, C, and M with intensities between 60 and 200 mR, using the new Wisconsin H α Mapper (WHAM). With the high spectral resolution of this instrument Tufte et al. (1998) were able to resolve the H α emission lines and to associate them with the corresponding HI emission lines of the investigated HVCs. Their results seem to support the hypothesis of photoionisation of the HVC gas by the ionising radiation in the Galactic halo. This would explain the similar H α fluxes and the small line widths observed in all studied directions. Similar results were reported by Weiner et al. (2001), Tufte et al. (2002), and Putman et al. (2003a) for several other HVCs, including compact and isolated ones.

Assuming photoionisation by the Galactic radiation field, HVCs would be located within the range of a few kpc out to about 40 kpc from the Galaxy (Putman et al. 2003a). The fluxes observed along the Magellanic Stream, however, are too high to be explained by the ionising radiation of the Galaxy alone. Thus, additional ionisation mechanisms are required such as the interaction of the Magellanic Stream with a diffuse Galactic halo gas or the presence of young stars which have not yet been associated with the Magellanic Stream.

1.4.4 X-ray emission from HVCs

The possibility of X-ray emission from HVCs was first addressed by Bone et al. (1983). They proposed that HVCs moving with high velocities through the Galactic corona could cause shocks which would result in diffuse soft X-ray emission. Deep pointed observations of HVC 90.5+42.5-130, a filament of complex C, with the X-ray satellite ROSAT by Kerp et al. (1994) finally resulted in the first detection of soft X-ray emission associated with an HVC. They observed ½-keV and ¾-keV emission at the edges of the cloud, suggesting that HVC 90.5+42.5-130 is interacting with a magnetised ambient medium with magnetic reconnection being the main mechanism to heat the gas to the required temperatures of a few times 10⁶ K.

In addition, Kerp et al. (1998) could demonstrate that both the $^{1}/_{4}$ keV and $^{3}/_{4}$ keV emission in the direction of HVC 90.5+42.5-130 is clearly anticorrelated with the HI column density of the HVC gas. They could show that the attenuation of the background X-ray emission by the high-velocity gas is too low to be detectable so that the anticorrelation must be due to excess X-ray emission from the rim of the HVC filament itself. Most likely the $^{1}/_{4}$ keV and $^{3}/_{4}$ keV emission originates from an interaction of complex C with gas in the Galactic halo. An important physical process which could contribute to the generation of soft X-ray emission is charge exchange between the neutral gas in complex C and highly charged ions in the hot halo gas. This situation was calculated by Lallement (2004) who determined X-ray emission measures comparable to those found by Kerp et al. (1999). The results of Kerp et al. (1994, 1996, 1998, 1999) provide additional evidence for complex C being nearby at heights above the Galactic disk of $z \approx 1.5 \dots 2.5$ kpc. The velocity bridges found between complex C and the HI emission of the Galactic disk support the idea that the observed X-ray emission originates from an impact of complex C onto the Galaxy.

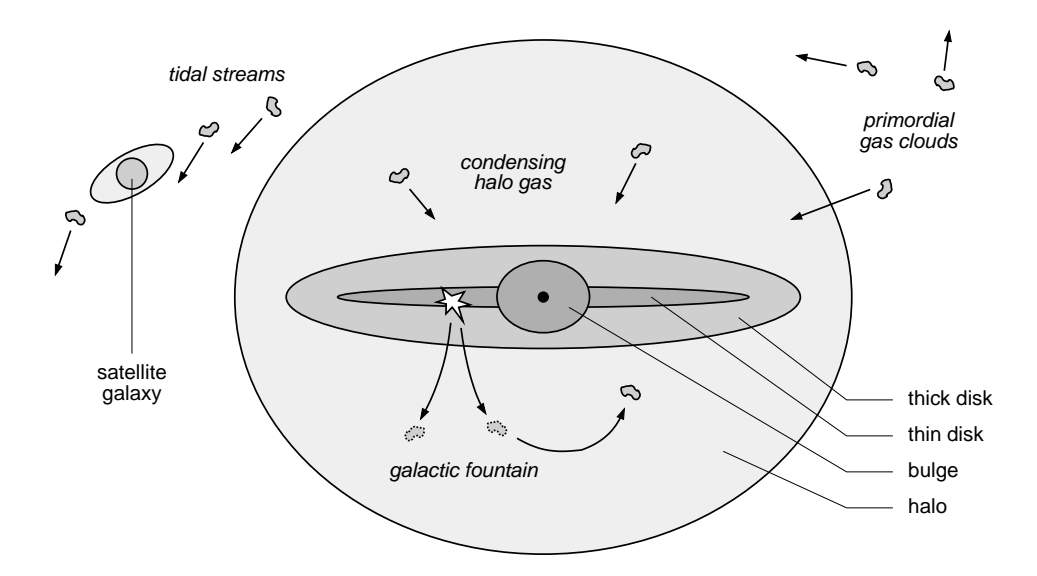


Fig. 1.8: Schematic overview of some of the hypotheses proposed for the origin of high-velocity clouds around the Milky Way. The sketch is not drawn to scale.

1.5 The origin of HVCs

The problem of explaining the origin of HVCs is closely linked to the problem of distance determination. Accordingly, the numerous hypotheses proposed over the years can be divided into three groups:

- Hypotheses placing the HVC population close to the Milky Way with heights of up to a few kpc above the plane
- Hypotheses placing the HVC population in the outer Galactic halo at distances of tens of kpc from the Milky Way
- Hypotheses placing the HVC population in the intergalactic space of the Local Group with distances of hundreds of kpc

A detailed discussion of the different hypotheses is provided by Oort (1966), Wakker & van Woerden (1997), and Bregman (2004). A schematic overview of some of the proposed formation scenarios can be found in Fig. 1.8.

1.5.1 Hypotheses about the origin of HVCs

The first comprehensive approach to explain the origin of HVCs was published by Oort (1966). After a compilation of HVC detections, Oort discussed several possible formation scenarios and their implications. One of the earliest hypotheses tried to explain HVCs as parts of nearby supernova shells (e.g., Prata 1964). In this case, HVCs should have heights above the Galactic plane of only a few hundred pc. This idea was already discarded by Oort (1966) for several reasons. First of all, supernova shells should be concentrated towards the Galactic plane, whereas most HVCs are found at higher Galactic latitudes. In

addition, both the approaching and receding part of the shells should be visible at different radial velocities, and strong $H\alpha$ emission should be present, both of which is not observed in connection with HVCs.

A related idea is that HVCs are being formed in the Galactic fountain process. This hypothesis was first suggested by Shapiro & Field (1976), Bregman (1980), and Kahn (1981). In the original model, hot gas ejected by supernovae expands to large heights above the Galactic disk. When the gas cools down, clouds can condense and fall back ballistically towards the Galactic plane. This model can explain both positive and negative radial velocities observed for HVCs, although the expected maximum velocity of the fountain gas of about $70...100 \; \mathrm{km} \, \mathrm{s}^{-1}$ appears to be significantly lower than the observed radial velocities of many HVCs. Additional predictions of the fountain model are solar metallicities of the HVC gas and heights above the Galactic plane of $z \lesssim 10 \; \mathrm{kpc}$. The Galactic fountain process is therefore unlikely to have caused most of the large HVC complexes which have clearly subsolar abundances (Wakker 2001).

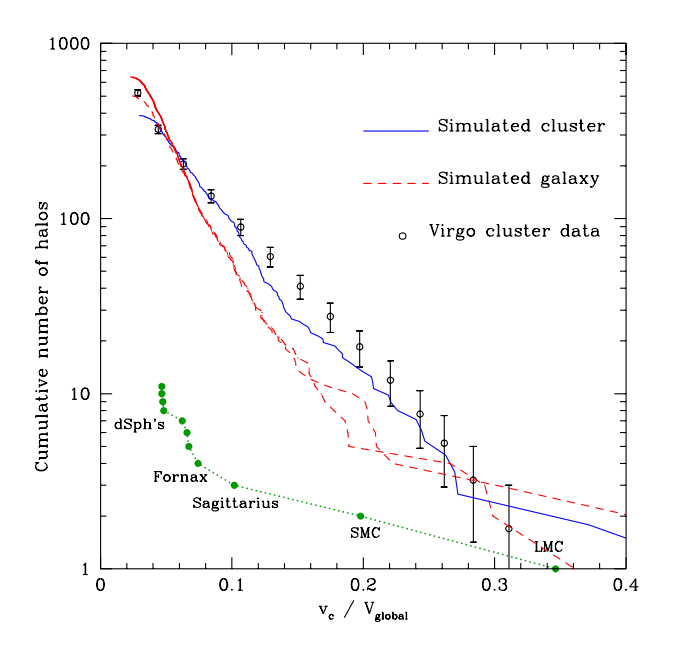
In a different approach, de Boer (2004) proposed the mass loss of halo red giant stars as a possible contribution to the observed infalling component of high-velocity gas. He estimated a corresponding total infall rate onto the Galactic disk of $7 \times 10^{-5} M_{\odot} \,\mathrm{kpc}^{-2} \,\mathrm{a}^{-1}$ which could contribute a significant fraction of the infalling HVCs. Given the low metal abundances expected for halo red giant stars, the subsolar abundances determined for some of the HVCs are in agreement with this hypothesis. We should keep in mind, though, that the errors of HVC metallicity measurements are large and that mixing with gas in the Galactic disk could have altered the abundances.

The idea that HVCs might be gas clouds condensing out of the hot Galactic corona was first proposed by Field (1962, 1965) and Dieter (1964). However, Oort (1966) argued that an implausibly high particle density of the Galactic corona of about 10^{-2} cm⁻³ would be required to keep HVCs in equilibrium. Furthermore, such high densities would not allow HVCs to reach the observed high velocities without getting destroyed.

The hypothesis favoured by Oort (1966, 1970) considers HVCs to be primordial gas left over from the formation of the Milky Way. While the gas would be accreted by the Galaxy it could heat and accelerate disk gas which would then cool down again and appear as HVCs. This hypothesis predicts heights of the HVCs above the Galactic plane of the order of 1 kpc and metallicities slightly lower than solar. In addition, all HVCs should show strong signs of interaction which is in good agreement with the numerous head-tail structures observed by Brüns et al. (2000, 2001) and Westmeier et al. (2005b).

Another possibility is that HVCs represent gas tidally stripped from dwarf galaxies during close encounters with the Milky Way. For the Magellanic Stream and the Leading Arm this is the most likely explanation (Mathewson et al. 1974; Gardiner & Noguchi 1996). In addition to tidal forces, ram-pressure forces may play an important role in the formation of the Magellanic Stream (see Mastropietro et al. 2005 and references therein). The Large and the Small Magellanic Cloud are known to have distances of $d_{\rm LMC} \approx 50$ kpc and $d_{\rm SMC} \approx 60$ kpc, respectively (Alves 2004; Hilditch et al. 2005). Due to the lack of stars the distances of the Magellanic Stream and the Leading Arm—in particular towards the far ends of both streams—are not well constrained and probably of the order of several 10 kpc. Olano (2004) even suggested that the entire population of HVCs observed around our Galaxy could have been formed in the interaction between the two Magellanic Clouds and the Milky Way.

Fig. 1.9: Cumulative number of darkmatter halos as a function of circular velocity, $v_{\rm c}$, according to Moore et al. (1999). The blue and red lines show the results of simulations. In addition, the galaxies of the Virgo cluster (black) and the known Milky Way satellites (green) are plotted for comparison. Towards smaller masses (i.e., small values of v_c) there is a large discrepancy between the predicted number of halos and the number of known satellite galaxies around the Milky Way. (Figure taken from Moore et al. 1999.)



Other HVCs may be connected to the tidal stream of the Sagittarius dwarf spheroidal galaxy (Ibata et al. 1994). Putman et al. (2004) made an attempt to identify the gaseous counterpart of the Sagittarius stream. Based on data from the *HI Parkes All-Sky Survey* (HIPASS; Barnes et al. 2001), they identified several HVCs with negative radial velocities along the orbit of the Sagittarius dwarf spheroidal galaxy, including complex L and the Anti-Centre complex.

Recently, Belokurov et al. (2006c) and Grillmair (2006) independently discovered a previously unknown stellar stream stretching tens of degrees across the northern sky. This "orphan stream" was studied in more detail by Belokurov et al. (2006a) on the basis of Sloan Digital Sky Survey (SDSS, York et al. 2000) data. They noticed that the stream lies on the same great circle around the Galactic centre as HVC complex A, suggesting a connection between these two structures. In this case, complex A would be another example of an HVC complex of tidal origin. Belokurov et al. (2006c) also determined the distance of different regions along the stream, yielding values in the range of 20...30 kpc. Hence, the "orphan stream" has a significantly larger distance from the Galaxy than complex A (distance bracket: 4...10 kpc) so that the alignment of both structures on the sky could as well be a chance coincidence.

1.5.2 HVCs as primordial dark-matter halos?

The probably most controversial hypothesis about the origin of HVCs in recent years was proposed by Blitz et al. (1999). They considered HVCs to be the gaseous components of primordial dark-matter halos left over from the formation of galaxies in the Local Group. These so-called dark-matter mini-halos are predicted by numerical simulations in the framework of CDM cosmology (Klypin et al. 1999; Moore et al. 1999; Kravtsov et al. 2004). However, there is a large discrepancy between the predicted and the observed number of halos around our Milky Way (Fig. 1.9). CDM/ΛCDM simulations predict several hundred dark-matter halos surrounding the Galaxy within about 300 kpc radius,

compared to only 11 known satellite galaxies within the same volume (Kroupa et al. 2005). This discrepancy has been named the *missing satellites problem*, a term which obviously represents the theoretical viewpoint, whereas from the observer's position the simulations seem to over-predict the number of Galactic satellites by a factor of about 100.

The suggestion by Blitz et al. (1999) was one of the first attempts to solve the missing satellites problem by assuming that most of the dark-matter mini-halos in the Local Group did not form stars on a grand scale and therefore remained dark. HVCs were the most plausible candidates for the missing satellites, although Blitz et al. (1999) had to exclude the Magellanic Stream (which was known to have a different origin) and the most extended HVC complexes A, C, and M (which were known or believed to be located only a few kpc above the Galactic disk) from their considerations. The spatial and kinematic parameters of the remaining HVCs were consistent with the dark-matter mini-halo hypothesis, implying a distribution across the entire Local Group with typical distances of hundreds of kpc. As a consequence, HVCs would have sizes in the range of about 10...30 kpc and enormous HI masses of the order of $10^7 M_{\odot}$.

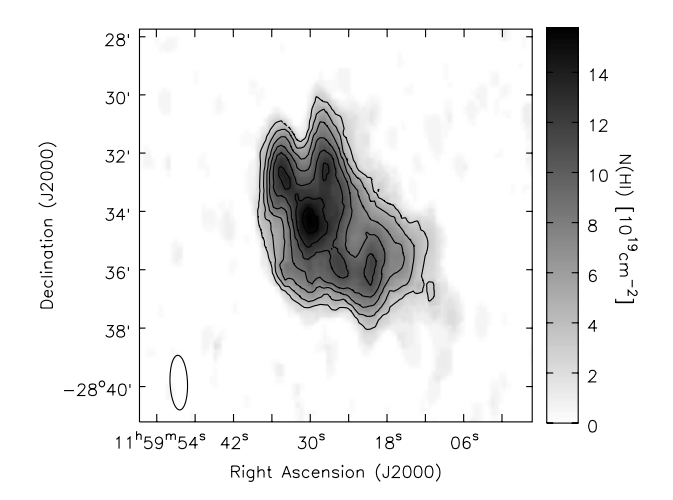
1.5.3 Compact high-velocity clouds

If HVCs were the missing satellites of the Local Group, their large distances from the Milky Way would imply accordingly small angular diameters on the sky. Based on this idea, Braun & Burton (1999) searched the Leiden/Dwingeloo Survey (LDS) of Galactic neutral hydrogen (Hartmann & Burton 1997) for compact and isolated HVCs which they suspected to be the most promising candidates for the primordial dark-matter halos across the Local Group. Their catalogue lists 66 so-called compact high-velocity clouds (CHVCs) in the northern sky with declinations above -30° . CHVCs have angular sizes of less than 2° FWHM and typical peak H I column densities of a few times 10^{19} cm⁻². In addition they are isolated in the sense that they are spatially and kinematically separated from Galactic H I emission and any neighbouring HVCs. An example for a particularly small CHVC is shown in Fig. 1.10. Completeness and quality of the catalogue of Braun & Burton (1999) are limited by the parameters of the LDS which was carried out with the 25-m radio telescope at Dwingeloo. The telescope has a fairly large HPBW of about 36' at the observing frequency of 1.4 GHz. The LDS was observed on a 30' grid² with a velocity resolution of about 1 km s⁻¹ and a final baseline RMS of about 70 mK.

Braun & Burton (1999) argued that the sub-class of 66 CHVCs might represent the expected Local Group population of missing satellites with typical distances of hundreds of kpc. In this case, CHVCs would be very large and massive objects with HI masses of the order of $10^7~M_{\odot}$. The most important argument of Braun & Burton (1999) is the dispersion of the radial velocities of the CHVC sample which decreases significantly from $\sigma_{\rm LSR} = 175~{\rm km\,s^{-1}}$ in the local standard-of-rest frame to only $\sigma_{\rm LGSR} = 88~{\rm km\,s^{-1}}$ in the Local Group standard-of-rest frame. This decrease suggests that CHVCs are kinematically coupled to the barycentre of the Local Group. However, in the Galactic standard-of-rest frame the velocity dispersion of $\sigma_{\rm GSR} = 95~{\rm km\,s^{-1}}$ is only slightly higher than in the LGSR. This result indicates that the velocity dispersion alone does not provide convincing evidence for the Local Group scenario, so that CHVCs might as well form a circumgalactic population.

² More precisely: $\Delta l \leq 30'/\cos b$ and $\Delta b = 30'$ in Galactic coordinates.

Fig. 1.10: HI column density map of HVC 289+33+251, taken from Brüns & Westmeier (2004). This CHVC was observed with the Australia Telescope Compact Array (ATCA) and is particularly compact with an angular diameter of less than 10'. The contours are separated by 2×10^{19} cm⁻², starting from 3×10^{19} cm⁻².



An improved CHVC catalogue was published by de Heij et al. (2002b) on the basis of an automated search of the LDS, listing 67 CHVCs in the sky north of -30° declination. In addition, Putman et al. (2002) compiled a catalogue of 179 CHVCs in the southern hemisphere below +2° declination, based on the HI Parkes All-Sky Survey (HIPASS; Barnes et al. 2001). The northern and southern hemisphere data were merged by de Heij et al. (2002a) into an all-sky catalogue comprising 216 CHVCs.³ Their positions and radial velocities are shown in Fig. 1.11. The systematic velocity structure imposed by the rotation of the Galaxy can clearly be seen in the map. Surprisingly, the distribution of CHVCs over the sky is not homogeneous. The all-sky catalogue does not contain any CHVCs north of +60° Galactic latitude. On the other hand there are several overdensities of clouds in the southern hemisphere and in particular near the Galactic south pole. The generally higher density of clouds in the southern hemisphere is a result of the higher sensitivity of the HIPASS compared to the LDS. Nevertheless, the observed overdensities are significant even within the HIPASS area alone. The positions of most of these overdensities are correlated with the leading and trailing parts of the Magellanic Stream, indicating that a significant number of CHVCs in the all-sky catalogue of de Heij et al. (2002a) could in fact be isolated fragments connected to the Magellanic Stream or the Leading Arm. There is another clear overdensity near $l = 30^{\circ}$, $b = -15^{\circ}$ which does not coincide with the Magellanic System but could be related to HVC complex GCN.

Numerous attempts have been made over the past years to test the hypothesis of a Local Group population of CHVCs. Sternberg et al. (2002) carried out hydrostatic simulations of pressure-supported CHVCs gravitationally dominated by dark matter. They considered two different scenarios with characteristic distances of the CHVCs from the Galaxy of 150 kpc (circumgalactic population) and $\gtrsim 750$ kpc (Local Group population), respectively. Their simulations clearly favour the circumgalactic case in which they are able to reproduce the peak H I column densities and the multi-phase structure of CHVCs as observed by Burton et al. (2001) with the Arecibo telescope. Sternberg et al. (2002) also find that CHVCs have to be confined by the pressure of an ambient medium to keep the gas neutral. The required pressure must exceed 50 K cm⁻³ which, at a distance of

³ The total number is not simply the sum of the two underlying catalogues because of the significant positional overlap between LDS and HIPASS.

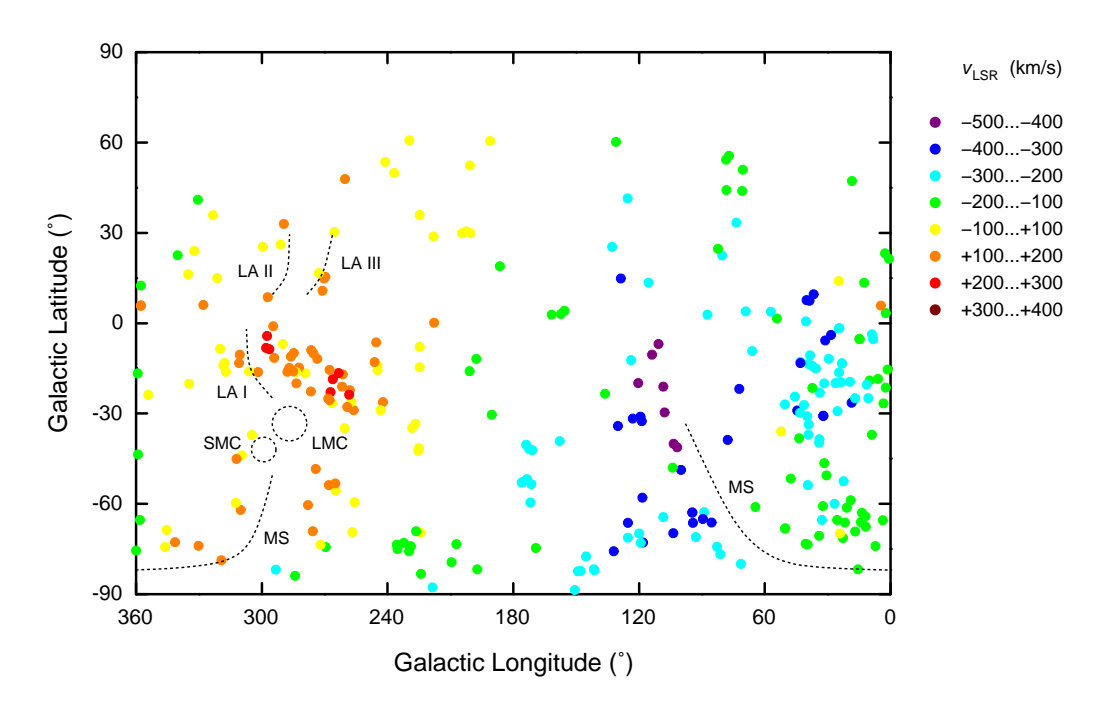


Fig. 1.11: All-sky map showing the distribution of CHVCs according to the catalogues published by de Heij et al. (2002b) and Putman et al. (2002). The colours of the dots represent the LSR radial velocities of the clouds. The positions of the Magellanic Clouds, the Magellanic Stream, and the Leading Arm are indicated by the dashed lines and circles for orientation. The global velocity structure with negative velocities around $l = 90^{\circ}$ and positive velocities around $l = 270^{\circ}$ is caused by the rotation of our Galaxy. Several concentrations of CHVCs can be seen, some of which may be connected with the Magellanic System. Note that there is not a single CHVC north of $b = 60^{\circ}$.

150 kpc, can be provided by the hot ionised Galactic corona (e.g., Sembach et al. 2003; Rasmussen et al. 2003).

Evidence for a circumgalactic CHVC population is also provided by observations. Several attempts to identify the equivalents of intergalactic CHVCs in nearby galaxy groups similar to the Local Group failed (Zwaan 2001; Braun & Burton 2001; Pisano et al. 2004). The resulting upper distance limits for CHVCs from the Galaxy are of the order of 150 kpc which is consistent with the results obtained by Sternberg et al. (2002). A few CHVCs were also detected in $H\alpha$ by Tufte et al. (2002) and Putman et al. (2003a), implying distances of only a few kpc if ionisation by the Galactic UV radiation field is assumed. There are several non-detections as well, but these need not be due to large distances from the Galaxy. The viewing geometry, the position of the clouds with respect to the spiral arms of the Galaxy, and incomplete $H\alpha$ mapping could instead be responsible for several of the non-detections. Additional evidence for a circumgalactic CHVC population is provided by sensitive HI observations which have uncovered complex morphologies suggesting that many HVCs and CHVCs are distorted by the ram pressure of an ambient medium through which they are moving (see the discussion in Section 1.3.5 and Fig. 1.7). Westmeier et al. (2005b) studied 11 CHVCs in HI with the 100-m radio telescope at Effelsberg of which only a single one had a spherical appearance. The results indicate that ram-pressure interaction plays an important role in the evolution of many CHVCs, suggesting that they are embedded in the low-density medium of the Galactic halo or corona instead of being spread throughout the Local Group.

1.6 Summary

Although there has been a lot of progress in the study and understanding of HVCs over the past years, many important details are still controversial. HVCs are believed to be mainly composed of hydrogen, often forming cold neutral cores embedded in more extended envelopes of warm neutral or ionised gas. No considerable amount of molecular gas or dust has ever been found in HVCs. Accordingly, all attempts to identify a stellar population in HVCs have failed. For a few large HVC complexes distance brackets have been determined, yielding heights above the Galactic disk of typically a few kpc. For the vast majority of HVCs, and in particular for the CHVCs, only indirect distance estimates are available, indicating upper distance limits of the order of 150 kpc for both HVCs and CHVCs. The lack of distance information also resulted in a large number of different hypotheses about the origin of HVCs, ranging from Galactic formation scenarios to the hypothesis that HVCs are primordial gas clouds left over from the formation of the Local Group.

Our current knowledge indicates that HVCs and CHVCs are most likely forming a circumgalactic population around the Milky Way. If this is true and if HVCs and CHVCs are a phenomenon occurring naturally in the evolution of all large spiral galaxies then we should be able to find populations of HVCs and CHVCs around other galaxies as well. Studying the HVCs around other galaxies would have two advantages: First, we would look at the HVC population from the outside, allowing us to directly determine the radial distribution. Second, the distances of the HVCs would be known, allowing us to determine important distance-dependent parameters such as the masses and sizes of the clouds. The nearest galaxy similar to the Milky Way is the Andromeda Galaxy, M 31, the other large spiral galaxy in the Local Group. Therefore, M 31 would be the ideal target for a deep H I survey which should uncover the expected clouds and provide direct evidence for the concept of circumgalactic HVCs.

The aim of this work is to detect and study the population of HVCs and CHVCs around M31 with the help of sensitive HI observations with the 100-m radio telescope at Effelsberg and the Westerbork Synthesis Radio Telescope (WSRT). In Chapter 2 our deep Effelsberg HI survey of a large area around the Andromeda Galaxy will be discussed. The aim of this survey was to detect the expected HVCs and CHVCs out to a projected distance from M 31 in excess of 100 kpc and to determine their radial distribution and H I mass function. Chapter 3 describes our follow-up synthesis imaging of individual HVCs around M31 with the WSRT with the aim of studying their physical parameters in more detail. These observations also helped us to find evidence for the origin of the studied HVCs. In Chapter 4 the first results of our project to identify Ca II and Na I absorption lines from circumgalactic HVCs in the spectra of distant quasars will be presented. The method of optical absorption spectroscopy provides the unique opportunity to study the low column density domain of the HVC population and to determine the metal abundances of the gas which is crucial to identify the origin of HVCs. Finally, Chapter 5 summarises our results and conclusions and provides an outlook on the next logical steps in the study of HVCs and their origin.

Effelsberg H I survey for HVCs around M 31

In this chapter our deep HI survey for HVCs and CHVCs around the Andromeda Galaxy (M31) with the 100-m radio telescope at Effelsberg is presented and discussed. Our survey covers an area of about $15^{\circ}\times5^{\circ}$ and confirms the existence of several regions of extra-planar gas and 17 individual HVCs around M31. The detected HVCs have HI masses of typically a few times $10^{5}~\rm M_{\odot}$ and projected distances from the centre of M31 of up to 50 kpc. With their masses and sizes they resemble the large HVC complexes near the Milky Way. However, we could not find any equivalents to the extended population of CHVCs around the Galaxy. This non-detection implies a strict upper limit for the distance of CHVCs from their host galaxy of about 60 kpc. Our results suggest that HVCs and CHVCs are forming circumgalactic populations around the Milky Way and M31 with distances of not more than a few ten kpc from their host galaxy. At such distances, HVCs would be embedded in the circumgalactic corona where they would be pressure-supported in addition to their own gravitational potential.

2.1 The Andromeda Galaxy

2.1.1 Historic studies

At a distance of 784 ± 30 kpc (Stanek & Garnavich 1998), the Andromeda Galaxy is the nearest large spiral galaxy comparable to our own Milky Way. With a total visual magnitude of $m_{\rm V} \approx 3.4$ mag it is an easy target for the naked eye so that it was likely known in prehistoric times. The oldest known report is from Abd al-Rahman al-Sufi, a Persian astronomer of the $10^{\rm th}$ century, who described the Andromeda Galaxy in his famous *Book of Fixed Stars* as a "small cloud" (al-Sufi 964; for a French translation see Schjellerup 1874). The first telescopic observations of the Andromeda Galaxy were conducted in 1612 by Simon Mayr (also known under his Latin synonym Marius) who compared its appearance with "the flame of a candle seen through horn" (Mayr 1614). Later, Charles

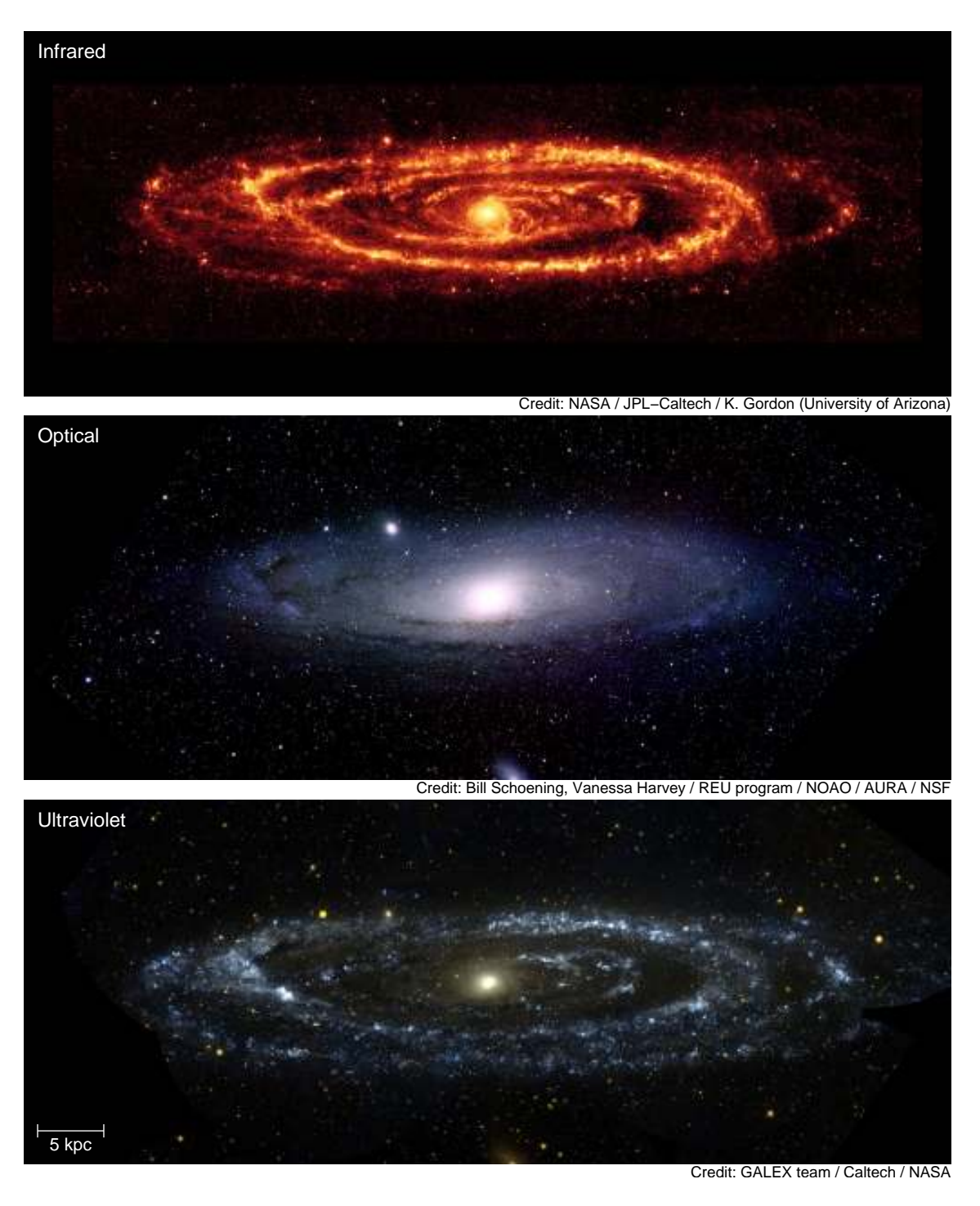


Fig. 2.1: The Andromeda Galaxy (M 31) at different wavelengths. All three images have the same scale and orientation. **Top:** The mid-infrared image at 24 μm wavelength, taken with MIPS on board the Spitzer Space Telescope, mainly traces the thermal emission of dust. **Middle:** The optical image, observed with the Burrell Schmidt telescope of the Warner and Swasey Observatory on Kitt Peak, Arizona, shows the distribution of young and old stars in the disk and bulge of M 31. **Bottom:** The near (red) and far (blue) ultraviolet view, observed with the Galaxy Evolution Explorer (GALEX), mainly traces the ring-like region of star formation in M 31.

Messier added the Andromeda Galaxy as object number 31 to his catalogue of nebulae and star clusters (Messier 1774), erroneously crediting Simon Mayr for the discovery.

Until the early 20th century, M 31 was believed to be a nearby object of our own Milky Way. In August 1885, a "new star" near the nucleus of M 31 was discovered independently by several astronomers (see Krüger 1885 for a compilation of different reports). This star, later named S Andromedae, was the first extragalactic supernova observed. At that time, M 31 was still widely believed to be a gas nebula within our own Milky Way so that the true nature and the importance of this supernova event were not recognised. Instead, the appearance of S And was reminiscent of an ordinary nova, supporting the idea of M 31 being a Galactic nebula. Hartwig (1885) even believed to observe a fading of Andromeda's nucleus which he considered evidence for a destruction of the gas under the influence of the "new star". A few years later, Roberts (1888) presented the first high-quality photographic images of M 31 on which the spiral structure was clearly seen in the outer regions of the galaxy. However, Roberts (1888) interpreted the spiral arms as concentric rings of "nebulous matter" and believed to see the formation of a new planetary system.

The first indication that the Andromeda Galaxy could be an extragalactic object came from spectroscopic observations by Scheiner (1898, 1899), demonstrating that M 31 had a continuous spectrum with absorption lines similar to those in the solar spectrum. This result proved that M 31 was composed of individual stars instead of being a gas nebula. In 1912, Vesto Melvin Slipher started spectroscopic observations of the Andromeda Galaxy, leading to the determination of its heliocentric radial velocity of -300 km s^{-1} (Slipher 1913) and the discovery of the rotation of M 31 (Slipher 1914). Slipher's observations casted the hypothesis of a Galactic origin of M 31 into doubt, because the observed radial velocity was much larger than the velocity of any known object in the Milky Way.

In the 1920s, Edwin Hubble studied the Andromeda Galaxy with the 100-inch telescope at Mount Wilson Observatory. On his photographic plates he could resolve the spiral arms of M 31 into swarms of individual stars among which he also found several Cepheids. From the derived distance it was obvious that M 31 was an extragalactic object and a galaxy similar to our own (Hubble 1929), although the distance measurement obtained by Hubble was by more than a factor 2 too small due to a wrong period-luminosity relationship for Cepheids. A modified period-luminosity relationship was later found by Walter Baade (see, e.g., Baade 1956) and led to more accurate results for the distance of M 31 (e.g., Baade & Swope 1963, 1965).

2.1.2 Modern studies

A comprehensive review of the study of the Andromeda Galaxy and its physical parameters in the second half of the $20^{\rm th}$ century is provided by Hodge (1992). M 31 is a large spiral galaxy (Arp 1964; Braun 1991) of Hubble type Sb. Unfortunately, the disk of M 31 is highly inclined with respect to the plane of the sky (Fig. 2.1) with an inclination angle of $i \approx 77^{\circ}.5$ (Simien et al. 1978) for the inner disk. In addition, the disk of M 31 shows a clear warp in both the stellar and neutral gas component (e.g., Roberts 1966; Roberts & Whitehurst 1975; Innanen et al. 1982; Sawa & Sofue 1982) resulting in a variation of the inclination angle as a function of galactocentric distance (e.g., Roberts & Whitehurst 1975). The position angle of the major axis with respect to the equatorial coordinate system is $\varphi = 37^{\circ}.7$ (Hodge 1992).



Fig. 2.2: The 100-m radio telescope at Effelsberg is operated by the *Max-Planck-Institut für Radioastronomie* (MPIfR) based in Bonn. It is one of the largest fully steerable radio telescopes in the world. The 21-cm receiver is installed in the primary focus cabin of the telescope.

Using the HI rotation curve, Carignan et al. (2006) recently determined a mass of $3.4 \times 10^{11}~M_{\odot}$ for M 31 within a radius of 35 kpc. The total mass of M 31 was derived by Evans et al. (2000) and Evans & Wilkinson (2000) on the basis of spectroscopic observations of M 31 satellites with the Keck telescope and the kinematics of globular clusters and planetary nebulae. Their study indicates a halo mass of M 31 of the order of $1 \times 10^{12}~M_{\odot}$ (see also Côté et al. 2000) with significant uncertainties resulting mainly from low-number statistics and uncertain satellite distances. The result of Evans & Wilkinson (2000) indicates that the total mass of M 31 is similar or even lower than that of the Milky Way of the order of $2 \times 10^{12}~M_{\odot}$ (Wilkinson & Evans 1999), refuting the accepted opinion that M 31 is more massive than the Milky Way (e.g., Hodge 1992).

A very deep optical survey of M 31 was carried out by Ferguson et al. (2002) with the Isaac Newton Telescope (INT) on the island of La Palma. Their study of red giant branch stars across an area of about 25 square degrees around M 31 uncovered a rich structure in the stellar component of the outer disk and halo of the Andromeda Galaxy. Their most exciting result is the discovery of a giant stellar stream in the south-eastern part of M 31 (Ibata et al. 2001a) which is believed to be the remnant of a tidal interaction between M 31 and one of its satellite galaxies, although the progenitor has not yet been unambiguously identified (Font et al. 2006). A detailed spectroscopic study of the stream with the 10-m Keck telescope was presented by Guhathakurta et al. (2006). In addition, Ibata et al. (2005) discovered that the stellar structures in the outer parts of M 31 show a common sense of rotation suggesting that they were formed in a large accretion event.

Results from the first detailed HI study of M 31 were presented by van de Hulst et al. (1957) based on data taken with the 25-m radio telescope at Dwingeloo. Their observations demonstrated that the HI column density had a local minimum in the direction of the centre of M 31. The giant neutral gas ring of M 31 was first clearly mapped by Roberts

(1966). It extends out to a distance of about 10 kpc along the major axis and dominates the appearance of M 31 in neutral hydrogen (see Fig. 2.10). Detailed H I observations also helped to define the spiral structure of the Andromeda Galaxy (e.g., Davies & Gottesman 1970; Sofue & Kato 1981). Recently, Braun & Thilker (2004) mapped a very large area around M 31 and M 33 in H I with the Westerbork Synthesis Radio Telescope in total-power mode. They discovered a very faint and diffuse H I bridge between both galaxies which also connects their systemic velocities. The H I column densities along the bridge are typically of the order of only a few times 10¹⁷ cm⁻². Braun & Thilker (2004) suggest this filament of neutral gas to be associated with the warm-hot intergalactic medium (WHIM) predicted by structure formation simulations (e.g., Davé et al. 1999, 2001).

2.1.3 The HVC population of M 31

The results summarised above illustrate that due to its proximity the Andromeda Galaxy has been studied in great detail to determine its morphological and dynamical properties. On the other hand, this proximity can also help us to identify the expected population of HVCs and CHVCs around M 31 with the help of deep H I observations with the largest available single-dish radio telescopes. Finding and studying the HVCs of M 31 in the 21-cm emission of neutral hydrogen has two major advantages. First, we would look at the HVC population from the outside, allowing us to directly determine the radial distribution of HVCs around M 31. Because of the widely unknown distances this is not possible for Galactic HVCs. Second, the distance towards M 31 and its HVC population is sufficiently well known, allowing us to determine important distance-dependent physical parameters such as size, H I mass, and H I mass density. Again, this is not directly possible in the case of Galactic HVCs due to their uncertain distances.

The first HI blind survey with the aim to detect HVCs around M 31 was carried out by Thilker et al. (2004) with the new 100-m Green Bank Telescope. They mapped an area of $7^{\circ} \times 7^{\circ}$ centred on M 31, corresponding to a projected area of about $95 \times 95 \text{ kpc}^2$. Within 50 kpc of M 31 they found about 20 discrete and fairly extended clouds with HI masses between 10^5 and $10^7 M_{\odot}$, including previously known Davies' Cloud (Davies 1975). Thilker et al. (2004) identified the discovered HI clouds with the first extensive extragalactic counterpart to the Galactic HVC population. The detected clouds are fairly large and massive and resemble the large HVCs and HVC complexes seen around the Milky Way.

The discovery of Thilker et al. (2004) immediately raises the question whether there is also a population of compact high-velocity clouds around M 31 and whether CHVCs near M 31 can be detected in a deep H I survey with a 100-m class radio telescope such as Effelsberg or the GBT. As noted before, the results of previous surveys of external galaxy groups (Zwaan 2001; Pisano et al. 2004) could not disclose any intra-group H I clouds not connected with dwarf galaxies. These non-detections of HVC equivalents in other galaxy groups lead to a strict upper limit for the distance of CHVCs/HVCs from the Galaxy of the order of 150 kpc. If we assume typical distances of CHVCs from the Milky Way of the order of 100 kpc we can estimate the expected 21-cm line intensities of potential CHVCs surrounding M 31. From deep H I observations of 11 CHVCs with the 100-m Effelsberg telescope (Westmeier et al. 2005b) we obtain a typical brightness temperature of $T_{\rm MW}^{\rm MW} \approx 0.75$ K averaged over a typical angular size of $\varphi_{\rm MW} = 30'$. If we

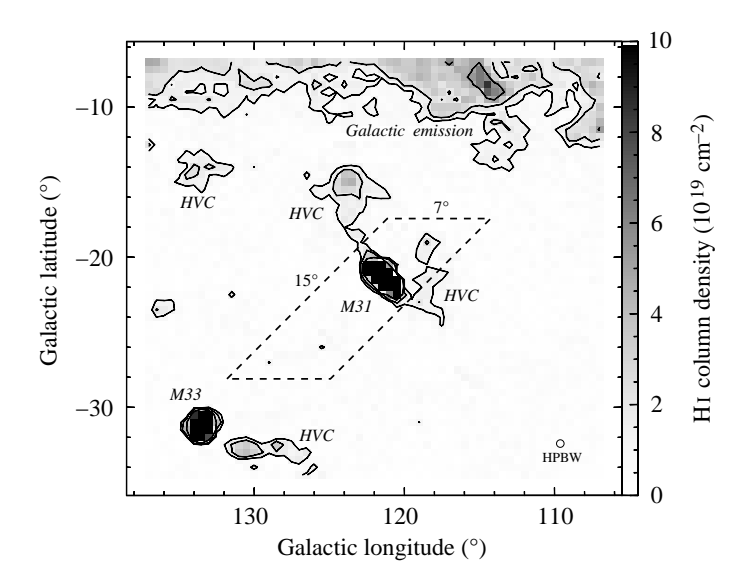


Fig. 2.3: HI column density map of a $30^{\circ} \times 30^{\circ}$ field around M 31 from the Leiden/Dwingeloo Survey (Hartmann & Burton 1997). The emission was integrated from -450 to -100 km s⁻¹ in the LSR frame. Apart from the emission of M 31 and M 33 a few Galactic HVCs are visible in the field. The dashed line outlines the field of our HI blind survey with the Effelsberg telescope.

place the same CHVCs at the distance of M 31 of 780 kpc (Stanek & Garnavich 1998) their typical angular sizes would be $\varphi_{\text{M 31}} = 4'$ which could no longer be resolved with the HPBW of the Effelsberg telescope of $\vartheta_{\text{Eff}} = 9'$. As a consequence, the observed brightness temperature would be reduced according to the beam filling factor:

$$T_{\rm B}^{\rm M\,31} = \frac{\varphi_{\rm M\,31}^2}{\vartheta_{\rm Eff}^2} T_{\rm B}^{\rm MW} = 140 \text{ mK}.$$
 (2.1)

A $3\,\sigma$ detection of potential M 31 CHVCs (i.e. a spectral baseline RMS of $\sigma = T_{\rm B}^{\rm M\,31}/3 = 45\,\rm mK$) can be achieved within only 30 s of integration time per pointing, using the 1024-channel autocorrelator at Effelsberg in regular frequency-switching mode and assuming a velocity resolution of 20 km s⁻¹ which should sufficiently resolve the spectral lines of the warm neutral medium. If CHVCs are a natural phenomenon in the evolution of large spiral galaxies and if the CHVCs of the Milky Way have typical distances of the order of 100 kpc we should be able to detect the CHVC population of M 31 in an H I blind survey with the Effelsberg telescope.

2.2 Observations, data reduction, and analysis

2.2.1 Observations

The observations for the H I blind survey of M 31 were carried out between July 2003 and August 2004 with the 100-m radio telescope at Effelsberg. The aim of our observations was to sample the gravitational potential well of M 31 out to a very large projected distance of more than 100 kpc to compare the radial distribution of CHVCs with the expectations from simulations and other observations. In addition, the survey would allow us to determine important physical parameters of the CHVC population such as the overall kinematics and the H I mass function. As a compromise between coverage and observing time we chose the mapping area outlined in Fig. 2.3. It extends out to an angular distance of about 10° from M 31 in the south-eastern direction, corresponding to a projected distance of about

Table 2.1: Observational parameters of the Effelsberg H I blind survey of M 31. The southern part of the map was observed with the old 1024-channel autocorrelator, whereas for the northern part we used the new 8192-channel autocorrelator (AK90). The final baseline RMS is given for a system temperature of 25 K at the given velocity resolution. The specified sensitivity is the baseline RMS times the spectral bin width at the original velocity resolution, converted to H I column density.

parameter	southern part	northern part	unit
autocorrelator	old	new	
bandwidth	6.3	10	MHz
polarisations	2	2	
channels per polarisation	512	4096	
velocity resolution	2.6	0.5	${\rm kms^{-1}}$
frequency switching	normal	in-band	
total integration time	180	180	S
final baseline RMS	45	60	mK
sensitivity	21	5.5	$10^{16} \ {\rm cm^{-2}}$
WNM sensitivity*	2.2	1.3	$10^{18} \ {\rm cm}^{-2}$
WNM mass detection limit*	8	5	$10^4~M_{\odot}$
* 1 · ·			1

^{*}For $T_{\rm B} > 3\,\sigma$ at 20 km s⁻¹ velocity resolution and a line width of 25 km s⁻¹ FWHM.

140 kpc which is about 2 /3 of the projected distance towards M 33. In this direction we expect the least confusion with H I emission from the Galactic plane. In the north-western direction our map extends out to about 5°, corresponding to 70 kpc in projection. The total area of our map is $15^{\circ} \times 5^{\circ}$ which covers about 0.2% of the entire sky.

The map was split into individual rows of constant declination with 35 pointings each. The individual pointings were separated in right ascension by $760'' \approx \text{HPBW} \times \sqrt{2}$. Adjacent rows were separated in declination by $380'' \approx \text{HPBW}/\sqrt{2}$ and shifted in right ascension by the same amount, resulting in an orientation angle of the entire map of 45° with respect to the equatorial coordinate system.¹ As a consequence, the final map is beam-by-beam sampled and oriented nearly perpendicular to the major axis of the disk of M 31. Aligning the map along the minor axis of M 31 has the advantage that we avoid confusion with the disk emission along the major axis as far as possible.

The southern part of the map was observed with the old 1024-channel autocorrelator, whereas the northern part was observed with the new 8192-channel autocorrelator (AK90). The reason for changing from the old to the new autocorrelator in early 2004 was that in August 2003 the quality and stability of the spectral baselines suddenly degraded. Several maxima and minima occurred over the bandpass, requiring a higher-order polynomial to accurately describe the shape of the baseline. The effect is illustrated with two example spectra in Fig. 2.4. The more severe problem was that the positions and amplitudes of the maxima and minima changed significantly over short timescales of the order of one hour, making a baseline correction difficult. In addition to the baseline problems the amount and strength of radio frequency interference (RFI) increased significantly over the second half of the year 2003. To investigate the interference problem in more detail we scanned

 $^{^1}$ The disk of M 31 has a position angle of about 38° with respect to the equatorial coordinate system.

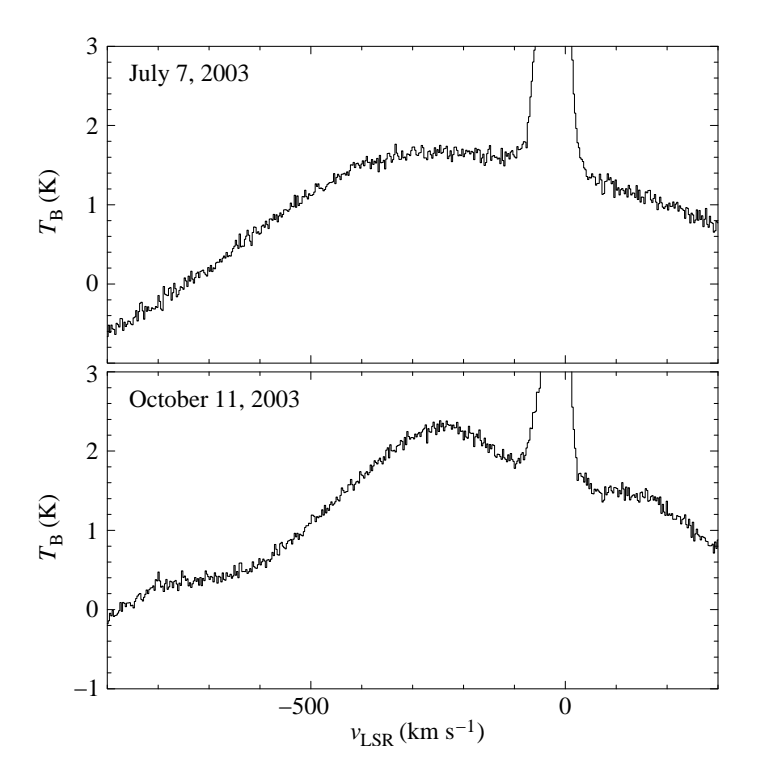


Fig. 2.4: Two example spectra from the Effelsberg HI blind survey of M 31, taken in July and October 2003. The shape of the spectral baseline is significantly more complex in the lower spectrum, requiring a higher-order polynomial for baseline correction. This degradation of the quality and stability of the spectral baseline was the motivation for using the new autocorrelator (AK90) for the northern part of the M 31 map.

the entire frequency band between 1290 MHz and 1480 MHz on November 22, 2003. We detected numerous RFI peaks all over the band, some of which had intensities of the order of 10 K. It turned out that we observed the highest RFI intensities when pointing the telescope in azimuth in the direction of the observatory building. Towards larger angular separations from the building the number of RFI peaks and their intensities decreased significantly, demonstrating that most of the RFI originated from electronic devices in the observatory building. We reported our results to the responsible people at the MPIfR who decided to conduct an extensive RFI test during which most of the electronic equipment at the observatory was switched off and on again to track down the sources of RFI within the building. Unfortunately, only a single RFI source was discovered: The webcam on top of the observatory building turned out to be responsible for a strong RFI peak of up to 20 K which had appeared in many spectra of the M 31 survey at a frequency near the Galactic H I emission. The remaining RFI sources could not be identified. The RFI problem will be solved with completion of the new Faraday room at Effelsberg which will host most of the electronic equipment that is currently placed in the observatory building.

The reason for the distorted spectral baselines, however, could not be uncovered. As the quality of the spectra was not sufficient for the objectives of our M 31 survey we decided to carry out test observations with the new 8192-channel autocorrelator (AK90). The test observations demonstrated that the AK90 provided a significantly better baseline quality and stability than the old 1024-channel autocorrelator. Thus, we decided to continue the survey in the northern direction using the AK90 instead of the old autocorrelator. Another advantage of using the AK90 is its larger bandwidth of 10 MHz. This allowed us to use the in-band frequency switching method which spends 100% of the integration time on source. As a result the signal-to-noise ratio in the northern part of the map is by a factor of about $\sqrt{2}$ higher than in the southern part. The technical specifications of the

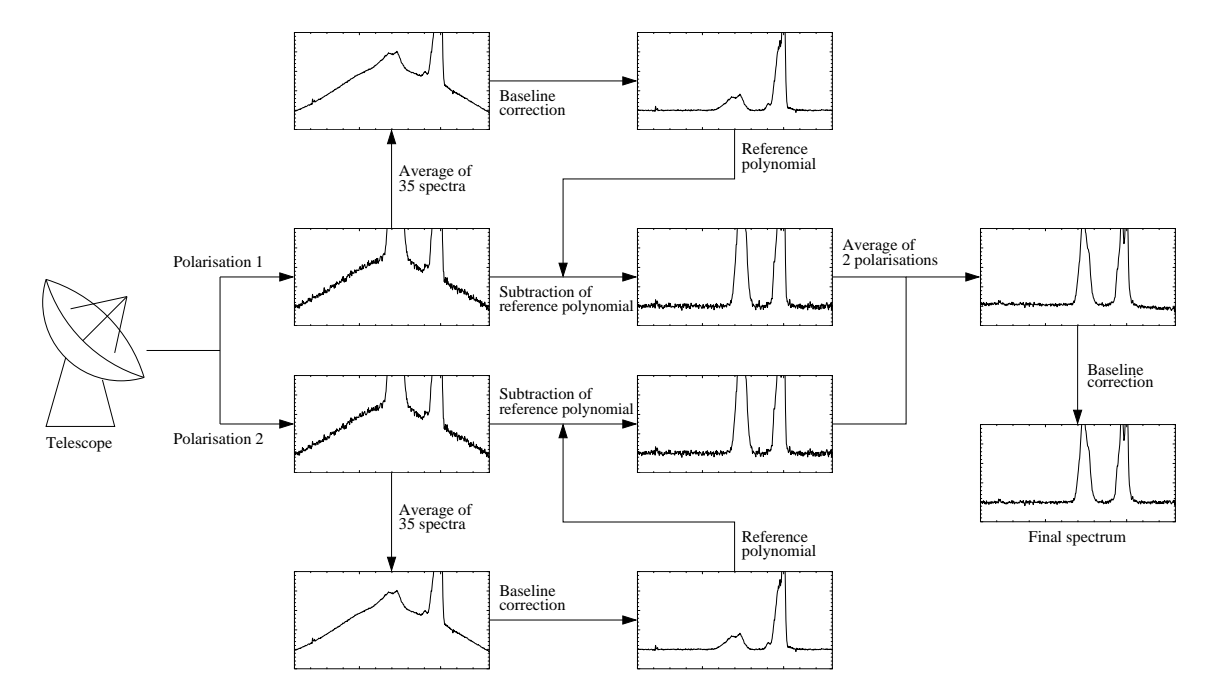


Fig. 2.5: Flow chart of the spectral baseline correction procedure for the southern part of the M 31 map with two polarisations. The procedure for the northern part of the map is similar but with four instead of two input spectra due to the additional reference spectra resulting from the in-band frequency switching mode.

two autocorrelators and the resulting spectral parameters for the two parts of the map are listed in Table 2.1. Throughout this document we follow the conservative approach of using the 1024-channel autocorrelator specifications as basis for all sensitivity-related parameters.

2.2.2 Data reduction

The standard flux calibration source S7 was observed every 6 hours and at the beginning and end of each observing run. The corresponding flux calibration factors for the two polarisations were determined by the software nautocal (based on the results obtained by Kalberla et al. 1982), yielding statistical calibration errors of the order of only 1% over an entire observing run of typically 10 to 15 hours. The calculated flux calibration factors were applied to the spectra using the software calib developed by Peter Kalberla.

The next step in the calibration procedure would have been stray radiation correction based on the study by Kalberla et al. (1980). Stray radiation is radiation from astronomical sources that enters the receiver through the antenna side lobes after reflection by the ground and the telescope structure. Depending on the telescope, the observing conditions, and the pointing direction in the sky, stray radiation can make up to 50% of the detected signal in extreme cases, leading to significant confusion (see Hartmann & Burton 1997 for a detailed discussion of the problem). Stray radiation originating from the Galactic disk should affect the radial velocity range within about $\pm 150~{\rm km\,s^{-1}}$ in the LSR frame where the strongest H I emission lines of the Milky Way are found. This velocity range overlaps with the radial velocities observed in some parts of M 31, so that stray radiation

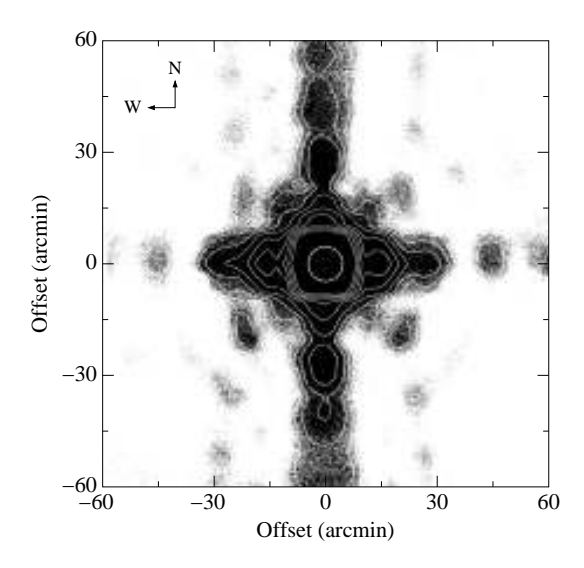


Fig. 2.6: Antenna pattern (from Kalberla et al. 1980) at $\lambda=21$ cm covering the main beam and near side lobes of the 100-m radio telescope at Effelsberg within an area of $2^{\circ} \times 2^{\circ}$. Black corresponds to high sensitivity. The inner circle indicates the -3 db level. The other contours are drawn from -12.5 db to -40 db in steps of 2.5 db. The antenna pattern was derived from combined observations of Cassiopeia A and Cygnus A.

correction was advisable. It turned out, however, that the stray radiation correction procedure nstrayof based on the results of Kalberla et al. (1980) created an artifical step of the order of 50 mK in the spectral baseline at radial velocities of $v_{\rm LSR} \approx -300~{\rm km\,s^{-1}}$. This step occurred at the edge of the velocity range which was processed by nstrayof and would have had no effect for the study of Galactic HI emission. In the case of M 31, however, the artifical step in the spectra interfered with the equally faint emission of the outer disk of M 31 and parts of the discovered high-velocity gas. Thus, we had to omit the stray radiation procedure completely to avoid a distortion of the spectral baselines. As nstrayof also carries out the correction for the main beam efficiency, $\eta_{\rm mb}$, of the telescope, we had to apply the correction by hand in our case, using the same value of $\eta_{\rm mb} = 0.72$ as nstrayof.

A related problem is that HI emission from the disk of M31 could have been detected through the near side lobes of the telescope and create the impression of extra-planar gas in proximity to the disk. The beam pattern of the Effelsberg telescope at $\lambda = 21$ cm was studied in detail by Kalberla et al. (1980) through combined observations of Cygnus A and Cassiopeia A. The resulting map is shown in Fig. 2.6. The overall crosswise structure results from diffraction by the four support legs. Significant side lobes can be found particularly in the north-south direction. At 1° angular distance from the pointing direction the sensitivity drops to about -30 dB (corresponding to -3.5 Np). Typical brightness temperatures of 20 K, as observed along the HI ring of M31, would therefore be attenuated to about 20 mK which is far below the noise level of our data at the original spectral resolution. The near side lobes in the east-west direction are not as extended as those in the north-south direction, but instead the sensitivity levels are somewhat higher near the pointing centre. At an angular distance of 15' the sensitivity drops to about -20 dB(corresponding to -2.3 Np), resulting in an attenuation of a 20 K signal to about 200 mK. This is of the same order of magnitude as the expected signals of high-velocity clouds around M31. The near side lobes, however, will only affect regions of the map which are in projection close to the HI disk of M31. All areas beyond a projected distance of the order of 10 kpc from the disk will not be influenced by stray radiation from M 31. In addition, stray radiation through the near side lobes should result in more extended emission, whereas CHVCs are expected to be unresolved. Consequently, stray radiation will not affect our observations since most of the expected CHVCs should be located at sufficiently large angular distances from the M 31 disk and will be unresolved by the HPBW of 9'.

To improve the quality of the spectral baseline correction we implemented a two-step baseline correction procedure. The first step was applied to each of the two polarisations separately.² All 35 spectra in one row of the map were averaged, and a polynomial of usually 8th order was fitted to the average spectrum after setting the line windows by hand. This constant reference polynomial—representing the average baseline over a time period of about two hours—was then subtracted from each individual spectrum of the row. The resulting spectra were already quite smooth as the baseline shape at Effelsberg was fairly stable over two hours. The second step was to average all spectra for one position and fit a polynomial to the resulting spectrum. Because of the previous subtraction of the reference polynomial a low-order polynomial was sufficient for the final averaged spectrum. In most cases, the baseline shape could be sufficiently described by a 4th or 5th order polynomial across a velocity range of 900 km s⁻¹. Only in very few cases a lower (down to 1st) or higher (up to 8th) order was necessary. The entire baseline correction procedure is illustrated in Fig. 2.5. After cutting out a few strong RFI peaks by hand, the resulting spectra were Hanning-smoothed to 4.1 km s⁻¹ velocity resolution and combined into a FITS data cube for further analysis.

2.2.3 Data analysis

The final survey consists of 3586 individual pointings for each of which a spectrum in the velocity range of $v_{\rm LSR} \approx -750\ldots +150~{\rm km\,s^{-1}}$ was available for further analysis.³ As we were interested in the detection of CHVCs around M 31, the survey was particularly optimised for the detection of compact sources with narrow spectral lines. In the inband frequency switching mode nearly 100% of the integration time is spent on source, maximising the sensitivity for the detection of faint CHVCs. The spectral baselines in this special observing mode, however, are not particularly smooth and stable, restricting the detectability of faint, diffuse sources.

To identify HVC/CHVC candidates of M 31 all spectra were searched by eye for potential emission lines. The criterion for HVC emission was a separation of the signal in phase space from the disk emission of M 31, where phase space is considered the observable three-dimensional sub-space consisting of the two spatial coordinates in the plane of the sky and the radial velocity as the only available kinematic component. Thus, signals could either be located along the same line of sight as the disk emission of M 31 but at different radial velocities, or they could be located outside the disk at any radial velocity.

2.2.4 Completeness of the data

Spatial coverage of the map

An important question arising from the approach of a visual inspection of the survey is the question of detectability and completeness of CHVC candidates. A first limitation of the completeness of our M 31 survey results from the spatial incompleteness of our

² Signal and reference spectra in the northern part of the map were also treated separately.

³ The systemic velocity of M 31 is $v_{\rm LSR} \approx -300~{\rm km\,s^{-1}}$.

map for larger radii. The geometric situation is illustrated in Fig. 2.7. There are five different regions for which analytic expressions for the spatial completeness have to be derived separately. The five regions are separated from each other at radii of 2°.5, 3°.5, 7°.9, and 12°.7 from the centre of M 31, corresponding to projected distances of 34.1 kpc, 48.2 kpc, 107.7 kpc, and 173.6 kpc if a distance of M 31 of 780 kpc is assumed (Stanek & Garnavich 1998). There are two ways of calculating the spatial completeness within these regions as a function of radial distance from the centre of M 31. The first possibility is to calculate the local filling factor at distance r from the centre of M 31 which is given by the ratio of the length of the arc intersecting the map over the total arc length $2\pi r$ of the full circle. The second way is to calculate the global filling factor of the map within a certain radius r, which is the ratio of the area being covered by the map within r over the total area πr^2 . Making the approximation of a Cartesian coordinate system, the local completeness function, $C_{\rm L}(r)$, is given by

$$C_{L}(r) = \begin{cases} 1 & (0 < r \le a) \\ 1 - \frac{2}{\pi} \arccos(a/r) & (a < r \le b) \\ \frac{7}{8} - \frac{1}{2\pi} [3\arccos(a/r) + \arccos(b/r)] & (b < r \le c) \\ \frac{3}{8} - \frac{1}{2\pi} [\arccos(a/r) + \arccos(2b/r)] & (c < r \le d) \\ 0 & (d < r) \end{cases}$$
(2.2)

with a=34.1 kpc, b=48.2 kpc, c=107.7 kpc, and d=173.6 kpc being the separations between the five regions. The equations for the global spatial completeness, $C_{\rm G}(r)$, are significantly more complex, especially in the outer regions of the map:

$$C_{G}(r) = \begin{cases} 1 & (0 < r \le a) \\ 1 - \frac{1}{\pi} [2\arccos(a/r) - \sin(2\arccos(a/r))] & (a < r \le b) \\ 1 + \frac{1}{2\pi r^{2}} \left[3a\sqrt{r^{2} - a^{2}} + b\sqrt{r^{2} - b^{2}} + a^{2} \right] \\ - \frac{1}{2\pi} [3\arccos(a/r) + \arccos(b/r) + \arccos(a/b)] & (b < r \le c) \\ \frac{1}{2} + \frac{a^{2} + c^{2} + a\sqrt{r^{2} - a^{2}}}{2\pi r^{2}} - \frac{\arctan(3) + \arccos(a/r)}{2\pi} \\ + \frac{c^{2}\sin(\psi)}{2\pi r^{2}} \left[\cos(\psi) + \sqrt{\frac{r^{2}}{c^{2}} - \sin^{2}(\psi)} \right] \\ - \frac{1}{2\pi} \arccos\left(\frac{c}{r}\sin^{2}(\psi) - \cos(\psi)\sqrt{1 - \frac{c^{2}}{r^{2}}\sin^{2}(\psi)}\right) & (c < r \le d) \\ \frac{b^{2} + c^{2}}{\pi r^{2}} & (d < r) \end{cases}$$

where $\psi \equiv (3\pi/4)$ – arctan(1/3). Again, a Cartesian coordinate system is used. The two spatial completeness functions $C_{\rm L}(r)$ and $C_{\rm G}(r)$ are plotted in Fig. 2.8 as a function of projected distance r from the centre of M 31. Within r=34 kpc the survey is complete. Outside r=176 kpc the local completeness becomes 0 whereas the global completeness decreases with $1/r^2$. At intermediate radii both functions have a more complex behaviour. They drop abruptly at r=34 kpc with the local completeness function $C_{\rm L}(r)$ decreasing much faster than the global completeness function $C_{\rm G}(r)$. Locally, 50% completeness is reached at a distance of $r_{50}=48$ kpc already, whereas on the global scale the corresponding radius is $r_{50}=77$ kpc. At a projected distance from M 31 of 100 kpc the completeness is $C_{\rm L}=12\%$ and $C_{\rm G}=36\%$. This means that out to 100 kpc our survey still covers more

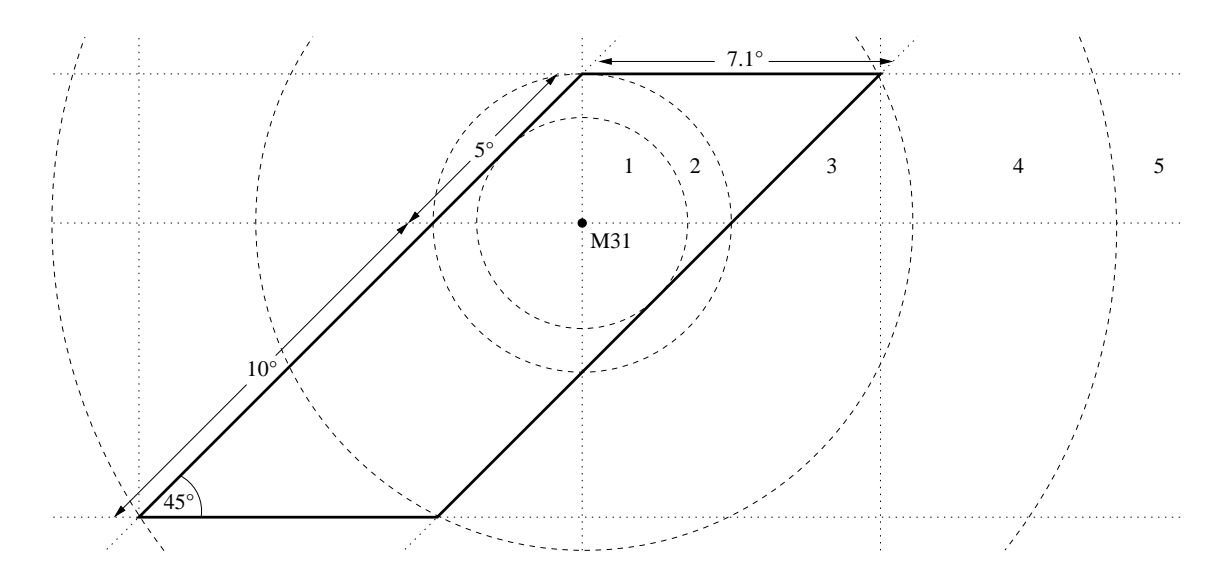


Fig. 2.7: The plot shows the geometry of the field (thick solid line) mapped around M 31. The dashed circles separate the five regions (labelled with numbers) for which the individual spatial completeness calculations had to be performed.

than a third of the total area, but the local completeness at this distance is already fairly low because the survey area is concentrated around the central region.

Spatial sampling of the map

Another reason for spatial incompleteness is related to the spatial sampling of the map. The individual pointings of the map are separated by the HPBW of the telescope of 9', so that the sensitivity is significantly decreased at positions which are located exactly in between four individual pointings. Assuming a two-dimensional Gaussian sensitivity function for the main beam, the sensitivity of each beam at the position in between four neighbouring beams (i.e. the corner of each grid element) is exactly 0.25. Averaging the four neighbouring beams results in a decrease of the RMS by a factor 2 and, thus, in a slightly higher effective sensitivity of 0.5. As a consequence, the sensitivity for unresolved sources is in the range of 0.5 to 1, depending on the source position relative to the grid. Extended sources are covered by several pointings so that their detectability is not reduced.

Flux detection limit

The next question is to which signal-to-noise ratio potential CHVCs can be detected. To answer this question, we simulated 500 spectra with a Gaussian RMS and a velocity resolution of $10.1~\rm km\,s^{-1}$. Each spectrum was multiplied with a sine function of random amplitude, wavelength, and phase shift to get arbitrary baseline shapes. With a probability of 15% a Gaussian spectral line was added to each spectrum. The line widths were randomly chosen between $15~\rm and~35~\rm km\,s^{-1}$, corresponding to what is expected for the warm neutral medium of CHVCs. The peak intensities were also assigned randomly with signal-to-noise ratios between 0 and 6. Our algorithm added 81 artifical spectral lines with the above mentioned parameters to the 500 spectra. The positions, intensities, and line

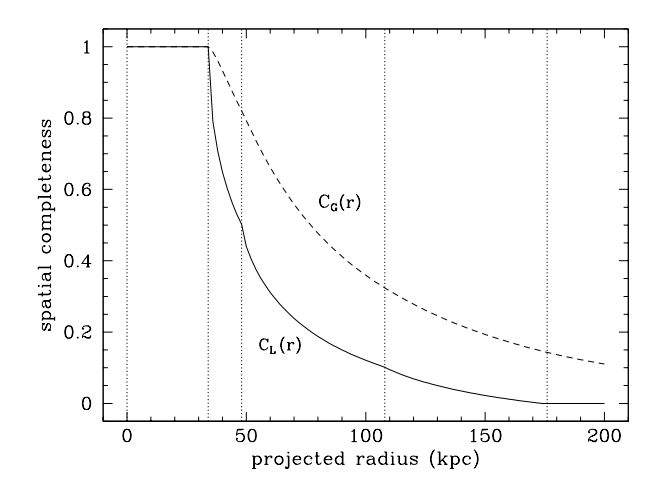


Fig. 2.8: Spatial completeness of the M 31 survey as a function of projected distance r from the center of M 31. The dashed line shows the global completeness function $C_{\rm G}(r)$ and the solid line the local completeness function $C_{\rm L}(r)$. The vertical dotted lines indicate the radii a, b, c, and d at which the completeness function changes abruptly due to the special geometry of the observed field.

widths of the 81 spectral lines were written to a data file for later comparison. Next, the entire data set of 500 artificial spectra was searched by eye to detect the hidden spectral lines.

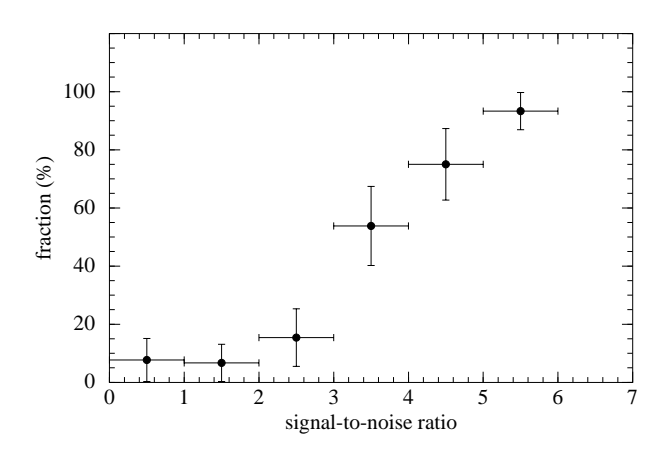
In total, 34 of the 81 signals could be identified. The resulting completeness function is shown in Fig. 2.9. At a peak intensity level of $3.5\,\sigma$ the completeness is about 50%. Above $5\,\sigma$ we are virtually complete with only a single of the 14 lines above $5\,\sigma$ being missed. Note that there are also two detections at about $1\,\sigma$. In both cases strong noise peaks have accidently increased the signal above the detection threshold. These results demonstrate that when using the classical $3\,\sigma$ criterion for the detectability of spectral signals we have to consider that source counts below the $5\,\sigma$ level suffer from incompleteness. On the other hand, detections are possible even at intensities below $3\,\sigma$ although the detection rate decreases significantly.

Confusion with Galactic HI emission

In optical astronomy the investigation of extragalactic objects is affected by extinction due to dust in the interstellar medium of the Galaxy. The strongest extinction is observed at low Galactic latitudes along the so-called zone of avoidance. The situation in HI spectroscopy is slightly different. Emission lines of extragalactic objects can be superposed on those of the Milky Way, making an identification and analysis difficult or even impossible. Galactic HI emission is found not only near the Galactic plane but all across the sky. However, only the radial velocity range around $v_{\rm LSR} = 0~{\rm km\,s^{-1}}$ is affected, whereas sources with radial velocities of $|v_{\rm LSR}| \gtrsim 100~{\rm km\,s^{-1}}$ are usually not subject to confusion with Galactic emission lines. In other words, the zone of avoidance in HI spectroscopy covers the entire sky but only a limited radial velocity range for each sight line.

The systemic radial velocity of M 31 is $v_{\rm LSR} \approx -300~{\rm km\,s^{-1}}$. On the approaching side of M 31 we observe radial velocities down to about $-600~{\rm km\,s^{-1}}$, implying values up to about $0~{\rm km\,s^{-1}}$ on the receding side. The latter is well within the velocity range of Galactic H I emission in this area which reaches out to about $-140~{\rm km\,s^{-1}}$. Hence, a major part of the receding side of M 31 is confused with Galactic emission. Blending effects could also affect the detection of HVCs around M 31. As the peak intensities of HVCs are expected to be small compared to the intensities of Galactic emission lines, HVCs superposed on

Fig. 2.9: Fraction of detected spectral lines as a function of signal-to-noise ratio, derived from the investigation of 500 artificial spectra as described in the text. About 50% of all signals with a peak intensity of $3.5\,\sigma$ are detected. Above $5\,\sigma$ we are virtually complete with only a single of the 14 lines above $5\,\sigma$ being missed.



Galactic emission are virtually undetectable. In our survey this should be the case for all potential HVCs with $v_{\rm LSR} \gtrsim -140~{\rm km\,s^{-1}}$, resulting in incompleteness with respect to certain radial velocities.

2.3 Search for the CHVC population of M 31

Column density maps of the entire survey area are displayed in Fig. 2.10. The upper map shows the entire flux integrated over a velocity range of $v_{\rm LSR} = -620\ldots -24~{\rm km\,s^{-1}}$. In the direction of M 31 the H I emission of the Milky Way disk reaches out to velocities of $v_{\rm LSR} \approx -140~{\rm km\,s^{-1}}$, resulting in a significant overlap with emission from the northeastern part of M 31. The filamentary emission of the Galactic disk can be seen all over the map with typical column densities of a few times $10^{20}~{\rm cm^{-2}}$. Two conspicuous features of M 31, the famous H I ring and the warp of the H I disk, are immediately visible in the map. The ring was first clearly detected by Roberts (1966) and has a radius of approximately 10 kpc. The central depression in the H I disk shows column densities of the order of 30% of the peak values found along the ring (Guibert 1974). The warping of M 31 can be seen towards the far ends of the disk, in particular in the north-eastern part, where the so-called perturbed outer arm (Whitehurst et al. 1978; Sawa & Sofue 1982) is significantly bent in the northern direction.

The lower map in Fig. 2.10 is a high-contrast logarithmic map of H I column densities of $10^{18} \dots 10^{22}$ cm⁻² in the velocity range of $v_{\rm LSR} = -620 \dots -139$ km s⁻¹. Here, the velocity range of Galactic H I emission is excluded with the restriction that some of the emission from the north-eastern end of the M 31 disk is also missing. In addition, we created a mask data cube which was smoothed in position and velocity. Only those elements with an intensity above 17.5 mK in the mask were also selected in the original data cube to contribute to the moment 0 map, resulting in a high-quality image showing H I column densities down to a few times 10^{18} cm⁻².

Apart from regular disk emission, several regions of extra-planar gas and isolated HI clouds are visible. The extra-planar gas emission is particularly prominent along the south-eastern edge of the disk, but extended, diffuse HI emission with column densities of $N_{\rm HI} \lesssim 10^{19}~{\rm cm}^{-2}$ is also present along the north-western edge. The most outstanding isolated HI cloud in the map is Davies' Cloud located about 1°.5 north-west of the centre of M 31. The cloud was discovered by Davies (1975) and studied in detail by de Heij et al.

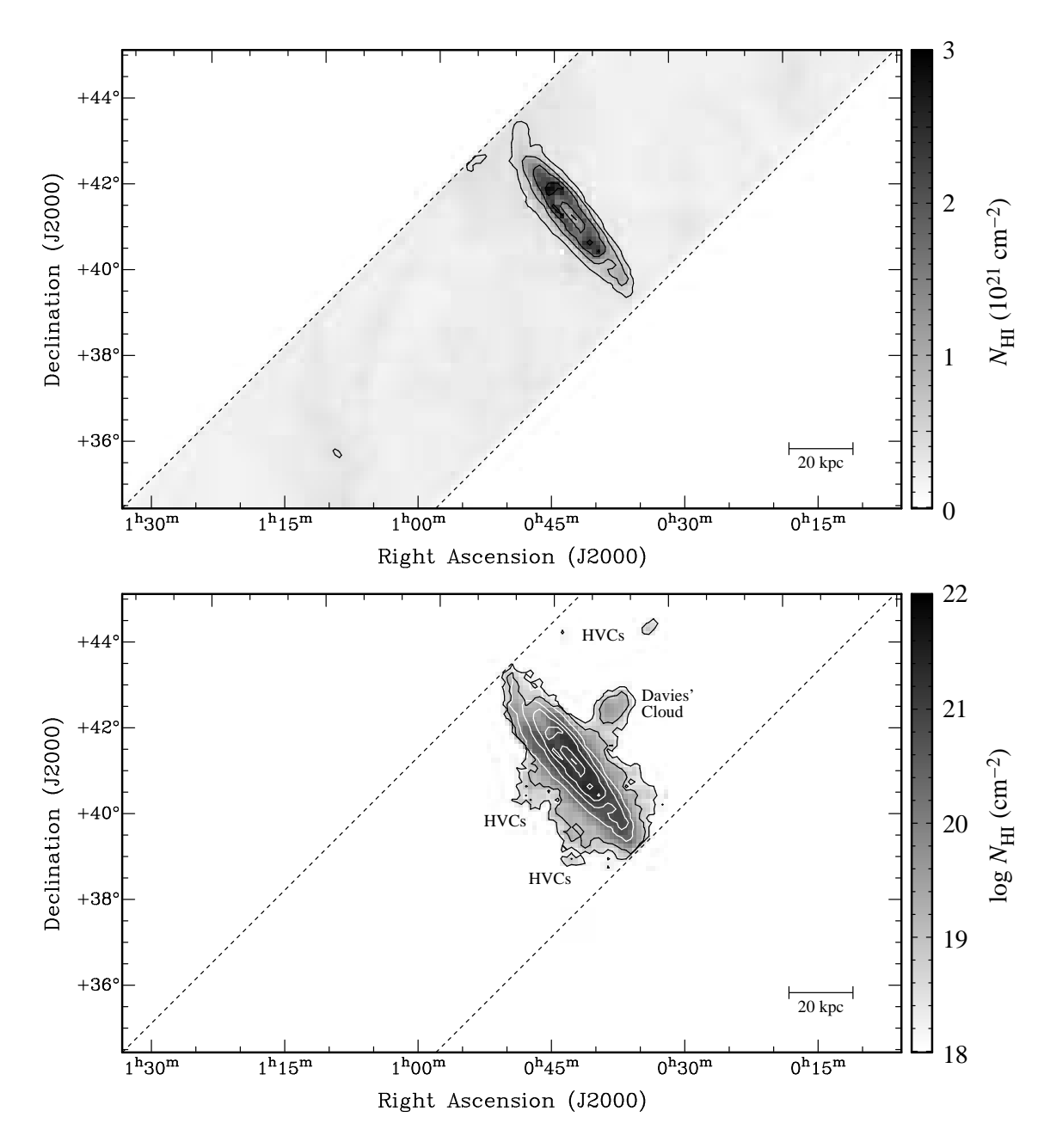


Fig. 2.10: HI column density maps of our blind survey of M 31 with the 100-m radio telescope at Effelsberg. Top: Integrated HI column density in the velocity range $v_{\rm LSR} = -620\ldots -24~{\rm km\,s}^{-1}$. The contour lines are drawn at 4, 8, 16, and $25\times 10^{20}~{\rm cm}^{-2}$. The diffuse and filamentary emission all over the map originates from Galactic HI at velocities of $v_{\rm LSR} > -140~{\rm km\,s}^{-1}$. Bottom: Integrated HI column density in the velocity range $v_{\rm LSR} = -620\ldots -139~{\rm km\,s}^{-1}$, using a special mask and a logarithmic intensity scale to emphasise the faint HI emission. The black contour lines correspond to 2×10^{18} and $1\times 10^{19}~{\rm cm}^{-2}$. The white contour lines are those from the upper map. Several regions of extra-planar gas and high-velocity clouds, of which Davies' Cloud is the most prominent, can be seen all around M 31.

(2002c) with the WSRT. A few more compact and isolated clouds can be seen all around the Andromeda Galaxy.

The clouds seen in Fig. 2.10 were already discovered by Thilker et al. (2004) in their HI survey of M 31 with the Green Bank Telescope. A comparison between their Fig. 2 and the lower map in Fig. 2.10 reveals a good correlation between the clouds seen in both surveys with the exception of a few extended clouds detected in the GBT data but not seen in the Effelsberg map. Those clouds without counterparts in the Effelsberg survey are typically very diffuse with HI column densities of the order of only 10^{18} cm⁻². They were only detected in the GBT data after smoothing the velocity resolution significantly to 72 km s⁻¹. With the frequency switching method such diffuse objects can hardly be detected in the Effelsberg data which was optimised for the detection of compact sources with narrow spectral lines.

2.3.1 Discovery of CHVC candidates

The extra-planar gas clouds detected in our Effelsberg survey are fairly close to M 31 with projected distances of less than 50 kpc. In addition, some of them are rather extended with angular diameters much larger than the typical 4' FWHM estimated for the expected CHVCs around M 31. With these parameters they resemble the more extended HVCs and HVC complexes seen around the Milky Way. But where are the expected equivalents of the compact high-velocity clouds? In addition to the more extended HVCs near the disk of M 31 we in fact discovered about 60 faint, compact, and isolated H I signals across the entire survey area. Given their distribution and intensities they are promising candidates for the sought-after CHVCs around M 31. The positions of all candidates, including the HVCs found near the disk of M 31, are plotted in the map in Fig. 2.11. Most of them are detected at only the 3σ level and at a single position only. To confirm their existence, follow-up observations of all CHVC candidates were mandatory.

The follow-up observations were carried out in June 2004 (southern part of the map) and July 2005 (northern part of the map) with the Effelsberg telescope. The existence of some of the objects (namely Davies' Cloud and the HVCs found by Thilker et al. 2004) had already been confirmed in previous publications so that we did not observe them again. The positions of all other HVC/CHVC candidates were re-observed in H I with a total integration time of 5-10 minutes, using the new autocorrelator AK90 with specifications similar to those given in Table 2.1. The resulting RMS at the original velocity resolution of $0.5~{\rm km\,s^{-1}}$ is about $45~{\rm mK}$.

The follow-up observations could not confirm any of the fainter CHVC candidates outside a projected radius of about 50 kpc around M 31. In a few cases, even stronger emission lines could not be confirmed. Example spectra of two unconfirmed candidates are presented in Fig. 2.12. On the left hand side the original (1A) and follow-up (1B) spectrum of a faint CHVC candidate is shown. These faint candidates were most likely caused by radio frequency interference or simply by noise peaks. The spectra on the right hand side of Fig. 2.12 show the original (2A) and follow-up (2B) spectrum of one of the strongest high-velocity signals detected in our survey. Signals of such high intensities must have been caused by strong radio frequency interference. During the observations of the corresponding region construction works were carried out on the observatory site in connection with the new Faraday cage being built at Effelsberg. The heavy equipment

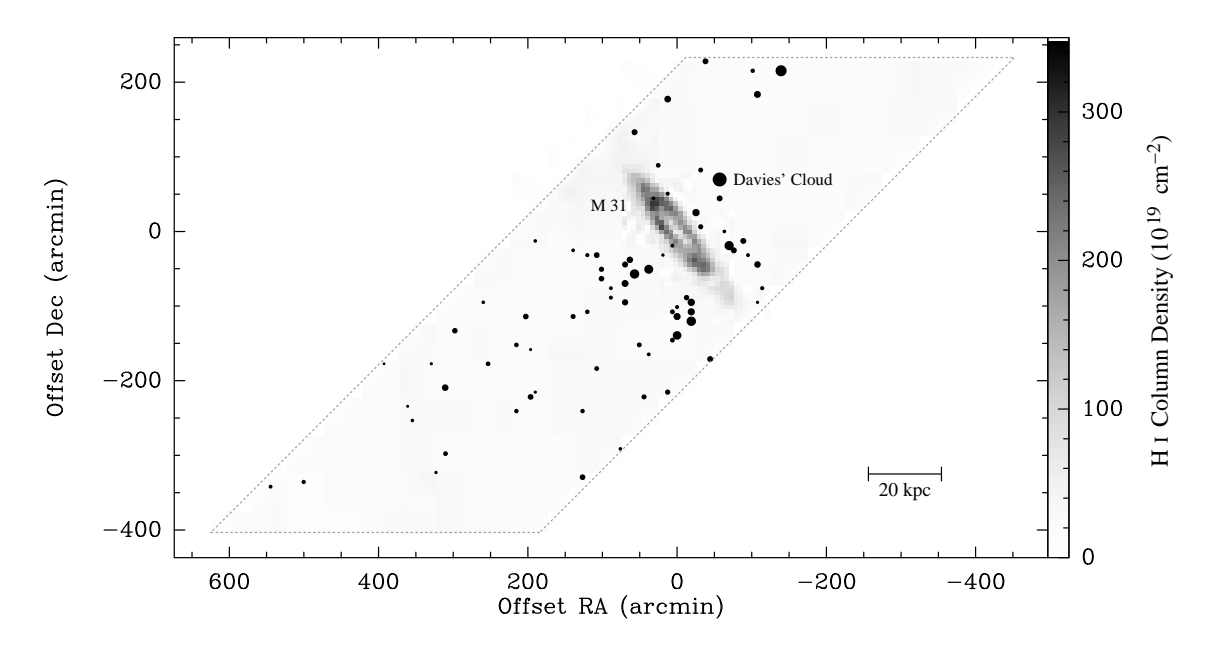


Fig. 2.11: HI column density map of M 31 showing the positions of all about 75 HVC/CHVC candidates as black dots, including the extended HVCs near the disk of M 31. The size of the dots corresponds to the HI peak column density of the candidates. Most of the faint candidates all across the survey area could not be confirmed, whereas most of the objects near the disk of M 31 are real.

used for these construction works is the most evident source of several strong emission lines detected in the course of our observations. In Fig. 2.13 the 17 HVC detections remaining after the follow-up observations are shown.

2.3.2 Consequences of our non-detection

What are the consequences of our failure to confirm any of the isolated, faint CHVC candidates? To answer this question, let us first make the very fundamental assumption that CHVCs are a general phenomenon occurring during the formation and evolution of large spiral galaxies. This assumption appears to be in accordance with most hypotheses for the origin of high-velocity clouds. If CHVCs were the result of outflows or winds from the galactic plane they should occur in all spiral galaxies. The intensity of the CHVC phenomenon, however, would strongly depend on the past and current star formation rate of the host galaxy. There has been evidence for the star formation rate of M31 being significantly lower than that of the Milky Way. Hodge (1992) compiles a star formation rate for M 31 in the range of $0.1...0.4~M_{\odot}~\rm{a}^{-1}$ from various older studies. Recently, Williams (2003) studied the star formation history of M 31 on the basis of B and Vphotometry of the stellar populations in six fields. He derived a slightly higher mean star formation rate for the entire disk of M 31 of the order of 1 M_{\odot} a⁻¹ over the past 64 million years. In contrast, the recent star formation rate of the Milky Way has been estimated to lie in the range of $0.8...13.0~M_{\odot}~\mathrm{a}^{-1}$ (Talbot 1980; Güsten & Mezger 1982; Turner 1984; Timmes et al. 1997). Thus, M 31 as a typical type Sb galaxy is more quiescent with respect to star formation than the Milky Way, which could result in a deficiency of neutral

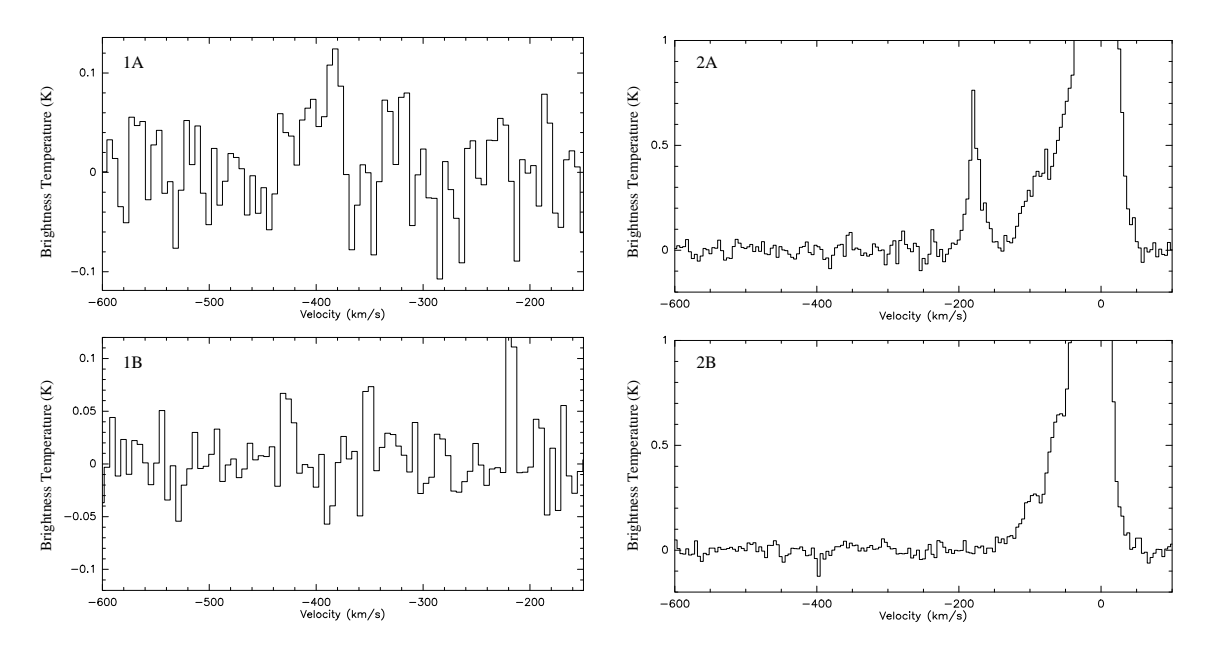


Fig. 2.12: Example spectra of a faint and a strong CHVC candidate from our Effelsberg survey (charts 1A and 2A). Both candidates could not be confirmed in our follow-up observations (charts 1B and 2B) and were probably caused by radio frequency interference. The strong signal in the spectrum in panel 2A was most likely caused by construction works carried out on the telescope site during the observations.

and ionised extra-planar gas originating from outflows and winds. In fact, M 31 was also found to have a slightly lower gas mass of $M_{\rm H}=4\times10^9~M_{\odot}$ than the Milky Way with $M_{\rm H}=5\times10^9~M_{\odot}$ (Hodge 1992). These effects could result in a less rich population of HVCs and CHVCs around M 31 compared to the Galaxy.

If CHVCs were the result of tidal interactions and the accretion of satellite galaxies, both the Milky Way and the Andromeda Galaxy should host a similar population of clouds. Both galaxies have about the same total mass of $1...2 \times 10^{12}~M_{\odot}$ (Evans & Wilkinson 2000; Wilkinson & Evans 1999) and host a similarly rich population of satellite galaxies within about 300 kpc radius (see, e.g., van den Bergh 1999, 2006 for a review of the Local Group). Numerous examples of tidal structures have been found around the Milky Way. These include stellar streams such as the Sagittarius stream (Ibata et al. 2001b), the Monoceros stream or ring (Yanny et al. 2003; Peñarrubia et al. 2005), and the recently discovered "orphan stream" (Belokurov et al. 2006c; Grillmair 2006) as well as a giant gas stream, the Magellanic Stream (including the Leading Arm), originating from the Magellanic Clouds. These streams are an overt sign of a rich accretion history of our Galaxy which could have contributed significantly to its extensive population of HVCs. A similar wealth of structures has been discovered around the Andromeda Galaxy. Ibata et al. (2001a) found the giant stellar stream of M 31 which is reminiscent of the Sagittarius stream around our own Galaxy. McConnachie et al. (2004) discovered an arc-like stellar feature which they suspected to be the tidal trail of NGC 205. A possible tidal interaction between M 31 and NGC 205 was already pointed out by Zwicky (1959). Ibata et al. (2005) announced the discovery of an extended stellar disk around M 31 with a common sense of rotation and a complex structure, indicating the accretion of one or more satellite galaxies by M 31 in the past. All these results suggest that the Andromeda Galaxy, too, has had a rich accretion history which could have resulted in a large amount of high-velocity gas.

Yet, the Milky Way and M 31 could have evolved in a slightly different way. As van den Bergh (1999) pointed out, the Andromeda Galaxy was likely formed as the result of several mergers of less massive progenitors. This is indicated by the de Vaucouleurs profile of the surface brightness, $\Sigma(r)$, of the spheroidal component of M 31 over a large range of radii, r, which is predicted in this case. The extended disk-like structure found by Ibata et al. (2005) and the discovery of the double nucleus of M 31 by Lauer et al. (1993) have supported this idea, whereas the Milky Way is believed to have formed in situ with only minor mergers during its evolution. In which way these two different evolution scenarios could have affected the formation of high-velocity clouds, however, remains unclear and can only be determined by detailed numerical simulations.

If CHVCs were the gaseous counterparts of primordial dark-matter mini-halos in the Local Group we would again expect to find comparable populations of CHVCs around both the Milky Way and M 31. Recent numerical simulations by Kravtsov et al. (2004) in the framework of Λ CDM cosmology, including gas and star formation, indicate that only a small fraction of the expected dark-matter satellites around Galaxy-sized halos are expected to contain a significant fraction of neutral gas, making them visible as CHVCs in the 21-cm line emission of HI. As the Milky Way and the Andromeda Galaxy have about the same total mass one would naively expect a similar number of dark-matter mini-halos around both galaxies. The results obtained by Kravtsov et al. (2004), however, have shown that the evolution of dark-matter satellites is vigorously affected by their environment. Close encounters of satellites with other satellites or their parent halo usually have a strong impact on their star formation history and gas content, thus determining the number of halos evolving into either satellite galaxies or CHVCs with neutral gas but without a noticeable stellar component. This strong dependence on evolution can explain the observation that several dwarf galaxies in the Local Group have a rich stellar population and a complex star formation history although they do not contain any significant amount of gas. In these cases, the gas simply may have been stripped in the course of interactions with other dark-matter halos. As noted before, the evolution of M 31 may have been different from that of the Milky Way, which could have influenced the evolution of darkmatter satellites around the two galaxies.

The populations of satellite galaxies around the Andromeda Galaxy and the Milky Way also show a few differences. The recent compilation by van den Bergh (2006) shows that, in contrast to the Galaxy, all inner satellites of M 31 are early-type objects. In addition, the dwarf spheroidals surrounding the Galaxy have significantly larger half-light radii than those around M 31, suggesting a different evolution. However, van den Bergh (2006) states that apart from these differences the satellite populations of M 31 and the Milky Way are quite similar with the exception of the Magellanic Clouds which have no counterpart in the Andromeda system. This suggests that the Magellanic Clouds may not have formed around the Galaxy but elsewhere in the Local Group (Byrd et al. 1994).

To summarise, although our own Milky Way and the Andromeda Galaxy have a similar total mass of the order of $10^{12} M_{\odot}$, their global evolution and star formation history may have been significantly different. This could have led to different HVC phenomena for both galaxies, whatever the exact formation scenario for HVCs may have been. With our current knowledge it is not possible to assess this problem in more detail, but we can still

try to compare the observational parameters of the HVCs around M 31 and the Galaxy. However, if we assume as a working hypothesis that both galaxies have a population of HVCs/CHVCs and that both populations have similar parameters we have to keep in mind that there may be systematic differences between the two HVC/CHVC populations.

Under the fundamental assumption that the Milky Way and M 31 have similar populations of CHVCs, we can use our non-detection in the case of M 31 to determine an upper limit for the distances of CHVCs from their host galaxies. This assumes that a similarly rich population of CHVCs is present around M 31 but the clouds are too small to be detected within the sensitivity of our data. This allows us to determine an upper limit for the H I mass of CHVCs, which, when applied to the Galactic CHVCs, provides us with an upper limit for their distance. We can get a first distance estimate from simple geometric considerations. As the expected CHVCs around M 31 should be unresolved with the HPBW of the Effelsberg telescope, the expected peak brightness temperatures of the M 31 CHVCs should mainly be determined by the beam filling factor, i.e. the solid angle of the CHVCs divided by the beam solid angle (see Eq 2.1). Thus, the distance of CHVCs can be estimated via

$$\frac{d}{d_{\rm M\,31}} = \frac{\tan\left[\vartheta_{\rm Eff}\,(T_{\rm B}^{\rm M\,31}/T_{\rm B}^{\rm MW})^{1/2}\right]}{\tan\left(\varphi_{\rm MW}\right)} \tag{2.4}$$

where $T_{\rm B}^{\rm MW}$ and $\varphi_{\rm MW}$ are the mean peak brightness temperature and mean angular diameter of the Galactic CHVCs, respectively. $T_{\rm B}^{\rm M31}$ denotes the detection limit of our Effelsberg M 31 survey, $d_{\rm M31}$ is the distance of M 31, and $\vartheta_{\rm Eff}$ is the HPBW of the telescope. Westmeier et al. (2005b) studied 11 Galactic CHVCs with the Effelsberg telescope, yielding $T_{\rm B}^{\rm MW} \approx 750$ mK and $\varphi_{\rm MW} \approx 30''$ FWHM. The approximate $3\,\sigma$ detection limit of our Effelsberg M 31 survey is $T_{\rm B}^{\rm M31} < 50$ mK at 20 km s⁻¹ velocity resolution which should still resolve the spectral lines of the warm neutral medium. The Effelsberg HPBW at 21 cm wavelength is $\vartheta_{\rm Eff} = 9'$, and the distance of M 31 is $d_{\rm M31} \approx 780$ kpc (Stanek & Garnavich 1998). Inserting these numbers into Eq. 2.4 yields an upper limit for the distance of CHVCs from their host galaxies of

$$d \lesssim 60 \text{ kpc}$$
. (2.5)

This distance limit is much lower than the 100 kpc we had assumed when preparing the Effelsberg survey based on previous results. If the condition holds that M 31 has a CHVC population similar in number, spatial distribution, and mass spectrum to that of the Milky Way, we have to assume that CHVCs are nearby objects with typical distances from their host galaxies of not more than a few ten kpc.

This has important consequences. Originally, CHVCs were considered candidates for primordial dark-matter halos distributed all across the Local Group (Braun & Burton 1999; de Heij et al. 2002a). They were identified by Braun & Burton (1999) as a homogeneous population of clouds, their small angular sizes indicating large distances of hundreds of kpc from the Milky Way. In this picture CHVCs would have been forming a physically distinct population of objects characterised by a common origin and evolution, whereas the "classical" HVCs would have been the result of Galactic outflows, tidal stripping, or accretion of gas in the vicinity of the Milky Way. Studies of external galaxy groups (e.g., Zwaan 2001; Pisano et al. 2004), however, failed to identify CHVC analogues in other groups, indicating that CHVCs are most likely objects in the circumgalactic environment

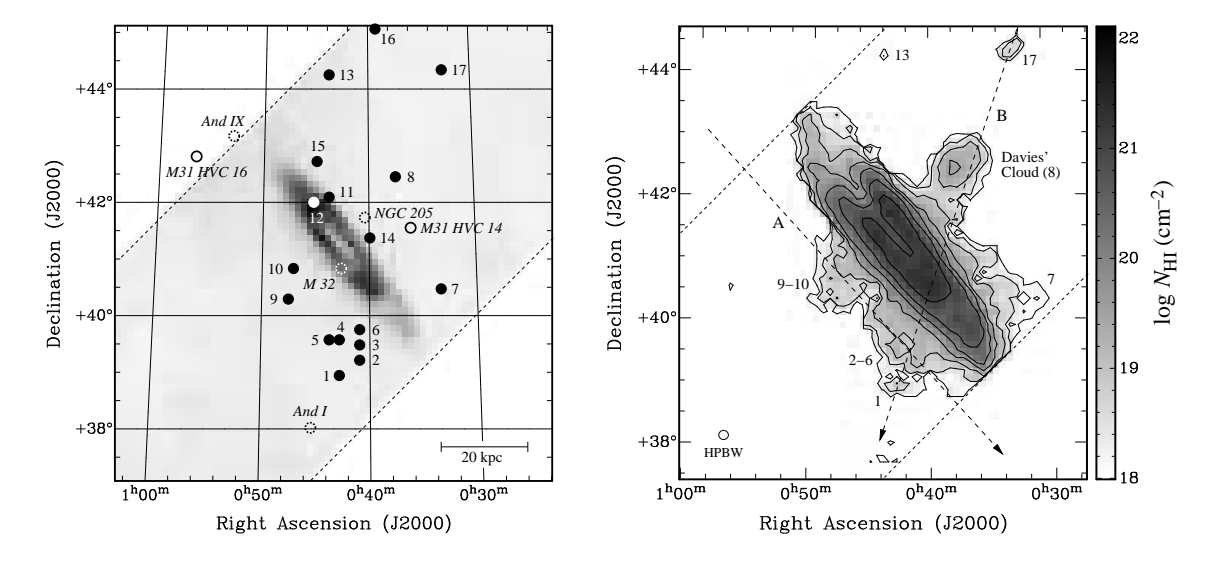


Fig. 2.13: Left: Locations of the 17 individual HVCs identified in our Effelsberg survey (filled circles) superposed on an HI column density map. Two HVCs studied with the WSRT (see Chapter 3) but not detected in our survey are plotted as solid open circles. The dashed open circles denote the positions of known satellite galaxies of M31. Right: HI column density map in the velocity range of $v_{\rm LSR} = -608...-135~{\rm km\,s}^{-1}$, using the same mask as for Fig. 2.10. The contours range from 18 to 22 dex in steps of 0.5 dex. The two dashed arrows indicate the lines for the position-velocity diagrams in Fig. 2.14.

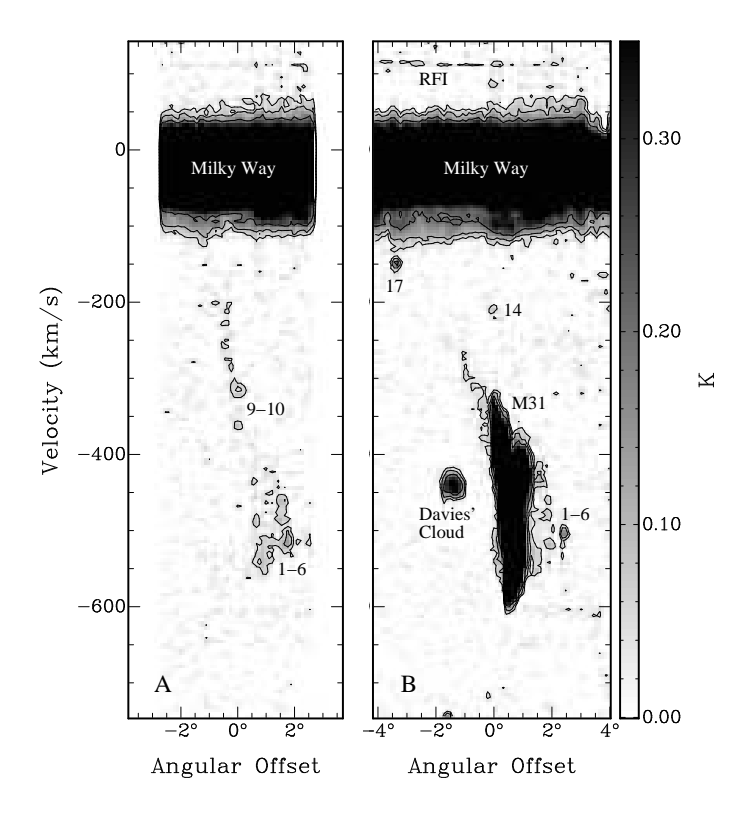
of the Milky Way. The strict upper limit we derived from the non-detection of an extended CHVC population around M 31 substantiates the concept of CHVCs being circumgalactic clouds in the vicinity of the Milky Way. Hence, their small angular diameters are not the result of large distances but of small physical sizes. As a consequence, the distinction between HVCs and CHVCs does not seem to be motivated by differences in the origin and nature of the clouds any more. Instead, the distinction between HVCs and CHVCs appears to be purely phenomenological without the implication of different formation scenarios.

2.4 The detected population of HVCs

2.4.1 General properties

With the follow-up observations of the CHVC candidates around M 31 the existence of some of the clouds closer to the disk of M 31 could indeed be confirmed. In total we could identify and verify 17 discrete HVCs in our Effelsberg survey. They were defined by being spatially or kinematically distinct from neighbouring H I clouds and disk emission from M 31. Each of the HVCs was later confirmed by follow-up observations with the Effelsberg telescope. An overview of all clouds and their observational parameters is given in Table 2.2 and Fig. 2.13. H I spectra for all clouds are shown in Fig. 2.16 and 2.17. Histograms of the projected distances, radial velocities, line widths, and H I column densities are presented in Fig. 2.15. All HVCs are located within a projected radius of about 50 kpc around M 31. Some of them are isolated in position and velocity, whereas others appear to be associated with the diffuse extra-planar gas near the edge of the H I disk of M 31. A few clouds, such

Fig. 2.14: The two panels show position-velocity diagrams along the lines indicated by the two dashed arrows in the column density map in the right panel of Fig. 2.13. In both cases several regions of extra-planar gas and HVCs around M31 can be seen. The contour levels are 50, 100, and 200 mK. Note that Davies' Cloud is completely isolated in phase space although in the column density map there appears to be a connection with the HI disk of M31.



as number 14 in our list, are seen in projection against the H I disk of M 31 and can only be discriminated by their different radial velocities. This situation is illustrated by the position-velocity diagrams in Fig. 2.14.

The radial velocities of the HVCs are in the range of $v_{\rm LSR} \approx -520\ldots -150~{\rm km\,s^{-1}}$. The distribution of radial velocities is not symmetric with respect to the systemic velocity of M 31 of $v_{\rm LSR} \approx -300~{\rm km\,s^{-1}}$. First of all, confusion with the H I emission of the Milky Way does not allow us to detect any HVCs at velocities above $-140~{\rm km\,s^{-1}}$, explaining the upper limit in the observed velocity range. Consequently, one or two more HVCs beyond this velocity limit could be missing in our sample due to confusion with Galactic emission. On the other hand, several of the detected clouds are arranged in a complex of HVCs near the south-eastern edge of the M 31 disk, resulting in very similar radial velocities in the range of about $-500\ldots -400~{\rm km\,s^{-1}}$.

The possibility of confusion with Galactic H I emission immediately raises the question whether HVCs near Galactic velocities might actually be associated with the Milky Way rather than M 31. Could it be that they are foreground objects of our own Galaxy instead? The detection of very compact and faint HVCs in the halo of the Milky Way (e.g., Brüns & Westmeier 2004; Hoffman et al. 2004; Richter et al. 2005) has shown that the criteria of small angular size and low H I column density are not sufficient to discriminate between HVCs near the Galaxy and M 31. Given the lack of distance information, it is in principle impossible to associate each individual cloud with M 31. The observational parameters of the detected HVCs, however, allow us to definitely associate the population as a whole with the Andromeda Galaxy. First of all, the clouds are clearly concentrated around M 31 with projected distances of less than about 50 kpc. If they were associated with the Milky Way we would expect them to be equally spread across the survey area. The probability to

Table 2.2: List of the 17 discrete HVCs around M 31 detected in our H I survey with the Effelsberg telescope. The columns denote the number of the cloud, its name according to other publications, right ascension, α , and declination, δ , the projected distance from the centre of M 31, $r_{\rm proj}$, of the column density maximum, the LSR radial velocity, $v_{\rm LSR}$, the FWHM of the spectral line, Δv , the peak H I column density, $N_{\rm H\,I}$, and the H I mass, $M_{\rm H\,I}$. Radial velocities are accurate within about $\pm 5~{\rm km\,s^{-1}}$, and the statistical uncertainties of line widths, column densities, and H I masses are of the order of 10%.

#	Name	α	δ	$r_{\rm proj}$	$v_{\rm LSR}$	Δv	$N_{ m HI}$	$M_{ m HI}$
		(J2000)	(J2000)	(kpc)	(km s)	$^{-1})$	$(10^{19} \text{ cm}^{-2})$	$(10^5~M_{\odot})$
1	HVC 1	$00^{\rm h}43^{\rm m}00^{\rm s}$	38°53′	32.5	-501	17	1.1	7.8
2	HVC 2	$00^{\rm h}41^{\rm m}06^{\rm s}$	$39^{\circ}16'$	27.6	-509	34	1.7	6.3
3	HVC 7	$00^{\rm h}41^{\rm m}06^{\rm s}$	$39^{\circ}28'$	24.9	-463	47	1.2	3.9
4	HVC 5	$00^{\rm h}43^{\rm m}00^{\rm s}$	$39^{\circ}31'$	23.9	-507	34	0.9	6.3
5	HVC 12	$00^{\rm h}43^{\rm m}17^{\rm s}$	$39^{\circ}35'$	23.0	-409	58	1.1	4.3
6	HVC 10	$00^{\rm h}41^{\rm m}05^{\rm s}$	$39^{\circ}41'$	22.0	-426	26	0.9	4.7
7	_	$00^{\rm h}33^{\rm m}18^{\rm s}$	$40^{\circ}32'$	26.2	-518	39	0.7	3.1
8	Davies' Cl.	$00^{\rm h}37^{\rm m}25^{\rm s}$	$42^{\circ}26'$	20.7	-442	21	3.9	130
9	_	$00^{\rm h}47^{\rm m}43^{\rm s}$	$40^{\circ}19'$	18.3	-324	71	1.6	5.9
10	_	$00^{\rm h}47^{\rm m}12^{\rm s}$	$40^{\circ}51'$	12.9	-282	67	1.4	5.0
11	_	$00^{\rm h}43^{\rm m}53^{\rm s}$	$42^{\circ}07'$	11.9	-266	16	0.4	1.2
12	_	$00^{\rm h}45^{\rm m}35^{\rm s}$	$42^{\circ}00'$	12.3	-223	13	0.3	1.0
13	HVC 15	$00^{\rm h}43^{\rm m}55^{\rm s}$	$44^{\circ}13'$	40.2	-266	30	0.9	3.5
14	HVC 13	$00^{\rm h}39^{\rm m}56^{\rm s}$	$41^{\circ}16'$	7.1	-207	14	0.5	6.4
15	_	$00^{\rm h}45^{\rm m}02^{\rm s}$	$42^{\circ}45'$	21.0	-206	21	0.5	1.7
16	_	$00^{\rm h}39^{\rm m}09^{\rm s}$	$45^{\circ}04'$	52.5	-165	17	0.6	2.2
_17	_	$00^{\rm h}32^{\rm m}42^{\rm s}$	44°20′	48.7	-149	11	0.9	8.2

have them distributed in a 50 kpc circle around M 31 by chance is of the order of only 10^{-6} in this case. Second, the observed radial velocities are nearly uniformly distributed around the systemic velocity of M 31 of $-300~{\rm km\,s^{-1}}$, though we are probably missing one or two HVCs with velocities above $-140~{\rm km\,s^{-1}}$. Furthermore, those HVCs with velocities of about $-500~{\rm km\,s^{-1}}$ would have significantly higher negative velocities than any previously known HVC around the Milky Way. Therefore, both the spatial and kinematic parameters of the detected HVCs strongly suggest that the population as a whole is associated with M 31, although we cannot make this statement for each individual HVC.

The observed line widths of the HVCs cover a very large range from about 10 to 70 km s⁻¹ FWHM. Line widths of less than 20 km s⁻¹ indicate the possible presence of a cold neutral gas component or a multi-phase cold/warm neutral medium which is probably unresolved by our 9' HPBW. A multi-phase medium is commonly found in Galactic HVCs and CHVCs (e.g., Cram & Giovanelli 1976; Brüns et al. 2000, 2001; Westmeier et al. 2005b). It can also be reproduced in hydrostatic simulations of HVCs (Sternberg et al. 2002) so that our evidence for the presence of a multi-phase medium in HVCs around M 31 is not surprising. Difficult to explain, however, is the detection of extremely broad lines in some of the clouds. In a few cases line widths as large as 60 or 70 km s⁻¹ FWHM are observed which can no longer be explained by thermal line broadening alone as the required temperatures would exceed 10⁵ K. The most likely explanation for large line

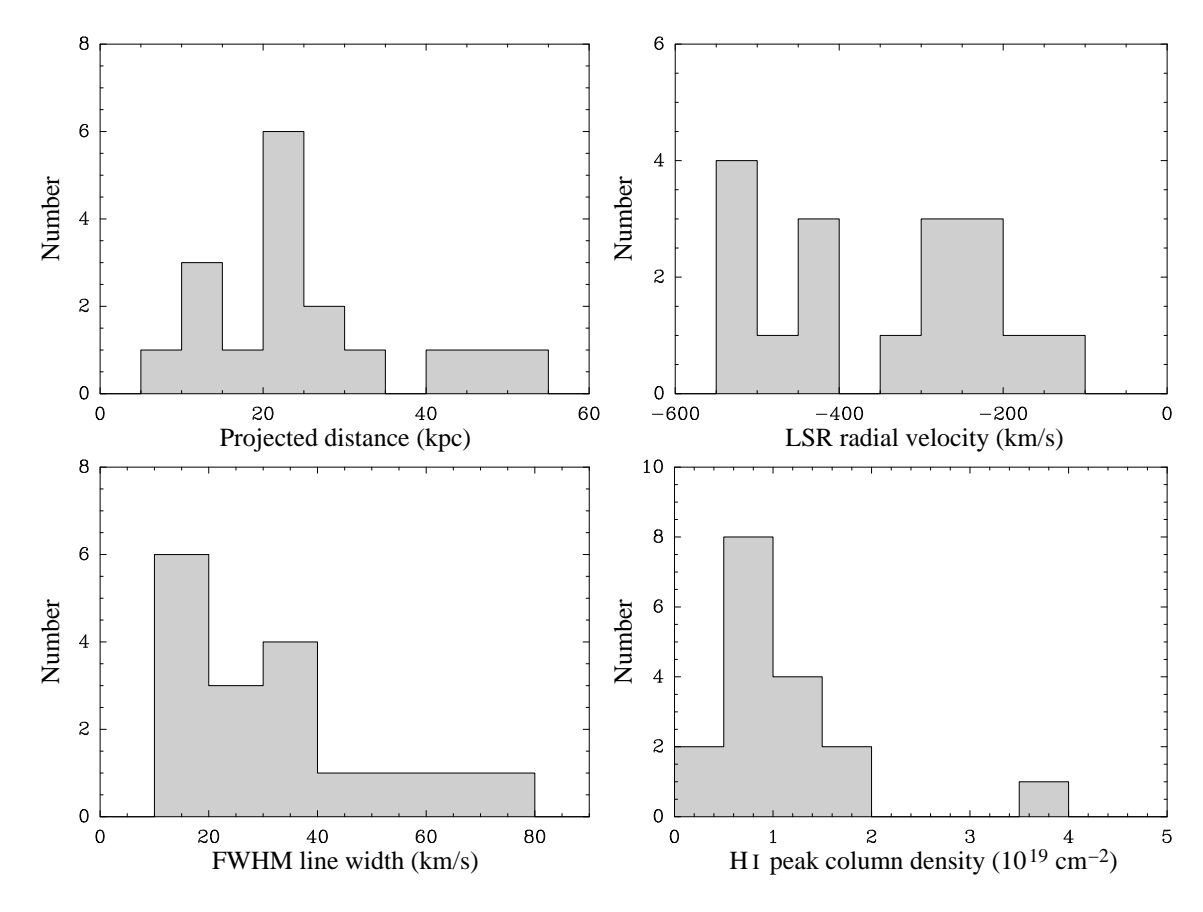


Fig. 2.15: Histograms of the projected distances, d_{proj} , the LSR radial velocities, v_{LSR} , the FWHM of the spectral lines, Δv , and the HI column densities, N_{HI} , of the 17 HVCs detected in our Effelsberg survey.

widths in excess of 30 or $40~\rm km\,s^{-1}$ FWHM is a high degree of internal kinematics within the area covered by the 9′ HPBW of the Effelsberg telescope (about 2 kpc in diameter at the distance of M 31). On the one hand, several clouds or clumps with slightly different radial velocities could be aligned along the line of sight. On the other hand, individual clouds could feature regular internal motions such as global rotation or gas flows.

The detected H I column densities are typically of the order of $10^{19}~\rm cm^{-2}$. This very low value indicates that most of the HVCs are probably not resolved by the Effelsberg telescope so that the column densities listed in Table 2.2 have to be considered mean values averaged over the 9′ HPBW of the telescope. In fact, our follow-up observations of some of the HVCs with the WSRT (see Chapter 3) revealed significantly higher peak column densities comparable to what is observed in the case of Galactic HVCs. The resulting H I masses of the HVCs—assuming a distance of 780 kpc (Stanek & Garnavich 1998)—are typically in the range of a few times $10^5~M_{\odot}$ with a mean value of $4.5\times10^5~M_{\odot}$. This excludes Davies' Cloud which has a significantly higher H I mass of $1.3\times10^7~M_{\odot}$. In fact, Davies' Cloud contributes about 65% of the total mass of all detected HVCs of $2\times10^7~M_{\odot}$. The total H I mass of all individual HVCs and regions of extra-planar gas around M 31 together is of the order of $5\times10^7~M_{\odot}$. The true value will be slightly higher as some of

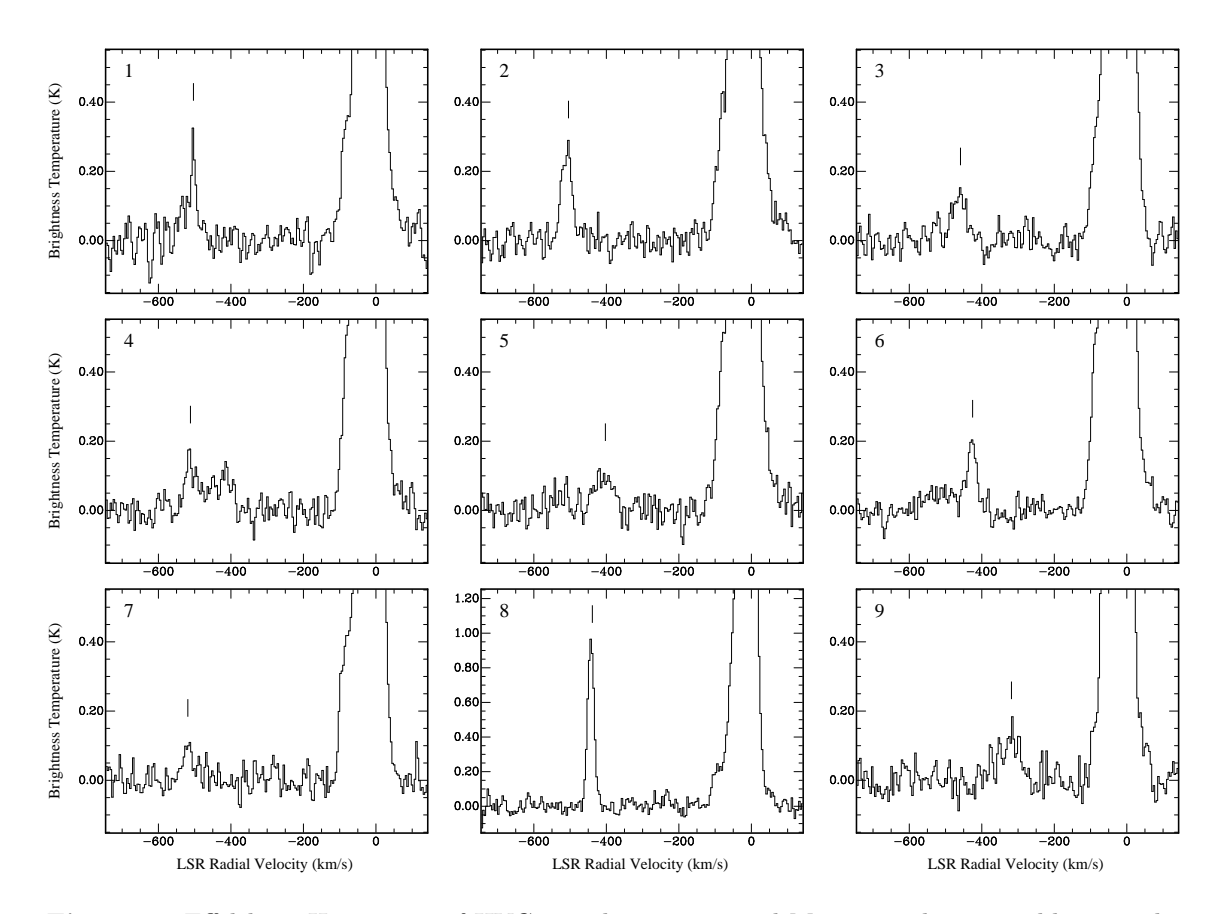


Fig. 2.16: Effelsberg HI spectra of HVCs number 1–9 around M 31 according to Table 2.2. The position of the spectral line belonging to the HVC is marked with a vertical line in each spectrum. The strong emission around $v_{\rm LSR}=0~{\rm km\,s^{-1}}$ is due to HI gas in the Galactic disk. Emission from the M 31 disk is not present in any of the spectra.

the gas may be missing due to blending with the HI emission of the Milky Way and of M 31 itself.

It is interesting at this point to compare the HI masses of the HVCs around M 31 with those of Galactic HVC complexes. For two complexes, A and WB, distance brackets have been published so far, implying HI mass ranges of $\log(M_{\rm H\,I}/M_\odot)=5.0\ldots6.3$ and $\log(M_{\rm H\,I}/M_\odot)=5.6\ldots5.7$, respectively. Both mass ranges are consistent with the HI masses observed for the HVCs around M 31, supporting our conclusion that they represent the analogues of the large HVC complexes seen around the Milky Way. Only the most extended HVC complexes have significantly larger masses. Unfortunately, only a lower distance limit for complex C of d>5 kpc (z>3.5 kpc) is available (van Woerden et al. 1999a), resulting in a lower limit for its HI mass of $1.2\times10^6~M_\odot$. The masses of the Magellanic Stream and the Leading Arm can be derived from numerical simulations in connection with HI observations. Connors et al. (2006) derived HI masses of $2.4\times10^8~M_\odot$ and $7.3\times10^7~M_\odot$, respectively, which are by orders of magnitude higher than those of the HVCs around M 31, including Davies' Cloud. The Magellanic Clouds, however, are a special case with no equivalent in the M 31 system.

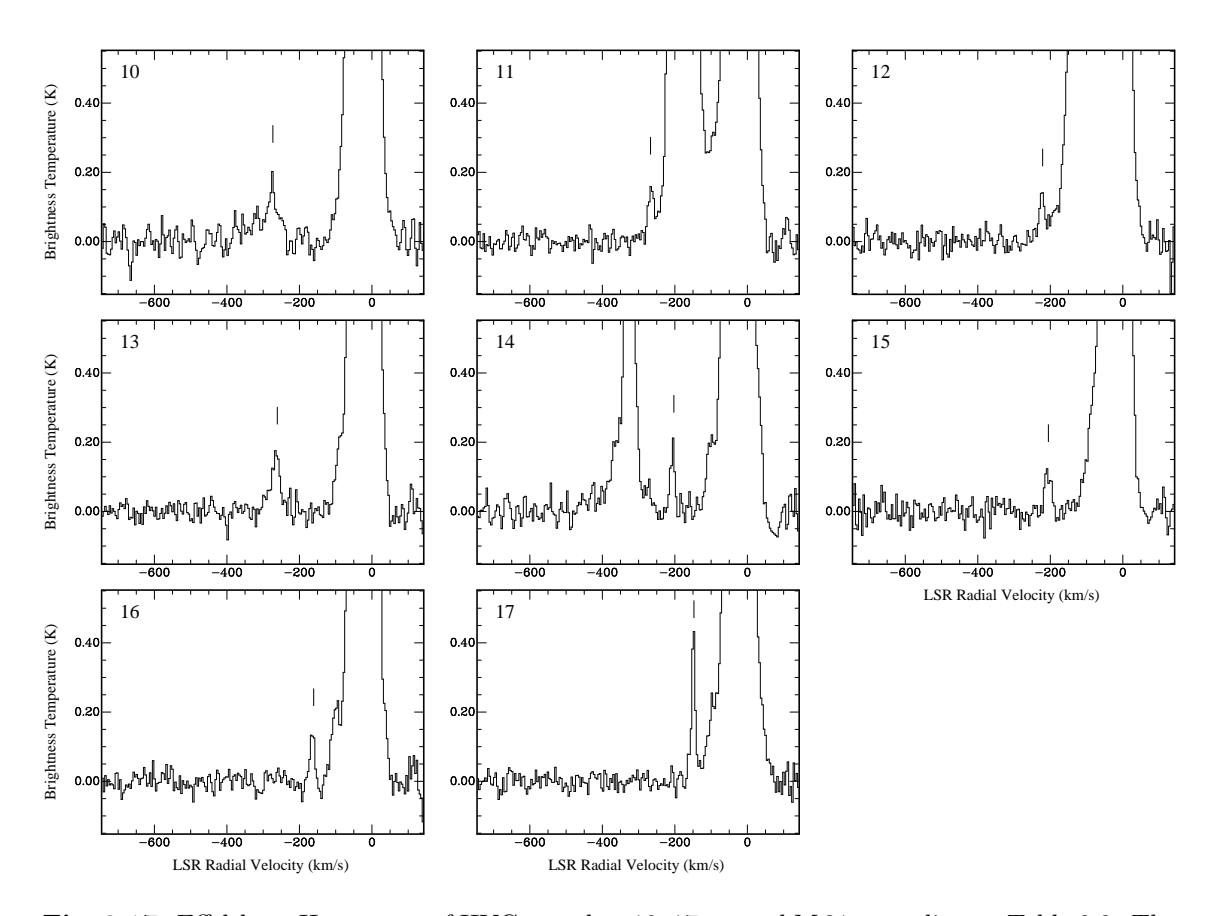


Fig. 2.17: Effelsberg HI spectra of HVCs number 10–17 around M 31 according to Table 2.2. The position of the spectral line belonging to the HVC is marked with a vertical line in each spectrum. The strong emission around $v_{\rm LSR} = 0~{\rm km\,s^{-1}}$ is usually due to HI gas in the Galactic disk. In a few spectra, however, emission from the M 31 disk is also present at different velocities.

To get an impression of the mass fraction of neutral hydrogen in the M 31 HVCs we can compare the observed H I masses of the HVCs with the FWHM of the spectral lines which, in the ideal case, should provide an estimate of the dynamical masses of the clouds. In Fig. 2.18 we have plotted the H I mass, $M_{\rm H\,I}$, versus the FWHM, Δv , for all HVCs detected in our sample. The error in line width is assumed to be 10%, whereas the error bars for the mass indicate our $3\,\sigma$ detection limit of $8\times10^4~M_{\odot}$. If the H I mass were proportional to the virial mass, all clouds should be scattered around a straight line running from the lower left to the upper right of the diagram. In its most simple form the virial equation reads

$$\Delta v^2 = \frac{8 \ln 2}{5} \frac{GM_{\text{vir}}}{R_{\text{vir}}} \approx \frac{GM_{\text{vir}}}{R_{\text{vir}}}, \qquad (2.6)$$

assuming an isothermal sphere with constant mass density and the same mass for all particles forming the cloud. We can now replace the virial mass, $M_{\rm vir}$, in Eq. 2.6 by the H I mass by introducing a factor $\alpha \equiv M_{\rm vir}/M_{\rm H\,I}$ such that

$$\Delta v^2 = \alpha \frac{GM_{\rm H\,I}}{R_{\rm wir}} \,. \tag{2.7}$$

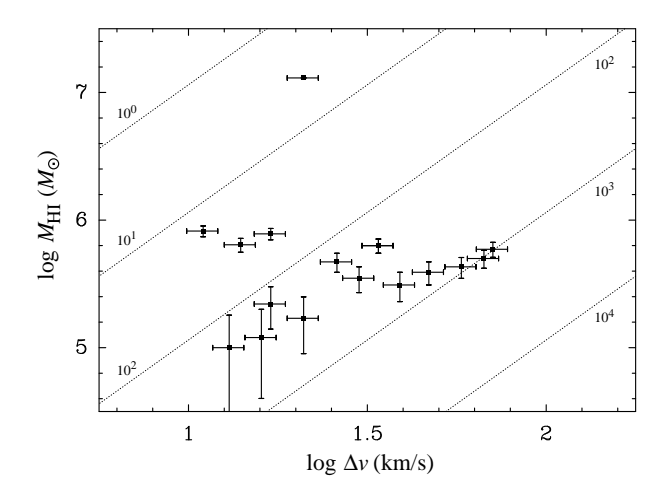


Fig. 2.18: HI mass, $M_{\rm H\,I}$, plotted against the FWHM of the spectral line, Δv , for all HVCs detected in our Effelsberg survey. The dotted lines indicate different values of $\alpha \equiv M_{\rm vir}/M_{\rm H\,I}$ under the assumption of a constant virial radius of $R_{\rm vir}=0.5$ kpc (see Eq. 2.7). Hence, clouds with a small $M_{\rm vir}/M_{\rm H\,I}$ ratio are located in the upper left region of the diagram, whereas clouds with a large $M_{\rm vir}/M_{\rm H\,I}$ ratio can be found at the lower right.

Lines of constant virial-to-H I mass ratio α according to Eq. 2.7 are also plotted in Fig. 2.18, assuming a constant virial radius of $R_{\rm vir}=0.5$ kpc for each cloud. This value for $R_{\rm vir}$ is suggested by our follow-up observations of several of the HVCs with the WSRT (see Chapter 3). Obviously, most of the HVCs are spread around $\alpha\approx 100$, suggesting that most of the HVCs around M 31 could be gravitationally dominated by other mass components such as ionised gas or dark matter. However, a few clouds show very high mass ratios of $\alpha\approx 1000$. In most of these cases we observe exceptionally broad H I lines with line widths exceeding 40 km s⁻¹ FWHM, suggesting that the clouds cannot be considered entities in dynamical equilibrium so that the observed line widths probably do not provide any meaningful estimate of the associated total mass. On the other hand, Davies' Cloud lies slightly off the other data points, resulting from its fairly narrow spectral lines combined with a very high H I mass. Nonetheless, its true mass ratio is $\alpha\approx 26$ due to its significantly larger angular size of about 30' FWHM, corresponding to a physical diameter of about 7 kpc.

Another possibility to stabilise the clouds in addition to their HI mass is through the pressure of an ambient medium. Assuming an isothermal sphere, the virial equation for a cloud with external pressure reads

$$4\pi R_{\rm vir}^3 P = \frac{3kTM_{\rm vir}}{\mu} - \frac{3GM_{\rm vir}^2}{5R_{\rm vir}},$$
(2.8)

where P is the external pressure, T is the gas temperature, and μ denotes the mean mass per particle (Spitzer 1978). Let us assume the virial mass to be equal to the HI mass and of the order of $M_{\rm vir}=10^5~M_{\odot}$. Then we can use Eq. 2.8 to determine the external pressure required to stabilise the cloud without any additional mass component. Assuming a virial radius of $R_{\rm vir}=0.5~{\rm kpc}$, a temperature of the warm neutral medium of $T=10^4~{\rm K}$, and a mean mass equal to the mass of a hydrogen atom of $\mu=1.674\times10^{-27}~{\rm kg}$, we obtain an external pressure of

$$P/k = 84 \text{ K cm}^{-3}$$
. (2.9)

Therefore, an external pressure of the order of $100~\rm K~cm^{-3}$ is sufficient to stabilise a typical HVC around M 31 in addition to its own gravitational potential. In this case no additional mass components, such as molecular gas or dark matter, would be necessary. The required

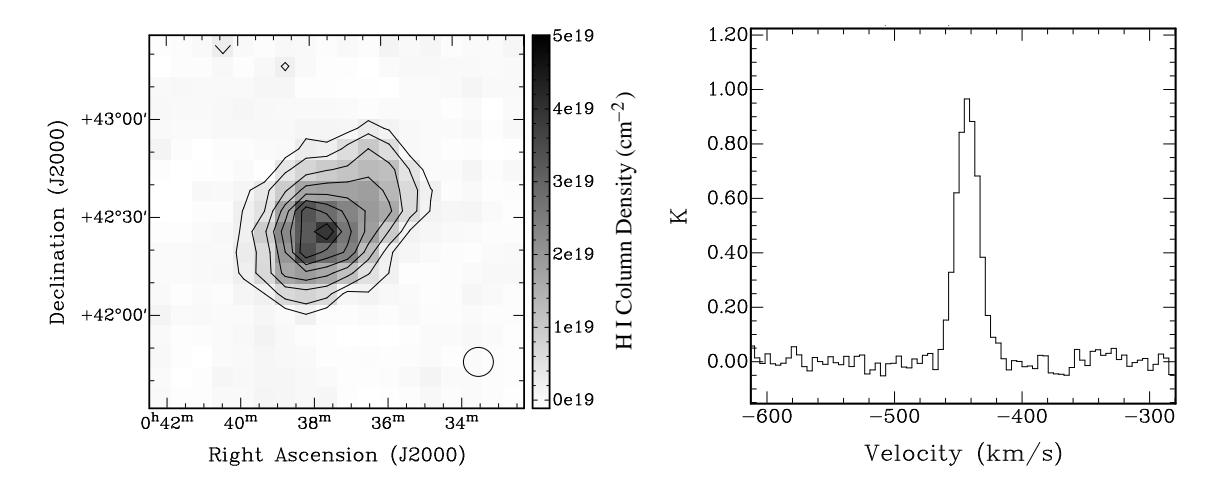


Fig. 2.19: HI column density map of Davies' Cloud. The outermost contour corresponds to 2×10^{18} cm⁻², and the remaining contour lines are drawn in steps of 5×10^{18} cm⁻², starting at 5×10^{18} cm⁻². On the right hand side the HI spectrum at the position of the column density maximum is shown. With an HI mass of about 1.3×10^7 M_{\odot} Davies' Cloud would be the by far most massive HVC around M 31.

pressure is of the order of what is expected for the ionised coronal gas around massive spiral galaxies with a temperature of about 10^6 K and a typical density of 10^{-4} cm⁻³ (e.g., Baldwin 1954; Sembach et al. 2003; Rasmussen et al. 2003). This result demonstrates that the HVCs observed around M 31 can be in pressure equilibrium with the circumgalactic hot corona without the need for any additional dark-matter component for stabilisation.

2.4.2 Discussion of individual objects

Davies' Cloud

As mentioned before, Davies' Cloud is the most massive individual HVC around M 31. Discovered by Davies (1975), it was studied in detail with the WSRT by de Heij et al. (2002c). It is located only about 1°5 north-west of M 31, corresponding to a projected distance of only about 20 kpc. With an angular diameter of about 30′ FWHM, corresponding to a physical size of roughly 7 kpc, Davies' Cloud is also the most extended HVC around M 31. Its appearance is not perfectly symmetric, but the column density maximum is slightly shifted in the direction of M 31 (see Fig. 2.19 for a column density map and an example spectrum). The resulting head-tail morphology can be considered as an indication for a distortion of Davies' Cloud by the ram pressure of its ambient medium. In the column density map in Fig. 2.13 Davies' Cloud appears to be connected with the disk emission of M 31. However, there is no such connection in phase space because the gas in the putative "bridge" has completely different radial velocities and does not provide any connection between Davies' Cloud and M 31. This isolation of Davies' Cloud in phase space becomes immediately obvious when looking at the position-velocity diagram in the right panel of Fig. 2.14.

The question whether Davies' Cloud is indeed associated with M 31 or whether it is a foreground object in the vicinity of the Milky Way is discussed in some detail by de Heij et al. (2002c). In their high-resolution synthesis observations with the WSRT they

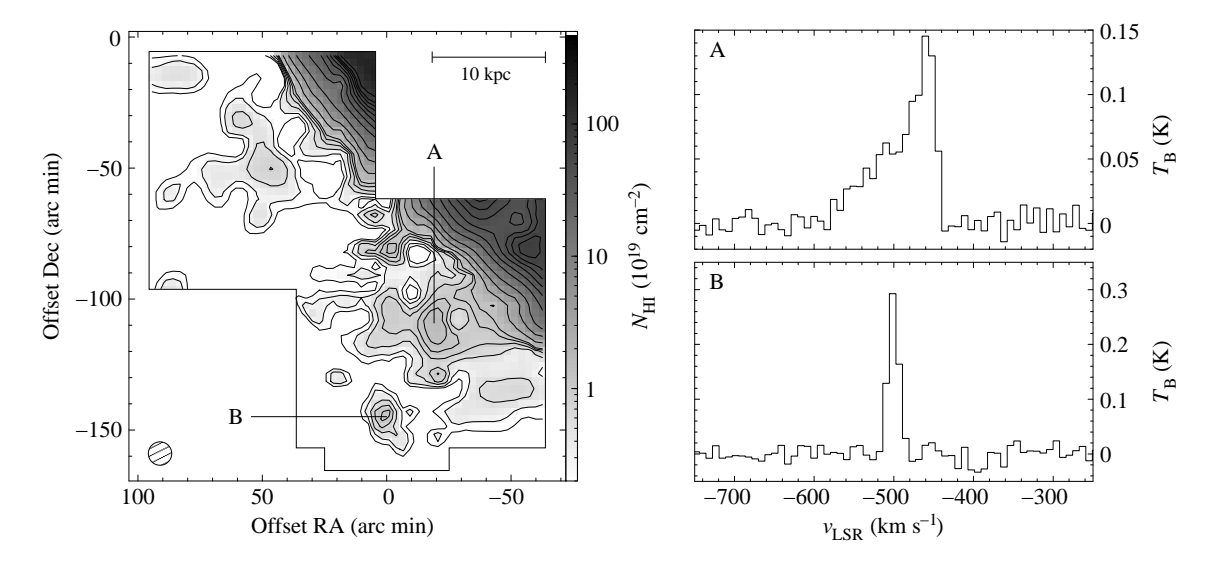


Fig. 2.20: HI column density map of the extra-planar gas found near the eastern and south-eastern edge of the disk of M 31. The centre of M 31 is located at offset (0,0). Contours are drawn at 0.1, 0.25, 0.5, 0.75, 1, 1.25, 2.5, 5, 10, 20, 30, 40, 50, 60, 70, 80, and 100×10^{19} cm⁻². Two example spectra at the positions labelled with A and B are shown on the right. The complex line profile at position A indicates the presence of compact substructures unresolved with the 9' HPBW of the Effelsberg telescope. The cloud at position B shows the highest intensities and quite narrow lines of only about 15 km s⁻¹ FWHM.

resolve the cold gas component of Davies' Cloud into an extended arc of compact clumps extending mainly along the eastern edge of the cloud. This configuration, in connection with the asymmetry of the diffuse neutral gas component, suggests that Davies' Cloud is interacting with an ambient low-density medium, presumably with the gaseous halo or corona of M 31. Another possibility, originally discussed by Davies (1975), is an association of Davies' Cloud with the Magellanic Stream. Braun & Thilker (2004) recently detected a faint northern extension of the Magellanic Stream in their WSRT total-power survey of a large area in the region around M 31 and M 33. In fact, Davies' Cloud lies within only about 5° of parts of the stream. However, the typical column densities of the stream in this region are much lower than that of Davies' Cloud. Moreover, the radial velocity of Davies' Cloud ($v_{\rm LSR} = -442~{\rm km\,s^{-1}}$) deviates significantly from the velocities of the gas associated with the Magellanic Stream ($v_{\rm LSR} \simeq -200~{\rm km\,s^{-1}}$). Therefore, a connection of Davies' Cloud with the Magellanic Stream is very unlikely. Instead, Davies' Cloud may indeed be associated with M 31.

Consequently, Davies' Cloud is probably a very massive object. Its H I mass of $1.3 \times 10^7 \ M_{\odot}$ is by about one or two orders of magnitude higher than the mass of complex A (see Section 2.4.1). Even the lower mass limit derived for the large HVC complex C is still an order of magnitude below the expected mass of Davies' Cloud. Only the Magellanic Stream and the Leading Arm are significantly more massive with H I masses of $2.4 \times 10^8 \ M_{\odot}$ and $7.3 \times 10^7 \ M_{\odot}$, respectively (Connors et al. 2006). While all the above-mentioned HVC complexes have a very elongated, filamentary structure, Davies' Cloud appears more or less spherical. This morphological difference is surprising. The filamentary structure of the HVC complexes hints at a tidal origin of the gas. The Magellanic Stream and the

Leading Arm are believed to be tidal streams in connection with the Magellanic Clouds, whereas potential progenitors of complexes A and C have not yet been identified, and additional hypotheses for their origin have been proposed (Wakker & van Woerden 1997). The spherical appearance of Davies' Cloud, however, is not reminiscent of a tidal structure at all. It is very unlikely that the cloud is significantly elongated along the line of sight as in this case we would expect to see very complex and broad spectral line profiles caused by a complex spatial and kinematic structure along the filament. Instead, the observed HI lines are rather narrow with $\Delta v \approx 20 \ \mathrm{km \, s^{-1}}$ (FWHM) and of Gaussian shape (Fig. 2.19), confirming our impression of an overall spherical morphology of Davies' Cloud.

Extra-planar gas south-east of M31

One of the most outstanding features detected in our survey is the region of extra-planar gas near the south-eastern edge of the H I disk of M 31. To study this area with better sensitivity we re-observed it with a longer integration time of 5 minutes per position in inband frequency-switching mode with the Effelsberg telescope, using the new autocorrelator AK90. The parameters are otherwise similar to those specified in Table 2.1. The resulting H I column density map of the entire region is shown in the left panel of Fig. 2.20. The total H I mass of the extra-planar gas in this area is about $2 \times 10^7 \ M_{\odot}$, thus even exceeding the H I mass of Davies' Cloud.

From the map it is obvious that the extra-planar gas is not totally diffuse but instead forming more or less extended concentrations and clumps. The clumpy structure is spatially not well resolved by our 9' HPBW. However, the individual clumps are characterised by different radial velocities which are kinematically well resolved by our spectral resolution. Two example spectra are presented in the right panel of Fig. 2.20. In many cases the spectral profiles are rather complex and can vary significantly between two neighbouring pointings of the map, indicating the presence of several individual clouds or clumps with angular sizes of a few arc minutes which are hardly resolved by the telescope beam. We could later confirm this clumpy structure in our follow-up synthesis observations of the area with the WSRT (see Section 3.3.2). Those clouds which could be spatially and kinematically separated in our Effelsberg survey were included in the list of individual M 31 HVCs in Table 2.2. The properties of the extra-planar gas and its possible origin are discussed in detail in connection with the WSRT follow-up observations in Chapter 3.

2.5 Comparison with models and theoretical predictions

One of the most fundamental questions arising from our observations is how the detected HVC population around M 31 relates to different models derived from other observations or theoretical considerations. To investigate this question we will compare the observational parameters of the HVCs in a statistical approach with different models and theoretical predictions.

2.5.1 The Local Group population model of de Heij et al. (2002a)

Based on the LDS and HIPASS, de Heij et al. (2002a) compiled an all-sky catalogue of CHVCs around the Milky Way. To investigate the distribution and origin of the CHVC

population, they constructed several Local Group population models with different parameters and compared the results with the observed parameters of CHVCs. The free parameters of their models include the Gaussian dispersion, σ , of the spatial distribution of CHVCs around their host galaxy in the range of $\sigma = 100 \text{ kpc} \dots 2 \text{ Mpc}$, the slope, β , of the HI mass spectrum in the range of $\beta = -2.0 \dots -1.0$, and the highest allowed HI mass, M_{max} , of the clouds in the range of $\log(M_{\text{max}}/M_{\odot}) = 6.0 \dots 9.0$. Using the χ^2 test and the Kolmogorov-Smirnov test, de Heij et al. (2002a) determined the parameter space providing the best representation of the observational parameters of CHVCs. One of the best-fitting models is their model #9 with $\sigma = 200 \text{ kpc}$, $\beta = -1.7$, and $M_{\text{max}} = 10^7 M_{\odot}$. Of the 6281 CHVCs originally present in their model, 4759 got disrupted by either ram pressure or tidal forces during their evolution, leaving about 1500 CHVCs around the Milky Way and M 31 left with a total HI mass of about $1.2 \times 10^9 M_{\odot}$.

According to model #9 of de Heij et al. (2002a), CHVCs would be spread all over the Local Group with clear concentrations around both the Milky Way and M 31. The question is whether this Local Group scenario is in agreement with the HVC population seen in our Effelsberg survey of M 31. To test this hypothesis, let us first reconstruct a similar model population which in addition accounts for the observational restrictions of our survey. The major restrictions resulting in incomplete coverage of the CHVC population of M 31, such as the limited spatial coverage of the map or the flux detection limit, were summarised and discussed earlier in Section 2.2.3. As most of these effects act in an asymmetric and non-linear manner, it is impossible to obtain simple analytic expressions for the statistical parameters of the modified model population. Thus, the most straightforward way of getting adequate models is to use numerical methods.

Construction of a similar model population

To construct a model similar to model #9 of de Heij et al. (2002a) we can randomly place particles around M 31 with the required distribution of parameters. The total number of HVCs around M 31 will be N=750, assuming an equipartition of the entire expected population between M 31 and the Milky Way. The positions of the clouds should be spherically-symmetric with a Gaussian radial distribution. As common random number generators only provide uniform random deviates, usually in the range of 0...1, we first have to find a way to obtain Gaussian deviates from uniform random numbers. The easiest and fastest way is to use the method introduced by Box & Muller (1958). Let x_1 and x_2 be two independent uniform random deviates in the range of $0 \le x_i \le 1$. Then

$$g_1 = \sqrt{-2 \ln x_1} \cos(2\pi x_2)$$
 and $g_2 = \sqrt{-2 \ln x_1} \sin(2\pi x_2)$ (2.10)

are two normal random deviates in the range of $-\infty < g_i < \infty$ with a dispersion of $\sigma = 1$. Using Eq. 2.10, we can assign each cloud in our model a radial distance from M 31 of

$$r = \left| \sqrt{-2\,\sigma^2 \ln x_1} \,\cos(2\pi x_2) \right| \tag{2.11}$$

with σ being the radial dispersion of the spatial distribution of our CHVC population.⁴ The remaining two spatial coordinates, the angles φ and ϑ , can be obtained by calculating uniformly distributed random points $\vec{p} = (x, y, z)$ within a sphere of radius unity in

⁴ As we need only one normal deviate we can use g_1 and omit the calculation of g_2 . Nonetheless, we have to provide two independent uniform deviates as input for g_1 .

Cartesian coordinates. The directions of these points, as seen from the point of origin of the coordinate system, are also uniformly distributed and can be used to calculate φ , uniformly distributed in the range of $0 \le \varphi < 2\pi$, and ϑ , following a sine-shaped distribution in the range of $0 \le \vartheta \le \pi$.

The next step is to assign each of the model clouds a radial velocity $v_{\rm rad}$. Again, we can make use of Eq. 2.10 to determine radial velocities with a Gaussian distribution around the systemic velocity of M 31 of $v_{\rm M\,31} \approx -300~{\rm km\,s^{-1}}$. The corresponding equation is

$$v_{\rm rad} = \sqrt{-2\,\sigma_v^2 \ln x_1} \,\cos(2\pi x_2) + v_{\rm M\,31} \,.$$
 (2.12)

Here, σ_v denotes the line-of-sight velocity dispersion of the entire population of CHVCs which is expected to be governed by the details of the mass model assumed for M 31. For the sake of simplicity we can take the same value for the velocity dispersion as observed for the population of globular clusters around M 31, i.e. $\sigma_v \approx 150 \text{ km s}^{-1}$ (Perrett et al. 2002).

The final step is to assign each cloud an HI mass $M_{\rm HI}$ such that the postulated HI mass spectrum is preserved. In the model of de Heij et al. (2002a) the authors assume a power-law mass spectrum with slope β and a maximum HI mass $M_{\rm max}$, thus

$$N(M_{\rm H\,I}) \sim M_{\rm H\,I}^{\beta}, \quad M_{\rm H\,I} \le M_{\rm max}.$$
 (2.13)

For their best-fitting model, de Heij et al. (2002a) find a slope of $\beta = -1.7$. To implement the above mass spectrum into the model, we have to find a function which converts a uniform deviate into a power spectrum. In our case, the corresponding function is rather simple and reads

$$M_{\rm H\,I} = M_{\rm min} \, x^{1/(\beta+1)} \tag{2.14}$$

with $M_{\rm H\,I} \leq M_{\rm max}$ and $\beta = -1.7$. Again, x is a uniform random deviate in the range of $0 \leq x \leq 1$. The HI masses, $M_{\rm H\,I}$, derived from Eq. 2.14 follow the power law defined in Eq. 2.13 with an additional factor $M_{\rm min}$ required to define the lower mass limit.

Consideration of the survey limitations

With these ingredients we are able to construct a model population of CHVCs around the Andromeda Galaxy similar to model #9 of de Heij et al. (2002a). To compare this model with our observations, we first have to account for the different observational limitations of our survey as discussed in Section 2.2.3. The most obvious limitation is the survey area for which we can account by simply removing all clouds from the model which, when projected onto the sky, are located outside the survey region. Next, we have to remove all clouds which suffer from blending with HI emission of the Galactic disk, namely all clouds with radial velocities $v_{\rm rad} > -140~{\rm km\,s}^{-1}$.

Slightly more complicated is the correct treatment of the flux detection limit of our survey. To assess whether a cloud of a certain mass can be detected with our survey we have to find a conversion between the HI mass and the observed flux of CHVCs. At distance d, the total observed flux F of an unresolved cloud of HI mass $M_{\rm HI}$ is given by

$$\frac{F}{\text{mJy km s}^{-1}} = 4.24 \times 10^3 \frac{M_{\text{H I}}}{M_{\odot}} \left(\frac{d}{\text{kpc}}\right)^{-2}$$
 (2.15)

according to Schneider (1997). The Effelsberg spectra, however, are given in terms of brightness temperature. Flux density, S, and brightness temperature, $T_{\rm B}$, can be converted via

$$T_{\rm B} = \frac{\lambda^2 S}{2 \,\mathrm{k} \,\Omega} \tag{2.16}$$

with k being the Boltzmann constant and Ω the solid angle of the telescope beam. For a constant wavelength of $\lambda = 21.1$ cm and a circular telescope beam of HPBW Θ , Eq. 2.16 can be simplified to

$$\frac{T_{\rm B}}{\rm K} = 606 \frac{S}{\rm mJy\,beam^{-1}} \left(\frac{\Theta}{\rm arcsec}\right)^{-2}.$$
 (2.17)

Assuming the source being unresolved, we can combine Eq. 2.15 and 2.17 to obtain a relation between the HI column density and the HI mass of a cloud, namely

$$\frac{N_{\rm H\,I}}{\rm cm^{-2}} = 4.68 \times 10^{24} \, \frac{M_{\rm H\,I}}{M_{\odot}} \left(\frac{\Theta}{\rm arcsec} \, \frac{d}{\rm kpc}\right)^{-2} \tag{2.18}$$

where we also made use of the conversion between the integrated brightness temperature, $\int T_{\rm B} dv$, and the HI column density, $N_{\rm HI}$, of a cloud under the fundamental assumption that the gas is optically thin. Assuming a Gaussian line profile with dispersion σ , we can easily determine the column density sensitivity of our survey from the brightness temperature sensitivity via

$$N_{\rm H\,I} = c_1 T_{\rm B} \int_{-\infty}^{\infty} \exp\left(-\frac{[v - v_0]^2}{2\,\sigma^2}\right) dv = c_1 \sqrt{\frac{-\pi}{4\ln 0.5}} \, T_{\rm B} \Delta v \approx c_1 T_{\rm B} \Delta v$$
 (2.19)

where $T_{\rm B}$ denotes the peak brightness temperature and v_0 the radial velocity of the spectral line. $\Delta v \approx 2.355\,\sigma$ is the FWHM of the spectral line. If $N_{\rm H\,I}$ is given in cm⁻² and $T_{\rm B}\Delta v$ in K km s⁻¹, the corresponding conversion factor is $c_1 = 1.823 \times 10^{18}$, again assuming optically thin gas.

Following the results of Westmeier et al. (2005b), the characteristic line width of Galactic CHVCs is in the range of about $20\dots25~{\rm km~s^{-1}}$ (FWHM) which is typical for the warm neutral gas with temperatures of the order of $10^4~{\rm K}$. Thus, a velocity resolution of about $20~{\rm km~s^{-1}}$ should match the expected line widths of potential M 31 CHVCs in our Effelsberg survey. The resulting RMS would be $\sigma\approx16~{\rm mK}$ with a corresponding brightness temperature sensitivity of $T_{\rm B}\geq3~\sigma\approx49~{\rm mK}$. With $\Delta v=25~{\rm km~s^{-1}}$ (FWHM) we obtain a column density detection limit for CHVCs according to Eq. 2.19 of $N_{\rm H\,I}\gtrsim2.2\times10^{18}~{\rm cm^{-2}}$. Inserting this column density limit into Eq. 2.18 yields a fundamental H I mass detection limit of our survey of

$$M_{\rm H\,I} \gtrsim 8 \times 10^4 \ M_{\odot} \,. \tag{2.20}$$

In the northern part of our survey the sensitivity is slightly improved due to the inband frequency-switching mode. The corresponding 3σ column density sensitivity there is $N_{\rm H\,I}\gtrsim 1.3\times 10^{18}~{\rm cm}^{-2}$, resulting in an H I mass detection limit of $M_{\rm H\,I}\gtrsim 5.5\times 10^4~M_{\odot}$.

As we have seen in Section 2.2.4, the detection rate of clouds at the $3.5\,\sigma$ level is about 50%. Below $2\,\sigma$, the detection rate drops to zero, whereas above $5\,\sigma$ we are virtually

complete (see Fig. 2.9). Thus, it is reasonable to construct a soft cut-off level with a linear increase in detection probability $P(T_{\rm B})$ such that

$$P(T_{\rm B}) = \begin{cases} 0 & \text{for } T_{\rm B} < 2\,\sigma \\ \frac{T_{\rm B}}{3\sigma} - \frac{2}{3} & \text{for } 2\,\sigma \le T_{\rm B} \le 5\,\sigma \\ 1 & \text{for } T_{\rm B} > 5\,\sigma \end{cases}$$
(2.21)

By converting the values for $T_{\rm B}$ into the corresponding H I masses (using Eq. 2.18 and 2.19) we are able to exclude clouds from the model with a certain probability expressed by Eq. 2.21 to account for the detection limit of our Effelsberg data.

Statistical methods

There are two common ways of comparing the CHVC model of M 31 with the data from our Effelsberg survey: the χ^2 test and the Kolmogorov-Smirnov test (KS test). A helpful discussion of both hypothesis tests can be found in Wall & Jenkins (2003).

The χ^2 test is probably one of the most frequently used statistical tests in astronomical research. It is normally used to compare data with different models for which analytic expressions are at hand. In our case, however, we have to compare two data sets, namely the output of the numerical model and the observational data from our survey. Hence, we would have to apply the non-parametric χ^2 two-sample test (Press et al. 1992; Wall & Jenkins 2003). A general disadvantage of the χ^2 test is that the data need to be binned. According to Wall & Jenkins (2003), at least 80% of all bins should contain more than five counts for the χ^2 test to produce meaningful results. This particular restriction does not allow us to perform the test on small data sets such as our Effelsberg survey with only 17 detected HVCs.

An alternative approach is the Kolmogorov-Smirnov test, again in its two-sample form (Press et al. 1992; Wall & Jenkins 2003). The KS test has two advantages over the χ^2 test. First, the data need not be binned, but each individual measurement is treated separately. This is very useful as, in contrast to the χ^2 test, there are no restrictions resulting from binning of the data. Second, the KS test is particularly powerful for small data samples and probably the only applicable hypothesis test for very small samples of only a few individual measurements where the χ^2 test would fail. Thus, the KS test is the most appropriate test in our case.

Comparison between model and data

To minimise statistical errors, we calculated the mean results of 1000 model HVC populations with parameters as specified above. The models were calculated consecutively with a computer programme written in the C programming language (Kernighan & Ritchie 1978). Each model originally contained 750 HVCs of which on average 595 were excluded from the model population by one of the incompleteness issues of our Effelsberg survey, leaving about 155 expected HVC detections left within our survey region. This number immediately illustrates that model #9 of de Heij et al. (2002a) overestimates the expected number of HVCs detected in our survey by about a factor 10. The resulting distribution of HVCs as a function of projected distance, $d_{\rm proj}$, from the centre of M 31 is plotted in the left diagram of Fig. 2.21. The dotted curve represents the original model containing

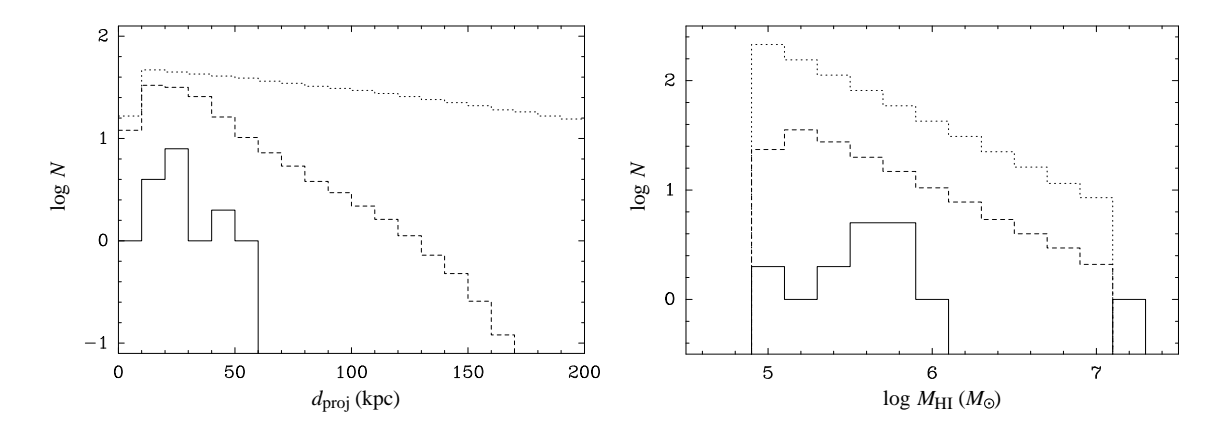


Fig. 2.21: Projected radial distribution (left) and H I mass spectrum (right) of HVCs around M 31 according to our Effelsberg observations (solid line) and our model (dotted/dashed lines) based on model #9 of de Heij et al. (2002a). In both diagrams the dotted line corresponds to the original model, whereas the dashed line represents the remaining model population after correcting for the different incompleteness issues of our survey.

750 HVCs. The dashed curve shows the final distribution after accounting for the incompleteness effects. The distribution drops abruptly beyond $d_{\rm proj}\approx 150$ kpc as a result of the limited survey region. The observed radial distribution is plotted for comparison as a solid line. It is obvious that both the total number and the radial distribution of the observed HVCs around M31 deviate significantly from the model. The observed HVCs are much closer to M31 than expected from the model, whereas no HVCs are observed at larger projected distances where the model still predicts several detections. To quantify these differences in radial distribution we carried out the KS test on the normalised cumulative radial distribution of the modelled and observed HVCs as plotted in the left panel of Fig. 2.22. The resulting KS statistic for the two distributions is D=0.32, hence rejecting the hypothesis that both samples are drawn from the same radial distribution on the 95% confidence level.

The deviations are similar when considering the HI mass spectrum. The modelled mass spectrum is shown in the right panel of Fig. 2.21. Again, the dotted curve is the original mass spectrum, whereas the dashed curve has been corrected for observational constraints. The modelled distribution mainly follows the power law defined by de Heij et al. (2002a). In contrast, the observed HI mass spectrum (solid line) does not appear to follow a power law at all. Instead, it peaks at $M_{\rm HI} \approx 5 \times 10^5 \ M_{\odot}$, indicating a lack of low-mass clouds compared to the model. On the other hand, Davies' Cloud is isolated at the high-mass end of the spectrum. To compare the observed and modelled mass spectra we again used the KS test on the normalised cumulative mass distributions as plotted in the right panel of Fig. 2.22. The resulting KS statistic is again D=0.32, therefore rejecting the hypothesis that both mass spectra are drawn from the same distribution on the 95% confidence level.

Obviously, the model proposed by de Heij et al. (2002a) does not provide a good and accurate description of our data. The model was motivated phenomenologically based on the population of CHVCs observed all over the sky. However, both the total number and

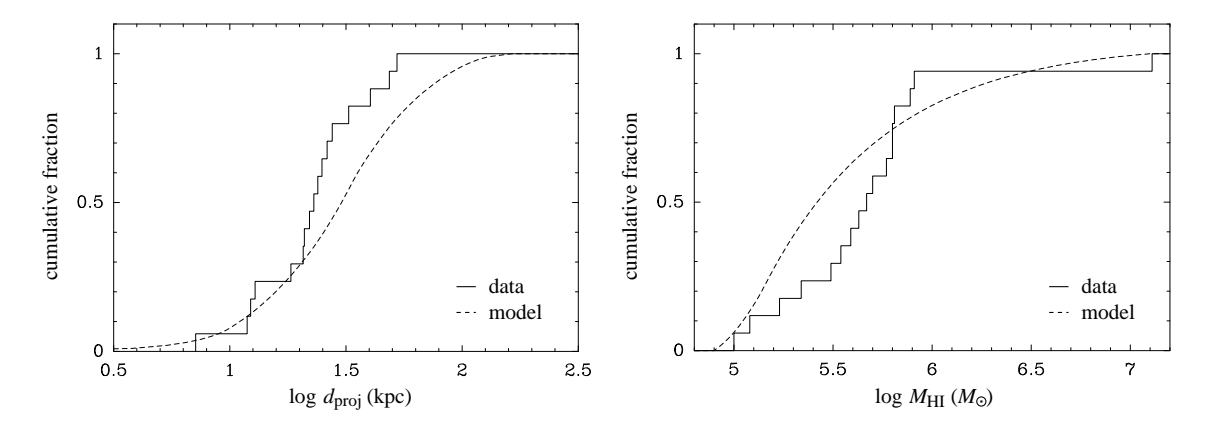


Fig. 2.22: Normalised cumulative distribution of HVCs as a function of projected distance, d_{proj} , from the centre of M 31 (left) and H I mass, $M_{\text{H I}}$ (right). The solid line shows the 17 detected HVCs from our survey, whereas the dashed curve is the expected distribution according to our model based on model #9 of de Heij et al. (2002a).

the radial distribution of the HVCs detected around M 31 do not agree with the predictions of the model. This result confirms our conclusion that HVCs/CHVCs are much closer to their host galaxies than previously assumed, implying not only smaller projected distances but also lower H I masses. Hence, a large fraction of the HVC population around M 31 may have H I masses below our $3\,\sigma$ detection limit of $8\times 10^4~M_\odot$ and could have remained undetected.

Modification of the original model

To study the radial distribution of the HVCs around M 31 in more detail, we modified the model of de Heij et al. (2002a) in order to determine the radial scale length, σ , of the modelled HVC population which provides the best fit to the observed distribution of projected radii. In practice we calculated several models covering the entire range of $\sigma = 20\dots 200$ kpc, but leaving all other parameters (total number of clouds, H I mass spectrum, etc.) fixed. Again, we calculated 1000 individual model populations for each value of σ to keep statistical errors small. We then compared the projected radial distribution of the model clouds with the observed one, again using the KS test. The results are presented in Fig. 2.23.

The left diagram of Fig. 2.23 shows the KS probability for the hypothesis that the projected radial distributions of observed and modelled HVCs agree as a function of radial scale length, σ , of the model population. The probability curve shows a very pronounced and narrow peak at $\sigma \approx 49$ kpc where the probability exceeds 80%. Towards larger, and in particular towards smaller, scale lengths the KS probability drops very quickly. For $\sigma = 100$ kpc the probability is of the order of 15%, and it decreases to only about 5% for the original de Heij et al. (2002a) model of $\sigma = 200$ kpc. The normalised cumulative radial distributions of model and data for the best-fitting case, $\sigma = 49$ kpc, are plotted in the right panel of Fig. 2.23. In comparison to the original model of de Heij et al. (2002a) in Fig. 2.22 the radial distribution is described much better, although model and data do not match in every detail. The observed HVC population shows a significantly steeper rise

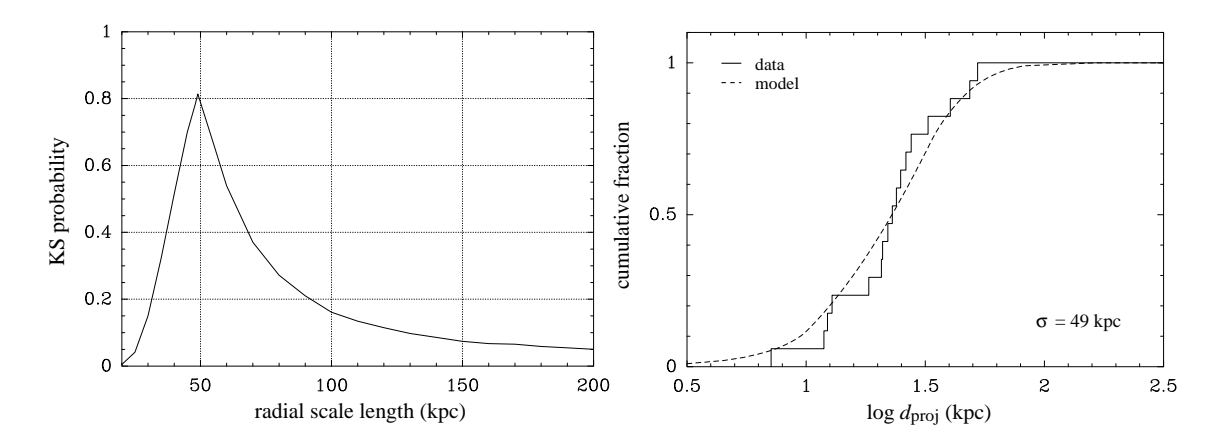


Fig. 2.23: Left: Kolmogorov-Smirnov probability for the hypothesis that the observed radial distribution of HVCs around M 31 follows a Gaussian distribution with radial scale length σ . There is a clear peak at $\sigma=49$ kpc with a probability in excess of 80%. Right: Comparison of the normalised cumulative distributions of observed (solid line) and modelled (dashed line) HVCs as a function of projected distance from the centre of M 31 for the best-fitting three-dimensional radial scale length of $\sigma=49$ kpc. The KS test in this case yields a statistic of D=0.15, resulting in a probability of p=81% that both samples were drawn from the same distribution.

in the radial profile than the model population. This steep rise is caused by the fact that 6 HVCs belong to the complex of clouds near the south-eastern edge of M 31, resulting in similar projected radii. The appearance of this complex suggests a common origin for these clouds.

Therefore, we also tried to count the entire complex as one single object instead of considering each HVC separately. The result is shown in Fig. 2.24. Again, there is a pronounced peak in the probability function. The best-fitting model is slightly shifted to $\sigma \approx 41$ kpc. The maximum probability, however, is significantly increased to p=98.8%, indicating that we can obtain a much better fit when combining all HVCs of the complex. At the same time, the peak in the probability function is broader than before, resulting in a wider range of feasible radial scale lengths. For example, at $\sigma=100$ kpc the KS test still yields a probability of more than 25% for an agreement in the radial profiles of observed and modelled HVCs. Even for the original model of de Heij et al. (2002a) with $\sigma=200$ kpc we still obtain a probability of more than 10%, thus excluding this model at not even 90% confidence level. When interpreting these numbers we have to keep in mind, though, that combining all HVCs in the complex leaves us with only 12 HVCs remaining around M 31.

In summary, the original Local Group population model of de Heij et al. (2002a) can be excluded with high confidence. Instead, our results support a more compact population with a radial scale length of $\sigma \simeq 50$ kpc. However, the radial scale length is not very strictly confined by our observations. Even for $\sigma = 100$ kpc we still obtain KS probabilities in the range of 15% to 25%.

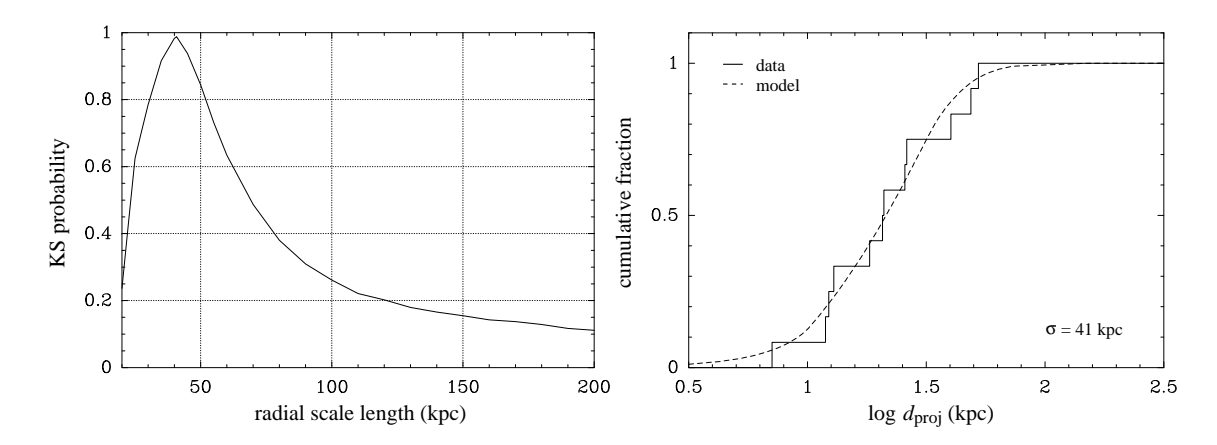


Fig. 2.24: Same as in Fig. 2.23, this time, however, counting the HVC complex near the south-eastern edge of M 31 as a single object. The radial scale length of the best-fitting model is slightly smaller, $\sigma \approx 41$ kpc, with a significantly increased probability of nearly 99%.

2.5.2 Comparison with the satellite galaxies of M 31

Like the Milky Way, M 31 hosts an extended group of satellite galaxies of which M 33 is the most massive one. An overview of the entire M 31 group—comprising all galaxies believed to be gravitationally bound to M 31—is given in Table 2.3 based on the compilations of McConnachie & Irwin (2006) and Koch & Grebel (2006). The list also includes the faint dwarf galaxies Andromeda IX–XIII recently discovered by Zucker et al. (2004, 2006b) and Martin et al. (2006). These detections have shown that a large number of low-mass satellites with very low surface brightness may still be awaiting their discovery and that the M 31 group, as presently known, is presumably incomplete. The most fundamental parameters provided by hierarchical structure formation scenarios (e.g., Klypin et al. 1999; Moore et al. 1999; Kravtsov et al. 2004) are the radial distribution and the mass spectrum of CDM satellites in orbit around their parent halo. To assess in which way HVCs and satellite galaxies around M 31 could be linked in the framework of CDM it is essential to compare the basic parameters of both populations with each other.

The radial distribution of the satellite galaxies around M 31 has been reasonably well determined (see, e.g., Koch & Grebel 2006 for an overview), although the relative errors of the galactocentric distances can be significant for the innermost satellites of M 31. Due to the lack of distance information, the spatial distribution of the HVCs around M 31, however, is completely unknown. Hence, the only feasible approach is to compare the projected positions of HVCs and satellite galaxies by discarding the distance information available for the M 31 satellites. Values for the projected distances ($d_{\rm proj} = d_{\rm M 31} \tan \xi$, with ξ being the angular separation between each satellite and the centre of M 31) are listed in Table 2.3 for all galaxies believed to be member of the M 31 group. A similar problem arises when trying to compare the mass spectrum of both populations, as for most of the M 31 satellite galaxies dynamical studies are not available. There have been H I studies, however, for all but the most recently discovered galaxies, although in four cases only upper limits resulting from non-detections are available. H I masses and references for the individual galaxies of the M 31 group are also listed in Table 2.3.

Table 2.3: List of the M 31 group according to McConnachie & Irwin (2006), Koch & Grebel (2006), Zucker et al. (2006b), and Martin et al. (2006). α and δ denote the equatorial coordinates in J2000.0, $d_{\rm proj}$ is the projected distance from the centre of M 31, and $M_{\rm H\,I}$ is the H I mass according to the specified reference. A dash (–) indicates that there is no H I mass determination available. References: [1] Carignan et al. (2006), [2] Emerson (1974), [3] Johnson & Gottesman (1983), [4] Mateo (1998), [5] Young & Lo (1997a), [6] Corbelli & Schneider (1997), [7] Wilcots & Miller (1998), [8] Young & Lo (1997b), [9] Lo et al. (1993), [10] Huchtmeier & Richter (1986), [11] Silich et al. (2006), [12] Barnes & de Blok (2004).

#	Name	Type	α	δ	d_{proj}	$M_{ m HI}$	Ref.
			(J2000)	(J2000)	(kpc)	(M_{\odot})	
1	M 31	Sb	$00^{\rm h}42^{\rm m}44^{\rm s}$	41°16′09″	0.0	5.0×10^{9}	[1]
2	M32	cE	$00^{\rm h}42^{\rm m}42^{\rm s}$	$40^{\circ}51'55''$	6.8	$< 1.5 \times 10^{6}$	[2]
3	$NGC\ 205$	dE	$00^{\rm h}40^{\rm m}22^{\rm s}$	$41^{\circ}41'07''$	6.9	3.8×10^{5}	[3]
4	And IX	dSph	$00^{\rm h}52^{\rm m}53^{\rm s}$	$43^{\circ}12'00''$	35.4	_	
5	And I	dSph	$00^{\rm h}45^{\rm m}40^{\rm s}$	$38^{\circ}02'28''$	46.8	$< 1 \times 10^{5}$	[4]
6	And III	dSph	$00^{\rm h}35^{\rm m}34^{\rm s}$	$36^{\circ}29'52''$	68.4	$< 8 \times 10^{4}$	[4]
7	And X		$01^{\rm h}06^{\rm m}34^{\rm s}$	$44^{\circ}48'16''$	75.7	_	
8	NGC 185	dE	$00^{\rm h}38^{\rm m}58^{\rm s}$	$48^{\circ}20'15''$	95.9	1.5×10^{5}	[3]
9	And XII		$00^{\rm h}47^{\rm m}27^{\rm s}$	$34^{\circ}22'29''$	96.2	_	
10	NGC 147	dE	$00^{\rm h}33^{\rm m}12^{\rm s}$	$48^{\circ}30'32''$	100.2	$< 3 \times 10^{3}$	[5]
11	And XI		$00^{\rm h}46^{\rm m}20^{\rm s}$	$33^{\circ}48'05''$	103.7	_	
12	And V	dSph	$01^{\rm h}10^{\rm m}17^{\rm s}$	$47^{\circ}37'41''$	109.2	_	
13	And XIII		$00^{\rm h}51^{\rm m}51^{\rm s}$	$33^{\circ}00'16''$	117.0	_	
14	And II	dSph	$01^{\rm h}16^{\rm m}30^{\rm s}$	$03^{\circ}25'09''$	142.8	_	
15	M33	Sc	$01^{\rm h}33^{\rm m}51^{\rm s}$	$30^{\circ}39'36''$	206.0	1.8×10^{9}	[6]
16	And VII	dSph	$23^{\rm h}26^{\rm m}31^{\rm s}$	$50^{\circ}41'31''$	225.9	_	
17	IC 10	dIrr	$00^{\rm h}20^{\rm m}17^{\rm s}$	$59^{\circ}18'14''$	258.3	3.2×10^{7}	[7]
18	And VI	dSph	$23^{\rm h}51^{\rm m}46^{\rm s}$	$24^{\circ}34'57''$	281.6	_	
19	LGS 3	dIrr/dSph	$01^{\rm h}03^{\rm m}53^{\rm s}$	$21^{\circ}53'05''$	283.4	4.2×10^{5}	[8]
20	Pegasus	dIrr/dSph	$23^{\rm h}28^{\rm m}36^{\rm s}$	$14^{\circ}44'35''$	469.4	1.3×10^{7}	[9]
21	UGCA 92	dIrr	$04^{\rm h}32^{\rm m}05^{\rm s}$	$63^{\circ}36'49''$	641.9	1.6×10^7	[10]
22	IC 1613	dIrr	$01^{\rm h}04^{\rm m}47^{\rm s}$	$02^{\circ}07'02''$	644.5	6.0×10^{7}	[11]
23	WLM	dIrr	$00^{\rm h}01^{\rm m}58^{\rm s}$	$-15^{\circ}27'39''$	1227.3	5.6×10^7	[12]
24	Aquarius	dIrr	$20^{\rm h}46^{\rm m}52^{\rm s}$	$-12^{\circ}50'53''$	3311.9	3.0×10^{6}	[9]

The left panel of Fig. 2.25 shows the histogram of H I masses of the 17 HVCs detected in our Effelsberg survey in comparison with the H I masses of the satellite galaxies of M 31 (including M 31 itself) according to Table 2.3. For the HVC masses a constant distance of 780 kpc (Stanek & Garnavich 1998) is assumed. The HVCs appear to be distributed around the low-mass end of the satellite galaxies, although there is a significant overlap between the two distributions. In particular Davies' Cloud—supposed it is at the distance of M 31—has a much larger H I mass than any other HVC observed around M 31. One should note, however, that for a significant fraction of M 31 satellites H I studies are

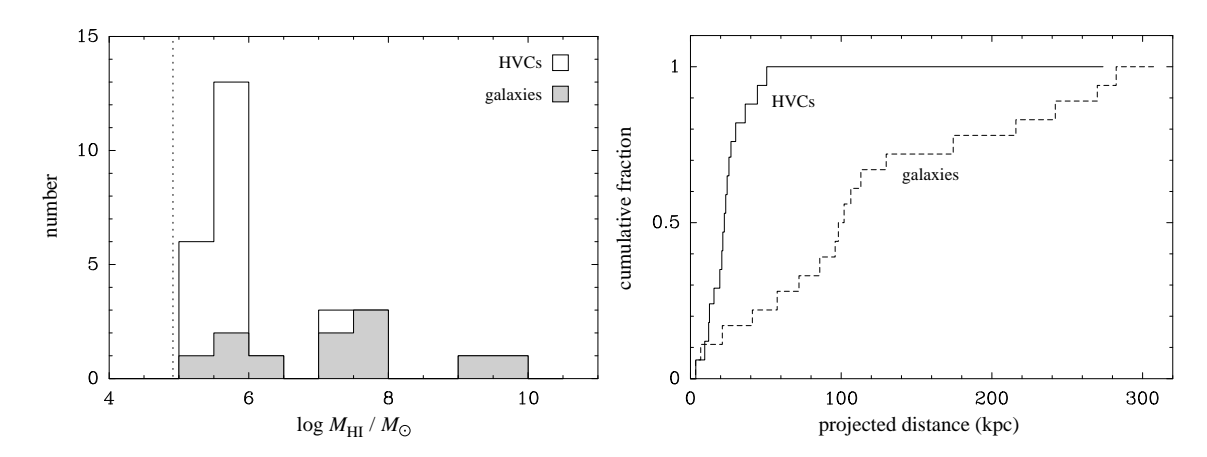


Fig. 2.25: Comparison of the HVCs detected around M 31 in our Effelsberg survey with the satellite galaxies of the M 31 group. Left: Histogram of the H I masses of HVCs (white) and satellite galaxies (grey, including M 31) based on Tables 2.2 and 2.3, respectively. The vertical line indicates our 3σ detection limit. Right: Cumulative fraction of HVCs (solid line) and satellite galaxies (dashed line) as a function of projected distance from the centre of M 31. Only satellites within a projected radius of 300 kpc around M 31 have been considered for the diagram.

either not available, or only upper mass limits have been determined from non-detections, implying that the mass histogram for the galaxies is subject to incompleteness issues.

In the right panel of Fig. 2.25 the cumulative fraction of HVCs and satellite galaxies is plotted as a function of projected distance. Only those satellite galaxies within a projected radius of 300 kpc around M 31 have been considered as they are roughly located within the expected virial radius of M 31 (see, e.g., Kravtsov et al. 2004). It is obvious that HVCs and satellite galaxies have a completely different radial distribution. All HVCs are found within a projected radius of about 50 kpc, whereas the satellite galaxies of M 31 are spread across the entire range of distances out to 300 kpc. The Kolmogorov-Smirnov test yields a statistic of D=0.78, resulting in a very low probability of only 1.6×10^{-5} that HVCs and satellite galaxies are drawn from the same distribution. The relatively steep rise of the HVC distribution between 20 and 30 kpc is a selection effect. It arises from the conspicuous concentration of HVCs near the south-eastern edge of the M 31 disk which leads to very similar projected distances for all HVCs of this complex. A selection effect can also explain the bump seen in the galaxy distribution at projected distances between 100 and 150 kpc. The recently discovered satellite galaxies Andromeda XI–XIII (Martin et al. 2006) are all located in the same region of the sky, resulting in very similar projected distances of the order of 100 kpc. The discovery of Andromeda XI-XIII suggests that many more faint satellite galaxies all around M 31 are still awaiting their discovery so that our current census of the M 31 group is most likely incomplete.

In Fig. 2.26 the logarithm of the HI mass, $M_{\rm HI}$, of HVCs (open squares) and satellite galaxies (filled squares) is plotted versus the logarithm of the projected distance, $d_{\rm proj}$. The distinction between HVCs and satellite galaxies is very obvious. The HVCs are concentrated in the lower left area of the diagram with lower HI masses and smaller projected distances, whereas the galaxies tend to concentrate in the upper right region of the diagram with typically higher HI masses and larger distances. When interpreting the

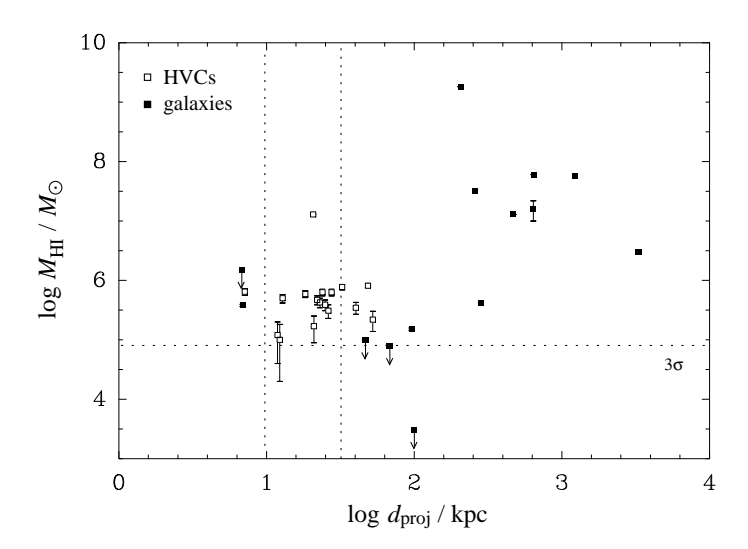


Fig. 2.26: HI mass versus projected distance of HVCs (open squares) and satellite galaxies (filled squares) around M 31. The horizonal line indicates our 3σ detection limit. The two vertical lines mark the outer edge of the M 31 HI disk along the minor and major axis. Although both groups tend to populate different regions of the diagram, it is important to note that for only a fraction of the M 31 satellites HI studies are available.

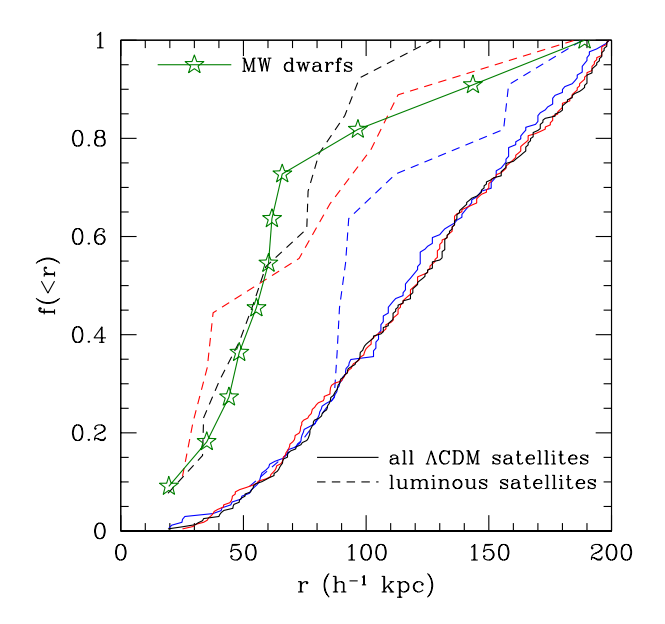
mass-distance diagram, however, we have to keep in mind that the incompleteness and selection effects discussed above apply. As a consequence, the separation between HVCs and galaxies in Fig. 2.26 may be an artifact of incomplete data. For several satellites of the M 31 group, H I measurements are either not available or only upper mass limits have been derived from non-detections. As this will particularly affect those galaxies with intrinsically low H I masses, a large number of data points could be missing in the low-mass domain.

If we assume the difference between HVCs and galaxies in Fig. 2.26 to be real, what could the physical reason for the observed discrepancies be? If both HVCs and satellite galaxies were the visible counterparts of dark-matter satellite halos, the differences in their radial distribution would be surprising. In this case, a physical mechanism would be required to prevent the presence of dark-matter-dominated neutral gas clouds at large galactocentric distances from M 31, e.g. through ionisation of the gas. This scenario will be discussed in more detail in the following Section 2.5.3 and in connection with our WSRT follow-up observations in Section 3.5. Another reason for the discrepancies in the radial distribution of HVCs and satellite galaxies could be a different origin of both groups of objects. If HVCs were of tidal origin or the result of condensing halo gas, galactic winds, or outflows, their proximity to M 31 would be a natural consequence. This option will also be discussed in more detail in Section 3.5.

2.5.3 Comparison with CDM simulations

A comparison with the results of CDM-based structure formation simulations carried out by Kravtsov et al. (2004) reveals significant differences in the radial distributions of both HVCs and satellite galaxies compared to the predicted population of dark matter satellites around Galaxy-sized halos. Within a radius of 200 h^{-1} kpc the mean distance of dark matter satellites of about 120 h^{-1} kpc is noticeably larger than that of the M 31 satellite galaxies of 85 h^{-1} kpc and dramatically larger (assuming $h \approx 0.7$) than the maximum projected distances of about 50 kpc observed for HVCs. Kravtsov et al. (2004) can partly solve this problem by including a simple model of star formation in dark matter halos in their simulations. According to their results only a small fraction of satellites have

Fig. 2.27: Fraction, f, of dark-matter satellites within a certain radius, r, from their Galaxy-sized parent halo according to the numerical models of Kravtsov et al. (2004). The solid lines represent the total number of satellites for three different model halos, whereas the dashed lines show only the luminous satellites predicted by the simulations. Known satellite galaxies around the Milky Way are plotted as stars for comparison. The figure was taken from Kravtsov et al. (2004).



actually formed stars to become luminous galaxies, whereas most halos remained dark (Fig. 2.27). Their model can not only reproduce the radial distribution and number of satellite galaxies observed around the Milky Way, but also the circular velocity function and the observed morphological segregation.

To investigate whether the remaining dark satellites in the simulations can be identified with the population of HVCs around M 31 or the Milky Way, Kravtsov et al. (2004) also determined the gas mass associated with each dark matter halo in their simulation. Within a radius of 200 h^{-1} kpc they find a total gas mass of $M_{\rm g} \approx 2 \times 10^9~M_{\odot}$, resulting in a corresponding neutral gas mass of $M_{\rm H\,I} \approx 2 \times 10^8~M_{\odot}$ if a neutral gas fraction of 10% is assumed (e.g., Maloney & Putman 2003). This value is one order of magnitude higher than the total H I mass of about $2 \times 10^7~M_{\odot}$ of the 17 HVCs identified in our Effelsberg survey. We should note, however, that some more neutral gas is present in diffuse, extraplanar gas clouds which are not resolved into individual objects with our 9' HPBW. On the other hand, the observed neutral gas mass in HVCs is totally dominated by a single object, Davies' Cloud, which contributes 65% of the total H I mass.

The total number of gaseous dark halos with $M_{\rm g} > 10^6~M_{\odot}$ (corresponding to $M_{\rm H\,I} \gtrsim 10^5~M_{\odot}$) in the simulations of Kravtsov et al. (2004) is about 50...100, but for the central 50 kpc their models predict only 2...5 such clouds. They conclude that part of the HVCs found by Thilker et al. (2004) around M 31 could be primordial dark matter halos, whereas others could instead be of tidal origin similar to the Magellanic Stream around the Milky Way. In our Effelsberg survey, however, we have not detected any additional HVCs beyond a projected radius of about 50 kpc with a 3 σ detection limit of $8 \times 10^4~M_{\odot}$. This discrepancy is surprising, given that more than 90% of the predicted gaseous halos should be located outside the radius of 50 kpc.

Because of the limited azimuthal range of our survey region we cannot assume to detect all of the expected gaseous halos. At a projected distance of 50 kpc our local completeness function drops below 50% (see Fig. 2.8), but nonetheless we still cover more than 1/3 of the total area within a projected radius of 100 kpc. Within a radius of 100 kpc Kravtsov et al.

(2004) expect about 35% of all dark matter halos, resulting in 18...35 expected gaseous halos with $M_{\rm g} > 10^6~M_{\odot}$, about ½ of which should be located within our survey area, resulting in a total number of expected HVCs in our survey in the range of about 6...12 (not taking into account the details of the radial distribution of dark-matter halos). This is less than the 17 HVCs identified in our data, supporting the concept of Kravtsov et al. (2004) that some of the detected HVCs may represent tidally stripped gas originating from satellite galaxies of M 31. However, we would expect the gaseous primordial dark matter halos to be spread across the entire survey area, whereas the detected HVCs are highly concentrated in the central region around M 31.

What is the reason for these discrepancies between the predictions of the CDM-based structure formations simulations by Kravtsov et al. (2004) and the parameters of the HVC population around M 31 resulting from our Effelsberg H I observations? On the one hand, the simulations may not yet be accurate enough to reproduce the neutral gas content of dark-matter satellites around Galaxy-sized halos. As Kraytsov et al. (2004) pointed out, the expected distribution and parameters of dark-matter satellites is a very sensitive function of their evolution. Close encounters between dark-matter halos in the past will have had a strong influence on the gas content and star formation history of the respective satellites. On the other hand, the detected HVCs might not be the gaseous correspondents of primordial dark-matter satellites at all, but other effects such as tidal stripping or the condensation of halo gas could have caused the observed HVCs. To investigate this problem in more detail we will need high-resolution synthesis observations of the M31 HVCs. This will allow us to study their structure in unprecedented detail and to find evidence for their origin. Therefore, we used the Westerbork Synthesis Radio Telescope (WSRT) to study some of the HVCs around M 31 with higher resolution and sensitivity. The results of these observations are be presented in Chapter 3.

2.6 Summary and conclusions

We carried out a deep H I blind survey of a large area around M 31 with the 100-m radio telescope at Effelsberg. The $3\,\sigma$ H I mass detection limit of our survey is $8\times 10^4~M_{\odot}$. With our observations we could confirm the existence of a population of HVCs around M 31 with projected distances of less than about 50 kpc and typical H I masses between 10^5 and $10^6~M_{\odot}$. Apart from 17 individual HVCs we also found several regions of diffuse extra-planar gas which are not spatially or kinematically resolved into separate clouds with the 9' HPBW of the telescope. The total H I mass of all detected HVCs and regions of extra-planar gas is of the order of $5\times 10^7~M_{\odot}$. The observations have demonstrated that M 31 is surrounded by an extended population of HVCs. However, two problems are connected to this detection:

- 1. The total number of HVCs around M 31 is by far smaller than the number of hundreds of HVCs observed around the Milky Way.
- 2. The detected HVCs are found within a projected distance of only 50 kpc from the centre of M 31 whereas different models and observations over the past years have suggested much larger distances of HVCs from their host galaxies of the order of 100 kpc and beyond.

The smaller number of HVCs observed around M31 compared to the Milky Way can have different reasons. First of all, the absolute number of clouds could indeed be smaller than in the case of our own Galaxy. As discussed in Section 2.3.2, the Milky Way and M 31 could have had a different evolution which could have influenced the characteristics of their respective HVC population. Without detailed knowledge of the formation mechanisms for HVCs, however, any attempt to solve this problem must be considered speculative. If, on the other hand, we assume that both galaxies have a similar population of HVCs, we can derive a very strict upper limit for the distances of HVCs, and CHVCs in particular, from their host galaxies of $d \lesssim 60$ kpc, based on the non-detection of a considerable population around M 31. This result is in excellent agreement with the observed extent of the detected HVCs near M31. It demonstrates that HVCs are most likely forming circumgalactic populations around the Milky Way and the Andromeda Galaxy with distances of not more than a few ten kpc. This result is in contradiction to the original suggestion by Blitz et al. (1999) that HVCs are spread all over the Local Group with typical distances of hundreds of kpc. Several observations (Zwaan 2001; Pisano et al. 2004) and simulations (Sternberg et al. 2002) already set upper limits for the distances of HVCs and CHVCs of the order of 150 kpc. With the strict limit derived from our Effelsberg survey we can now definitely rule out the Local Group hypothesis proposed by Blitz et al. (1999).

Our results are directly supported by $H\alpha$ detections of HVCs and CHVCs (e.g., Tufte et al. 2002; Putman et al. 2003a) which suggest upper distance limits of the order of 10 kpc under the assumption that the clouds are ionised by the Galactic UV radiation field. The distance limits derived from $H\alpha$ observations are in excellent agreement with the distances and distance limits obtained from our Effelsberg survey. Our results are also supported by the distance brackets of the order of a few kpc which have been determined for a few HVC complexes around the Milky Way (Danly et al. 1993; Wakker et al. 1996; Ryans et al. 1997; van Woerden et al. 1999b; Wakker 2001; Thom et al. 2006). Therefore, HVCs and CHVCs cannot be the primordial dark-matter-dominated satellites throughout the Local Group with HI masses of the order of $10^7 M_{\odot}$. As a consequence, the distinction between HVCs and CHVCs seems no longer justified. CHVCs were originally defined by Braun & Burton (1999) as the potential primordial dark-matter mini-halos left over from the formation of the Local Group. Their small angular sizes compared to the large HVC complexes would have been a result of their large distances from the Galaxy of hundreds of kpc. Our Effelsberg survey has shown, however, that both HVCs and CHVCs must be very close to their host galaxies so that the small angular sizes of CHVCs simply reflect their small physical sizes instead of large distances.

The apparently small distances and sizes of both HVCs and CHVCs also raise the question whether they are associated with any significant amount of dark matter. The dynamical considerations in Section 2.4.1 have shown that the observed spectral line widths of some of the HVCs around M 31 imply very high virial-to-HI mass ratios of the order of 100...1000. The measured line widths, however, could be dominated by internal kinematics and projection effects along the line of sight or across the telescope beam so that they are most likely not an accurate measure for the underlying dynamical mass of the cloud. Instead, HVCs could be stabilised by the pressure of the hot ionised corona around M 31 in which they are embedded. The expected pressures of the order of 100 K cm⁻³ (e.g., Sembach et al. 2003; Rasmussen et al. 2003) are sufficient to stabilise HVCs in addition to their observed HI masses and without the need for any additional mass components.

Our results suggest that most HVCs—given their small distances from M 31—are probably mainly pressure-confined and need not be associated with gravitationally dominant dark-matter halos. However, more sensitive and detailed interferometric observations are necessary to probe the internal dynamics of the HVCs around M 31. The results of such a study will be presented in the next chapter.

The next logical step in the study of HVCs around M 31 will be the determination of their origin. Our large-scale H I survey has been an important approach to detect and catalogue the expected population of HVCs. The 9' HPBW of the Effelsberg telescope, however, corresponds to a fairly poor spatial resolution of 2 kpc which is not sufficient to resolve the internal structure of the clouds. Therefore, the next step will be an interferometric study of the HVCs around M 31. With available instruments, such as the WSRT or the VLA, we can easily reach angular resolutions of the order of 1' at $\lambda = 21$ cm, corresponding to a spatial resolution of 200 pc. This should resolve the large HVCs near M 31 which would provide us with the opportunity to determine their spatial and kinematic structure with an accuracy comparable to what can be achieved with single-dish telescopes in the case of Galactic CHVCs. Therefore, we used the WSRT to map some of the HVCs around M 31 in H I with high angular resolution with the aim of determining their structure and origin. These observations and their results will be introduced and discussed in the next chapter.

Follow-up synthesis observations of M 31 HVCs

In this chapter I present and discuss the results of our follow-up HI synthesis observations with the WSRT of some of the HVCs found near M31. Part of the chapter has been adapted from the corresponding referred journal article (Westmeier et al. 2005a). In total, we detect 16 individual HVCs in seven out of nine studied fields. The clouds have typical HI masses of a few times $10^5 M_{\odot}$ and sizes of the order of 1 kpc. Some of the HVCs, in particular the conspicuous HVC complex near the south-eastern edge of M31, are most likely of tidal origin in connection with the giant stellar stream (Ibata et al. 2001a) or satellite galaxies of M31. The remaining three detected HVCs are completely isolated from any known dwarf galaxy or structure in the stellar component of M31. They are the most promising candidates for the primordial dark-matter mini-halos predicted by structure formation scenarios based on CDM cosmology. A comparison with the simulations of Sternberg et al. (2002) and Kravtsov et al. (2004) shows that their results are consistent with the observed parameters of the HVCs around M31. All our results suggest that the HVCs discovered around M31 are the relics of structure formation. Hence, HVCs are tracers for the rich accretion history and evolution of large spiral galaxies like the Milky Way and the Andromeda Galaxy.

3.1 Introduction

Our deep HI survey of a large area around M 31 with the 100-m radio telescope at Effelsberg demonstrated that M 31 is surrounded by a population of HVCs with HI masses of typically a few times $10^5~M_{\odot}$. In contrast to the predictions of CDM structure formation scenarios (Kravtsov et al. 2004) all 17 discrete HVCs found near M 31 have projected distances of less than about 50 kpc from the centre of M 31. A similar upper distance limit of 60 kpc can be derived from the non-detection of the expected extended population of CHVCs around the Andromeda Galaxy. Obviously, HVCs and CHVCs are forming a circumgalactic population around M 31 and the Milky Way with distances of $\lesssim 50~\mathrm{kpc}$



Fig. 3.1: The 25-m antennas of the Westerbork Synthesis Radio Telescope (WSRT) which is operated by the Stichting Astronomisch Onderzoek in Nederland (ASTRON) based in Dwingeloo.

from their respective host galaxy. Our result appears to be in contradiction to the original proposal by Blitz et al. (1999) that HVCs are the gaseous correspondents of primordial dark-matter halos left over from structure formation in the Local Group.

This discrepancy immediately raises the question of the origin of the HVCs detected around M31. Unfortunately, the 9' HPBW of the Effelsberg telescope, corresponding to a spatial resolution of 2 kpc at the distance of M 31, is not able to resolve most of the HVCs, indicating that they have typical angular sizes of only a few arc minutes. Therefore, we decided to carry out high-resolution synthesis observations of several HVCs near M 31 with the Westerbork Synthesis Radio Telescope (WSRT) with the aim of resolving their structure. At a wavelength of $\lambda = 21$ cm, the WSRT provides a synthesised beam of less than 1' FWHM. This corresponds to a very high spatial resolution of the order of 200 pc or even better. Thus, observing the HVCs around M 31 with the WSRT would provide us with sufficiently high spatial resolution to resolve their structure to a degree comparable to what can be achieved with single-dish telescopes in the case of Galactic CHVCs. This will allow us to determine the morphology of the clouds and to detect possible head-tail structures or other signs of tidal or ram-pressure distortion. This will help us to find out to which extend the HVCs could be the result of tidal stripping in connection with close encounters between M 31 and its satellite galaxies. We will also be able to study the internal structure and resolve the cold gas component in the cores, only hinted at by the Effelsberg observations. Resolving the internal kinematics will help us to assess whether the clouds are associated with any significant amount of dark matter.

Reduction and analysis of the WSRT data were carried out during my participation in the ASTRON/JIVE Summer Student Programme 2004 in collaboration with Robert Braun (ASTRON, Dwingeloo, The Netherlands) and David Thilker (Johns Hopkins University, Baltimore, USA). In this chapter I will present and discuss the results and conclusions of our observations. Part of the chapter has been adapted from the corresponding refereed journal article (Westmeier et al. 2005a).

¹ The actual angular resolution will depend on the specific weighting and tapering of the visibility data, whereas the intrinsic angular resolution of the WSRT at $\lambda = 21$ cm is about 13" FWHM.

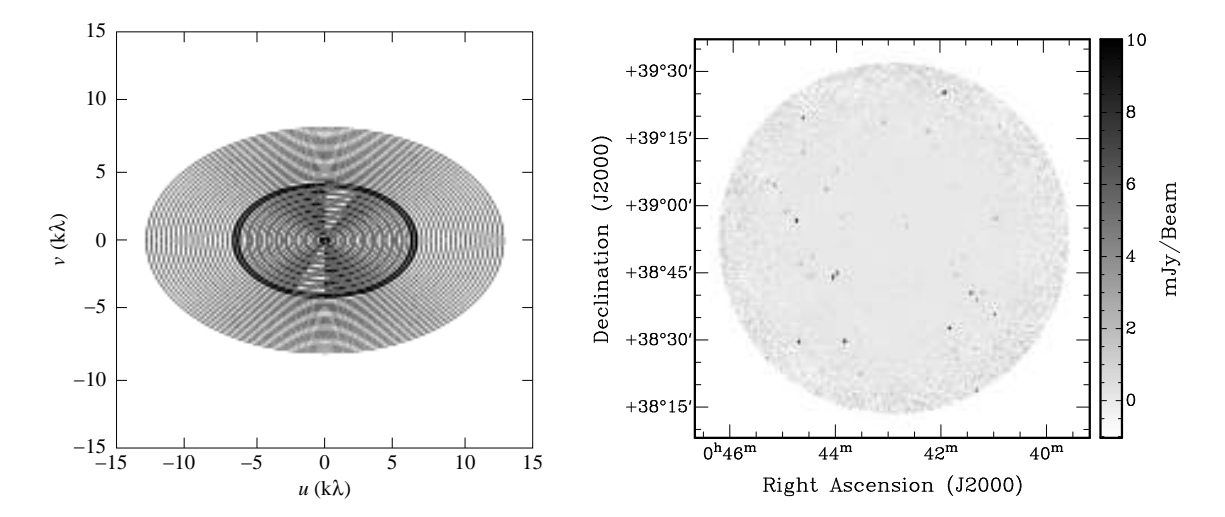


Fig. 3.2: WSRT observations in the direction of M 31 HVCs 2–12. **Left:** Total *uv* coverage of the data in the maxi-short configuration after a complete 12-hour track. **Right:** 21-cm continuum image. The numerous point sources in the continuum map were used for self-calibration.

3.2 Observations and data reduction

3.2.1 Sample selection

In total we selected nine fields around M 31 for our follow-up observations with the WSRT. The fields were selected on the basis of the GBT survey of M 31 by Thilker et al. (2004). They were chosen to cover the brightest and most conspicuous HVCs found in the GBT survey and cover about half of the entire population of discrete HVCs found within 50 kpc projected distance of M 31. The targets cover the different morphological types of clouds found in the GBT data and include HVCs with both large and small angular separations from the disk of M 31. The most prominent object, Davies' Cloud, was already studied in great detail (Davies 1975; de Heij et al. 2002c) so we did not include it in our survey. An overview of the nine fields is given in Fig. 3.3.

3.2.2 Observations

The nine selected fields were observed in the 21-cm line emission of neutral atomic hydrogen, using the WSRT (Fig. 3.1) in the so-called Maxi-Short configuration. This configuration provides particularly good sampling of the shortest east-west baselines (36, 54, 72, and 90 m) and provides optimum imaging performance for extended sources. The WSRT being an east-west interferometer, a complete 12-hour track for each field was observed. Each coverage was preceded and followed by observations of the external calibrator sources CTD 93 and 3C 147 (CTA 39). In the left panel of Fig. 3.2 the resulting uv coverage for one of the nine fields is plotted for illustration.

The correlator provided 1024 spectral channels for each of the two linear polarisations. To improve the signal-to-noise ratio, the 1024 channels were equally divided among two independent IF bands tuned to the same central frequency, resulting in 512 channels for the final spectrum. By later averaging these two IF bands we were able to decrease the

digitisation noise by a factor $\sqrt{2}$. As a result, the noise level in the final images is about 5% lower in comparison with the normal single-IF mode. With a bandwidth of 5 MHz the corresponding original velocity resolution is about 2 km s⁻¹ which is sufficient to resolve the spectral lines of both the warm and cold neutral medium.

3.2.3 Data reduction

The data reduction was performed with the NRAO Astronomical Image Processing System (AIPS). After reading in and preparing the data for the reduction procedure, we flagged all data affected by radio frequency interference and by shadowing of the telescopes, using the tasks SPFLG and UVFLG. Next, the standard bandpass, gain, and flux calibration was carried out, using the two external calibrators. As the calibrators were observed only at the beginning and at the end of each 12-hour track, they only allow a linear interpolation of the complex gain solution over the entire observation. To further improve the gain solution, we self-calibrated on the continuum sources in each field in an iterative procedure. The right panel of Fig. 3.2 shows the continuum map of one of the nine studied fields as an example. Each field typically covered several dozen point sources, most of which will be distant galaxies or quasars. In each iteration the continuum image, deconvolved with the CLEAN algorithm (Högbom 1974), was used to improve the gain solution which was then applied in the next iteration step. The solution interval for the gain solution was decreased with each iteration down to 1 or 2 minutes in the final step. In the final iteration we calibrated amplitude and phase, whereas in all previous steps only the phase was calibrated. The self-calibration procedure provided us with a clean component model of the continuum emission which was then subtracted from the visibility data. The resulting gain solution tables of the continuum data file were finally copied and applied to the original spectral line data.

As the emission of most HVCs covered by our observations was quite faint and extended, we applied a Gaussian uv taper, declining to 30% amplitude at 1.25 k λ radius (≈ 260 m), before transforming and deconvolving the data cube. For deconvolution we applied the CLEAN algorithm (originally developed by Högbom 1974), using the AIPS task IMAGR. The resulting synthesised beam has a FWHM of about 2', corresponding to a spatial resolution of about 450 pc at the distance of M 31. For the brightest and most compact clouds we also produced images with a higher angular resolution of 30" FWHM (using a uv taper radius of 5 k $\lambda \approx 1$ km), corresponding to a spatial resolution of about 100 pc. Each image was finally corrected for the primary beam shape of the WSRT with a HPBW of about 36'. In addition, the velocity resolution was smoothed to 12 km s⁻¹ in all data cubes to further increase the signal-to-noise ratio, given that the typical detected linewidth was about 25 km s⁻¹. For the 2' resolution maps we obtain an RMS sensitivity of about 1 mJy/beam towards the centre of the field, corresponding to a brightness temperature RMS of 40 mK. This implies an H I column density sensitivity of 2.6×10^{18} cm⁻² ($3 \sigma \times 1$ channel) for emission filling the 2' beam.

Table 3.1: Physical parameters of the high-velocity clouds found near M 31. The columns specify: the cloud name; the right ascension, α , and declination, δ ; the peak column density, $N_{\rm H\,I}$, at 2' resolution; the heliocentric radial velocity, $v_{\rm hel}$; the average line width (FWHM) of the H I lines, Δv ; the cloud diameter, D (FWHM); the H I mass, $M_{\rm H\,I}$; the H I mass in the GBT data of Thilker et al. (2004), $M_{\rm H\,I}^{\rm GBT}$; the H I mass from our Effelsberg survey, $M_{\rm H\,I}^{\rm Eff}$; the virial mass, $M_{\rm vir}$; the average H I volume density, $n_{\rm H\,I}$; the value of the velocity gradient, δv ; the position angle of the velocity gradient, φ (measured in the mathematically negative sense with 0° being north); and the ellipticity, e. A distance of 780 kpc was assumed for all clouds to calculate their sizes, masses, and densities. In the last two rows we have calculated the mean value, $\langle x \rangle$, and the standard deviation, σ_x , of some parameters of M 31 HVCs 1–16.

cloud name	α	δ	$N_{ m HI}$	$v_{ m hel}$	Δv	D	$M_{ m H~I}$	$M_{ m HI}^{ m GBT}$	$M_{ m H~I}^{ m Eff}$	$M_{ m vir}$	n_{HI}	δv	φ	\overline{e}
	(J2000)	(J2000)	(10^{19})	(km		(kpc)		(M_{\odot})	(10^5)	M_{\odot})	(10^{-2})	$(\mathrm{km}\mathrm{s}^{-1}$	(°)	
	()	()	cm^{-2}		,	(F ·)	(-	()	(-	()	cm^{-3}	kpc^{-1}	()	
M 31 HVC 1	$0^{\rm h}42^{\rm m}53^{\rm s}$	38°52′	11.1	-503	17.3	0.72	5.2	4.8	7.8	230	10.9	7.7	349	0.24
$M31~\mathrm{HVC}~2$	$0^{\rm h}41^{\rm m}03^{\rm s}$	$39^{\circ}16'$	9.5	-511	29.6	0.75	5.0		6.3	690	9.3	9.7	188	0.12
$M31~\mathrm{HVC}~3$	$0^{\rm h}40^{\rm m}11^{\rm s}$	$39^{\circ}21'$	3.4	-509	18.5	0.93	2.2			330	2.1	8.4	239	0.28
$M31~\mathrm{HVC}~4$	$0^{\rm h}43^{\rm m}07^{\rm s}$	$39^{\circ}20'$	4.2	-518	21.0	0.56	1.3			260	5.8	4.1	98	0.22
$M31~\mathrm{HVC}~5$	$0^{\rm h}42^{\rm m}51^{\rm s}$	$39^{\circ}31'$	5.8	-512	25.3	1.13	6.0		6.3		3.3			0.48
$M31~\mathrm{HVC}~6$	$0^{\rm h}42^{\rm m}31^{\rm s}$	$39^{\circ}41'$	1.8	-517	17.3	0.53	0.6			170	3.2	4.1	334	0.42
$M31~\mathrm{HVC}~7$	$0^{\rm h}41^{\rm m}03^{\rm s}$	$39^{\circ}26'$	3.7	-464	20.3	1.27	3.5		3.9		1.3	10.7	280	0.40
$M31~\mathrm{HVC}~8$	$0^{\rm h}41^{\rm m}47^{\rm s}$	$39^{\circ}28'$	3.0	-476	32.1	0.92	2.1				2.1	15.5	291	0.36
M31~HVC~9	$0^{\rm h}43^{\rm m}13^{\rm s}$	$39^{\circ}39'$	1.8	-448	19.1	0.69	0.8			260	1.9	12.7	252	0.51
M31~HVC~10	$0^{\rm h}41^{\rm m}03^{\rm s}$	$39^{\circ}38'$	3.9	-432	30.2	1.20	5.0		4.8		2.3	14.7	262	0.38
M31~HVC~11	$0^{\rm h}43^{\rm m}32^{\rm s}$	$39^{\circ}27'$	0.9	-454	30.2	0.43	0.2			410	2.0			0.26
M31~HVC~12	$0^{\rm h}43^{\rm m}49^{\rm s}$	$39^{\circ}33'$	1.3	-390	30.8	1.5	1.5		4.3		0.3			
M31~HVC~13	$0^{\rm h}39^{\rm m}35^{\rm s}$	$41^{\circ}15'$	1.3	-211	22.8	2.6	3.5	8.7	6.4		0.2	4.6	233	0.65
M31~HVC~14	$0^{\rm h}36^{\rm m}04^{\rm s}$	$41^{\circ}34'$	2.9	-512	24.0	1.11	2.5	3.0			1.4			0.61
M31~HVC~15	$0^{\rm h}43^{\rm m}50^{\rm s}$	$44^{\circ}14'$	4.8	-273	26.5	1.07	5.2	5.2	3.5	790	3.3	4.5	176	0.37
$M31~\mathrm{HVC}~16$	$0^{\rm h}56^{\rm m}25^{\rm s}$	$42^{\circ}47'$	3.4	-164	25.9	1.26	3.9	4.4		890	1.5	8.9	115	0.43
M 31 HVC A	$0^{\rm h}40^{\rm m}23^{\rm s}$	39°41′	2.5	-455	32.1	1.04	1.9				1.3			0.56
M31~HVC~B	$0^{\rm h}39^{\rm m}54^{\rm s}$	$39^{\circ}33'$	1.9	-468	39.5	0.91	1.3				1.3			0.57
$\langle x \rangle$			3.9		24.4	1.04	3.0			450	3.2	8.8		0.38
σ_x			± 2.8		± 5.1	± 0.52	± 1.9			± 270	± 3.0	± 4.1		± 0.15

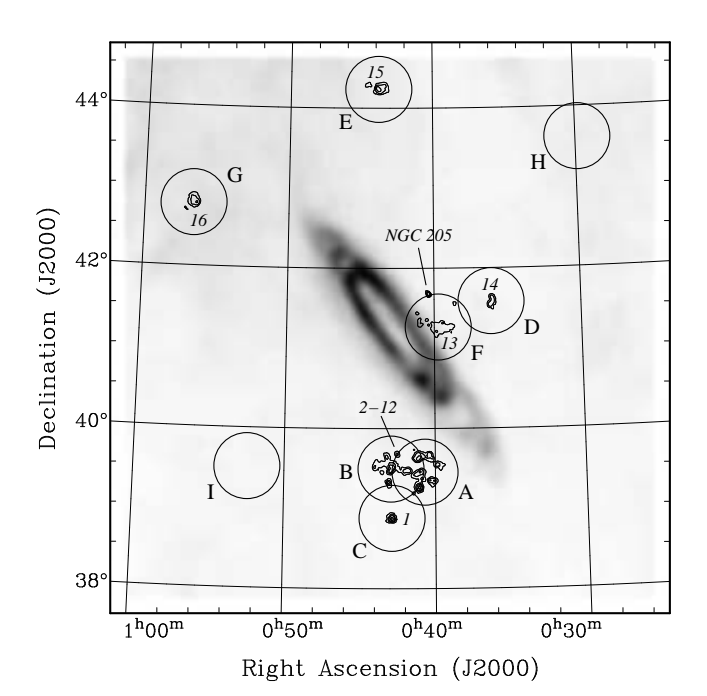


Fig. 3.3: Overview of the 9 fields (black circles, labelled with capital letters) observed around M 31 with the WSRT. The greyscale image shows for comparison the H I column density based on the GBT data of Thilker et al. (2004). The black contour lines represent the H I column density of the HVCs detected with the WSRT (labelled with numbers) and of NGC 205. In fields H and I no reliable signal of HVC gas was found within the sensitivity and resolution of our WSRT data.

3.3 Results

In two of the nine fields around M 31, labelled H and I in Fig. 3.3, no high-velocity gas was detected. In both cases the emission of the high-velocity gas is probably too faint or diffuse to be detected within the sensitivity of our WSRT data given the finite column density sensitivity noted above $(2.6 \times 10^{18} \text{ cm}^{-2} \text{ over } 12 \text{ km s}^{-1})$. In all other fields we clearly detect the HVCs at more than 5σ significance. In total we identify 16 discrete HVCs which have been named M 31 HVC X, where X is the catalogue number assigned to each HVC. Maps of all clouds are presented in Fig. 3.5 and 3.11–3.19. High-resolution maps of some of the HVCs can be found in Fig. 3.20 and 3.21. The observational parameters of all clouds are summarised in Table 3.1. Under the assumption of a distance of 780 kpc (Stanek & Garnavich 1998) we obtain a mean linear size of the 16 HVCs around M 31 of about 1 kpc FWHM and a mean H I mass of $3 \times 10^5 M_{\odot}$.

3.3.1 General properties of the HVCs

The HI column densities were derived from the zeroth moment of the spectra under the general assumption that the optical depth of the gas is negligible. The derived peak column densities are in the range of $N_{\rm H\,I} \simeq 10^{19} \dots 10^{20}$ cm⁻² with a mean value of about 4×10^{19} cm⁻². These values are significantly higher than those derived from our Effelsberg observations (Section 2.4.1), indicating that most of the HVCs were not resolved by the 9' HPBW of the Effelsberg telescope. Hence, the HI column densities derived from the Effelsberg survey have to be considered mean values smeared out over the telescope beam. The much higher column densities determined from our WSRT data are in very good agreement with those typically observed for Galactic HVCs and CHVCs (e.g., Braun & Burton 1999; Brüns et al. 2000; Westmeier et al. 2005b), indicating that the WSRT is able to resolve the internal structure of the HVCs.

From the integrated column density, $N_{\rm HI}^{\rm tot}$, we can directly calculate the HI mass of each cloud via $M_{\rm HI} = m_{\rm H} \, d^2 \tan^2 \varphi \, N_{\rm HI}^{\rm tot}$, where $m_{\rm H}$ is the mass of a hydrogen atom, d is the distance of the cloud, and φ denotes the angular size of a resolution element of the map. Assuming a distance of 780 kpc, the observed HI masses are in the range of a few times $10^4 \, M_\odot$ to $6 \times 10^5 \, M_\odot$. For the isolated clouds in the direction of M 31 we have also listed in Table 3.1 the HI masses derived from the GBT data of Thilker et al. (2004). These values are in good agreement with our WSRT observations, showing that also the diffuse envelopes of warm neutral gas are completely detected with the WSRT. Only for the most extended and diffuse cloud, M 31 HVC 13, we see only about 40% of the total flux detected by the GBT. For those HVCs detected in our Effelsberg survey we have also listed again the respective HI masses. In most cases, the Effelsberg masses agree very well within the expected errors with the corresponding GBT and WSRT masses. In one or two cases we observe slightly larger differences of the order of 20–30% which will have their origin in the observational constraint that the Effelsberg survey is not fully sampled so that somewhat larger uncertainties in the Effelsberg masses are expected.

The diameters of the HVCs were determined by fitting a Gaussian to the radial column density distribution. By dividing the HI mass by the volume defined by the FWHM of this Gaussian, we can estimate a mean HI volume density, $n_{\rm HI}$, for each cloud under the additional assumption of spherical symmetry. The derived densities are typically of the order of a few times $10^{-2}~\rm cm^{-3}$. These volume densities are between two and three orders of magnitude higher than the densities of $10^{-5}\dots 10^{-4}~\rm cm^{-3}$ expected for an extended circumgalactic corona in which the HVCs around the Milky Way and M 31 might be embedded (Sembach et al. 2003; Rasmussen et al. 2003).

The mean radial velocities of the HVCs were calculated from the first moment of the spectra. Most values are more negative than the M 31 systemic velocity of $v_{\rm LSR} \approx -300~{\rm km\,s^{-1}}$. However, this is a selection effect, because most of the HVCs detected around M 31 belong to the filamentary complex of clouds with similar radial velocities near the south-eastern edge of the galaxy. By fitting a Gaussian to the spectral lines we extracted the line widths with typical values in the range of about $20...30~{\rm km\,s^{-1}}$ FWHM at 2' resolution. These values correspond to an upper limit for the kinetic temperature of the gas of the order of $10^4~{\rm K}$. Similar line widths are observed for the Galactic HVCs (e.g., Wakker & van Woerden 1997; Braun & Burton 1999; Westmeier et al. 2005b), and they are typical for the warm neutral medium (Braun 1997). Thilker et al. (2004) already noted that the large line widths of the HVCs discovered in the GBT survey of M 31 require a significant fraction of undetected mass to allow for a purely gravitational stabilisation of the clouds.

Many HVCs also show a relatively complex internal kinematics, with conspicuous radial velocity gradients observed across several of the clouds. We determined the radial velocity gradients across some of the HVCs by fitting a plane P(x,y) = cx + dy + f to the first moment maps $v_{\rm hel}(x,y)$. The χ^2 minimisation provided us with values for the parameters c, d, and f from which we calculated the absolute value $\delta v = \sqrt{c^2 + d^2}$ and the direction $\varphi = 90^{\circ} - \arctan{(d/c)}$ of the velocity gradient. In this definition the position angle, φ , is measured in the usual (east of north) sense. The velocity gradients are listed in Table 3.1 for those clouds where a meaningful fit could be obtained. The method, of course, only provides us with a linear approximation of an average global velocity gradient across each cloud, whereas the observed gradients are not expected to be perfectly linear and, on the

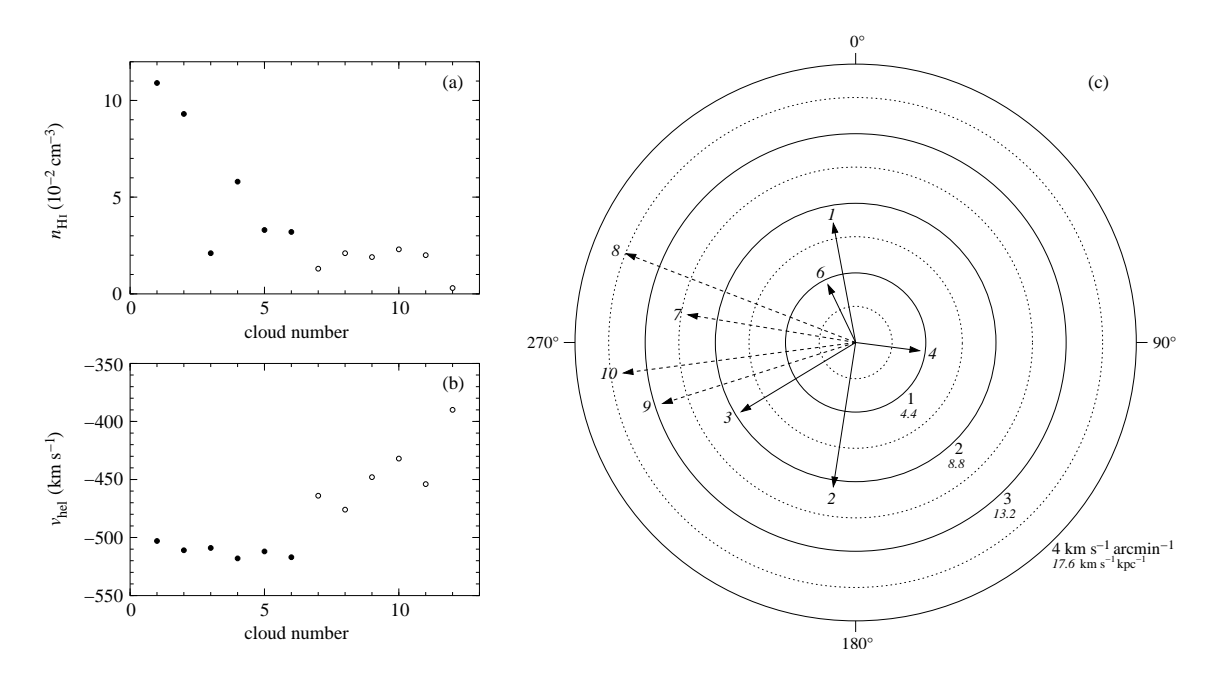


Fig. 3.4: (a) H I volume densities, $n_{\rm H\,I}$, and (b) heliocentric radial velocities, $v_{\rm hel}$, of M 31 HVCs 1–12. M 31 HVCs 1–6 (\bullet) have similar radial velocities, and they are much more condensed with typically higher densities. M 31 HVCs 7–12 (\circ), in contrast, are more diffuse with lower densities and rather different radial velocities. In (c) we have plotted the value of the velocity gradient across some of the clouds (labelled with italic numbers) in km s⁻¹ arcmin⁻¹ (labelled from 1 to 4) against the direction of the gradient in degrees. It turns out that the gradients across M 31 HVCs 1–6 (solid arrows) have arbitrary orientations whereas the typically larger gradients across M 31 HVCs 7–10 (dashed arrows) are all oriented in about the same direction. Note that for M 31 HVCs 5, 11, and 12 we could not obtain a meaningful fit for the velocity gradient.

local scale, will deviate from the average value and direction determined from the planar fits described above.

The ellipticities of the HVCs were obtained by fitting an ellipse to the column density distribution. The parameters of the ellipse were derived from a weighted second moment analysis, following the procedure described by Banks et al. (1995). The ellipse centre was fixed by the first moment of the column density distribution. From the calculation of the second moments we then derived the major and minor axis, a and b, of the ellipse. The ellipticities given in Table 3.1 are defined by e = 1 - (b/a). Only M 31 HVC 12 was so diffuse and extended that a meaningful fit could not be obtained.

3.3.2 Description of individual HVCs

M31 HVC 1

M 31 HVC 1 is located about half a degree south of M 31 HVCs 2–12. This proximity together with similar radial velocities suggests a connection with M 31 HVCs 2–12. M 31 HVC 1 reveals the highest peak column density detected among all clouds in our sample with $N_{\rm H\,I}=1.1\times10^{20}~{\rm cm}^{-2}$ at an angular resolution of 2' FWHM. The corre-

sponding HI mass is $M_{\rm HI} = 5 \times 10^5 \, M_{\odot}$. Maps and profiles of the cloud are presented in Fig. 3.11. At first glance, M 31 HVC 1 has a spherically-symmetric appearance. Furthermore, it shows a systematic radial velocity gradient, measuring about 15 km s⁻¹ in an approximately north-south direction. The high brightness of M 31 HVC 1 allowed us to additionally generate a map with 30" angular resolution which is shown in Fig. 3.20. The high-resolution column density map resolves M 31 HVC 1 into a fairly compact core with a peak column density of more than 2×10^{20} cm⁻² which is embedded in a more diffuse envelope with a conspicuous extension in the northern direction. We also produced a data cube with higher velocity resolution which shows that the spectral lines in the direction of the core have significantly smaller line widths of only about 6 km s⁻¹ FWHM, indicating the presence of cold gas in the core (Fig. 3.7). This morphology suggests that clumps of cold neutral gas are embedded in an envelope of warm neutral gas, resembling the core-envelope structures observed in many Galactic HVCs and CHVCs.

M 31 HVCs 2-12

M 31 HVCs 2–12 form the probably most remarkable structure detected in our survey. They are crowded in an area in the sky of about 1° in size, forming an HVC complex located in projection close to the edge of the H I disk of M 31. An overview of the whole field is shown in Fig. 3.5 while maps and profiles of some individual clouds are presented in Fig. 3.12, 3.13, 3.14, and 3.15. Maps with 30" resolution of some of the HVCs are shown in Fig. 3.20 and 3.21. The individual clouds in this complex of HVCs appear to be arranged in individual filaments intersecting each other at different angles. This filamentary structure is even more conspicuous in the velocity field as clouds along the apparent filaments have very similar radial velocities. At the same time, the radial velocities of the clouds cover a very large range of $-520 \text{ km s}^{-1} \lesssim v_{\text{hel}} \lesssim -390 \text{ km s}^{-1}$, so velocity gradients of up to 130 km s⁻¹ are observed across angular distances of only a few arc minutes. This complex velocity structure is revealed by the position-velocity diagrams in Fig. 3.6.

There also appears to be a morphological distinction between some of the filaments. M 31 HVCs 2–6 (and also M 31 HVC 1 which is presumably associated with the HVC complex) have very similar radial velocities of $v_{\rm hel} \approx -520...-500~{\rm km\,s^{-1}}$. Furthermore, they all show high peak fluxes and mean volume densities as well as being fairly condensed. M 31 HVCs 7–12, in contrast, have significantly different radial velocities of $v_{\rm hel} \approx -480...-390~{\rm km\,s^{-1}}$, and they are more diffuse with typically lower peak fluxes and volume densities. The average H I volume densities and the heliocentric radial velocities of the 12 HVCs are plotted in Fig. 3.4 (a) and (b). A distinction between the two different groups of HVCs in this area can also be made on the basis of the velocity gradients observed across the clouds which are plotted in Fig. 3.4 (c). While the velocity gradients across M 31 HVCs 1–6 have arbitrary orientations, the somewhat larger gradients observed across M 31 HVCs 7–12 appear to be oriented in the same direction.

Two other clouds at the north-western edge of the map have been named M 31 HVC A and B. Both are fairly diffuse with only moderate H I peak column densities and relatively broad spectral lines which distinguishes them from the HVCs discussed before. The radial velocities along the two clouds seem to follow those observed for the H I disk of M 31 which was also covered at the edge of our field of view and which can partly be seen in the upper-right corner of the column density map in Fig. 3.5. The differences with respect

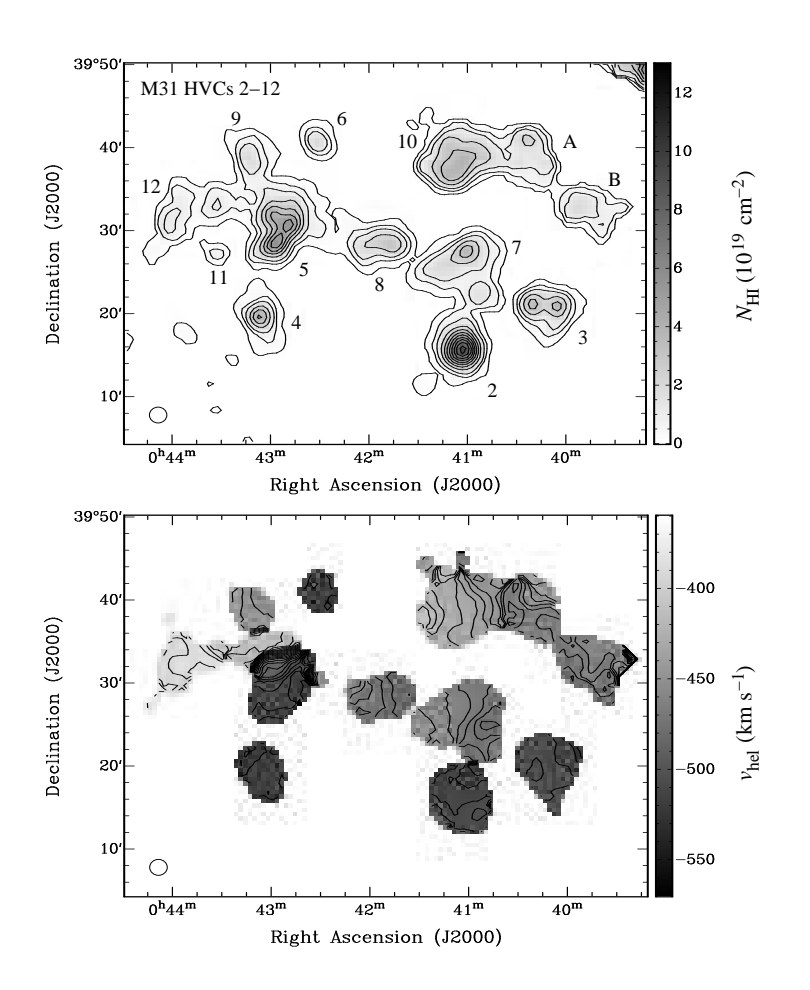


Fig. 3.5: Map of the HI column densities (top) and the heliocentric radial velocities (bottom) of M31 HVCs 2–12. The contours in the upper map are drawn at 1×10^{18} cm⁻², 5×10^{18} cm⁻², and from 1×10^{19} cm⁻² in steps of 1×10^{19} cm⁻². The contours in the lower map are separated by 5 km s^{-1} .

to the other HVCs in this area and the similarities with the disk emission of M 31 suggest that M 31 HVCs A and B might represent gas of an outer disk component of M 31.

M31 HVC 13

M 31 HVC 13 is rather diffuse and extended. It has fairly low column densities and appears to be fragmented into smaller clumps towards the eastern edge. Maps and profiles are shown in Fig. 3.16. M 31 HVC 13 appears in projection against the H I disk of M 31. But its radial velocity is different by about 130 km s⁻¹ from that of the disk gas observed in this direction, so that it is presumably located outside the disk plane of M 31. It lies only about half a degree south of NGC 205, the satellite galaxy of M 31. H I emission from NGC 205 was also detected at the edge of our field of view. Remarkably, the radial velocities of the gas observed in NGC 205 and M 31 HVC 13 cover essentially the same range. Despite the positional and velocity correspondence we do not detect a continuous H I bridge between these two objects at our sensitivity.

M 31 HVCs 14-16

The remaining three HVCs observed near M 31 are all positionally isolated from each other and from the disk of M 31. Maps and profiles are shown in Fig. 3.17, 3.18, and

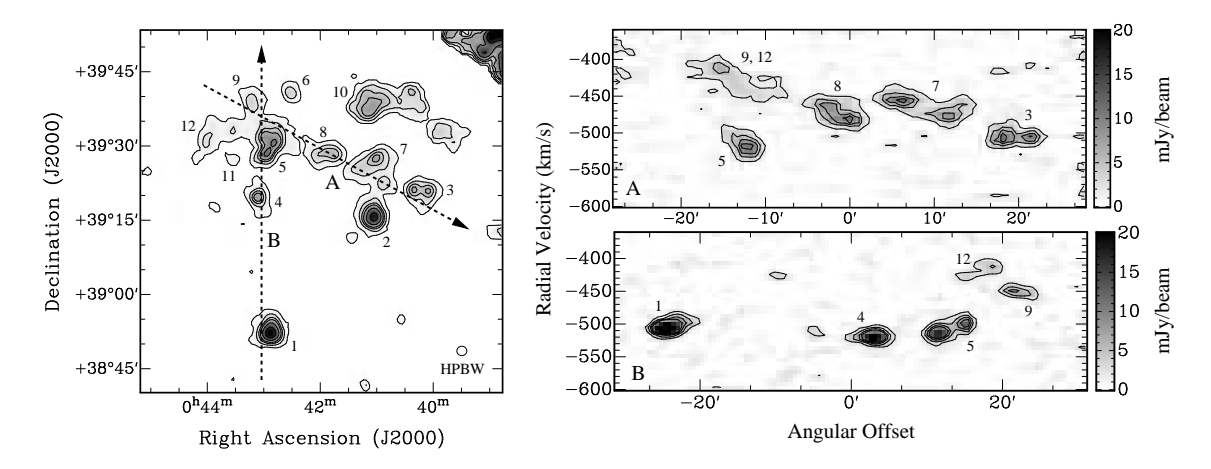


Fig. 3.6: The two panels on the right show position-velocity diagrams along the lines indicated by the two arrows in the column density map on the left. In both cases several HVCs of the complex near the south-eastern edge of M 31 can be seen. The contour levels are 2.5, 5.0, 7.5, and 10.0 mJy beam⁻¹.

3.19. All three clouds clearly deviate from a spherically-symmetric appearance. While M 31 HVC 14 is elongated and slightly bent, M 31 HVCs 15 and 16 exhibit a pronounced head-tail structure. A compact core appears to be embedded in an asymmetric envelope which forms an extended tail in one direction. Head-tail structures like these are also widely observed in the case of Galactic HVCs (Brüns et al. 2000, 2001; Westmeier et al. 2005b). They are suggestive of a distortion of the clouds by the ram pressure of an ambient medium. HVCs 14–16 are probably embedded in the circumgalactic corona of M 31 which could account for the observed morphologies.

3.4 The internal structure of the HVCs

3.4.1 Multi-phase structure

In a few cases the intensities of the HVCs are high enough to allow for the construction of data cubes with higher spectral resolution to search for the cold neutral medium. For the fields in the direction of the HVC complex (M 31 HVCs 1–12) we prepared data cubes with velocity resolutions of 4 and 6 km s⁻¹. Towards some of the brightest clouds in this direction we clearly detect narrow spectral lines suggesting the presence of compact cores of cold or multi-phase cold/warm gas. Two example spectra are shown in Fig. 3.7. Some of the clouds in the direction of the HVC complex have line widths of $\lesssim 12 \ \rm km \, s^{-1}$ FWHM, implying gas temperatures of $\lesssim 3000 \ \rm K$ if a Maxwellian velocity distribution is assumed for the hydrogen atoms. As most of the clouds are barely resolved even in our WSRT observations, beam-smearing effects could dominate the observed line widths. Therefore, the real gas temperatures may be significantly lower than the upper limits derived from the spectral line widths.

Particularly interesting is the case of M 31 HVC 1 where we find a two-component profile towards the centre of the cloud (upper panel of Fig. 3.7). A narrow line compo-

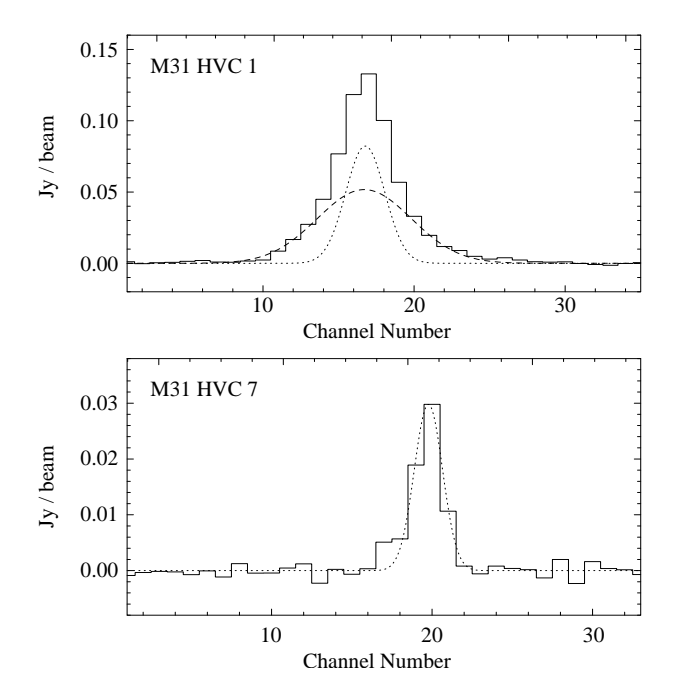


Fig. 3.7: High-resolution H I spectra of M 31 HVC 1 (top) and M 31 HVC 7 (bottom) with 4 and 6 km s⁻¹ velocity resolution, respectively. The results of Gaussian fits are plotted as dashed and dotted lines. M 31 HVC 1 shows a clear multi-phase profile with a narrow component (dotted line, 6.3 km s⁻¹ FWHM) superposed on a broad component (dashed line, 15.1 km s⁻¹ FWHM). The spectral line of M 31 HVC 7, with a FWHM of 12.8 km s⁻¹, is barely resolved and indicates that cold gas is probably also present in this cloud.

nent of cold neutral gas is superposed on a broad component of warm neutral gas. This configuration suggests that a compact core of either cold or multi-phase gas is embedded in a warm envelope, although the core is spatially and kinematically unresolved. For the cold component we derive a line width of 6.3 km s⁻¹ FWHM, implying an upper limit for the gas temperature of about 900 K. In contrast, the warm component shows a line width of 15.1 km s⁻¹ FWHM, corresponding to an upper temperature limit of 5000 K. Twocomponent line profiles are widely observed in the case of Galactic HVCs and CHVCs (e.g., Wolfire et al. 1995; Burton et al. 2001; Westmeier et al. 2005b), indicating that cold or multi-phase cold/warm neutral cores are common. As noted before, the multiphase structure of HVCs and CHVCs can also be reproduced by the hydrostatic simulations of Sternberg et al. (2002) under the assumption that the clouds are additionally stabilised by the pressure of an external medium. With our high-resolution WSRT observations we are now able to demonstrate that the HVCs around M 31 have an internal structure which is very similar to that of the HVCs around the Milky Way. The multi-phase medium found in M 31 HVC 1 provides additional evidence for the assumption that the HVC population of M 31 is embedded in a hot circumgalactic corona which would also explain the head-tail morphologies observed in a few cases.

3.4.2 Dynamical masses

Three clouds, M 31 HVCs 1, 2, and 6, have a spherical appearance combined with a pronounced gradient in radial velocity. Two more clouds, M 31 HVCs 8 and 10, have a pronounced, linear velocity gradient, although they appear slightly elliptical. If we assume these velocity gradients to be caused by a rotation of the clouds we can try to estimate their dynamical masses

$$M_{\rm dyn} = \frac{R v_{\rm rot}^2}{G} \tag{3.1}$$

Table 3.2: Parameters for the determination of the dynamical masses of M 31 HVCs 1, 2, 6, 8, and 10. δv is the observed radial velocity gradient across the angular extent, ϑ , of each cloud as extracted from the one-dimensional cuts in Fig. 3.11, 3.12, and 3.15 and from the map in Fig. 3.5. $M_{\rm dyn}$ denotes the lower limit for the derived dynamical mass, and $M_{\rm H\,I}$ is the HI mass as listed in Table 3.1.

Object	δv	ϑ	$M_{ m dyn}$	$M_{ m HI}$	$M_{ m HI}/M_{ m dyn}$
	$(\mathrm{km}\mathrm{s}^{-1})$	(arcsec)	$(10^5 \ M_{\odot})$	$(10^5~M_{\odot})$	•
M 31 HVC 1	14	400	>86	5.2	<6%
$M31~\mathrm{HVC}~2$	10	400	> 44	5.0	< 11%
$M31~\mathrm{HVC}~6$	13	100	> 19	0.6	< 3%
$M31~\mathrm{HVC}~8$	35	540	> 730	2.1	< 0.3%
$M31~\mathrm{HVC}~10$	37	540	> 810	5.0	< 0.6%

where R is the radius of the cloud, $v_{\rm rot}$ is the rotation velocity at the edge, and G denotes the gravitational constant. The velocity gradients, δv , over the angular extent, ϑ , were estimated from the one-dimensional cuts across the clouds. The corresponding values are summarised in Table 3.2 together with the calculated dynamical masses and HI masses. Because of the unknown inclination angle, i, of the clouds the observed velocity gradient, δv , only gives us a lower limit of the rotation velocity with $v_{\rm rot} = \delta v/(2\cos i)$. Nonetheless, the obtained lower limits for the dynamical masses of the five clouds are already by one or two orders of magnitude higher than the observed HI masses. If the assumption of rotation is correct we are seeing only a small fraction of the clouds' masses in neutral atomic hydrogen. Additional mass components, such as ionised gas or dark matter, would be required in this case to account for the observed velocity gradients.

On the other hand, the observed velocity gradients could also be the result of turbulent processes in the course of an interaction between the clouds and M 31. In this case, the HVCs would probably not be gravitationally bound entities but transient phenomena caused by tidal and ram-pressure forces. As a consequence, the determined dynamical masses would become meaningless. With our current data a distinction between these two options is not possible. In Section 3.5.1 we will see, however, that M 31 HVCs 1–12 are most likely the result of a tidal interaction in connection with the giant stellar stream (Ibata et al. 2001a) of M 31, suggesting that turbulent processes could have contributed to the complex velocity structure of M 31 HVCs 1–12.

3.4.3 Virial masses

A similar result can be derived by applying the virial theorem, assuming spherical symmetry and, for simplicity, a constant mass density. We can justify the assumption of virialisation by making a simple estimate of the dynamical timescales of the clouds. If we consider the mean diameter of the HVCs to be $D \approx 1$ kpc and the mean FWHM of the spectral lines to be $\Delta v \approx 25 \text{ km s}^{-1}$ we obtain an estimate for the dynamical timescale of $\tau_{\rm dyn} = D/\Delta v \approx 4 \times 10^7$ a. This timescale is short compared with the expected orbital timescales of the HVCs relative to M 31, about 10^9 a, over which changing tidal

forces might be active. Thus, we can assume that the HVCs are at least close to internal dynamical equilibrium so that we can apply the virial theorem which, in our case, reads

$$\frac{\Delta v^2}{8 \ln 2} = \frac{GM_{\text{vir}}}{5R} \,. \tag{3.2}$$

Here, $M_{\rm vir}$ is the virial mass of the cloud, R is the cloud radius, G denotes the gravitational constant, and Δv is the FWHM of the H I lines. Solving Eq. 3.2 for the virial mass and inserting the parameters given in Table 3.1 yields virial masses of the order of a few times $10^7 M_{\odot}$ for the most condensed clouds in our sample. The calculated virial masses lead to a typical mass fraction of neutral hydrogen of less than 1%. Although these are small values, we have to consider that the observed line widths are probably only upper limits for the velocity dispersion of the gas since internal kinematics or turbulence can result in an additional broadening of the spectral lines. Furthermore, stabilisation of the clouds can also be provided by the pressure of the ambient medium. As discussed in detail in Section 2.4.1, a pressure of the order of $P/k = 100 \text{ K cm}^{-3}$ is sufficient to stabilise the HVCs around M 31 without any additional mass components (see Eq. 2.8).

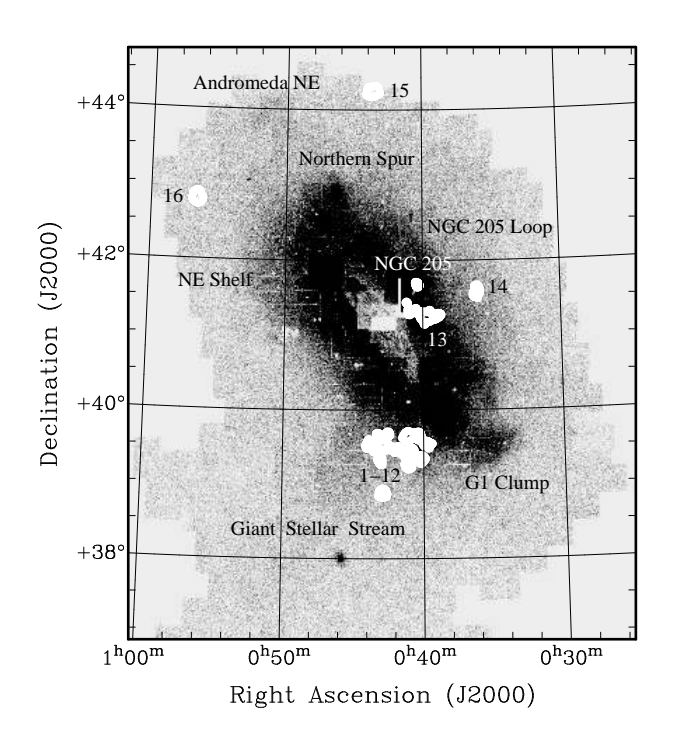
It should also be stressed that the application of the virial theorem to HI clouds is open to justified criticism. Not only does the calculation of virial masses depend upon a number of assumptions with respect to the object symmetry, but the simple form of Eq. 3.2 also demands a homogeneous population of particles with identical masses. It is doubtful that the velocity dispersion of the HI component alone would provide a realistic estimate of the total mass of HVCs. Moreover, the calculation of dynamical masses according to Eq. 3.1 is in conflict with the virial theorem in the form of Eq. 3.2. The virial theorem requires random motions of the particles instead of a regular rotation of the cloud. Either the dynamical mass or the virial mass of a particular cloud can be correct but not both at the same time. By calculating virial masses, we can only expect to assess the order of magnitude of the entire mass of a cloud which, in our case, seems to confirm the necessity of a large amount of additional mass, such as ionised gas or dark matter, to stabilise the HVCs observed in our survey.

3.5 The origin of the HVCs

3.5.1 Evidence for tidal interaction

One of the most remarkable structures detected in our WSRT observations is the filamentary complex of HVCs near the south-eastern edge of the HI disk of M31, consisting of M31 HVCs 1–12. This complex was already detected in our Effelsberg survey and in the GBT survey of Thilker et al. (2004) as an outstanding region of extra-planar gas. What could the origin of this remarkable structure be? Thilker et al. (2004) already noticed that the HVC complex is partly overlapping with the giant stellar stream of M31 discovered by Ibata et al. (2001a), suggesting that both could be connected. The situation is shown in Fig. 3.8 where the greyscale image represents the distribution of red giant branch (RGB) stars in a large field around M31 as published by Ferguson et al. (2006). The outer disk of M31 shows a lot of substructure reaching out to projected distances of tens of kpc. The giant stellar stream stands out against the diffuse stellar background as a conspicuous overdensity of RBG stars in the south-eastern quadrant of the map. The

Fig. 3.8: The map shows the distribution of red giant branch stars in a large field around M31, based on the Keck/Deimos survey data presented by Ferguson et al. (2006). The white areas show the locations of the HVCs (labelled with numbers) and of NGC 205 on the basis of our WSRT HI data. The giant stellar stream can be seen as the conspicuous overdensity of stars in the south-eastern part of the map. M 31 HVCs 1–12 partly overlap with the southern edge of the stream and with the extended stellar disk of M31. The remaining HVCs do not appear to coincide with any known structure or satellite galaxy of M31 except for M 31 HVC 13 which is located near NGC 205.



HVCs detected with the WSRT are plotted as white areas. Obviously, the positions of M 31 HVCs 1–12 are overlapping with parts of the stream close to the disk of M 31. This remarkable positional correlation suggests that the H I gas is associated with the stellar stream.

Additional evidence comes from the kinematics of the stream. Ferguson et al. (2006) present the results of radial velocity measurements of the stellar component at four positions along the stream. The heliocentric radial velocities range from $-550~{\rm km\,s^{-1}}$ close to the disk of M 31 up to $-325~{\rm km\,s^{-1}}$ about 4° away from the disk. In the region of the H I gas, the radial velocities of the stellar component are of the order of $-500~{\rm km\,s^{-1}}$ which is in excellent agreement with the velocities found for some of the HVCs in this region. On the other hand, the velocity structure of the HVC complex is very complicated. Several filaments of clouds with different radial velocities appear to intersect each other at various angles, making a direct comparison with the velocities of the stellar stream challenging. Furthermore, the gas is subject to ram-pressure interaction whereas the stars in the stream can be considered collisionless, so that the velocities of stars and gas could be different even if both had the same origin. Nonetheless, our results suggest that the HVC complex detected near the south-eastern edge of M 31 is the gaseous counterpart of the giant stellar stream and of tidal origin.

In addition to having a degree of organization into filamentary structures, it is striking that many of the HI clouds of the HVC complex, particularly HVCs 2–6 seen in Fig. 3.5, have large internal velocity gradients which are typically not directed along the filaments. This circumstance suggests that even within this region of likely overall tidal origin, there may well be dynamical effects related to localised dark matter concentrations.

Another example of a cloud that is likely of tidal origin is M 31 HVC 13 which is located about half a degree south of NGC 205 and covers the same radial velocities as the gas observed towards this satellite galaxy of M 31. A possible tidal interaction between

NGC 205 and M 31 was already suggested by Zwicky (1959), based on the discovery of extended, faint arms emanating from both ends of NGC 205. Recently, McConnachie et al. (2004) reported the discovery of an arc-like structure in the distribution of blue RGB stars north of NGC 205 which may be part of a stellar stream originating from the tidal interaction with M 31. In a colour-magnitude diagram the red giant branch of the arc is noticeably bluer than that of the M 31 disk component but very similar to the red giant branch of NGC 205. Based on this similarity in colour, McConnachie et al. (2004) concluded that the arc is composed of stars originating from NGC 205. Unfortunately, M 31 HVC 13 is located on the opposite side of NGC 205 with respect to this presumable tidal trail. The expected stellar arm on this side of NGC 205, however, cannot be detected due to confusion with stars in the disk of M 31. Furthermore, our current sensitivity has not permitted detection of a continuous H I bridge between NGC 205 and M 31 HVC 13, so a physical association remains circumstantial.

Our results indicate that tidal interaction could have played a significant role in forming several of the HVCs detected near M 31. This interpretation can also explain why most of the HVCs are found very close to the disk of M 31 where tidal forces are expected to be strongest.

3.5.2 Evidence for dark-matter-dominated clouds

Due to the known distance of M 31 our observations allowed us to determine the important distance-dependent physical parameters of the HVCs around M 31 which are essentially unknown for the HVCs and CHVCs of the Milky Way. With their masses and sizes, the HVCs observed around M 31 are remarkably similar to the HVCs considered by Sternberg et al. (2002) in their hydrostatic simulations. For their circumgalactic model, Sternberg et al. (2002) assumed spherical, pressure-confined, dark-matter-dominated clouds at typical distances from the Galaxy of the order of 150 kpc. The original aim of the simulations was to explain the population of CHVCs as defined by Braun & Burton (1999) and to understand their observational parameters as determined by Braun & Burton (2000) and Burton et al. (2001). For the circumgalactic case, Sternberg et al. (2002) predict typical HI masses of $3 \times 10^5 M_{\odot}$ and a radial scale length of the HI column density distribution of 0.5 kpc. The typical peak HI column density of their model clouds is 5×10^{19} cm⁻². A comparison with the HVC properties listed in Table 3.1 reveals that these parameters are in excellent agreement with those found for the population of HVCs covered by our WSRT observations.

The HVCs modelled by Sternberg et al. (2002) are gravitationally dominated by a dark-matter halo for which a Burkert profile (Burkert 1995) was assumed. For the circumgalactic case, Sternberg et al. (2002) assumed a virial mass of the halo of the order of $10^8~M_{\odot}$. This implies a virial-to-H I mass ratio of the order of $\alpha=300$, which corresponds to a very small neutral gas fraction of only 0.3%. Despite the substantial dark matter content, the halo would not be massive enough to retain the warm gas. Therefore, the clouds have to be additionally stabilised by the pressure of an external medium with at least $P/k \approx 50~{\rm K~cm^{-3}}$. As discussed earlier in Section 2.4.1, the expected circumgalactic hot ionised corona could provide the required external pressure stabilisation. In this case, the central gas density of the modelled HVCs would be $N_{\rm H} \approx 2 \times 10^{-2}~{\rm cm^{-3}}$ which is

again in excellent agreement with the observed mean neutral gas densities of the HVCs around M 31 as listed in Table 3.1.

This remarkable agreement between the hydrostatic simulations of dark-matter-dominated HVCs by Sternberg et al. (2002) and the observed parameters of the HVCs detected in our WSRT observations suggests that some of the clouds could indeed be primordial, dark-matter-dominated clouds as originally assumed by Blitz et al. (1999) and Braun & Burton (1999). This could particularly be true for M 31 HVCs 15 and 16, which are completely isolated from all other HVCs and from M 31 and any of its known satellite galaxies. The required pressure confinement by the corona of M 31 could also explain the head-tail morphologies observed for these two clouds. As the clouds are moving with high velocities through their environment their outer parts will be distorted and stripped by the ram-pressure of the ambient medium (see, e.g., Quilis & Moore 2001; Konz et al. 2002).

One problem in connection with the primordial dark-matter halo hypothesis is the spatial extent of the HVC population. From simulations we would expect the HVCs to be spread out to distances of about 300 kpc from M 31 (see the detailed discussion in Section 2.5.3). The observed HVCs, however, have projected distances from M 31 of not more than 50 kpc. The simulations of Sternberg et al. (2002) now allow us to find a plausible explanation for this discrepancy. At larger distances from M 31 the density of the circumgalactic environment is expected to decrease. At some distance, the density will drop below the value of about 50 K cm⁻³ which is required in addition to the gravitational potential to retain the warm gas of the HVCs. This has two consequences: First, the clouds would not be stable any more because the gas would no longer be bound. Second, the gas density would be too low to provide sufficient shielding against the ionising intergalactic radiation field. Consequently, the gas would be mainly ionised and no longer detectable in the 21-cm emission of neutral hydrogen.

Another problem is the relatively small number of HVCs detected around M 31. Structure formation simulations on the basis of CDM cosmology predict hundreds of darkmatter satellites around Galaxy-sized halos (e.g., Klypin et al. 1999; Moore et al. 1999), whereas only 15–20 individual HVCs have been found around M 31. This problem was already discussed in detail in Section 2.5.3 in connection with the HVCs detected in our Effelsberg HI survey. Recent numerical simulations by Kravtsov et al. (2004) confirmed the significant overabundance of dwarf-like dark-matter halos in the models in comparison to the relatively small number of observed dwarf galaxies around the Milky Way. They also included a simple model of star formation in dark-matter halos which, for the first time, can reproduce both the circular velocity function as well as the radial distribution of dwarf galaxies around the Milky Way. For the central 50 kpc around M 31, the model of Kravtsov et al. (2004) predicts only 2-5 dark-matter halos with associated gas masses, $M_{\rm g}>10^6~M_{\odot}$, that have not undergone significant internal star formation. They concur with our conclusion that only a subset of the HVCs found near M 31 might represent primordial dark-matter halos while the remaining clouds might be the result of tidal interaction.

Obviously, the dark-matter mini-halo model for HVCs by Sternberg et al. (2002) provides a plausible explanation for some of the HVCs near M 31, in particular M 31 HVCs 14–16 which are all isolated in position-velocity space from both the stellar stream and any known dwarf companion of M 31. Tidal interaction during their evolution as well as instability and ionisation at larger distances from M 31 can also explain the small number

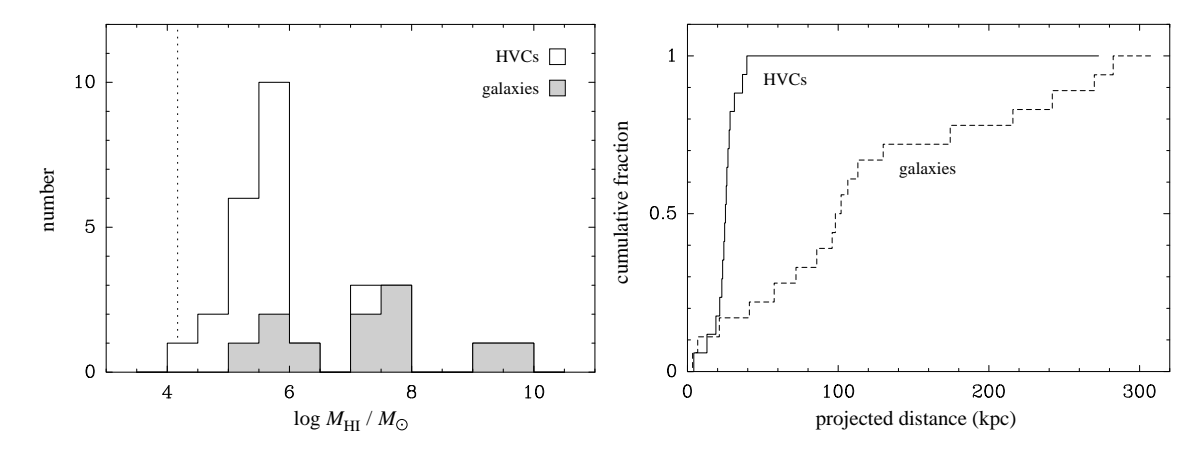


Fig. 3.9: Comparison of the HVCs detected around M 31 in our WSRT observations with the satellite galaxies of the M 31 group. Left: Histogram of the H I masses of HVCs (white, including Davies' Cloud) and satellite galaxies (grey, including M 31) based on Tables 3.1 and 2.3, respectively. The vertical line indicates our 5σ detection limit. Right: Cumulative fraction of HVCs (solid line) and satellite galaxies (dashed line) as a function of projected distance from the centre of M 31. Only satellites within a projected radius of 300 kpc around M 31 have been considered for the diagram.

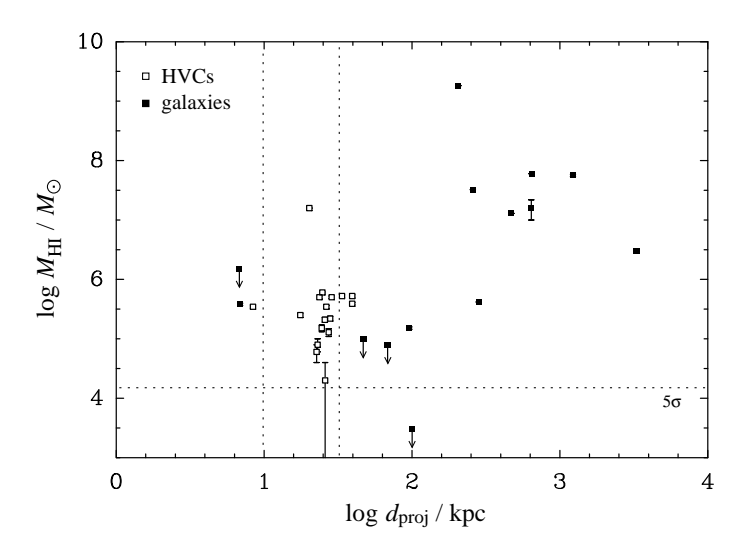
of HVCs and their proximity to M 31. If the mini-halo hypothesis is true, HVCs would be sensitive test particles to probe the physical conditions in the circumgalactic environment of large spiral galaxies.

3.5.3 Comparison with the satellite galaxies of M 31

Following the discussion in Section 2.5.2, we can again compare the radial distribution and the HI mass spectrum of the HVCs detected in our WSRT observations with the satellite galaxies of the M31 group. Given the lack of dynamical studies and three-dimensional HVC distances, only HI masses and projected distances can be compared. The left panel of Fig. 3.9 shows the histogram of HI masses of the 16 HVCs detected with the WSRT and of Davies' Cloud in comparison with the HI masses of the satellite galaxies of M31 (inlcuding M31 itself) according to Table 2.3. For the HVC masses we again assume a constant distance of 780 kpc (Stanek & Garnavich 1998). The mass distribution is similar to the one in Fig. 2.25 which is based on the Effelsberg HI survey. Due to the somewhat better mass sensitivity the histogram is slightly stretched towards the lower-mass end, although all clouds with $M_{\rm HI} < 10^5~M_{\odot}$ are part of the extended complex of HVCs near the south-eastern edge of M31.

In the right panel of Fig. 3.9 the cumulative fraction of HVCs and satellite galaxies is plotted as a function of projected distance. The HVCs again include Davies' Cloud, and only those satellite galaxies within a projected radius of 300 kpc around M 31 have been considered as they are roughly located within the virial radius of M 31 (e.g., Kravtsov et al. 2004). The distribution is very similar to that of the HVCs in our Effelsberg survey in Fig. 2.25. Again, it is obvious that HVCs and satellite galaxies have a completely different radial distribution. All HVCs are found within a projected radius of 40 kpc, whereas

Fig. 3.10: HI mass versus projected distance of HVCs (open squares, including Davies' Cloud) and satellite galaxies (filled squares) around M31. The horizonal line indicates our 5σ detection limit. The two vertical lines mark the outer edge of the M 31 H I disk along the minor and major axis. Although both groups tend to populate different regions of the diagram, it is important to note that for only a fraction of the M31 satellites HI studies are available.



the satellite galaxies of M 31 are equally spread across the entire range of distances out to 300 kpc. The relatively steep rise of the HVC distribution due to the HVC complex near the M 31 disk is even more prominent, as 12 of the detected HVCs are part of this complex. Consequently, the Kolmogorov-Smirnov test yields an even lower probability of only 3×10^{-6} (corresponding to D = 0.83) that HVCs and satellite galaxies are drawn from the same distribution.

In Fig. 3.10 the logarithm of the HI mass, $M_{\rm HI}$, of HVCs (open squares, including Davies' Cloud) and satellite galaxies (filled squares) is plotted versus the logarithm of the projected distance, $d_{\rm proj}$. The differences between HVCs and satellite galaxies are again obvious. The HVCs are concentrated in the lower left part of the diagram with lower HI masses and smaller projected distances, whereas the galaxies tend to concentrate in the upper right region of the diagram with typically higher HI masses and larger distances.

With our discussion in the previous paragraphs the observed discrepancy in the radial distribution of HVCs and satellite galaxies, as plotted in Fig. 3.10, can now be explained. On the one hand, some of the HVCs around M31 are most likely the result of tidal interactions, naturally explaining their smaller galactocentric distances compared to the population of satellite galaxies. Other HVCs are promising candidates for dark-matter halos. According to the hydrostatic simulations of Sternberg et al. (2002), however, even dark-matter-dominated HVCs have to pressure-confined in addition to their gravitational potential in order to retain their neutral gas. At some distance from M31 the density of the circumgalactic corona will drop below the critical value required to stabilise HVCs, resulting in small galactocentric distances of the HVC population compared to the population of satellite galaxies.

We can also understand that the HI masses of the galaxies tend to be higher than those of the HVCs. The more gas a dark-matter satellite contains, the more likely will it exceed the star formation threshold of $\Sigma > 5~M_{\odot}~{\rm pc}^{-2}$ (see, e.g., Kennicutt 1998), where Σ denotes the surface mass density of the gas. Therefore, only the most massive halos are expected to form stars, whereas low-mass halos will appear as HVCs if they can retain their neutral gas. This is investigated in more detail by the numerical simulations of Kravtsov et al. (2004) which also account for star formation in dark-matter halos. With

their simulations they can reproduce both the observed circular velocity function as well as the radial distribution of dwarf galaxies around the Milky Way.

3.6 Summary and conclusions

With a HPBW of 9', corresponding to a spatial resolution of 2 kpc at the distance of M 31, both the Effelsberg telescope and the GBT were not able to resolve most of the HVCs found near M 31. To study the internal structure and origin of the HVCs, high-resolution H I synthesis observations are therefore inevitable. Consequently, we observed nine fields centred on the most conspicuous HVCs around M 31 with the Westerbork Synthesis Radio Telescope. Our final data cubes have an H I mass detection limit of the order of $10^4~M_{\odot}$ and a resolution of 2' FWHM, corresponding to a spatial resolution of 450 pc. In total, we detect 16 individual HVCs with typical H I masses of a few times $10^5~M_{\odot}$ and sizes of the order of 1 kpc.

The most remarkable structure detected in our observations is the complex of 12 HVCs near the south-eastern edge of the neutral gas disk of M 31. The clouds in this complex appear to be arranged in various filaments intersecting each other. The filamentary structure is particularly prominent in the velocity map where clouds along individual filaments have very similar radial velocities. At the same time, the complex overlaps with the giant stellar stream of M 31 in both position and velocity. This overlap in connection with the filamentary structure suggests that the HVC complex is of tidal origin and represents the gaseous equivalent of the giant stellar stream. Another potential tidal structure is M 31 HVC 13 which is located only half a degree south of NGC 205. Again, the radial velocities are similar to those of the gas in NGC 205, suggesting a tidal origin of the high-velocity gas. However, within the sensitivity of our data we did not detect any gas bridge connecting NGC 205 and M 31 HVC 13.

The remaining three HVCs are isolated from the stream and any known satellite galaxy of M 31. They are the most promising candidates for the primordial dark-matter-dominated satellites predicted by structure formation scenarios based on CDM cosmological models. A comparison with the hydrostatic models of Sternberg et al. (2002) reveals that the H I masses, sizes, and peak column densities predicted by their circumgalactic model are in excellent agreement with the typical parameters of the HVCs observed around M 31. The HVCs modelled by Sternberg et al. (2002) are gravitationally dominated by a dark-matter halo with a virial mass of $M_{\rm vir} \simeq 10^8~M_{\odot}$ and additionally stabilised by an external pressure of $P/k \gtrsim 50~{\rm K\,cm^{-3}}$. The hot circumgalactic corona can provide this pressure and account for the morphological distortions observed in M 31 HVCs 14–16.

Two problems are connected with this interpretation. First, the total number of HVCs around M 31 is by far smaller than the number of expected dark-matter mini-halos (Klypin et al. 1999; Moore et al. 1999). Second, all HVCs were found within a projected distance of 50 kpc from M 31 whereas structure formation scenarios predict much larger distances of up to 300 kpc. The small number of clouds can be explained by Kravtsov et al. (2004) who simulated a Galaxy-sized dark-matter halo. They found that only a small fraction of dark-matter satellites were able to retain their gas during their evolution. Most of the halos lost their gas in tidal interactions with other satellites. The number of clouds predicted by the simulations of Kravtsov et al. (2004) within 50 kpc of M 31 is in good

agreement with the observed number of clouds if we assume that the model is realistic and that some of the detected HVCs are not primordial but of tidal origin. The fact that we do not find any additional HVCs beyond 50 kpc can be explained by the model of Sternberg et al. (2002). At larger distances from M 31 the density of the circumgalactic environment will drop below the critical value required to stabilise the clouds. As a result, the gas cannot be retained any more and, in addition, will be ionised by the extragalactic radiation field.

Obviously, our observations provide us with a consistent picture in which different mechanisms have contributed to the observed population of HVCs. Some of the clouds are most likely of tidal origin in connection with the stellar stream and NGC 205. The remaining three HVCs are promising candidates for dark-matter-dominated satellites. Our results are in remarkable agreement with the simulations of Sternberg et al. (2002) and Kravtsov et al. (2004).

The next logical step in the study of the HVC population around M 31, and of HVCs in general, will be a critical test of the scenario developed above. An important tool is the determination of metal abundances through absorption spectroscopy of suitable background objects such as stars or distant quasars. This would allow us to determine whether the gas could be of primordial origin or has been processed in the Milky Way and M 31 or in one of their satellite galaxies. Due to the large angular diameters of many HVCs around the Galaxy a sufficiently large number of background quasars or AGN are available for absorption spectroscopy. The resulting metallicity measurements, as summarised in Section 1.3.3, indicate that the large HVC complexes—with the exception of complex M—have metal abundances of the order of 10% of the corresponding solar values, demonstrating that the gas must have been processed. Previous studies have focussed on the large HVC complexes with high HI column densities. However, to get a better overview of the distribution of column densities and metal abundances of highvelocity gas in the Galactic halo, a more systematic study of a large number of random sight lines through the halo will be necessary. The first results of such a systematic study of the neutral gas distribution in the halo will be presented and discussed in the following chapter.

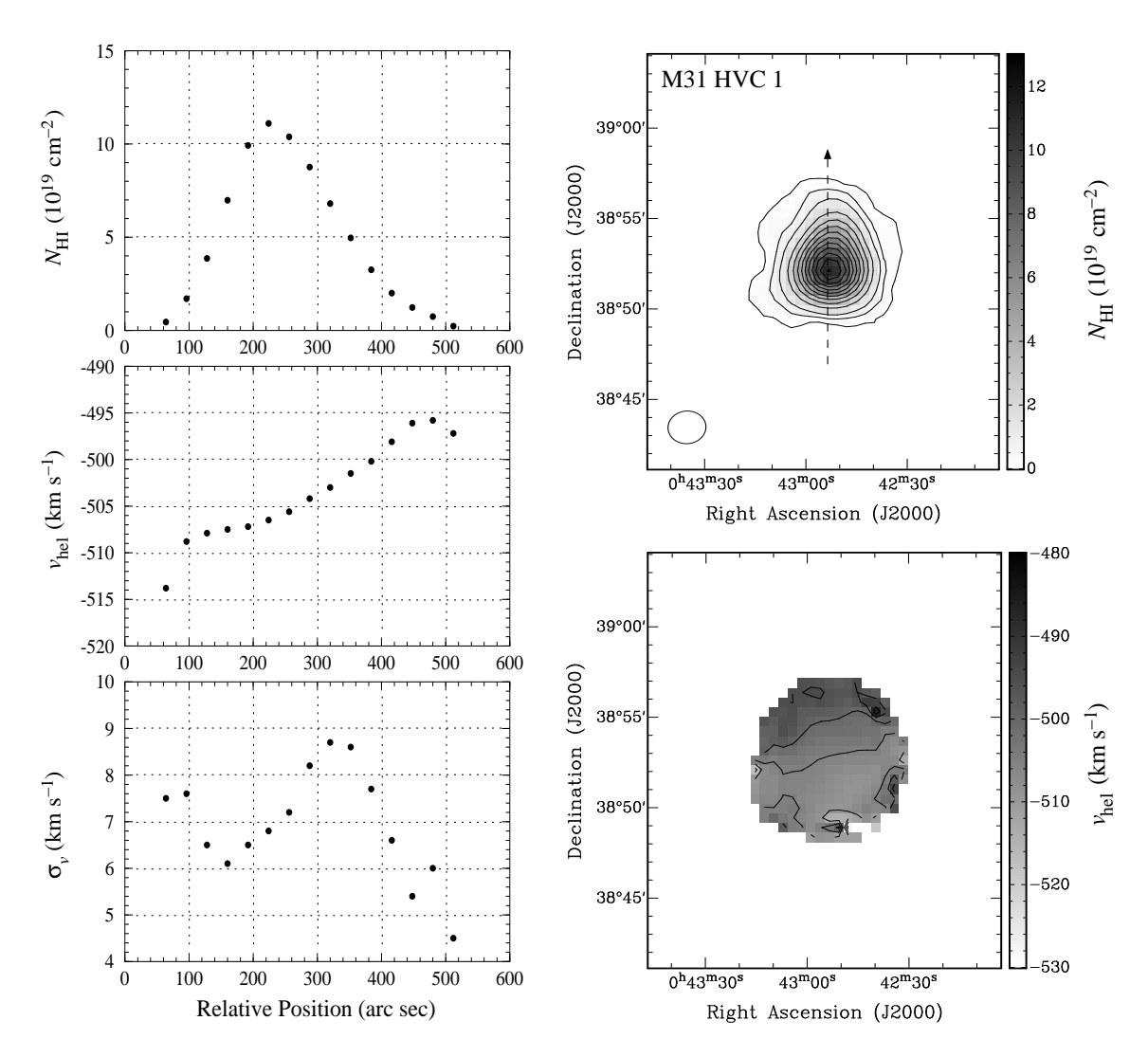


Fig. 3.11: M 31 HVC 1. The upper right map displays the HI column density. The contours are drawn at 1×10^{18} cm⁻², 5×10^{18} cm⁻², and from 1×10^{19} cm⁻² in steps of 1×10^{19} cm⁻². The lower right map shows the heliocentric radial velocity. The contours are separated by 5 km s⁻¹. The diagrams on the left hand side show from top to bottom: the HI column density, the heliocentric radial velocity, and the velocity dispersion of the gas along the cut marked by the arrow in the column density map.

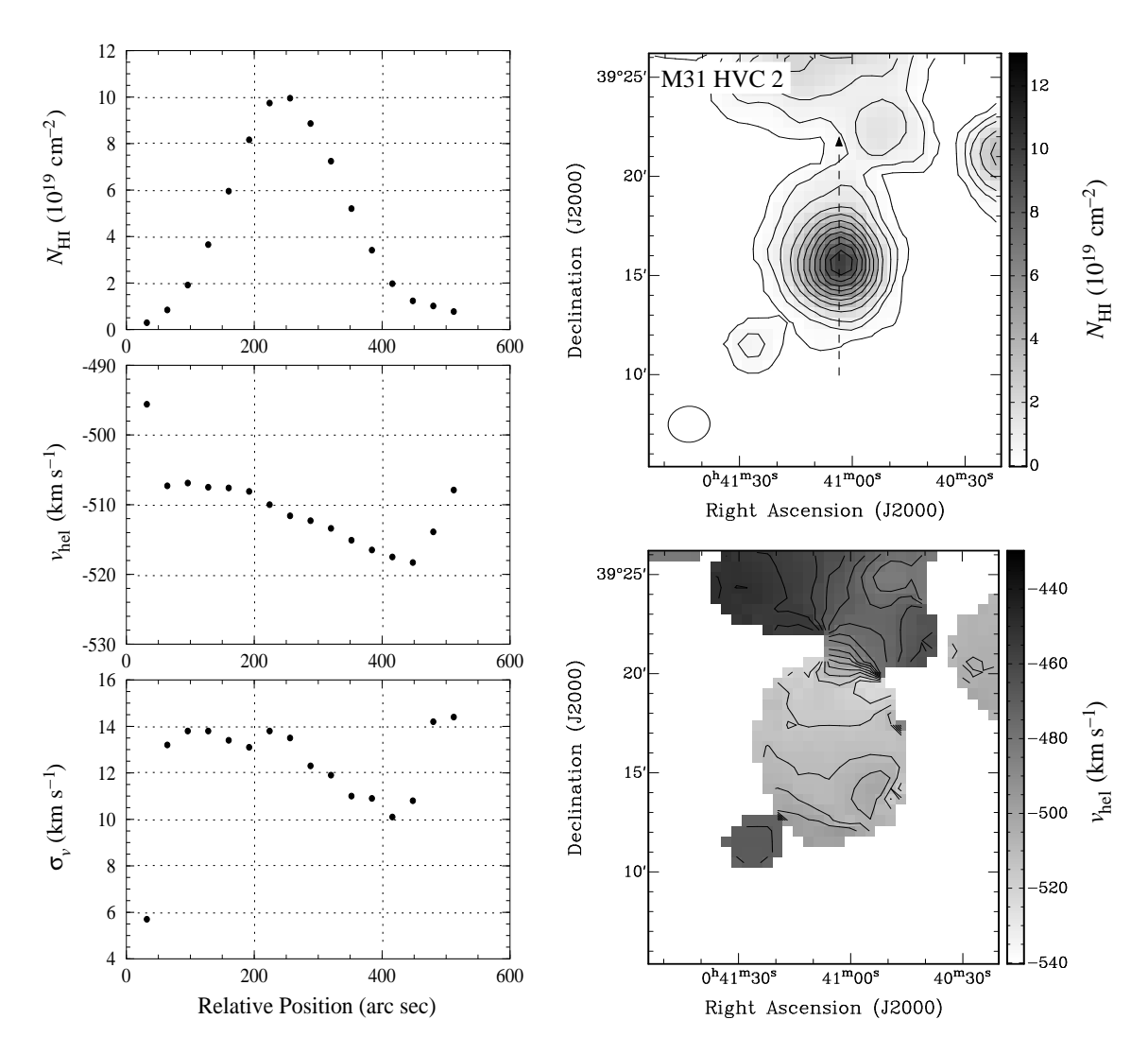


Fig. 3.12: M 31 HVC 2. The upper right map displays the HI column density. The contours are drawn at 1×10^{18} cm⁻², 5×10^{18} cm⁻², and from 1×10^{19} cm⁻² in steps of 1×10^{19} cm⁻². The lower right map shows the heliocentric radial velocity. The contours are separated by 5 km s⁻¹. The diagrams on the left hand side show from top to bottom: the HI column density, the heliocentric radial velocity, and the velocity dispersion of the gas along the cut marked by the arrow in the column density map.

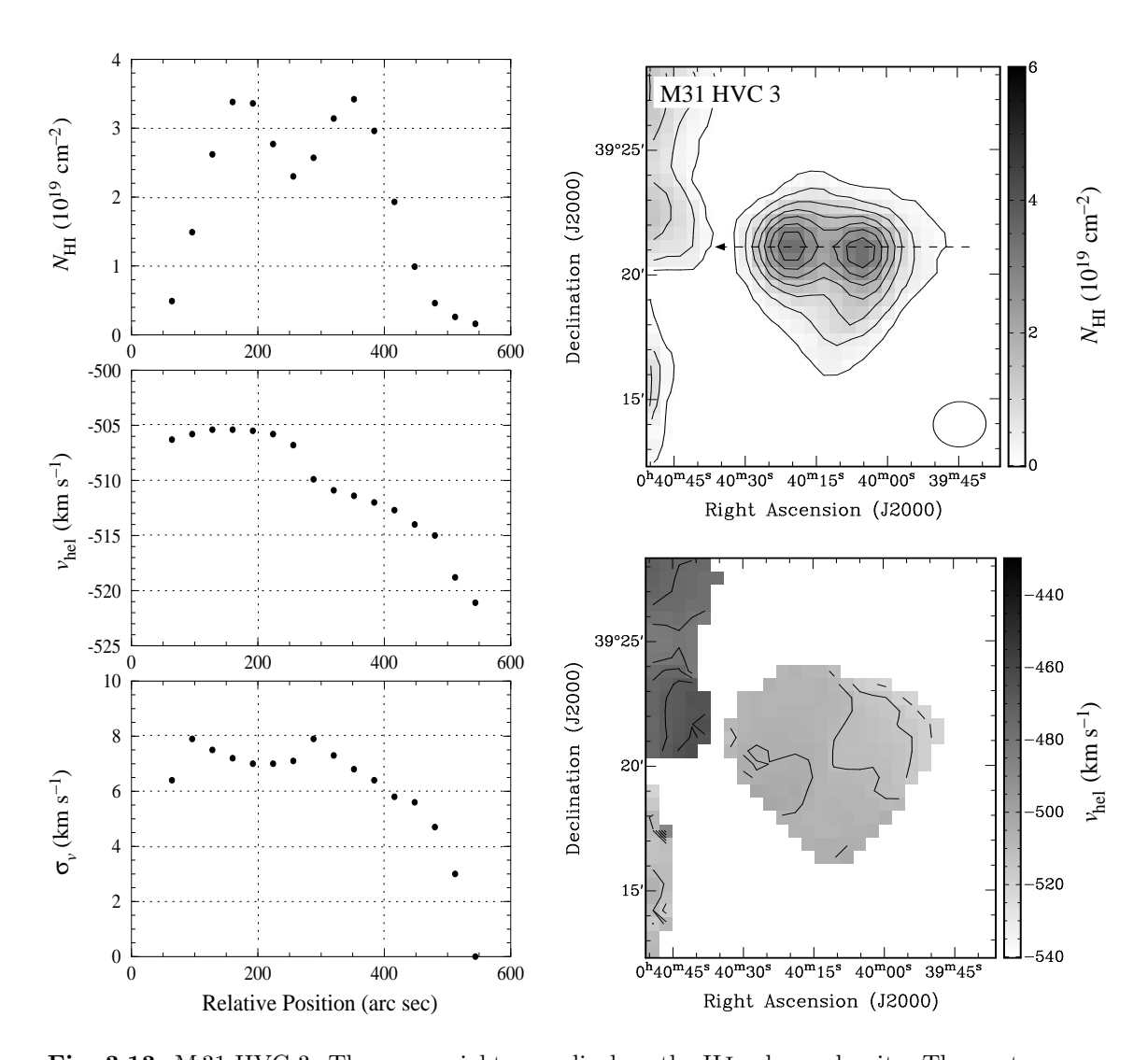


Fig. 3.13: M 31 HVC 3. The upper right map displays the H I column density. The contours are drawn at 1×10^{18} cm⁻² and from 5×10^{18} cm⁻² in steps of 5×10^{18} cm⁻². The lower right map shows the heliocentric radial velocity. The contours are separated by 5 km s^{-1} . The diagrams on the left hand side show from top to bottom: the H I column density, the heliocentric radial velocity, and the velocity dispersion of the gas along the cut marked by the arrow in the column density map.

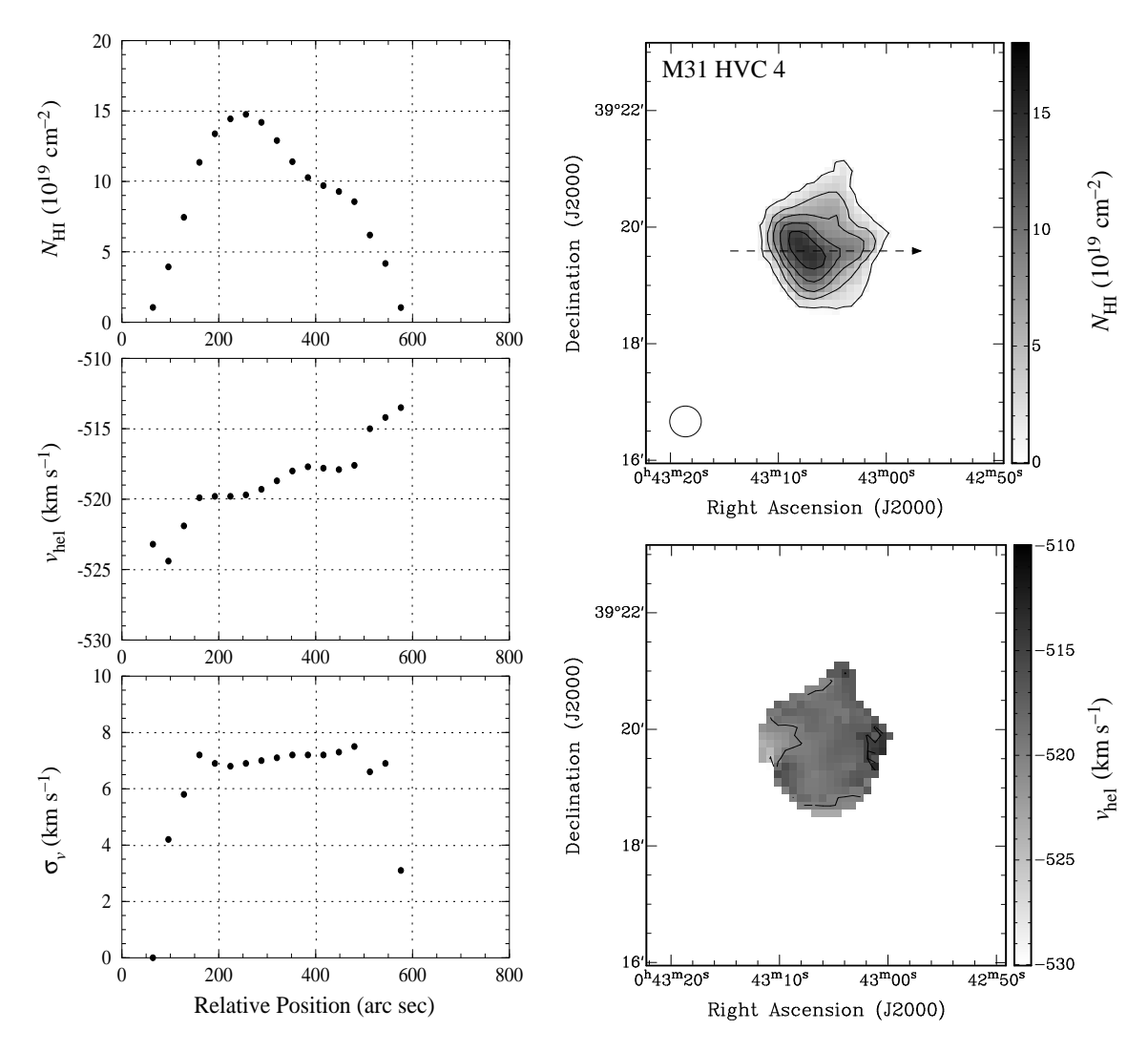


Fig. 3.14: M 31 HVC 4. The upper right map displays the HI column density. The contours are drawn from 1×10^{19} cm⁻² in steps of 3×10^{19} cm⁻². The lower right map shows the heliocentric radial velocity. The contours are separated by 5 km s⁻¹. The diagrams on the left hand side show from top to bottom: the HI column density, the heliocentric radial velocity, and the velocity dispersion of the gas along the cut marked by the arrow in the column density map.

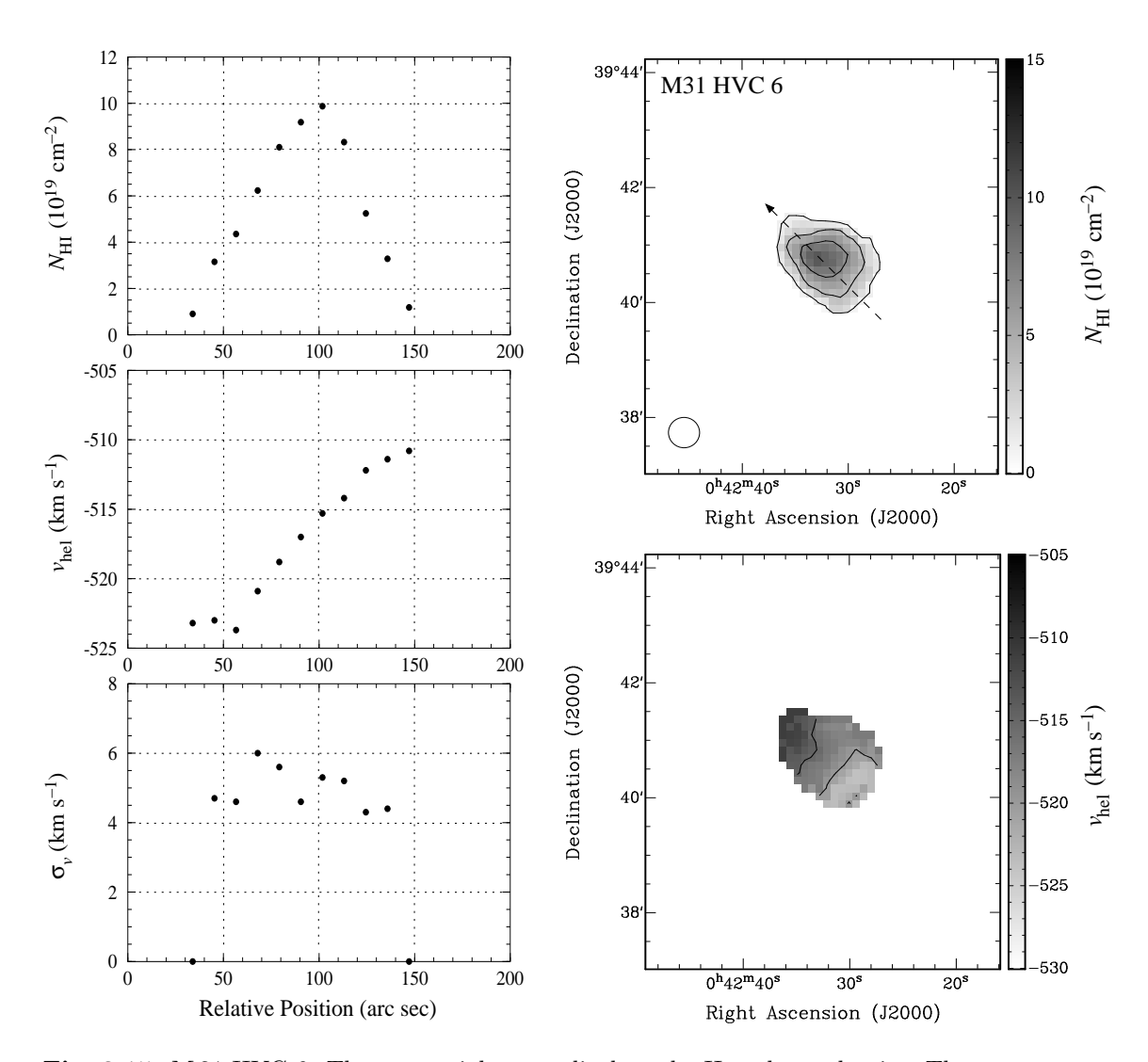


Fig. 3.15: M 31 HVC 6. The upper right map displays the HI column density. The contours are drawn from 1×10^{19} cm⁻² in steps of 3×10^{19} cm⁻². The lower right map shows the heliocentric radial velocity. The contours are separated by 5 km s⁻¹. The diagrams on the left hand side show from top to bottom: the HI column density, the heliocentric radial velocity, and the velocity dispersion of the gas along the cut marked by the arrow in the column density map.

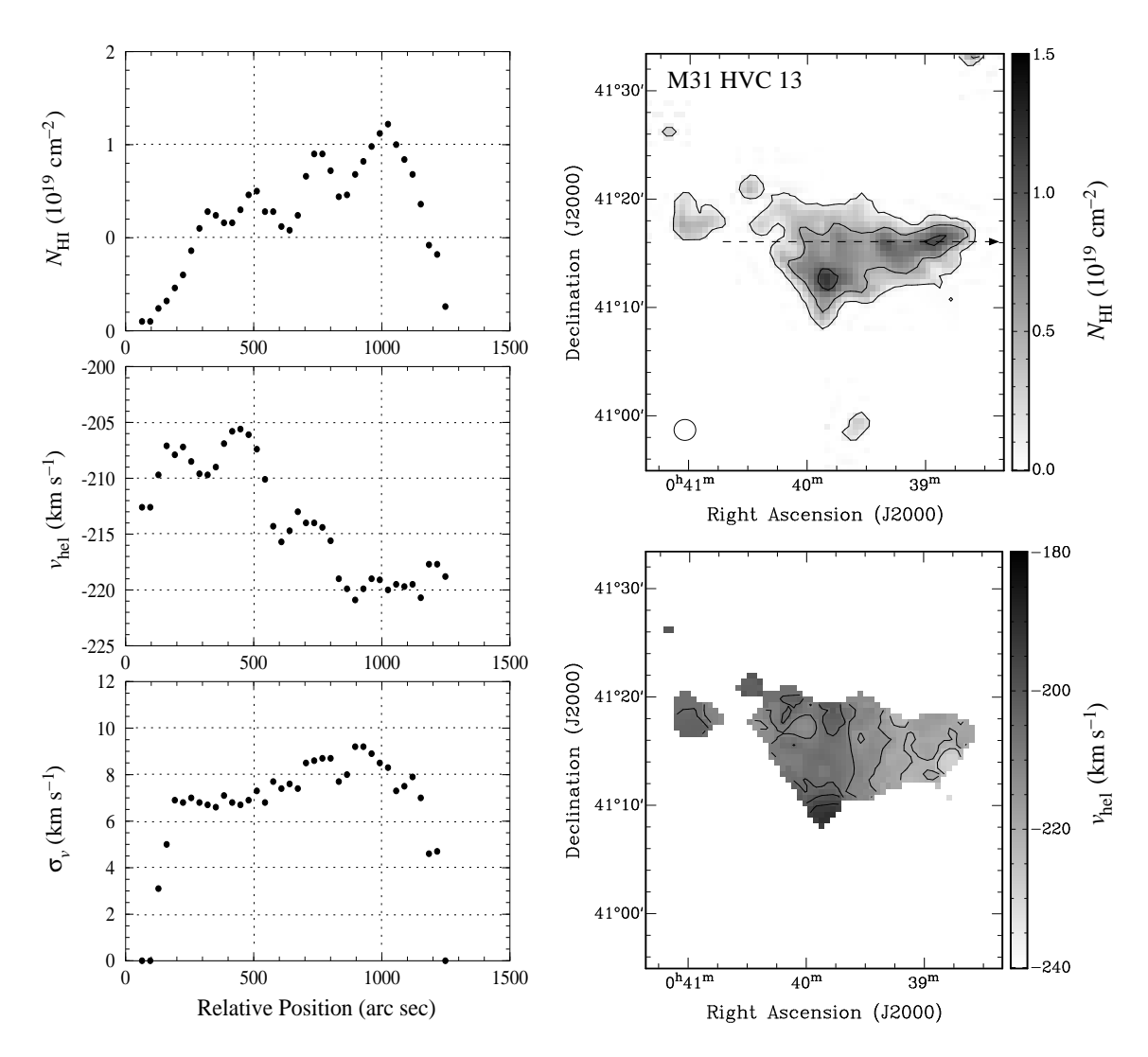


Fig. 3.16: M 31 HVC 13. The upper right map displays the H I column density. The contours are drawn at 1×10^{18} cm⁻² and from 5×10^{18} cm⁻² in steps of 5×10^{18} cm⁻². The lower right map shows the heliocentric radial velocity. The contours are separated by 5 km s^{-1} . The diagrams on the left hand side show from top to bottom: the H I column density, the heliocentric radial velocity, and the velocity dispersion of the gas along the cut marked by the arrow in the column density map.

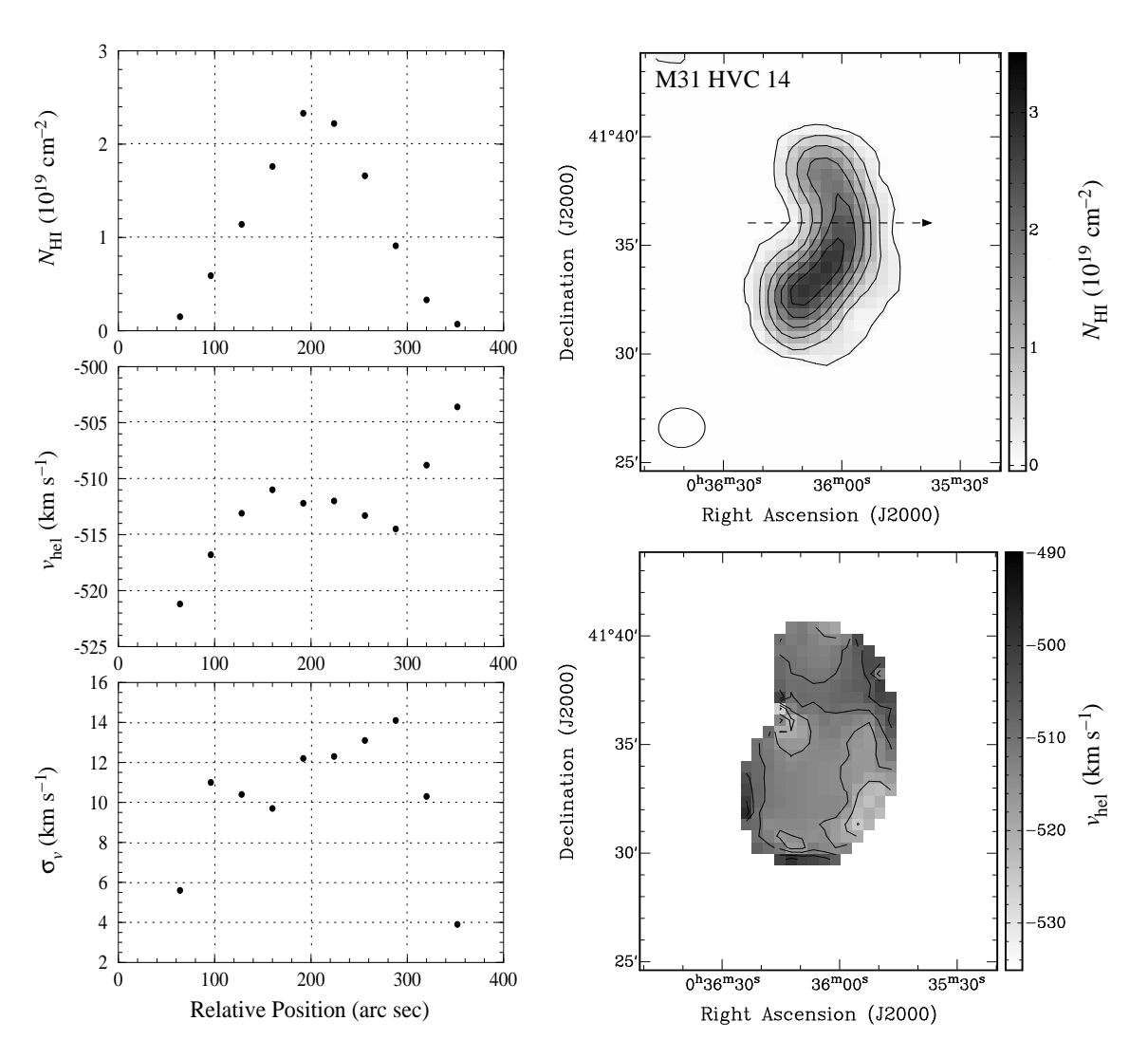


Fig. 3.17: M 31 HVC 14. The upper right map displays the H I column density. The contours are drawn at 1×10^{18} cm⁻² and from 5×10^{18} cm⁻² in steps of 5×10^{18} cm⁻². The lower right map shows the heliocentric radial velocity. The contours are separated by 5 km s^{-1} . The diagrams on the left hand side show from top to bottom: the H I column density, the heliocentric radial velocity, and the velocity dispersion of the gas along the cut marked by the arrow in the column density map.

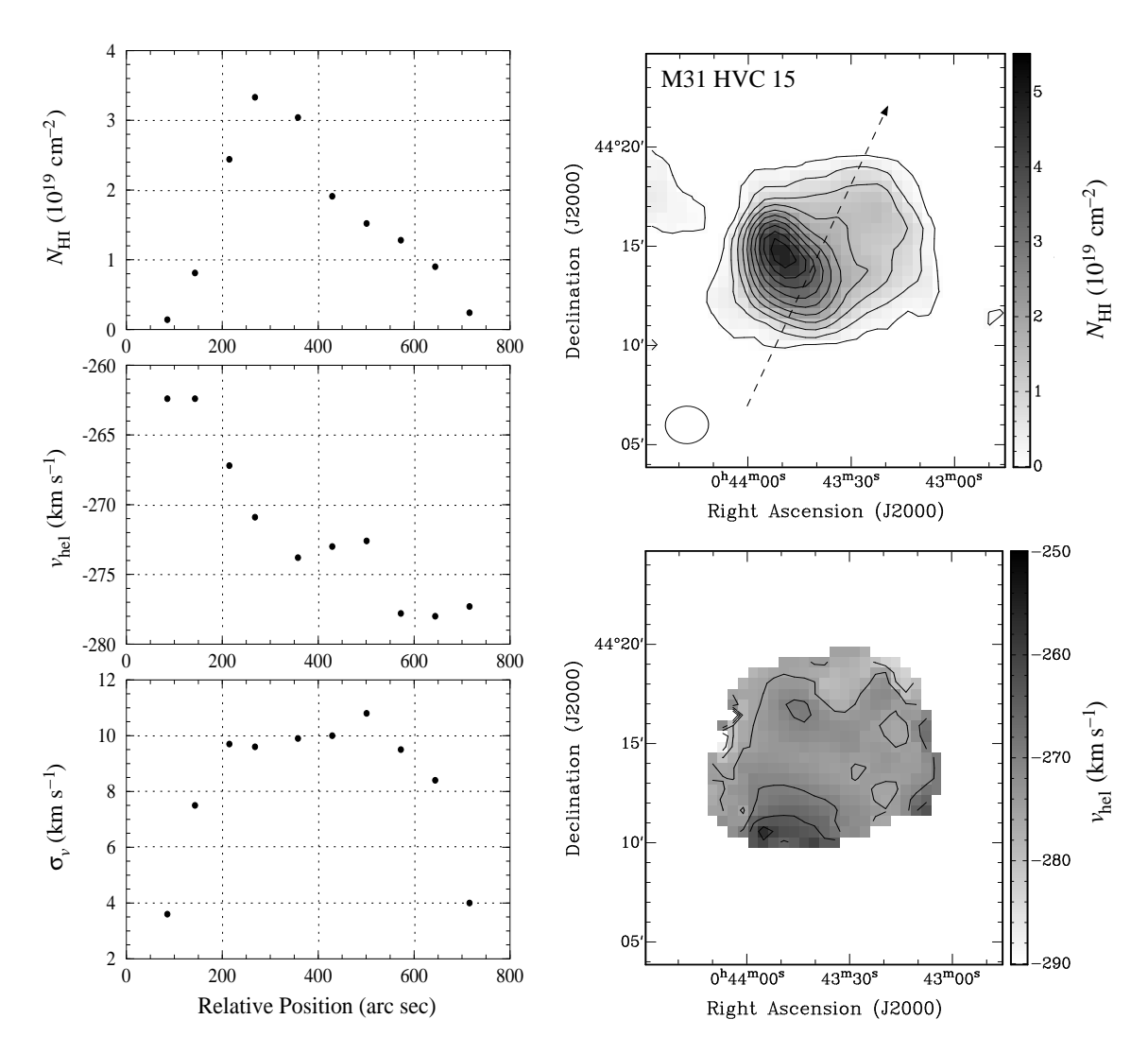


Fig. 3.18: M 31 HVC 15. The upper right map displays the H I column density. The contours are drawn at 1×10^{18} cm⁻² and from 5×10^{18} cm⁻² in steps of 5×10^{18} cm⁻². The lower right map shows the heliocentric radial velocity. The contours are separated by 5 km s^{-1} . The diagrams on the left hand side show from top to bottom: the H I column density, the heliocentric radial velocity, and the velocity dispersion of the gas along the cut marked by the arrow in the column density map.

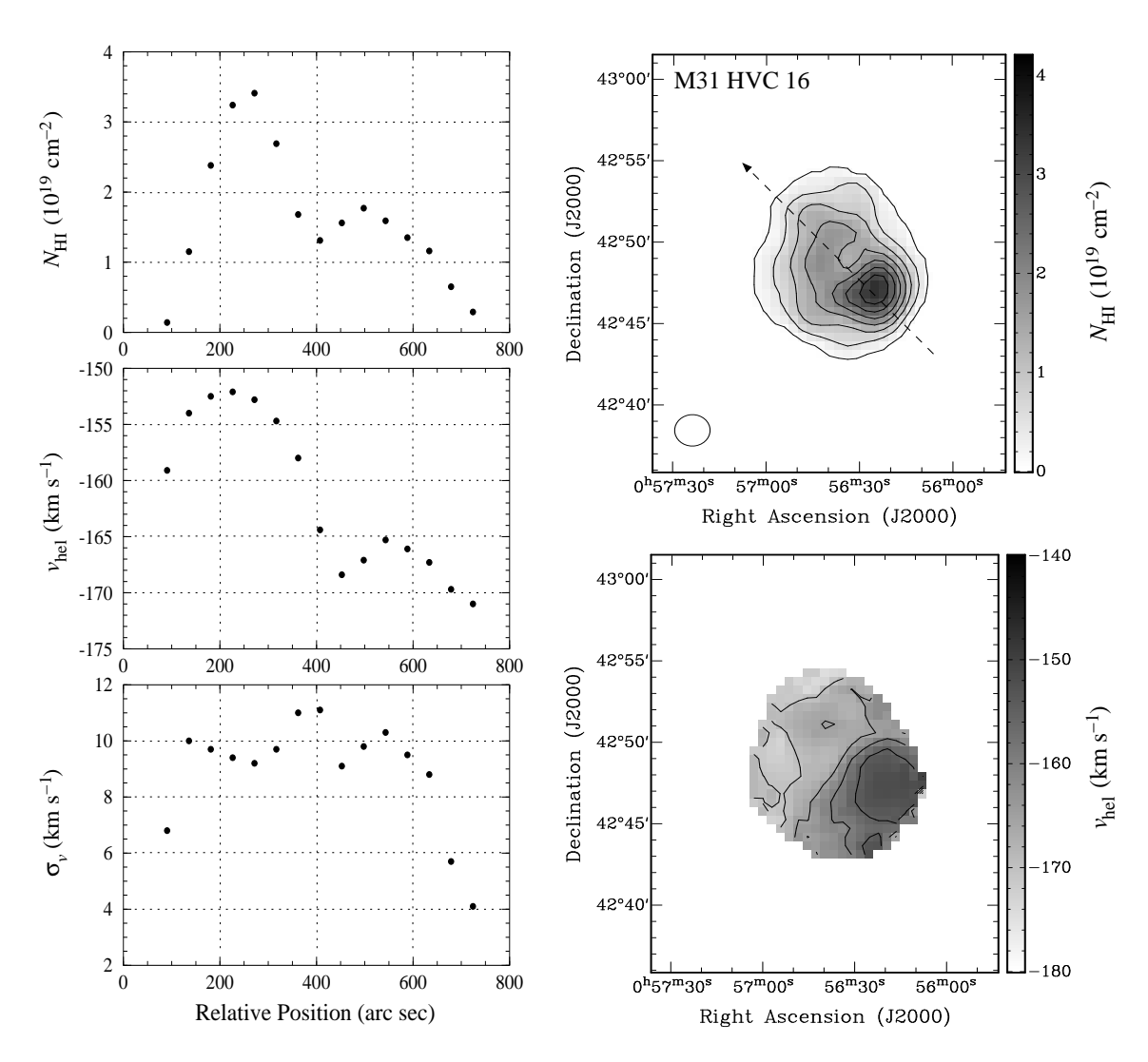


Fig. 3.19: M 31 HVC 16. The upper right map displays the H I column density. The contours are drawn at 1×10^{18} cm⁻² and from 5×10^{18} cm⁻² in steps of 5×10^{18} cm⁻². The lower right map shows the heliocentric radial velocity. The contours are separated by 5 km s^{-1} . The diagrams on the left hand side show from top to bottom: the H I column density, the heliocentric radial velocity, and the velocity dispersion of the gas along the cut marked by the arrow in the column density map.

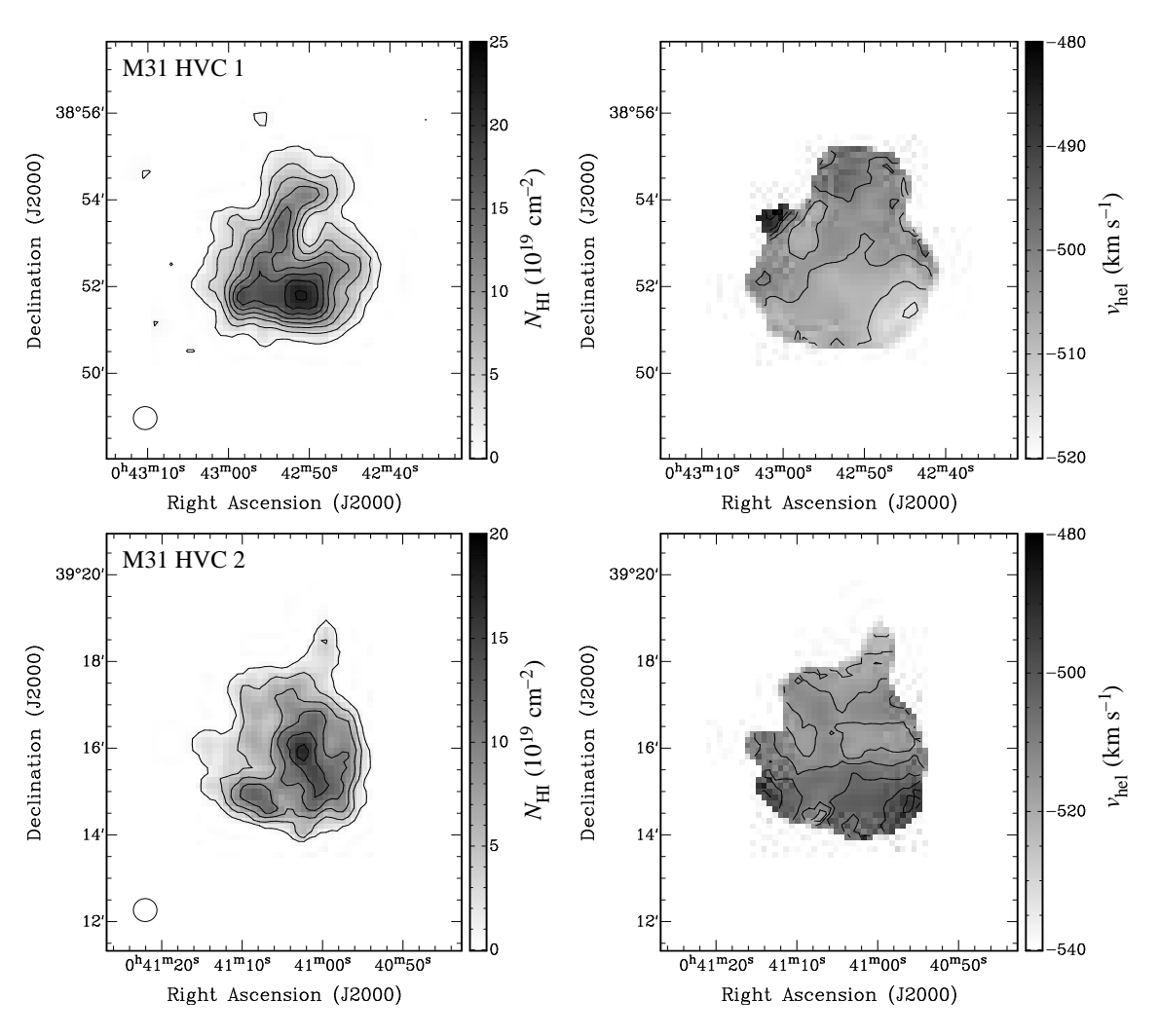


Fig. 3.20: Maps of the HI column density (left) and the heliocentric radial velocity (right) of M 31 HVCs 1 and 2 with a higher angular resolution of about 30". The contours in the column density maps are drawn from 1×10^{19} cm⁻² in steps of 3×10^{19} cm⁻². The contours in the radial velocity maps are drawn in steps of 5 km s^{-1} . Both clouds show compact sub-structure which is not resolved in the 2' maps.

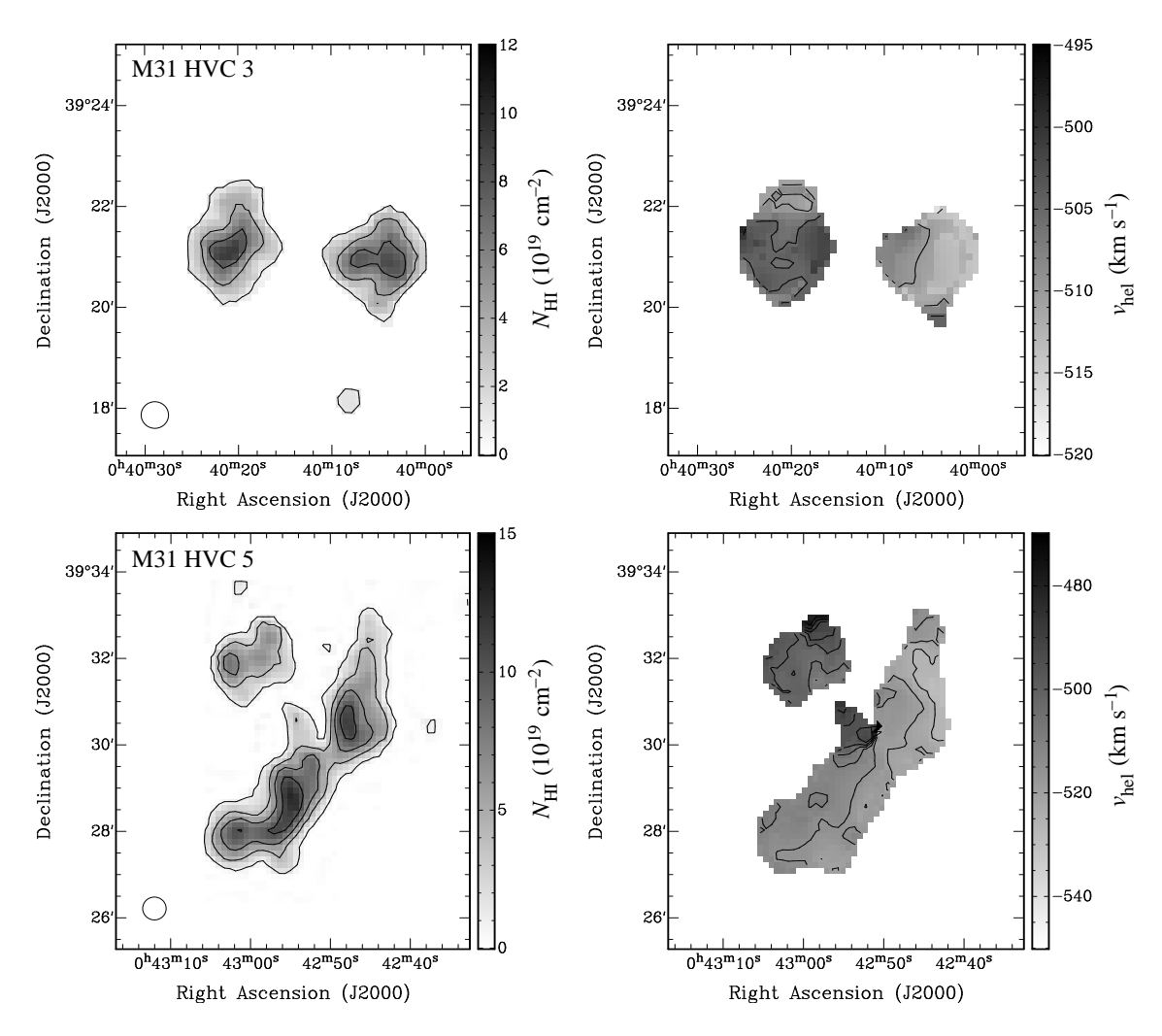


Fig. 3.21: Maps of the HI column density (left) and the heliocentric radial velocity (right) of M 31 HVCs 3 and 5 with a higher angular resolution of about 30". The contours in the column density maps are drawn from 1×10^{19} cm⁻² in steps of 3×10^{19} cm⁻². The contours in the radial velocity maps are drawn in steps of 5 km s^{-1} . Both clouds break up into sub-clumps which are hardly resolved in the 2' maps.

Low column density gas in the Galactic halo

In this chapter I will present the first results of optical absorption line studies of high-velocity gas in the Galactic halo. Using data taken with UVES at the VLT, we found high-velocity Ca II and Na I absorption in the direction of the quasar PKS 1448–232. Follow-up HI observations with the VLA uncovered several compact clumps of neutral gas in this direction. Unfortunately, the sight line towards PKS 1448–232 passes only the outer envelope of one of the clumps so that we are not able to determine the HI column density and, thus, the Ca II and Na I abundances in this direction. A more extensive study of quasar sight lines through the Galactic halo is under way (Ben Bekhti et al., in prep.), indicating that a large fraction of the sky is covered with neutral, intermediate- or high-velocity gas with low column densities. The next steps will be to study the connection of this population of neutral halo clouds with the ionised high-velocity gas as traced by O VI absorption Sembach et al. (2003), and to finally extend these absorption line studies to external galaxies like M 31. This chapter has been adapted from the corresponding refereed journal article (Richter, Westmeier, & Brüns 2005).

4.1 Introduction

Our observations of the HVC population around M 31 have demonstrated that HVCs are circumgalactic objects with distances of $\lesssim 50$ kpc from their host galaxies. A single origin for all HVCs is unlikely. Instead, we have evidence that some of the HVCs around M 31 could be of tidal origin, whereas others are good candidates for primordial dark-matter-dominated satellites.

The next step in studying the HVCs around the Milky Way and M 31 will be to test the scenario established in the previous chapters. The most promising method is the determination of metal abundances of the gas in HVCs. This would allow us to distinguish between the different hypotheses to explain their origin. As discussed in Section 1.3.3, for several of the HVC complexes around the Milky Way metallicity measurements are already

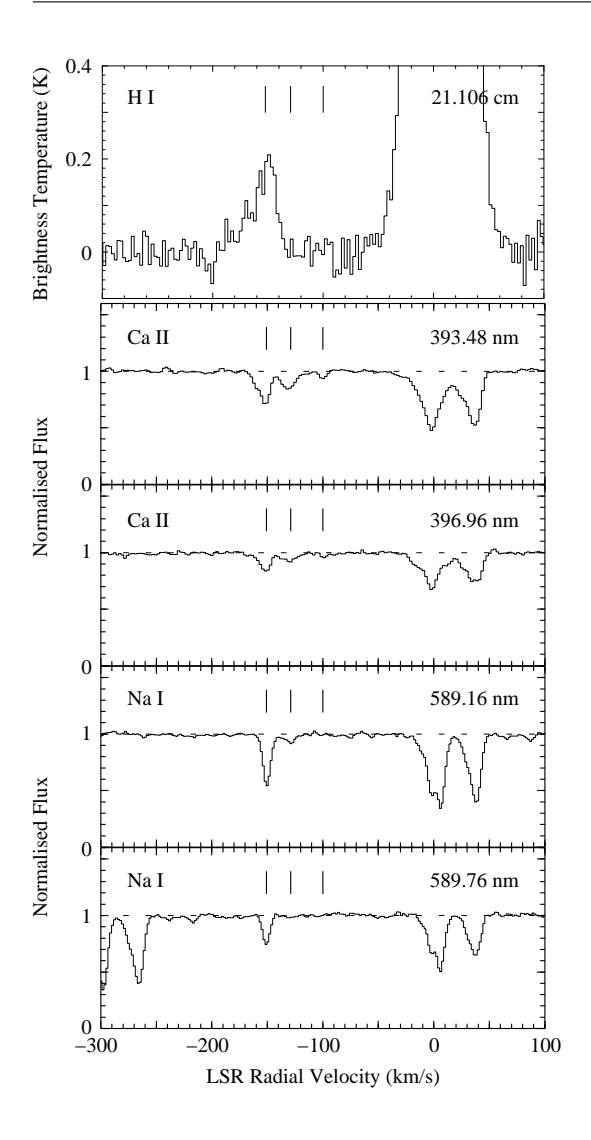


Fig. 4.1: HI emission and Ca II and Na I absorption spectra in the direction of the quasar PKS 1448–232 as observed with Effelsberg and the VLT, respectively. Three high-velocity absorption lines at $v_{\rm LSR} \approx -150$, -130, and $-100~{\rm km\,s^{-1}}$ can be seen in Ca II absorption, indicated by the dashes above the spectra. Surprisingly, only the strongest of these lines is also detected in HI emission with Effelsberg. The HI column density is about $8\times10^{18}~{\rm cm^{-2}}$. The asymmetric line profile seen in Ca II absorption is also obvious in the HI line, indicating that both originate from the same region in space.

available, indicating abundances of the order of a tenth of the corresponding solar values for several different species. The only exception known so far is complex M which has solar abundances (Tufte et al. 1998; Wakker 2001). The results demonstrate that the large HVC complexes cannot be primordial but must have been processed in some way.

All these measurements were obtained through absorption spectroscopy of distant AGN and quasars or Galactic halo stars located behind the HVCs. Absorption spectroscopy has the advantage that it is very sensitive to low column densities which are undetectable in emission. This allows us to study the low column density part of the high-velocity gas distribution in the Galactic halo which cannot be observed in the 21-cm line of HI. Among the easiest species to detect in absorption are the Ca II H and K lines at $\lambda = 3968.5$ and 3933.7 Å, respectively, and the Na I D₁ and D₂ lines at $\lambda = 5895.9$ and 5890.0 Å, respectively. They are characterised by large oscillator strengths and can be detected with ground-based optical telescopes.

In the past, the highly ionised high-velocity gas around the Milky Way has been systematically studied by Sembach et al. (2003) in the OVI doublet at $\lambda = 1031.9$ and 1037.6 Å in the far-ultraviolet. Their results indicate that about 60% of the sky is covered

with ionised high-velocity gas. However, relatively little attention has been paid so far to the abundance and distribution of the neutral component of high-velocity gas in the Galactic halo below the detection limit of the large H I surveys of $N_{\rm H\,I} \lesssim 10^{19}$ cm⁻². Using more sensitive H I observations with the 305-m Arecibo telescope, Hoffman et al. (2004) found a population of "mini HVCs" with low H I column densities of typically a few times 10^{18} cm⁻² and diameters of $\lesssim 35'$. A similarly small and faint "ultra-compact HVC" (see Fig. 1.10 for an H I column density map) was detected by Brüns & Westmeier (2004) with the Effelsberg telescope and the Australia Telescope Compact Array (ATCA). Towards the Large Magellanic Cloud, Richter et al. (2003) have detected far-ultraviolet absorption by molecular hydrogen and various weakly ionised metals in a dense gas filament in the halo that has a total H I column density of about 10^{18} cm⁻² and a thickness of only about 40 AU ($\approx 6 \times 10^9$ km).

In this chapter I will report on the discovery of small-scale, low column density high-velocity clouds in the Galactic halo in Ca II and Na I absorption towards the quasar PKS 1448–232 and other extragalactic background sources. A large part of this chapter has been adapted from the corresponding refereed journal article (Richter, Westmeier, & Brüns 2005). Studying the frequency and distribution of these low column density absorbers is important to better understand the connection between the different gas phases in the halo of the Milky Way, to study the metal abundances of the high-velocity gas, and to link the column density distribution of neutral gas in the Galactic halo to the properties of absorption line systems in the circumgalactic environment of other galaxies. Unfortunately, we were not able to determine the abundances of Ca II and Na I in the direction of PKS 1448–232. A more extensive study of quasar sight lines, however, is under way (Ben Bekhti et al., in prep.) and will allow us to determine the properties of low column density halo clouds in great detail.

4.2 Observations

4.2.1 Optical spectroscopy with UVES

The optical spectra of PKS 1448–232 were obtained in June 2001 with the *Ultraviolet* and Visual Échelle Spectrograph (UVES) at the ESO Very Large Telescope (VLT). The observations were part of the UVES Large Programme "The Evolution of the Intergalactic Medium" with Jacqueline Bergeron as principal investigator. The spectral resolution of the data is $R \approx 42\,000$, corresponding to a velocity resolution of about 6.6 km s⁻¹ FWHM. The raw data were reduced using the UVES pipeline implemented in the *European Southern Observatory Munich Image Data Analysis System* (ESO-MIDAS), including flat-fielding, bias and sky subtraction, and a relative wavelength calibration. For the analysis of the spectra the FITLYMAN package of MIDAS was used (Fontana & Ballester 1995) which delivers velocity centroids, column densities, and Doppler parameters (*b*-values) by fitting a Voigt profile to the absorption lines.

Parts of the UVES spectra in the direction of PKS 1448–232 are shown in Fig. 4.1. Apart from the components near velocities of zero which originate from local gas in the Galactic disk, three high-velocity absorption components are visible in Ca II and Na I absorption at radial velocities of $v_{\rm LSR} \approx -150$, -130, and $-100~{\rm km\,s^{-1}}$. The column densities determined for both Ca II and Na I are in the range of about $10^{11} \dots 10^{12}~{\rm cm^{-2}}$.

The weakest component at $v_{\rm LSR} \approx -100~{\rm km\,s^{-1}}$ was not detected in NaI absorption, resulting in an upper limit for the column density of $N_{\rm NaI} < 7 \times 10^{10}~{\rm cm^{-2}}$. Our UVES results are summarised in Table 4.1.

4.2.2 HI observations with Effelsberg

To see if there is an H I counterpart in the direction of PKS 1448–232 we first examined the LAB Survey (Kalberla et al. 2005; Hartmann & Burton 1997) which does not show any significant sign of H I emission in the corresponding velocity range. The RMS of the LAB survey data at 4 km s⁻¹ velocity resolution is about 40 mK, pointing towards an upper limit for the brightness temperature of $T_{\rm B} \lesssim 100$ mK. Next, we used the 100-m telescope at Effelsberg to integrate for about 20 minutes on the position of the quasar, resulting in the spectrum presented in the top panel of Fig. 4.1. The RMS is about 15 mK at 5 km s⁻¹ velocity resolution. The Effelsberg data show a clear emission line at $v_{\rm LSR} \approx -150$ km s⁻¹, corresponding to the strongest absorption line seen in the UVES data. Surprisingly, the two weaker components in the UVES spectra at $v_{\rm LSR} \approx -130$ and -100 km s⁻¹ are not detected in emission and must either lie below our detection limit or suffer from confusion with the detected emission. The asymmetric line profile is obvious in both the H I and Ca II lines, indicating that both originate from the same region in space.

The H I line observed with Effelsberg has a peak brightness temperature of $T_{\rm B}=0.2$ K and a column density of $N_{\rm H\,I}=8\times10^{18}$ cm⁻². The fact that the line is not detected in the LAB Survey indicates that the angular size of the emitting region is smaller than the HPBW of the 25-m Dwingeloo telescope of 36′, resulting in a reduced brightness temperature due to beam smearing. From the relatively large Na I/Ca II ratio we conclude that despite the broad H I line of $\Delta v=23$ km s⁻¹ FWHM the temperature of the gas must be fairly low. All this leads us to conclude that the emission and absorption observed in the direction of PKS 1448–232 originates from compact, cold, neutral gas clumps.

4.2.3 HI observations with the VLA

Based on these results we proposed to re-observe the sight line towards PKS 1448-232 in HI with the NRAO Very Large Array (VLA). The observations (two coverages of 6 hours each) were carried out in June 2004 with the VLA in the DnC configuration. This compact hybrid configuration is especially well suited for extended sources with a declination of $\delta < -15^{\circ}$ for which a full uv coverage cannot be obtained (see Fig. 4.2 for the resulting uv coverage). We selected the quasar 1331+305 (3C286) as flux and bandpass calibrator and the galaxy 1526-138 as gain calibrator. For each of the two polarisations the correlator provided a bandwidth of 1.56 MHz with 256 spectral channels, resulting in a channel separation of 1.3 km s⁻¹. After flagging the data affected by radio frequency interference, we carried out the standard bandpass, flux, and gain calibration, using the NRAO Astronomical Image Processing System (AIPS). After a linear interpolation of the gain solutions determined for the 1526-138 measurements, we improved the gain calibration by self-calibrating on the continuum sources in the field. This was done in an iterative procedure with solution intervals decreasing down to only 1 minute in the final iteration. This was possible due to the strong continuum emission of PKS 1448-232 itself which was the by far strongest source in our field (Fig. 4.2).

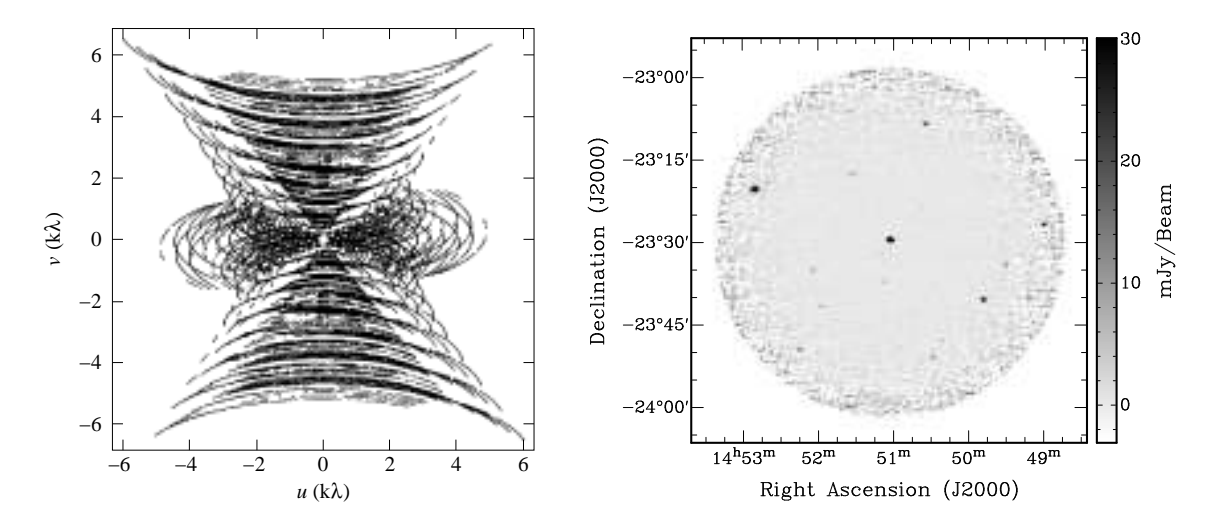


Fig. 4.2: VLA observations in the direction of the quasar PKS 1448–232. **Left:** Total *uv* coverage of the data in the DnC hybrid configuration, comprising two coverages of 6 hours each. **Right:** 21-cm continuum image. PKS 1448–232 is the bright source in the centre of the field. The point sources in the continuum map were used for self-calibration.

After successful calibration we deconvolved the data cube using the CLEAN algorithm originally developed by Högbom (1974). To increase the signal-to-noise ratio, the angular resolution was reduced by applying a Gaussian uv taper with a radius of 1 k λ at the 30% level. In addition, we smoothed the spectra to a channel width of 5.1 km s⁻¹. The resulting synthesised beam has a FWHM of about 2'. The RMS in the final data cube is 1.4 mJy/beam towards the centre of the field, corresponding to a brightness temperature RMS of 50 mK.

4.3 Results and discussion

An HI column density map of our VLA data is shown in Fig. 4.3. As expected from the previous results, the VLA observations uncover the presence of several compact high-velocity clumps of neutral hydrogen labelled with A–D. Following the usual convention of naming HVCs after their Galactic coordinates, we will refer to this cloud as HVC 335+32. According to the parameters given by Wakker & van Woerden (1991), PKS 1448–232 is located only a few degrees away from HVC complex L, and the detected high-velocity gas has similar radial velocities, suggesting that HVC 335+32 is part of complex L. In this case, our UVES observations would be the first detection of this HVC complex in absorption. The detection of Ca II absorption towards the star HD 135485 was already reported by Albert et al. (1993). They concluded, however, that the observed high-velocity absorption lines were likely caused by circumstellar material which was later confirmed by Danly et al. (1995) based on the absence of other species at similar radial velocities.

The observed peak brightness temperatures of the HI clumps of HVC 335+32 are in the range of 0.3...0.4 K with peak column densities in the range of $4...8 \times 10^{18}$ cm⁻². The radial velocity of the gas of $v_{\rm LSR} \approx -150$ km s⁻¹ is similar to the velocities observed for the strongest Ca II absorption component and the Effelsberg HI detection. Again, we

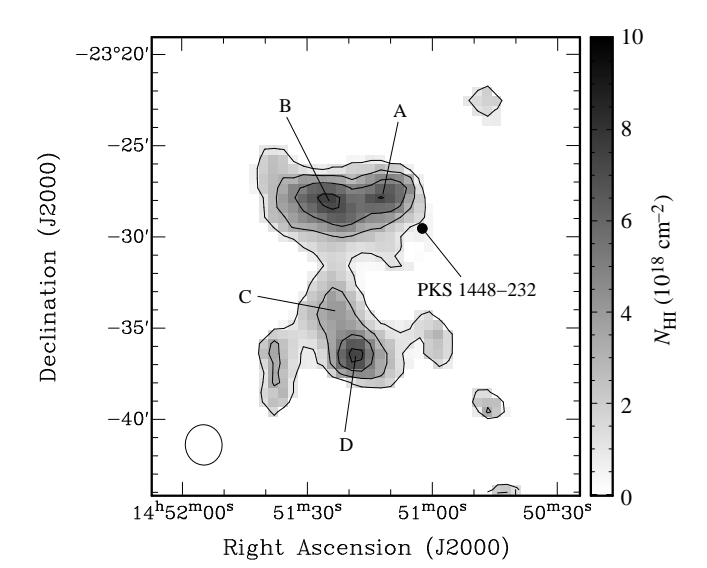


Fig. 4.3: HI column density map of the high-velocity gas observed in the direction of PKS 1448–232 with the VLA in the velocity range of $v_{\rm LSR} = -170\ldots -130~{\rm km\,s}^{-1}$. The contours are drawn at 1, 3, 5, and $7\times 10^{18}~{\rm cm}^{-2}$. Several small HI clumps with low column densities are detected, labelled from A to D. The sight line towards PKS 1448–232 passes the outer envelope of clump A. The beam size is shown in the lower left corner of the map.

do not detect the two fainter components in emission, implying that they are below our detection limit. The detected clumps have angular diameters of about 3', corresponding to a physical size of the order of 10 pc if the same distance of 10 kpc as for complex L is assumed (Weiner et al. 2001; Putman et al. 2003a). The results of our VLA observations are summarised in Table 4.2.

Two example spectra of clumps A and C are presented in Fig. 4.4. In the direction of clump C we detect only a single line component with a fairly small line width of $6.2~{\rm km\,s^{-1}}$ FWHM, implying an upper limit for the kinetic temperature of the gas of $T_{\rm kin} \lesssim 900~{\rm K}$. Given the relatively high Na I/Ca II ratio and the possibility of non-thermal motions, the gas temperature might be significantly lower than the derived upper limit.

Unfortunately, the sight line towards PKS 1448–232 passes only the outer envelope of clump A, so that we are not able to determine the HI column density in this direction. In combination with the unknown ionisation conditions, this eliminates any possibility of calculating the abundances of Ca II and Na I.

Weiner et al. (2001) and Putman et al. (2003a) found strong H α emission from complex L with emission measures of typically several hundred mR. Assuming photo-ionisation by Galactic radiation as the source of the observed H α fluxes, the inferred distance of complex L from the Galaxy would roughly be of the order of 10 kpc, placing it above the Galactic centre and fairly close to the Galaxy. If we assume HVC 335+32 to be a part of complex L at a similar distance, we can estimate distance-dependent physical parameters such as the mass and the pressure of the gas. By summing the detected H I column density over clumps A–D, we obtain a total H I mass as a function of distance, d, of

$$M_{\rm H\,I} = m_{\rm H} d^2 \tan^2 \vartheta \sum_{x,y} N_{\rm H\,I}(x,y) = 16 \ M_{\odot} \left(\frac{d}{10 \ \rm kpc}\right)^2$$
 (4.1)

where m_H is the mass of a hydrogen atom, ϑ is the angular size of a resolution element of the image, and $N_{HI}(x,y)$ is the detected column density for each pixel (x,y). From the observed peak column density we can also infer the mean density of each clump, assuming spherical symmetry. The typical angular size of the clumps is $\varphi = 3'$ FWHM with a peak

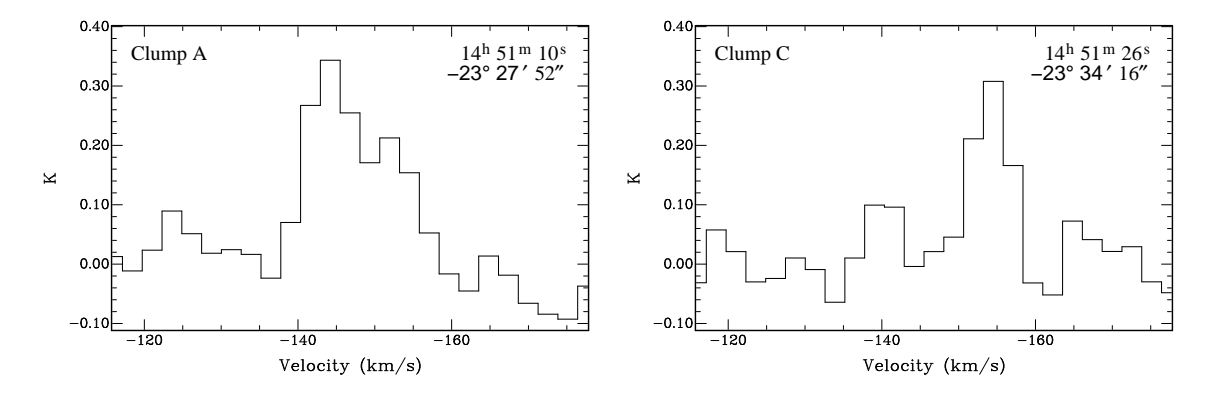


Fig. 4.4: Two example spectra of clump A (left) and clump C (right). In the direction of clump C we detect only a single 21-cm component with a line width of 6.2 km s⁻¹ FWHM, whereas the line profiles in the direction of clump A are more complex and indicate the superposition of multiple components along the line of sight.

column density of $N_{\rm H\,I}\approx 7.3\times 10^{18}~{\rm cm^{-2}}$ for clumps A, B, and D. The resulting H I density is

$$n_{\rm H\,I} = \frac{N_{\rm H\,I}}{d\tan\varphi} = 2.7 \times 10^{-1} \,\rm cm^{-3} \left(\frac{d}{10 \,\rm kpc}\right)^{-1}.$$
 (4.2)

Note that this is only an estimate of the mean density of the neutral hydrogen gas observed in the clumps under the assumption that their spatial extent along the line of sight is similar to the observed extent in the plane of the sky. Using the upper limit for the kinetic temperature of 900 K and the density derived above, we can estimate an upper limit for the pressure of the gas of

$$P/k = n_{\rm H\,I}T \lesssim 240 \,\,{\rm K\,cm^{-3}} \left(\frac{d}{10 \,\,{\rm kpc}}\right)^{-1}.$$
 (4.3)

Both the derived density and pressure are fairly low but in good agreement with the values predicted for high-velocity Galactic fountain gas at $z \approx 10$ kpc above the Galactic plane with solar abundances (Z=1) and a dust-to-gas ratio of D/G=0.3 indicating moderate dust destruction (Wolfire et al. 1995; their Fig. 1b). The estimated upper limit for the pressure of HVC 335+32, however, is by one order of magnitude lower than the prediction for infalling primordial gas with Z=D/G=0.01 (Fig. 1e in Wolfire et al. 1995), suggesting a Galactic origin of HVC 335+32.

Our detection of high-velocity Ca II and Na I absorption connected with compact, cold H I clumps along a random line of sight raises the question, whether such low column density clumps are common in the Galactic halo. A recent study of a large number of QSO sight lines based on UVES data indicates that about 40% of the randomly selected sight lines show intermediate- and high-velocity absorption line systems of Ca II and, in a few cases, Na I (Ben Bekhti et al., in prep.). Follow-up observations with the Effelsberg telescope show that many of these absorption systems are also connected with H I emission lines with brightness temperatures ranging from about 0.1 K up to several K. Some of the detections seem to be related to known HVC complexes such as the Magellanic Stream, whereas other sight lines appear to be completely isolated from any known HVC. The

Table 4.1: Summary of the UVES Ca II and Na I observations of PKS 1448–232. The specified parameters are the LSR radial velocity of the line, $v_{\rm LSR}$, the column density, $N_{\rm Ca\,II}$, and b-value, $b_{\rm Ca\,II}$, of Ca II, and the column density, $N_{\rm Na\,I}$, and b-value, $b_{\rm Na\,I}$, of Na I for all three detected absorption line components.

$v_{\rm LSR}$	$\log N_{ m CaII}$	b_{CaII}	$\log N_{ m NaI}$	$b_{ m NaI}$
$(\mathrm{km}\mathrm{s}^{-1})$	(cm^{-2})	$(\mathrm{km}\mathrm{s}^{-1})$	(cm^{-2})	$(\mathrm{km}\mathrm{s}^{-1})$
-101	11.00 ± 0.04	4.0 ± 1.2	≤ 10.84	_
-130	11.62 ± 0.03	8.3 ± 2.7	10.96 ± 0.10	5.1 ± 2.1
-152	11.83 ± 0.03	6.6 ± 2.3	11.77 ± 0.04	2.2 ± 1.3

Table 4.2: Summary of the VLA HI observations in the direction of PKS 1448–232. The specified parameters are the name of the clump, the right ascension and declination, α and δ , the LSR radial velocity, $v_{\rm LSR}$, the FWHM of the spectral line, Δv , the HI peak column density, $N_{\rm HI}$, the peak brightness temperature, $T_{\rm B}$, and the upper limit of the kinetic temperature of the gas, $T_{\rm kin}^{\rm max}$, as derived from the observed line width. Radial velocities and line widths were obtained by fitting a Gaussian to the averaged spectrum of each clump.

Clump	α	δ	$v_{ m LSR}$	Δv	$N_{ m HI}$	$T_{ m B}$	$T_{\rm kin}^{\rm max}$
	(J2000)	(J2000)	$(\mathrm{km}\mathrm{s}^{-1})$	$(\mathrm{km}\mathrm{s}^{-1})$	(cm^{-2})	(K)	(K)
A	$14^{\rm h}51^{\rm m}12^{\rm s}$	$-23^{\circ}27'45''$	-147	13.7	$7.1 \cdot 10^{18}$	0.34	4200
В	$14^{\rm h}51^{\rm m}25^{\rm s}$	$-23^{\circ}28'00''$	-151	11.3	$7.5 \cdot 10^{18}$	0.34	2900
\mathbf{C}	$14^{\rm h}51^{\rm m}23^{\rm s}$	$-23^{\circ}34'00''$	-153	6.2	$4.0\cdot10^{18}$	0.32	900
D	$14^{\rm h}51^{\rm m}18^{\rm s}$	$-23^{\circ}36'30''$	-155	11.0	$7.4\cdot10^{18}$	0.38	2700

detected CaII lines are comparatively narrow, suggesting the presence of compact, cold clumps or filaments rather than diffuse, extended structures. Our results indicate that the covering fraction of these low column density gas clumps is indeed large.

Furthermore, with typical HI column densities of $N_{\rm H\,I} \lesssim 10^{19}$ cm⁻² and a complex velocity structure, the observed Ca II absorption lines resemble those of the strong Mg II systems with equivalent widths of $W_{2796} < 1$ Å commonly observed within an impact parameter of about $35\,h^{-1}$ kpc of luminous galaxies (e.g., Bergeron & Boissé 1991; Ding et al. 2005). The strong Mg II systems are believed to sample both disk and halo gas in galaxies. At low HI column densities a significant fraction of the gas is expected to be ionised. Thus, the observed Ca II absorption line systems may also be related to the highly ionised HVCs detected in C IV and O VI absorption (Sembach et al. 2003).

4.4 Summary and conclusions

Our observations in the direction of the quasar PKS 1448–232 with the VLT, the VLA, and Effelsberg have shown that low column density gas with high radial velocities is present in this direction. In Ca II and Na I absorption we detect three components with different velocities, only the strongest of which is also seen in neutral hydrogen. Our VLA

observations have uncovered the presence of individual HI clumps with angular sizes of only a few arc minutes. Assuming an association of the gas with HVC complex L and a distance of the order of 10 kpc, the total HI mass of the clumps would be 16 M_{\odot} , and the size of each clump would be of the order of 10 pc. Unfortunately, the sight line towards PKS 1448–232 passes only the outer envelope of clump A so that we are unable to determine the neutral gas column density in this direction. This eliminates any possibility of calculating the abundances of Ca II and Na I.

However, a more extensive study of quasar sight lines with VLT and Keck telescope data (Ben Bekhti et al., in prep.) is under way. Preliminary results have shown that a large fraction of the sky is covered with neutral, intermediate- or high-velocity gas with low column densities. The next task will be to determine the Ca II and Na I abundances of the gas and to find out how this population of halo clouds is connected with the large HVC complexes and the ionised high-velocity gas in the halo as traced by O VI absorption lines (Sembach et al. 2003). The final and most challenging step will then be to extend these systematic absorption line studies to M 31, using bright stars in the disk of M 31 as background objects.

Summary and outlook

5.1 The search for HVCs around M 31

For more than 40 years HVCs around the Milky Way have been studied with different techniques with the aim of determining their properties and origin. These studies have been hampered by the fact that for most HVCs distances are unknown or only poorly constrained by theoretical considerations. To deal with the problem of distance determination, several external galaxy groups have been observed in search of HVCs (e.g., Zwaan 2001; Braun & Burton 2001; Pisano et al. 2004). Due to their limited H I mass sensitivities these surveys did not detect any equivalent of the HVC population observed around our Galaxy. The study of M 31 by Thilker et al. (2004) and this work finally marked the breakthrough in our attempts to identify the equivalents of HVCs in other galaxies and to determine their distribution and origin. Our search for HVCs around M 31 provides for the very first time the necessary mass sensitivity and spatial resolution to detect and study an extended population of discrete HVCs around a galaxy other than our own. Our observations are a major step forward in our understanding of HVCs and their role in the formation and evolution of galaxies.

The most important results of our M 31 observations with the 100-m radio telescope at Effelsberg and the Westerbork Synthesis Radio Telescope are:

- 1. M 31 is surrounded by a population of about 15–20 HVCs with typical HI masses of a few times $10^5 M_{\odot}$. Only Davies' Cloud has a significantly higher HI mass of $1.3 \times 10^7 M_{\odot}$. The detected HVCs have diameters of the order of 1 kpc and typical HI densities of a few times 10^{-2} cm⁻³. With these parameters, the discovered HVCs resemble the **large HVC complexes** observed around the Milky Way (Wakker & van Woerden 1991, 1997; Wakker 2001).
- 2. The detected HVCs are forming a **circumgalactic population** with projected distances of less than about 50 kpc from the centre of M 31. No HVCs were found beyond this radius although our Effelsberg survey reaches out to projected distances in excess of 100 kpc.

- 3. The expected extended population of **hundreds of CHVCs** (Braun & Burton 1999; de Heij et al. 2002a) was **not detected** in our Effelsberg survey. Assuming that the Milky Way and M 31 have a similar CHVC population, CHVCs must be located within about 60 kpc of their host galaxies. This distance limit is consistent with the spatial distribution of the large HVCs found around M 31. Consequently, the small angular sizes of CHVCs reflect their **small physical sizes** and are not due to large distances from the Galaxy.
- 4. Some of the HVCs, in particular the conspicuous HVC complex near the south-eastern edge of M 31, are most likely of **tidal origin** in connection with the giant stellar stream (Ibata et al. 2001a) or satellite galaxies of M 31. Other HVCs are completely isolated from any known dwarf galaxy or structure in the stellar component of M 31. They are the most promising candidates for the **primordial dark-matter mini-halos** predicted by structure formation scenarios based on CDM cosmology (Klypin et al. 1999; Moore et al. 1999; Kravtsov et al. 2004).

The H I column densities, masses, and sizes of the HVCs found around M 31 are in remarkable agreement with the results of hydrostatic simulations of dark-matter-dominated CHVCs made by Sternberg et al. (2002). Hence, some of the HVCs near M 31, in particular the isolated ones, could in fact be primordial, dark-matter-dominated satellite halos in the M 31 system. To stabilise the clouds in addition to their dark-matter potential an external pressure of at least $P/k \approx 50 \text{ K cm}^{-3}$ would be required. This pressure can be provided by the hot, ionised circumgalactic corona (Sembach et al. 2003; Rasmussen et al. 2003) with typical temperatures of a few times 10^6 K and electron densities of the order of 10^{-4} cm⁻³. Furthermore, the ambient medium can account for the observed distortions of some of the HVCs through the process of ram-pressure stripping (Quilis & Moore 2001; Konz et al. 2002).

There are two problems connected with the interpretation of HVCs as dark-matter mini-halos. First of all, the total number of clouds is much lower than the number of expected satellite halos in the M 31 system. This problem, however, is solved by the structure formation models of Kravtsov et al. (2004) which indicate that most dark-matter satellites around M 31 could have lost their gas during their evolution through tidal stripping during close encounters with other halos. Kravtsov et al. (2004) predict only 2-5 dark-matter satellites with corresponding gas masses to be left within 50 kpc of M 31. This is in excellent agreement with our observations if we assume that the model is realistic and that only a few of the discovered HVCs are primordial whereas others have a tidal origin. However, this leads us to the second problem: The radial extent of the observed HVC population is significantly smaller than the extent of the expected population of dark-matter halos. A solution for this problem could arise from the required pressure confinement of the HVCs in the simulations of Sternberg et al. (2002). At some distance from M 31 the pressure of the external coronal gas will drop below the value of $P/k \approx 50 \text{ K cm}^{-3}$ required to stabilise the clouds in addition to their gravitational potential. As a result, the warm gas could no longer be retained and, moreover, would be ionised by the intergalactic radiation field. Therefore, the simulations of Sternberg et al. (2002) and Kravtsov et al. (2004) can explain both the number and distribution of the HVCs discovered around M 31.

More than 40 years after their discovery our results provide us for the very first time with a consistent picture of the presumable origin and evolution of high-velocity clouds.

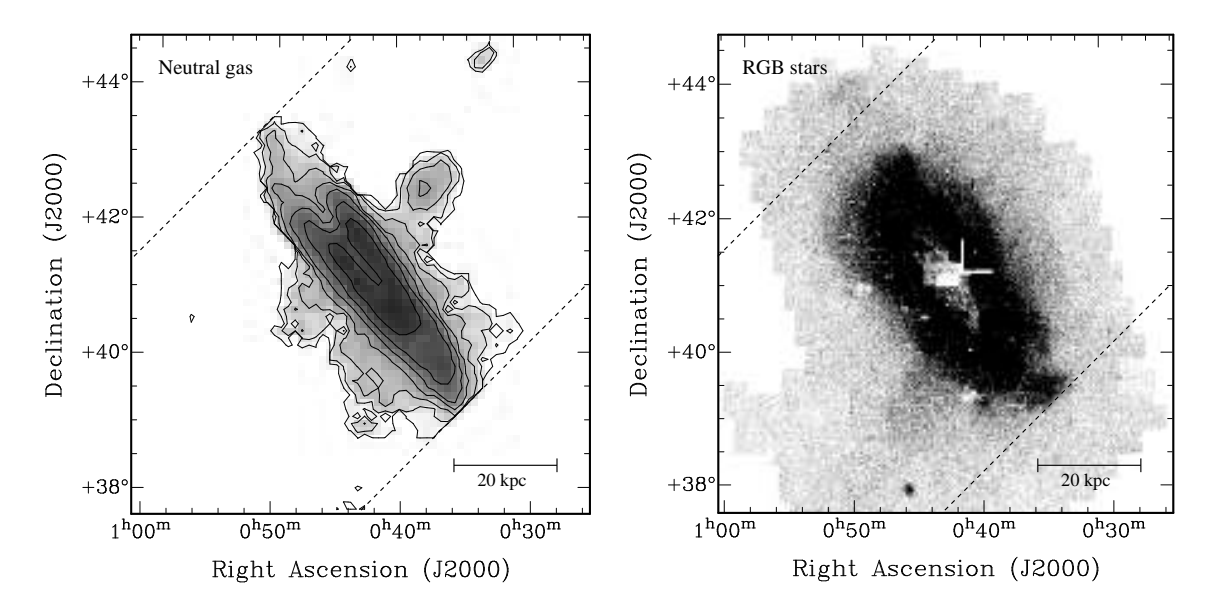


Fig. 5.1: Comparison of the Andromeda Galaxy in neutral hydrogen (left) and RGB stars (right). The HI map is based on our Effelsberg survey with parameters similar to the right panel of Fig. 2.13. The map of RGB stars is taken from Ferguson et al. (2006). The dashed lines outline the edge of the Effelsberg map. In both images the outer regions of M 31 show a very complex structure suggesting a rich accretion history and evolution which is traced by both the gaseous and stellar component of M 31.

Most likely, HVCs do not have a single origin. Some of them are probably the result of tidal interactions between M31 and its present or former satellite galaxies. These HVCs are found particularly close to the disk of M31 where tidal forces are expected to be strongest. Other HVCs are isolated from M31 and any of its dwarf satellites. Their physical parameters are in excellent agreement with the assumption that they represent the primordial dark-matter mini-halos predicted by CDM-based structure formation scenarios. All our results suggest that HVCs are the relics of structure formation, tracing the rich accretion history and evolution of large spiral galaxies like M31 and the Milky Way.

This is illustrated once more in Fig. 5.1 which compares the distribution of neutral gas (based on our Effelsberg data) with the distribution of RGB stars in M 31 (based on the data presented by Ferguson et al. 2006). Both maps show a remarkably similar and complex structure in the outer regions of M 31 providing evidence for ongoing evolution. Investigating the connection between the stellar and gaseous structures will be one of the challenges of our future studies of M 31 and its HVC population.

There is one more discrepancy between the HVC populations of M 31 and the Milky Way. The number of HVCs found around M 31 is of the order of 20, whereas hundreds of HVCs and CHVCs are known around the Galaxy (Wakker & van Woerden 1991; de Heij et al. 2002a; Putman et al. 2002). If we assume that M 31 hosts a similarly rich population we have to conclude that the distances and H I masses of most of the HVCs around the Galaxy must be so small that—if placed at the distance of M 31—they would fall below the detection limit of our survey. As a consequence, hundreds of HVCs with small projected distances and H I masses below $10^5 M_{\odot}$ should be spread all around M 31. Their existence

and origin still have to be determined. Possible origins include gas from galactic winds or outflows, clouds condensing out of halo gas, or tidal structures which are in an advanced state of being accreted by the Milky Way or M 31. In fact, the large amount of extraplanar gas around M 31, which was not resolved by the Effelsberg telescope, suggests the possibility of an extensive population of undiscovered HVCs close to M 31. Only deep H I synthesis observations of a larger field around M 31 with sensitive instruments like the VLA or WSRT will be able to uncover this population of clouds.

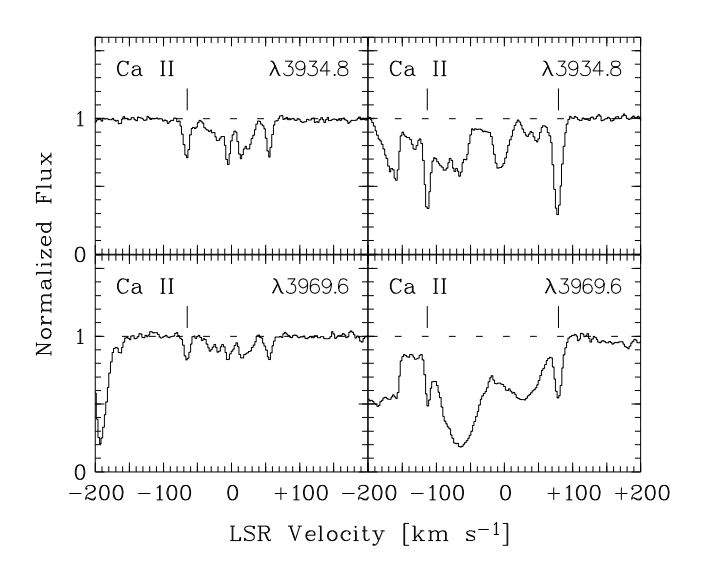
5.2 Optical absorption line studies of HVCs around M 31

The next logical step in the study of the HVC population around M 31 is the determination of the spatial distribution and metal abundances of the gas. As discussed in Chapter 4, the most promising method is the study of absorption lines in the spectra of background objects such as halo stars or distant quasars. With the study of quasar absorption line systems the *Hubble Space Telescope* (HST) has revolutionised our view of the intergalactic medium. One of the key projects of HST is to understand the composition and evolution of the intergalactic medium (e.g., Bahcall et al. 1993; Jannuzi et al. 1998). Absorption line methods have also been successfully applied to determine the metallicities and upper or lower distance limits of several HVC complexes around the Milky Way (see Section 1.3.3 and Wakker (2001) for a comprehensive review). Extending these studies to the HVCs around M 31 would constitute a major step forward in our understanding of structure formation and galaxy formation in the framework of CDM cosmology.

The brightest and easiest objects for absorption line studies of M 31 would be bright background quasars and AGN. The number density of suitable objects, however, is rather low, so that we cannot expect to have a sufficient coverage of the detected high-velocity gas around M 31. An alternative approach would be the study of luminous stars and young star clusters in M 31 as background sources for high-resolution optical spectroscopy. Several of the HVCs found near M 31 are seen in projection against or near the disk of M 31, therefore being ideal targets for absorption line studies. In addition, our spectroscopic observations of quasars with UVES at the VLT (Chapter 4) have demonstrated that we observe intermediate- and high-velocity Ca II absorption lines in about 40% of all sight lines through the Galactic halo (see Fig. 5.2 for two examples). Extending these studies to M 31 will provide us with the unique opportunity to study the metal abundances of the HVCs around M31. In addition, we will be able to constrain the three-dimensional structure of the gas distribution for the very first time which will be crucial to associate the HVCs with corresponding structures in the extended stellar component (such as the giant stellar stream) and to determine the direction of motion of the gas with respect to M 31 (infall or outflow).

The stellar halo objects used to study the Galactic HVCs, such as RR Lyrae stars (e.g., van Woerden et al. 1999b) and field horizontal branch (FHB) stars (e.g., Thom et al. 2005, 2006), are far too faint to be explored at the distance of M 31 even with the largest ground-based telescopes. However, massive O and B stars, the most luminous supergiants in the Milky Way, will be bright enough. They reach absolute magnitudes of $M_{\rm V} \simeq -10\ldots -5$ mag, resulting in apparent magnitudes of $m_{\rm V} \simeq 15\ldots 20$ mag at the distance of M 31. This range of magnitudes is well within reach of high-resolution optical

Fig. 5.2: Ca II absorption in the direction of the quasars HE 1341–1020 (left) and HE 0109–3518 (right), taken from Richter et al. (2005). Towards both sight lines we detect high-velocity Ca II H and K lines which are marked with dashes. Similar studies in the direction of bright stars in M 31 can help to determine the origin of the HVCs discovered around M 31.



spectroscopy with modern telescopes in the 5–10 m range. Luminous B stars have been successfully used by Smoker et al. (2004) to probe several sight lines through the Galactic halo in the Ca II K line at $\lambda=3933.7$ Å. Luminous supergiants have been spectroscopically studied also in M 31, e.g. by McCarthy et al. (1998), to determine the metallicities of the stars. Furthermore, Bresolin et al. (2001) carried out spectroscopic observations of several luminous stars (including one B and six A supergiants) in the galaxy NGC 3621 with FORS at the VLT. Their observations have demonstrated that even across a distance of 6.7 Mpc spectroscopic observations of individual stars can be successful. Hence, early-type supergiants are the most promising targets for absorption spectroscopy of high-velocity gas in the halo of M 31.

Another option will be the spectroscopic study of massive, young star clusters in M 31. This method was successfully applied to the four brightest H II regions in M 33 by Bluhm et al. (2003) with the aim of detecting molecular hydrogen in the ISM of M 33. Their observations were carried out in the ultraviolet with FUSE, but the cumulative luminosity of numerous young O and B stars can also be used in the optical to search for the absorption lines of HVCs in M 31. When using extended star clusters, however, we can no longer expect to have a "pencil beam" as in the case of quasars or individual stars. This introduces systematic uncertainties in the obtained column densities and thus in the derived metal abundances. This effect and its implications are discussed in detail by Bluhm et al. (2003). Consequently, spectroscopic observations of bright star clusters can help to detect absorption lines of HVCs and to study the three-dimensional structure of the HVC population, but they will probably not allow us to obtain accurate metal abundance measurements.

A detailed catalogue of bright stars in M 31 was published by Berkhuijsen & Humphreys (1989). In total they identified about 700 stars brighter than $m_{\rm V}=20$ mag possibly associated with M 31, about 300 of which are O stars. The stars are spread all over M 31 with clear concentrations along the spiral arms. This catalogue can serve as a basis for identifying promising targets for spectroscopic observations. Along the major axis of M 31 the stars found by Berkhuijsen & Humphreys (1989) extend out to a radius of about 1°.5 from the centre, allowing us to probe the halo of M 31 out to about 20 kpc.

The most promising line transition for the study of HVCs around M 31 would be the Ca II H and K lines at wavelengths of 3968.5 Å and 3933.7 Å, respectively. Both transitions have large oscillator strengths and are frequently used for absorption line studies of the ISM. In the case of successful Ca II detections it should also be possible to identify other typically strong transitions such as Na I, Mg II, or even Fe II, which will be important to constrain the physical conditions in the absorbing gas. High spectral resolution of the order of $R \equiv \lambda/\Delta\lambda \gtrsim 10\,000$ will be required to sufficiently resolve the expected line widths of the cold neutral gas. On the other hand, the small line widths of the ISM will be helpful as they can easily be discriminated against the very broad intrinsic stellar absorption lines of massive early-type stars. As most of the high-velocity gas observed around the Andromeda Galaxy has radial velocities incompatible with a participation in the regular rotation of M 31, the absorption lines of the HVCs can easily be separated from those of the interstellar medium in M 31. Consequently, optical absorption line studies of individual stars or star clusters in M 31 in combination with systematic high-resolution H I observations will allow us to study the metal abundances and the distribution of HVCs around M 31 in unprecedented detail.

The discoverers of high-velocity clouds, Christiaan Alexander Muller, Jan Hendrik Oort, and Ernst Raimond, already supposed that HVCs are located in the corona of our Galaxy. In their discovery paper (Muller et al. 1963) they concluded:

"Il n'y a actuellement pas de possibilité de mesurer les distances. Si les nuages étaient des objects proches et de courte vie situés près du plan galactique, leur nombre serait étonnamment élevé. Par conséquent, nous tendons à conclure que les objets observés sont situés dans la couronne de notre galaxie."

More than 40 years later we can confirm their assumption with our M 31 observations. This has become possible by making the important step from our Milky Way to the Andromeda Galaxy. With the observations described and proposed above we will finally be able to solve the mystery of HVCs within the next years. The new generation of sensitive optical and radio telescopes will allow us to study the properties of HVCs in great detail—including their mass spectrum, metal abundances, and distribution—and to investigate their role in the formation and evolution of galaxies.

List of common abbreviations

- CDM Cold Dark Matter The CDM theory assumes that a dominant fraction of the matter in our universe is made up of particles which have low kinetic energy (cold) and cannot be observed by their electromagnetic radiation (dark). In this theory the large structures in the universe, such as galaxies or galaxy clusters, have formed hierarchically (bottom-up scenario). Extended by dark energy, with a relative energy density of Ω_{Λ} , it is referred to as Λ CDM.
- CHVC Compact High-Velocity Cloud CHVCs are isolated high-velocity clouds (HVCs) with angular diameters of less than 2°. They were defined by Braun & Burton (1999) as a sub-class of HVCs with the aim of identifying the expected Local Group population of dark matter satellites predicted by cold dark matter simulations.
- CNM Cold Neutral Medium The cold phase of the neutral gas component of the Galactic disk or of gas clouds in general. The CNM is characterised by H I line widths of typically less than 10 km s⁻¹ FWHM, corresponding to an upper limit of the kinetic temperature of the gas of less than about 10³ K. In the case of high-velocity clouds, line widths as low as 2 km s⁻¹ FWHM have been observed towards compact, cold clumps with corresponding gas temperatures below 100 K.
- **FWHM** Full Width at Half Maximum The full width, usually of a Gaussian function, at half of the peak value. The FWHM and the dispersion, σ , of a Gaussian function are related via FWHM = 2.35σ .
- **GBT** Green Bank Telescope The Robert C. Byrd Green Bank Telescope is the largest fully-steerable radio telescope in the world with an aperture size of 100 by 110 metres. It is operated by the National Radio Astronomy Observatory (NRAO) near the village of Green Bank, West Virginia and replaced the old 90-m telescope which collapsed in 1988.
- GSR Galactic Standard of Rest Velocity rest frame which accounts for all components of motion of the observer up to the regular rotation velocity of the Galactic disk of $220 \ \mathrm{km \, s^{-1}}$. The GSR frame is particularly useful to describe objects located outside the Galactic disk.
- **HIPASS** HI Parkes All-Sky Survey The HIPASS is an extragalactic HI all-sky survey of the sky south of $+2^{\circ}$ declination. It was carried out with the 64-m radio telescope

- at Parkes in Australia and described in detail by Barnes et al. (2001). It was recently extended to a declination of $+25^{\circ}30'$ (Wong et al. 2006).
- **HPBW** Half-Power Beam Width The width of the main beam of a telescope at half of its maximum sensitivity.
- **HVC** High-Velocity Cloud HVCs are gas clouds around the Milky Way with high radial velocities incompatible with a simple model of Galactic rotation. They were discovered by Muller et al. (1963) in the 21-cm line of neutral, atomic hydrogen. Equivalents of HVCs have also been found around external galaxies.
- **LDS** Leiden/Dwingeloo Survey The LDS is a Galactic H I all-sky survey of the sky north of -30° declination. It was carried out with the 25-m radio telescope at Dwingeloo in the Netherlands by Hartmann & Burton (1997).
- LGSR Local Group Standard of Rest Velocity rest frame which accounts for all components of motion of the observer up to the peculiar motion of the Milky Way with respect to the Local Group barycentre. The LGSR frame is particularly useful for objects associated with the Local Group as a whole.
- LSR Local Standard of Rest Velocity rest frame which accounts for all components of motion of the observer up to the peculiar velocity of the sun with respect to its local environment of 16.5 km s⁻¹. The LSR frame is particularly useful for objects located in the Galactic disk.
- VLA Very Large Array The VLA is one of the world's most powerful radio interferometers. Its 27 antennas are arranged in a Y-shaped configuration with a maximum separation of 36 km. The VLA is operated by the National Radio Astronomy Observatory (NRAO) near Socorro, New Mexico.
- WNM Warm Neutral Medium The warm phase of the neutral gas component of the Galactic disk or of gas clouds in general. The WNM is characterised by typical H I line widths of the order of 25 km s⁻¹ FWHM, corresponding to an upper limit of the kinetic temperature of the gas of the order of 10⁴ K.
- WSRT Westerbork Synthesis Radio Telescope Radio interferometer operated by the Netherlands Foundation for Research in Astronomy (ASTRON). The east-west array is located near the village of Westerbork in the Dutch province of Drenthe. It has a maximum baseline of 2.7 km and is made up of 14 telescopes, each with an aperture size of 25 m.

Akeson, R. L. & Blitz, L. 1999, ApJ, 523, 163

Albert, C. E., Blades, J. C., Morton, D. C., Lockman, F. J., Proulx, M., & Ferrarese, L. 1993, ApJS, 88, 81

Alves, D. R. 2004, New Astronomy Review, 48, 659

Arnal, E. M., Bajaja, E., Larrarte, J. J., Morras, R., & Pöppel, W. G. L. 2000, A&AS, 142, 35

Arp, H. 1964, ApJ, 139, 1045

Baade, W. 1956, PASP, 68, 5

Baade, W. & Swope, H. H. 1963, AJ, 68, 435

Baade, W. & Swope, H. H. 1965, AJ, 70, 212

Bahcall, J. N., Bergeron, J., Boksenberg, A., et al. 1993, ApJS, 87, 1

Bajaja, E., Arnal, E. M., Larrarte, J. J., Morras, R., Pöppel, W. G. L., & Kalberla, P. M. W. 2005, A&A, 440, 767

Baldwin, J. E. 1954, Nature, 174, 320

Baldwin, J. E. 1957, in H. C. van de Hulst (ed.), *Proceedings from 4th IAU Symposium*, 233, Cambridge University Press, Cambridge, UK

Banks, T., Dodd, R. J., & Sullivan, D. J. 1995, MNRAS, 272, 821

Barbieri, C. V., Fraternali, F., Oosterloo, T., Bertin, G., Boomsma, R., & Sancisi, R. 2005, A&A, 439, 947

Barnes, D. G. & de Blok, W. J. G. 2004, MNRAS, 351, 333

Barnes, D. G., Staveley-Smith, L., de Blok, W. J. G., et al. 2001, MNRAS, 322, 486

Belokurov, V., Evans, N. W., Irwin, M. J., et al. 2006a, ApJ, in press (astro-ph/0605705)

Belokurov, V., Zucker, D. B., Evans, N. W., et al. 2006b, ApJ, 647, L111

Belokurov, V., Zucker, D. B., Evans, N. W., et al. 2006c, ApJ, 642, L137

Ben Bekhti, N., Brüns, C., Kerp, J., & Westmeier, T. 2006, A&A, 457, 917

Bergeron, J. & Boissé, P. 1991, A&A, 243, 344

van den Bergh, S. 1999, A&ARv, 9, 273

van den Bergh, S. 2006, AJ, 132, 1571

Berkhuijsen, E. M. & Humphreys, R. M. 1989, A&A, 214, 68

Blitz, L., Spergel, D. N., Teuben, P. J., Hartmann, D., & Burton, W. B. 1999, ApJ, 514, 818

Bluhm, H., de Boer, K. S., Marggraf, O., Richter, P., & Wakker, B. P. 2003, A&A, 398, 983

de Boer, K. S. 2004, A&A, 419, 527

de Boer, K. S., Altan, A. Z., Bomans, D. J., Lilienthal, D., Moehler, S., van Woerden, H., Wakker, B. P., & Bregman, J. N. 1994, A&A, 286, 925

Bone, D. A., Sanford, P., & Hartquist, T. W. 1983, Ap&SS, 89, 173

Boomsma, R., Oosterloo, T. A., Fraternali, F., van der Hulst, J. M., & Sancisi, R. 2005, A&A, 431, 65

Box, G. E. P. & Muller, M. E. 1958, Annals of Mathematical Statistics, 29, 610

Braun, R. 1991, ApJ, 372, 54

Braun, R. 1997, ApJ, 484, 637

Braun, R. & Burton, W. B. 1999, A&A, 341, 437

Braun, R. & Burton, W. B. 2000, A&A, 354, 853

Braun, R. & Burton, W. B. 2001, A&A, 375, 219

Braun, R. & Thilker, D. A. 2004, A&A, 417, 421

Bregman, J. N. 1980, ApJ, 236, 577

Bregman, J. N. 2004, *High-Velocity Clouds*, 341, Astrophysics and Space Science Library, Vol. 312, Kluwer Academic Publishers, Dordrecht, Boston, London, ISBN 978-1-4020-2578-5

Bresolin, F., Kudritzki, R.-P., Mendez, R. H., & Przybilla, N. 2001, ApJ, 548, L159

Brück, M. T. & Hawkins, M. R. S. 1983, A&A, 124, 216

Brüns, C., Kerp, J., Kalberla, P. M. W., & Mebold, U. 2000, A&A, 357, 120

Brüns, C., Kerp, J., & Pagels, A. 2001, A&A, 370, L26

Brüns, C., Kerp, J., Staveley-Smith, L., Mebold, U., Putman, M. E., Haynes, R. F., Kalberla, P. M. W., Muller, E., & Filipovic, M. D. 2005, A&A, 432, 45

Brüns, C. & Westmeier, T. 2004, A&A, 426, L9

Burkert, A. 1995, ApJ, 447, L25

Burton, W. B., Braun, R., & Chengalur, J. N. 2001, A&A, 369, 616

Byrd, G., Valtonen, M., McCall, M., & Innanen, K. 1994, AJ, 107, 2055

Carignan, C., Chemin, L., Huchtmeier, W. K., & Lockman, F. J. 2006, ApJ, 641, L109

Combes, F. & Charmandaris, V. 2000, A&A, 357, 75

Connors, T. W., Kawata, D., & Gibson, B. K. 2006, MNRAS, 371, 108

Corbelli, E. & Schneider, S. E. 1997, ApJ, 479, 244

Côté, P., Mateo, M., Sargent, W. L. W., & Olszewski, E. W. 2000, ApJ, 537, L91

Cram, T. R. & Giovanelli, R. 1976, A&A, 48, 39

Danly, L., Albert, C. E., & Kuntz, K. D. 1993, ApJ, 416, L29

Danly, L., Lee, Y. P., & Albert, C. E. 1995, BAAS, 27, 860

Davé, R., Cen, R., Ostriker, J. P., Bryan, G. L., Hernquist, L., Katz, N., Weinberg, D. H., Norman, M. L., & O'Shea, B. 2001, ApJ, 552, 473

Davé, R., Hernquist, L., Katz, N., & Weinberg, D. H. 1999, ApJ, 511, 521

Davies, J., Sabatini, S., Davies, L., Linder, S., Roberts, S., Smith, R., & Evans, R. 2002, MNRAS, 336, 155

Davies, R. D. 1975, MNRAS, 170, 45

Davies, R. D. & Gottesman, S. T. 1970, MNRAS, 149, 237

Dieter, N. H. 1964, AJ, 69, 288

Dieter, N. H. 1965, AJ, 70, 552

Ding, J., Charlton, J. C., & Churchill, C. W. 2005, ApJ, 621, 615

Emerson, D. T. 1974, MNRAS, 169, 607

Evans, N. W. & Wilkinson, M. I. 2000, MNRAS, 316, 929

Evans, N. W., Wilkinson, M. I., Guhathakurta, P., Grebel, E. K., & Vogt, S. S. 2000, ApJ, 540, L9

Ferguson, A., Chapman, S., Ibata, R., Irwin, M., Lewis, G., & McConnachie, A. 2006, in L. Stanghellini, J. R. Walsh, & N. G. Douglas (eds.), Planetary Nebulae Beyond the Milky Way, 286, Springer-Verlag, Berlin, ISBN 978-3-540-31011-2

Ferguson, A. M. N., Irwin, M. J., Ibata, R. A., Lewis, G. F., & Tanvir, N. R. 2002, AJ, 124, 1452

Field, G. B. 1962, Interstellar Matter in Galaxies, W. A. Benjamin, Inc., New York

Field, G. B. 1965, ApJ, 142, 531

Font, A. S., Johnston, K. V., Guhathakurta, P., Majewski, S. R., & Rich, R. M. 2006, AJ, 131, 1436

Fontana, A. & Ballester, P. 1995, ESO Messenger, 80, 37

Fraternali, F., van Moorsel, G., Sancisi, R., & Oosterloo, T. 2002, AJ, 123, 3124

Gardiner, L. T. & Noguchi, M. 1996, MNRAS, 278, 191

Grillmair, C. J. 2006, ApJ, 645, L37

Guhathakurta, P., Rich, R. M., Reitzel, D. B., Cooper, M. C., Gilbert, K. M., Majewski, S. R., Ostheimer, J. C., Geha, M. C., Johnston, K. V., & Patterson, R. J. 2006, AJ, 131, 2497

Guibert, J. 1974, A&A, 30, 353

Güsten, R. & Mezger, P. G. 1982, Vistas in Astronomy, 26, 159

Hartmann, D. & Burton, W. B. 1997, Atlas of Galactic Neutral Hydrogen, Cambridge University Press, Cambridge, UK, ISBN 978-0-521-47111-4

Hartwig, E. 1885, AN, 112, 355

de Heij, V., Braun, R., & Burton, W. B. 2002a, A&A, 392, 417

de Heij, V., Braun, R., & Burton, W. B. 2002b, A&A, 391, 159

de Heij, V., Braun, R., & Burton, W. B. 2002c, A&A, 391, 67

Hilditch, R. W., Howarth, I. D., & Harries, T. J. 2005, MNRAS, 357, 304

Hodge, P. 1992, *The Andromeda Galaxy*, Astrophysics and Space Science Library, Kluwer Academic Publishers, Dordrecht, Boston, London, ISBN 978-0-7923-1654-1

Hoffman, G. L., Salpeter, E. E., & Hirani, A. 2004, AJ, 128, 2932

Högbom, J. A. 1974, A&AS, 15, 417

Hopp, U., Schulte-Ladbeck, R. E., & Kerp, J. 2003, MNRAS, 339, 33

Hubble, E. P. 1929, ApJ, 69, 103

- Huchtmeier, W. K. & Richter, O. G. 1986, A&AS, 63, 323
- van de Hulst, H. C., Raimond, E., & van Woerden, H. 1957, Bull. Astr. Inst. Netherlands, 14, 1
- Ibata, R., Chapman, S., Ferguson, A. M. N., Lewis, G., Irwin, M., & Tanvir, N. 2005, ApJ, 634, 287
- Ibata, R., Irwin, M., Lewis, G., Ferguson, A. M. N., & Tanvir, N. 2001a, Nature, 412, 49
- Ibata, R., Irwin, M., Lewis, G. F., & Stolte, A. 2001b, ApJ, 547, L133
- Ibata, R. A., Gilmore, G., & Irwin, M. J. 1994, Nature, 370, 194
- Innanen, K. A., Kamper, K. W., van den Bergh, S., & Papp, K. A. 1982, ApJ, 254, 515
- Irwin, M. J., Belokurov, V., Evans, N. W., et al. 2007, ApJ, in press, astro-ph/0701154
- Ivezić, Ž. & Christodoulou, D. M. 1997, ApJ, 486, 818
- Jannuzi, B. T., Bahcall, J. N., Bergeron, J., et al. 1998, ApJS, 118, 1
- Johnson, D. W. & Gottesman, S. T. 1983, ApJ, 275, 549
- Kahn, F. D. 1981, *Investigating the Universe*, 1, Astrophysics and Space Science Library, Vol. 91, D. Reidel Publishing Co., Dordrecht, ISBN 978-90-277-1325-4
- Kalberla, P. M. W., Burton, W. B., Hartmann, D., Arnal, E. M., Bajaja, E., Morras, R., & Pöppel, W. G. L. 2005, A&A, 440, 775
- Kalberla, P. M. W. & Haud, U. 2006, A&A, 455, 481
- Kalberla, P. M. W., Mebold, U., & Reich, W. 1980, A&A, 82, 275
- Kalberla, P. M. W., Mebold, U., & Reif, K. 1982, A&A, 106, 190
- Kennicutt, R. C. 1998, ApJ, 498, 541
- Kernighan, B. W. & Ritchie, D. M. 1978, *The C Programming Language*, Prentice Hall, Englewood Cliffs, NJ, ISBN 978-0-13-110163-0
- Kerp, J., Burton, W. B., Egger, R., Freyberg, M. J., Hartmann, D., Kalberla, P. M. W., Mebold, U., & Pietz, J. 1999, A&A, 342, 213
- Kerp, J., Lesch, H., & Mack, K.-H. 1994, A&A, 286, L13
- Kerp, J., Mack, K.-H., Egger, R., Pietz, J., Zimmer, F., Mebold, U., Burton, W. B., & Hartmann, D. 1996, A&A, 312, 67
- Kerp, J., Pietz, J., Kalberla, P. M. W., Burton, W. B., Egger, R., Freyberg, M. J., Hartmann, D., & Mebold, U. 1998, in D. Breitschwerdt, M. J. Freyberg, & J. Trümper (eds.), The Local Bubble and Beyond, 457, Springer-Verlag, Berlin, Heidelberg, New York, ISBN 978-3-540-64306-7

Kim, K.-T., Minh, Y. C., & Hasegawa, T. I. 1989, Journal of the Korean Astronomical Society, 22, 25

Klypin, A., Kravtsov, A. V., Valenzuela, O., & Prada, F. 1999, ApJ, 522, 82

Koch, A. & Grebel, E. K. 2006, AJ, 131, 1405

Konz, C., Brüns, C., & Birk, G. T. 2002, A&A, 391, 713

Kravtsov, A. V., Gnedin, O. Y., & Klypin, A. A. 2004, ApJ, 609, 482

Kroupa, P., Theis, C., & Boily, C. M. 2005, A&A, 431, 517

Krüger, E. 1885, AN, 112, 245

Kutyrev, A. S. 1986, Astron. Tsirkulyar, 1396, 3

Kutyrev, A. S. & Reynolds, R. J. 1989, ApJ, 344, L9

Lallement, R. 2004, A&A, 422, 391

Lauer, T. R., Faber, S. M., Groth, E. J., et al. 1993, AJ, 106, 1436

Lo, K. Y., Sargent, W. L. W., & Young, K. 1993, AJ, 106, 507

Maloney, P. R. & Putman, M. E. 2003, ApJ, 589, 270

Martin, N. F., Ibata, R. A., Irwin, M. J., Chapman, S., Lewis, G. F., Ferguson, A. M. N., Tanvir, N., & McConnachie, A. W. 2006, MNRAS, 371, 1983

Mastropietro, C., Moore, B., Mayer, L., Wadsley, J., & Stadel, J. 2005, MNRAS, 363, 509

Mateo, M. L. 1998, ARA&A, 36, 435

Mathewson, D. S., Cleary, M. N., & Murray, J. D. 1974, ApJ, 190, 291

Mayr, S. 1614, Mundus Iovialis anno M.DC.IX Detectus Ope Perspicilli Belgici, Johann Laur, Nürnberg

McCarthy, J. K., Venn, K. A., Lennon, D. J., Kudritzki, R.-P., & Puls, J. 1998, ASP Conf. Ser., 131, 197

McConnachie, A. W. & Irwin, M. J. 2006, MNRAS, 365, 902

McConnachie, A. W., Irwin, M. J., Lewis, G. F., Ibata, R. A., Chapman, S. C., Ferguson, A. M. N., & Tanvir, N. R. 2004, MNRAS, 351, L94

Messier, C. 1774, Histoire de l'Académie Royale des Sciences, Année 1771, 435

Miville-Deschênes, M.-A., Boulanger, F., Reach, W. T., & Noriega-Crespo, A. 2005, ApJ, 631, L57

Moore, B., Ghigna, S., Governato, F., Lake, G., Quinn, T., Stadel, J., & Tozzi, P. 1999, ApJ, 524, L19

Muller, C. A., Oort, J. H., & Raimond, E. 1963, C.R. Acad. Sc. Paris, 257, 1661

Olano, C. A. 2004, A&A, 423, 895

Oort, J. H. 1966, Bull. Astr. Inst. Netherlands, 18, 421

Oort, J. H. 1970, A&A, 7, 381

Peñarrubia, J., Martínez-Delgado, D., Rix, H. W., Gómez-Flechoso, M. A., Munn, J., Newberg, H., Bell, E. F., Yanny, B., Zucker, D., & Grebel, E. K. 2005, ApJ, 626, 128

Perrett, K. M., Bridges, T. J., Hanes, D. A., Irwin, M. J., Brodie, J. P., Carter, D., Huchra, J. P., & Watson, F. G. 2002, AJ, 123, 2490

Pisano, D. J., Barnes, D. G., Gibson, B. K., Staveley-Smith, L., Freeman, K. C., & Kilborn, V. A. 2004, ApJ, 610, L17

Prata, S. W. 1964, Bull. Astr. Inst. Netherlands, 17, 511

Press, W. H., Teukolsky, S. A., Vetterling, W. T., & Flannery, B. P. 1992, Numerical Recipes in C: The Art of Scientific Computing, Cambridge University Press, Cambridge, UK, ISBN 978-0-521-43108-8

Putman, M. E., Bland-Hawthorn, J., Veilleux, S., Gibson, B. K., Freeman, K. C., & Maloney, P. R. 2003a, ApJ, 597, 948

Putman, M. E., Gibson, B. K., Staveley-Smith, L., et al. 1998, Nature, 394, 752

Putman, M. E., de Heij, V., Staveley-Smith, L., et al. 2002, AJ, 123, 873

Putman, M. E., Staveley-Smith, L., Freeman, K. C., Gibson, B. K., & Barnes, D. G. 2003b, ApJ, 586, 170

Putman, M. E., Thom, C., Gibson, B. K., & Staveley-Smith, L. 2004, ApJ, 603, L77

Quilis, V. & Moore, B. 2001, ApJ, 555, L95

Rasmussen, A., Kahn, S. M., & Paerels, F. 2003, in J. L. Rosenberg & M. E. Putman (eds.), *The IGM/Galaxy Connection: The Distribution of Baryons at* z=0, 109, Kluwer Academic Publishers, Dordrecht, ISBN 978-1-4020-1289-1

Recillas-Cruz, E. 1982, MNRAS, 201, 473

Reid, M. J. 1993, ARA&A, 31, 345

Reynolds, R. J. 1987, ApJ, 323, 553

Richter, P., de Boer, K. S., Widmann, H., Kappelmann, N., Gringel, W., Grewing, M., & Barnstedt, J. 1999, Nature, 402, 386

Richter, P., Sembach, K. R., & Howk, J. C. 2003, A&A, 405, 1013

Richter, P., Sembach, K. R., Savage, B. D., Murphy, E. B., & Wakker, B. P. 2000, Bulletin of the American Astronomical Society, 32, 1404

Richter, P., Westmeier, T., & Brüns, C. 2005, A&A, 442, L49

Roberts, I. 1888, MNRAS, 49, 65

Roberts, M. S. 1966, ApJ, 144, 639

Roberts, M. S. & Whitehurst, R. N. 1975, ApJ, 201, 327

Routly, P. M. & Spitzer, L. 1952, ApJ, 115, 227

Ryans, R. S. I., Keenan, F. P., Sembach, K. R., & Davies, R. D. 1997, MNRAS, 289, 83

Sawa, T. & Sofue, Y. 1982, PASJ, 34, 189

Scheiner, J. 1898, AN, 148, 325

Scheiner, J. 1899, ApJ, 9, 149

Schjellerup, H. C. F. C. 1874, Description des étoiles fixes composée au milieu du dixième siècle de notre ère par l'astronome persan Abd-al-Rahman al-Sûfi, St. Petersburg

Schneider, S. E. 1997, PASA, 14, 99

Sembach, K. R., Wakker, B. P., Savage, B. D., Richter, P., Meade, M., Shull, J. M., Jenkins, E. B., Sonneborn, G., & Moos, H. W. 2003, ApJS, 146, 165

Shapiro, P. R. & Field, G. B. 1976, ApJ, 205, 762

Siegel, M. H., Majewski, S. R., Gallart, C., Sohn, S. T., Kunkel, W. E., & Braun, R. 2005, ApJ, 623, 181

Silich, S., Lozinskaya, T., Moiseev, A., Podorvanuk, N., Rosado, M., Borissova, J., & Valdez-Gutierrez, M. 2006, A&A, 448, 123

Simien, F., Athanassoula, E., Pellet, A., Monnet, G., Maucherat, A., & Courtès, G. 1978, A&A, 67, 73

Simon, J. D. & Blitz, L. 2002, ApJ, 574, 726

Slipher, V. M. 1913, Lowell Observatory Bulletin, 1, 2.56

Slipher, V. M. 1914, Lowell Observatory Bulletin, 1, 2.66

Smoker, J. V., Lynn, B. B., Rolleston, W. R. J., et al. 2004, MNRAS, 352, 1279

Sofue, Y. & Kato, T. 1981, PASJ, 33, 449

Songaila, A., Bryant, W., & Cowie, L. L. 1989, ApJ, 345, L71

Spitzer, L. 1956, ApJ, 124, 20

Spitzer, L. 1978, *Physical Processes in the Interstellar Medium*, John Wiley & Sons, New York, Chichester, Brisbane, Toronto, ISBN 978-0-471-02232-9

Spitzer, L., Epstein, I., & Hen, L. 1950, Annales d'Astrophysique, 13, 147

Stanek, K. Z. & Garnavich, P. M. 1998, ApJ, 503, 131

Sternberg, A., McKee, C. F., & Wolfire, M. G. 2002, ApJS, 143, 419

al-Sufi, A. 964, Kitab al-Kawatib al-Thabit al-Musawwar, Isfahan

Talbot, R. J. 1980, ApJ, 235, 821

Thilker, D. A., Braun, R., Walterbos, R. A. M., Corbelli, E., Lockman, F. J., Murphy, E., & Maddalena, R. 2004, ApJ, 601, L39

Thom, C., Gibson, B. K., & Christlieb, N. 2005, ApJS, 161, 147

Thom, C., Putman, M. E., Gibson, B. K., Christlieb, N., Flynn, C., Beers, T. C., Wilhelm, R., & Lee, Y. S. 2006, ApJ, 638, L97

Timmes, F. X., Diehl, R., & Hartmann, D. H. 1997, ApJ, 479, 760

Tufte, S. L., Reynolds, R. J., & Haffner, L. M. 1998, ApJ, 504, 773

Tufte, S. L., Wilson, J. D., Madsen, G. J., Haffner, L. M., & Reynolds, R. J. 2002, ApJ, 572, L153

Turner, B. E. 1984, Vistas in Astronomy, 27, 303

Wakker, B. P. 1991, A&A, 250, 499

Wakker, B. P. 2001, ApJS, 136, 463

Wakker, B. P. 2004, High-Velocity Clouds, 25, Astrophysics and Space Science Library, Vol. 312, Kluwer Academic Publishers, Dordrecht, Boston, London, ISBN 978-1-4020-2578-5

Wakker, B. P. & Boulanger, F. 1986, A&A, 170, 84

Wakker, B. P., Howk, C., Schwarz, U., van Woerden, H., Beers, T., Wilhelm, R., Kalberla, P. M. W., & Danly, L. 1996, ApJ, 473, 834

Wakker, B. P., Murphy, E. M., van Woerden, H., & Dame, T. M. 1997, ApJ, 488, 216

Wakker, B. P. & van Woerden, H. 1991, A&A, 250, 509

Wakker, B. P. & van Woerden, H. 1997, ARA&A, 35, 217

Wall, J. V. & Jenkins, C. R. 2003, Practical Statistics for Astronomers, Cambridge Observing Handbooks for Research Astronomers, Cambridge University Press, Cambridge, UK, ISBN 978-0-521-45416-2

Wannier, P. & Wrixon, G. T. 1972, ApJ, 173, L119

Wannier, P., Wrixon, G. T., & Wilson, R. W. 1972, A&A, 18, 224

Weiner, B. J., Vogel, S. N., & Williams, T. B. 2001, in J. E. Hibbard, M. Rupen, & J. H. van Gorkom (eds.), *Gas and Galaxy Evolution*, 515, ASP Conference Series, San Francisco, ISBN 978-1-58381-077-4

Westmeier, T., Braun, R., & Thilker, D. A. 2005a, A&A, 436, 101

Westmeier, T., Brüns, C., & Kerp, J. 2005b, A&A, 432, 937

Whitehurst, R. N., Roberts, M. S., & Cram, T. R. 1978, in E. M. Berkhuijsen & R. Wielebinski (eds.), *Structure and properties of nearby galaxies*, 175, D. Reidel Publishing Co., Dordrecht, ISBN 978-90-277-0874-8

Wilcots, E. M. & Miller, B. W. 1998, AJ, 116, 2363

Wilkinson, M. I. & Evans, N. W. 1999, MNRAS, 310, 645

Williams, B. F. 2003, AJ, 126, 1312

van Woerden, H., Peletier, R. F., Schwarz, U. J., Wakker, B. P., & Kalberla, P. M. W. 1999a, in B. K. Gibson & M. E. Putman (eds.), *Stromlo Workshop on High-Velocity Clouds*, 1, ASP Conference Series, San Francisco, ISBN 978-1-886733-87-9

van Woerden, H., Schwarz, U. J., Peletier, R. F., Wakker, B. P., & Kalberla, P. M. W. 1999b, Nature, 400, 138

Wolfire, M. G., McKee, C. F., Hollenbach, D., & Tielens, A. G. G. M. 1995, ApJ, 453, 673

Wong, O. I., Ryan-Weber, E. V., Garcia-Appadoo, D. A., et al. 2006, MNRAS, 371, 1855

Yanny, B., Newberg, H. J., Grebel, E. K., et al. 2003, ApJ, 588, 824

York, D. G., Adelman, J., Anderson, J. E., Jr., et al. 2000, AJ, 120, 1579

Young, L. M. & Lo, K. Y. 1997a, ApJ, 476, 127

Young, L. M. & Lo, K. Y. 1997b, ApJ, 490, 710

Zucker, D. B., Belokurov, V., Evans, N. W., et al. 2006a, ApJ, 643, L103

Zucker, D. B., Kniazev, A. Y., Bell, E. F., et al. 2004, ApJ, 612, L121

Zucker, D. B., Kniazev, A. Y., Martinez-Delgado, D., et al. 2006b, ApJ, submitted (astro-ph/0601599)

Zwaan, M. A. 2001, MNRAS, 325, 1142

Zwicky, F. 1959, *Multiple Galaxies*, 373, Handbuch der Physik, Springer-Verlag, Berlin, Göttingen, Heidelberg

Acknowledgements

First of all, I would like to express my gratitude to my thesis advisor and first referee, Jürgen Kerp, for offering me this project. Without his constant support and motivation this thesis would not exist. I am also grateful to my second referee, Klaas S. de Boer, my "fachnaher" and "fachangrenzender Gutachter", Klaus Desch and Andreas Bott, and my external referee, Mary E. Putman, for reviewing this thesis.

Furthermore, I would like to thank *Robert Braun* and *Christian Brüns* for their continuous encouragement and support during my project. I would also like to thank my other scientific collaborators, namely *Nadya Ben Bekhti, Erwin de Blok, Philipp Richter, David Thilker*, and *Christopher Thom*. I am also grateful to the *telescope operators* and *technical staff* at Effelsberg, the WSRT, and the VLA for their assistence in the observations.

This work was supported by the *Deutsche Forschungsgemeinschaft* (DFG) through projects KE 757/4–1 and KE 757/4–2. Moreover, I am grateful to *ASTRON* in Dwingeloo for offering me a place in their Summer Student Programme 2004, and to *Peter Schneider* for providing me additional financial support during the final stage of my thesis.

I would also like to thank all my friends and colleagues here in Bonn for a good and inspiring working environment, in particular *Claudia Brüns*, *Jens Kauffmann*, and *Benjamin Winkel*.

Last but not least, I am grateful to *Bi-Qing* for her love and support, and for being my motivation and source of inspiration throughout the final stage of my thesis.